UNIVERSITY OF LIVERPOOL

Innovative Multispectral Optoacoustic Tomography Strategies for Evaluating Different Aspects of Renal Function

Thesis submitted in accordance with the requirements of the University of Liverpool for the degree of Doctor in Philosophy

by

James Littlewood

August 2022

Abstract

Kidney disease carries significant morbidity, mortality, and cost while its prevalence is rising. Preclinical work utilising different kidney injury models to evaluate novel therapies is a valuable step in the transition of treatments from lab to clinic. An accurate measurement of kidney function is important in this setting to make appropriate conclusions about the efficacy of a therapy. Measuring kidney function by dynamic contrast enhanced (DCE) imaging offers the distinct benefit of separately measuring left and right kidney function which can differ even in health. Additionally, measuring both kidneys in a unilateral injury model offers the advantage of an internal control.

This thesis aims to assess whether near-infrared (NIR) dyes and their clearance in multispectral optoacoustic tomography (MSOT) can be used to measure the renal excretory functions of glomerular filtration and tubular secretion in health and a surgical model of ischaemia reperfusion injury (IRI). The dyes ABZWCY-HPβCD (glomerular filtration marker) and STAR FLUOR 770 Acid (potential tubular secretion marker) are examined for this purpose. We explore the best metrics of quantifying renal injury in DCE MSOT and whether the application of mathematical models could allow the measurement glomerular filtration rate (GFR) or tubular secretion rate (TSR) in a single kidney. Finally, the MSOT clearance kinetics of these dyes are compared to more standard measures of renal health: sinistrin clearance, histology, and dimercaptosuccinic acid (DMSA) uptake.

ABZWCY-HPβCD, STAR FLUOR 770 Acid, and the renal clearance of the two dyes can be detected by MSOT in C57BL/6 albino mice. However, light fluence impairs the accurate absolute quantification of these dyes at the depth of the aorta.

ABZWCY-HPβCD shows significantly different MSOT renal kinetics from the current standard MSOT renal contrast agent, IRDye 800CW. In combination with a modified Patlak-Rutland model, ABZWCY-HPβCD can be used to calculate a single kidney GFR. This method showed a greater correlation with GFR measured by sinistrin clearance than MSOT model-free measures.

STAR FLUOR 770 Acid has shown significant protein binding and evidence of biliary clearance both in MSOT and fluorescence imaging. However, it is partially cleared by the kidneys and spectrally unchanged following this. DCE MSOT measured STAR FLUOR 770 Acid clearance does not correlate with split renal function measured by the tubular uptake of DMSA. STAR FLUOR 770 Acid clearance shows recovery 3 weeks after IRI, while DMSA uptake and histology show ongoing tubular injury.

The results indicate that DCE MSOT is a fast, safe, flexible, and approachable imaging modality for evaluating different renal excretory functions. Further, the NIR dye ABZWCY-HPβCD appears suitable for measuring single kidney GFR in MSOT. STAR FLUOR 770 Acid requires further assessment as a tubular secretion marker. Improvements and validation of fluence correction algorithms will facilitate absolute quantification in MSOT that will further its ability to determine renal clearance rates.

Acknowledgements

I would like to thank my supervisors at iThera Medical and the University of Liverpool: Prof Murray, Dr Devling, Dr Burton, Dr Wilm, Prof Bearon, and Dr Levy. I have been well supported and given thoughtful and kind advice throughout my work. Despite the complications of the coronavirus pandemic, I have always been well accommodated and encouraged to persevere.

At iThera Medical I have been lucky enough to approach any member of the team and receive advice. In addition to Dr Devling and Dr Burton, I would like to thank Thomas Sardella, Patricia Smole, Stefan Morscher, and Alexa Hasenbach. They have provided valuable insight while assessing my imaging work and answering my questions about the highly technical aspects of photoacoustic imaging.

At the University of Liverpool, I would like to also thank Dr Taylor, Prof Poptani, Prof Ressel, Dr Sharkey, Dr Harwood, Katherine Triviño Cepeda, Alejandra Hernández-Pichardo, Andreea Luchian, and Soham Mukherjee. They have provided me with practical assistance, a wealth of knowledge and, in many cases, both. Thank you to all the animal technicians for their advice and training, specifically Sarah, Emily, Esther, Jo, Rees, and Katharine. A particular thank you to Dr Harwood who performed the surgical aspects of this project without which this body of work would be much smaller. Thank you to Dr Sharkey and Dr Harwood for assisting me in the multimodality imaging experiments.

Thank you to our collaborators at Heidelberg University, Germany, Utrecht University, Netherlands, and Cyanagen, Italy: Prof Gretz, Yinuo Xie, Prof Masereeuw, João Ferreira, Dr Perciaccante, and Srishti Vajpayee. Thank you for the provision of the dyes for my work and the invaluable advice you provided. Thanks to Srishti for all her dye synthesis work. Thanks to Yinuo and João for their assessments of STAR FLUOR 770 Acid.

Thank you to Dr Shahed Ahmed and Dr Rebecca Brown who have encouraged me to take the time out of clinical practice to complete this PhD and supported me to continue despite the clinical pressures of the last two years.

Thank you to my family: my mum, dad, and brother. I could not be where I am without what you have given me.

Finally, thank you to my wife, Ashleigh. I dedicate my thesis to you, my favourite person.

Contents

List of Figures

List of Tables

List of Equations

List of Presentations and Publications

Preprint Review - Hernandez Pichardo, A. et al. Computed tomography lacks sensitivity to image gold labelled mesenchymal stromal cells in vivo as evidenced by multispectral optoacoustic tomography. http://biorxiv.org/lookup/doi/10.1101/2022.06.15.495483 (2022) doi:10.1101/2022.06.15.495483.

Oral Presentation - Modelling Renal Function in Multispectral Optoacoustic Tomography. Cheshire and Merseyside Nephrology Research Afternoon 13th May 2022 (Liverpool, UK)

Oral and Poster Presentation - MSOT Strategies for Evaluating Different Aspects of Renal Function in Rodents. Renaltoolbox International Conference 2022. 6th April 2022 (Liverpool, UK)

Oral Presentation - A Custom Compartment Model of Single Kidney Glomerular Filtration Rate Using Multispectral Optoacoustic Tomography. UK Kidney Week 2021. 4th October 2021 (Virtual, UK)

Oral Presentation - Developing mathematical models to assess renal function: challenges and solutions. EPSRC Liverpool Centre for Mathematics in Healthcare Research showcase and future directions 2021. 5th July 2021 (Virtual, UK)

Published Review - Amadeo, F. et al. Mesenchymal stromal cells: what have we learned so far about their therapeutic potential and mechanisms of action? Emerg Top Life Sci 5, 549–562 (2021).

Published Review - McWilliam, S. J. et al. The complex interplay between kidney injury and inflammation. Clin Kidney J (2020) doi:10.1093/ckj/sfaa164.

Poster Presentation - Evaluating glomerular filtration in mice by measuring near-infrared dyes with Multispectral Optoacoustic Tomography. Optoacoustic Imaging Meeting 2019. 14th November 2019 (Essen, Germany)

List of Abbreviations

ABC	ATP-binding cassette
ADH	Antidiuretic hormone
AIF	Arterial input function
AKI	Acute kidney injury
ATN	Acute tubular necrosis
ATP	Adenosine triphosphate
AUC	Area under the curve
AUC C:P ratio	Area under the curve cortex to pelvis ratio
BR	Baumann Rudin
BSA	Body surface area
BW	Body weight
CI	Confidence intervals
CKD	Chronic kidney disease
CKD EPI	Chronic kidney disease epidemiology collaboration
CT	Computed tomography
DCE	Dynamic contrast enhanced
DMSA	Dimercaptosuccinic acid
DOTA	Tetraxetan
DTPA	Diethylenetriaminepentaacetic acid
EDTA	Ethylenediaminetetraacetic acid
eGFR	Estimated glomerular filtration rate
ESRF	End stage renal failure
FITC	Fluorescein isothiocyanate
FSHL	Fluorescein isothiocyanate-sinistrin half-life
FUR	Fractional uptake rate
FVV	Fractional vascular volume
GFR	Glomerular filtration rate
HPβCD	2-hydroxylpropyl-beta-cyclodextrin
αKG	α-ketoglutarate
ICG	Indocyanine green
IRI	Ischaemia reperfusion injury
IV	Intravenous
KDIGO	Kidney Disease: Improving Global Outcomes
MAG3	Mercaptoacetyltriglycine
MDRD	Modification of Diet in Renal Disease
MPRs	Modified Patlak-Rutland with spine blood vessel arterial input function
MRI	Magnetic resonance imaging
mSO_2	Multispectral optoacoustic tomography oxygen saturation
MSOT	Multispectral optoacoustic tomography
NC3R	National centre for the replacement, refinement, and reduction of animals in research
NIR	Near-infrared
OAT	Organic anion transporter
OCT	Organic cation transporter

PAH	Para-aminohippuric acid
PBC	Probenecid
PBS	Phosphate buffered saline
PK	pharmacokinetic
PR	Patlak-Rutland
PRa	Patlak-Rutland with aorta arterial input function
PRs	Patlak-Rutland with spine blood vessel arterial input function
PTC	Proximal tubular cell
ROI	Region of interest
SCID	Severe combined immunodeficient
SK-GFR	Single kidney glomerular filtration rate
SLC	Solute carrier
SPECT	Single-photon emission computed tomography
Tc-99m	Technetium-99m
TD	Transcutaneous device
T^{MAX}	The time from injection of a contrast agent to the peak in the renal cortex
T^{MAX} Delay	The time between the peak in the renal cortex and the peak in the renal pelvis
TSR	Tubular secretion rate
UK	United Kingdom
USA	United States of America

1 Introduction

This thesis will focus on the use of dynamic contrast enhanced (DCE) multispectral optoacoustic tomography (MSOT) using two near-infrared (NIR) dyes to measure glomerular filtration rate (GFR) and tubular secretion rate (TSR) in health and ischaemia reperfusion injury (IRI).

1.1 Kidney Disease

1.1.1 Acute Kidney Injury

Acute Kidney Injury (AKI) is defined as a sudden decrease in kidney function that can be attributed to many different causes[1,2]. This deterioration in function is typically detected by changes in serum creatinine or the volume of urine produced, both of which are markers of excretory function[1,2]. The result can be a spectrum of disease from asymptomatic patients to life threatening illness resulting from the inability to regulate body water, pH, and excrete metabolic waste[3]. AKI is a frequent diagnosis in patients admitted to hospital: It is responsible for 1-4% of hospital admissions and it is diagnosed in up to 20% of adult hospital inpatients[4–8]. AKI has a significant associated mortality, morbidity, and cost[3]. Europe has seen a pooled mortality between 17.2 and 26.3%, and the world has seen a mean mortality of 23%[7]. AKI is associated with the initiation and progression of Chronic Kidney Disease (CKD)[3,9]. Patients who have AKI are 8.8 times more likely to develop CKD and 3.1 times more likely to develop end stage renal failure (ESRF)[9]. Even patients with the mildest degree of AKI show greater losses in renal function in the long term than a matched cohort without AKI[10]. CKD and ESRF carry their own morbidity and mortality burdens. AKI has a significant financial burden. A patient admitted with AKI will cost between £3000 and £5000 for their inpatient care and the lifetime care cost for one years' worth of AKI patients was approximated at £179 million in England in 2014[11–13].

1.1.2 Chronic Kidney Disease and End Stage Renal Failure

CKD is the long term and often progressive loss of kidney function. CKD is a significant and growing cause of mortality globally – death due to CKD has increased by 89% between 1990 and 2016[14,15]. It has been proposed that the adaptive changes the kidney makes in response to injury are maladaptive and lead to fibrosis and sclerosis resulting in the progressive nature of CKD[16]. There are no current treatments for established CKD that can restore renal function. CKD management is focused on preventing progression by treating the underlying cause and risk factors for progression. Further episodes of AKI in patients with CKD are common and harmful, increasing the probability that a patient will require organ support or

die[17]. CKD can progress to ESRF where the function of the kidneys falls below the physiological requirements of the body. Without renal transplant or dialysis (collectively known as renal replacement therapy), ESRF is ultimately fatal. The number of people expected to require renal replacement therapy is projected to be between 4.9 million and 9.7 million by 2030[18].

All forms of dialysis carry a significant cost[3,19]. 0.05% of the UK population has ESRF but their care costs the UK's National Health Service 2% of its total budget[20]. In 2008, haemodialysis was estimated to cost more than £35,000 per year per patient, while the cost of peritoneal dialysis was estimated at more than £21,000 per year per patient[19]. Dialysis is associated with a reduced quality of life[3]. Haemodialysis carries potential complications that can relate to vascular access, allergy, infection, coagulation, haemodynamic stress leading to hypoperfusion of other organs, or inadequate dialysis[21]. Peritoneal dialysis carries complications relating to catheter position, infection, hernias, fluid leaks, prolapse, gastrointestinal disturbance, and peritoneal membrane related dialysis failure[22]. Both haemodialysis and peritoneal dialysis carry a significant risk of cardiovascular death though this is likely due to different mechanisms[23].

Renal transplantation is found to have significant long term survival benefits when compared with dialysis[24,25] as well as being ultimately less expensive and improving the quality of life for patients[26]. However, there is a significant ongoing shortage of donor organs[27]. In the UK, both the numbers of deceased kidney donor transplants and living kidney donor transplants have fallen by 22% and 60% respectively[27]. Additionally, renal transplantation is generally associated with long term immunosuppressant use which increases the risk of infection, cancer, hypertension, and worsening transplant function[28].

1.1.3 Kidney Function

The term 'kidney function' is used synonymously with GFR. However, the kidneys perform a number of functions via a range of physiological mechanisms[29]. They are the principle organ of excretion, clearing the blood of metabolic waste products via filtration and secretion. They achieve homeostasis of water, pH, and electrolytes. They produce hormones responsible for red blood cell production (erythropoietin), calcium balance (calcitriol), and maintenance of blood pressure (renin). In the clinic, kidney health is most often assessed by the measurement of serum creatinine which is a marker of renal excretory function and can be used to estimate GFR. GFR is associated with the loss of tubular, metabolic, and endocrine function, as well as the loss of functional renal mass[30,31].

Measurement of kidney health, function, and injury is important because renal disease frequently presents asymptomatically, and is associated with significant morbidity and mortality[3,17,32]. Accurate and repeatable measures of kidney function are necessary in both the preclinical and clinical setting to deliver disease screening, diagnosis, prognosis, and to quantify therapeutic response.

1.1.4 The Importance of Accurate Preclinical Assessment of Renal Function

Investigation of renal disease and assessment of novel treatments is vitally important for addressing the growing health crisis presented by CKD and ESRF. Prevention and amelioration of AKI is key to this goal. Animal models have previously facilitated a deep understanding of the molecular mechanisms of AKI and CKD[16,33–36]. While there are valid questions regarding animal injury models and their equivalence to human pathology, direct investigation of AKI via renal biopsy in humans is hard to justify in the most common cause of AKI (acute tubular necrosis, ATN) where no specific treatment options exist[37]. In addition, the superiority of alternatives to animals experiments are yet to be proven[38,39]. Tissue engineering has shown great promise, but might ignore the impact of a pathology or therapy on the whole organism via organ crosstalk or an indirect mechanism of action[34,40–42]. Phase 0 studies in humans may assist in resolving this, but further validation and standardisation is required[43].

An NC3R approach focused on the minimal and applicable use of animals is most appropriate[44]. Where an animal model is implemented, accurate and reproducible outcome measurements that are relevant to human disease are crucial. These should be accompanied by the minimisation of suffering for animals.

1.1.5 Ischaemia-Reperfusion Injury

IRI is the process of the restriction of blood flow to a tissue followed by the restoration of its perfusion. Both the ischaemic and reperfusion phases contribute to injury[45]. IRI has significant clinical relevance. The mechanisms involved in IRI are implicated in solid organ transplantation, tissue infarction and vascular restoration (angioplasty, cardiac bypass), and tissue hypoperfusion (thrombosis, haemorrhage, inflammation, allergy, neurological damage, gastrointestinal fluid losses, heart failure, and sepsis amongst others)[45–47]. An increased duration of ischaemic time between organ harvest and implantation is associated with an increased graft failure rate of kidney transplants[48]. ATN, the most common cause of AKI, is frequently caused by conditions resulting in kidney hypoperfusion (sepsis, trauma, vascular surgery, burns)[2]. Several different animal models of ATN exist to mimic these

pathological conditions. These include surgical clamping of renal blood vessels, sepsis induced by pathogen infusion or bowel puncture, and nephrotoxic drug injury[49–52]. While surgical clamping of the vasculature benefits from being technically simple, titratable, and reproducible, it neither fully represents the conditions at renal transplant (complete extraction and cold ischaemia) nor the toxic insult and exact immune cascade that occurs in the more clinically prevalent septic injury[46,50,52,53].

1.2 Kidney Anatomy

1.2.1 Human Kidney Anatomy

Information for this section was provided by Kriz et al[54] and Bailey et al[55] unless otherwise referenced.

Humans have two 12 cm long kidneys that are retroperitoneal and drain into a single pelvic bladder. The gross anatomy of the human kidney is shown in Figure 1.1. The kidney broadly divides its parenchyma into an outer layer, the cortex, and an inner layer, the medulla. These surround the renal pelvis which is where urine collects before draining via the ureter to the bladder. The parenchyma consists of the nephrons, collecting ducts, blood vessels, and interstitium.

The human kidneys contain 200,000 to 2.7 million functional units known as nephrons (Figure 1.2)[56,57]. These are situated radially with the glomerulus in the cortex and the collecting ducts running through the medulla to the papilla and renal pelvis. Nephrons produce and tailor the urine which then drains into the renal pelvis via the collecting ducts. A reduced number of nephrons is associated with reduced renal function and an increased risk of developing kidney disease[56]. The kidney has a distinctive blood supply: arterioles initially feed specialised capillaries in the cortex (the glomeruli) which then subsequently feed the vasa recta and associated capillary beds in the medulla. This results in a relative hypoxia in the deeper tissues of the kidney. Finally, the interstitium containing fibroblasts, immune cells, interstitial fluid, and extracellular matrix exists between the nephrons and blood supply. The interstitium provides structural support, immune responses to injury and infection, and endocrine functions[58,59].

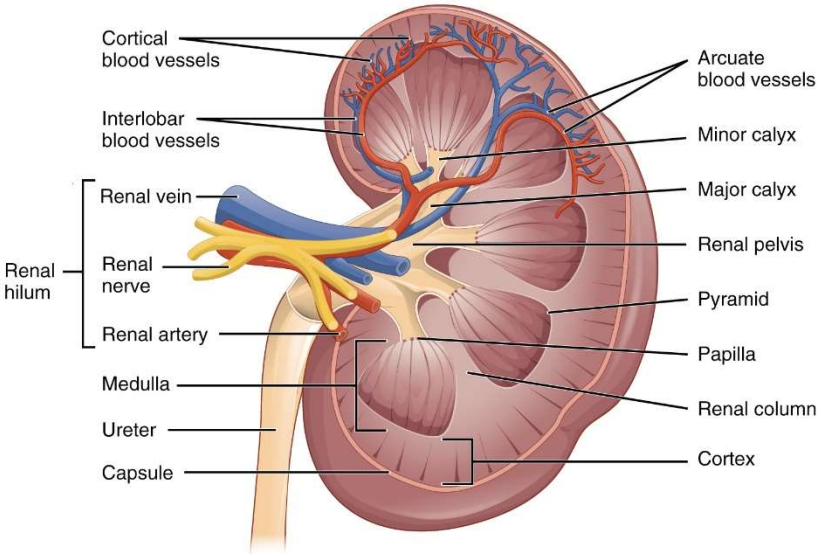

Figure 1.1: Gross Anatomy of the Kidney
Adapted from OpenStax (2016)[60] on a Creative Commons Attribution 4.0 International License. Download for free at http://cnx.org/contents/14fb4ad7-39a1-4eee-ab6e-3ef2482e3e22@8.24

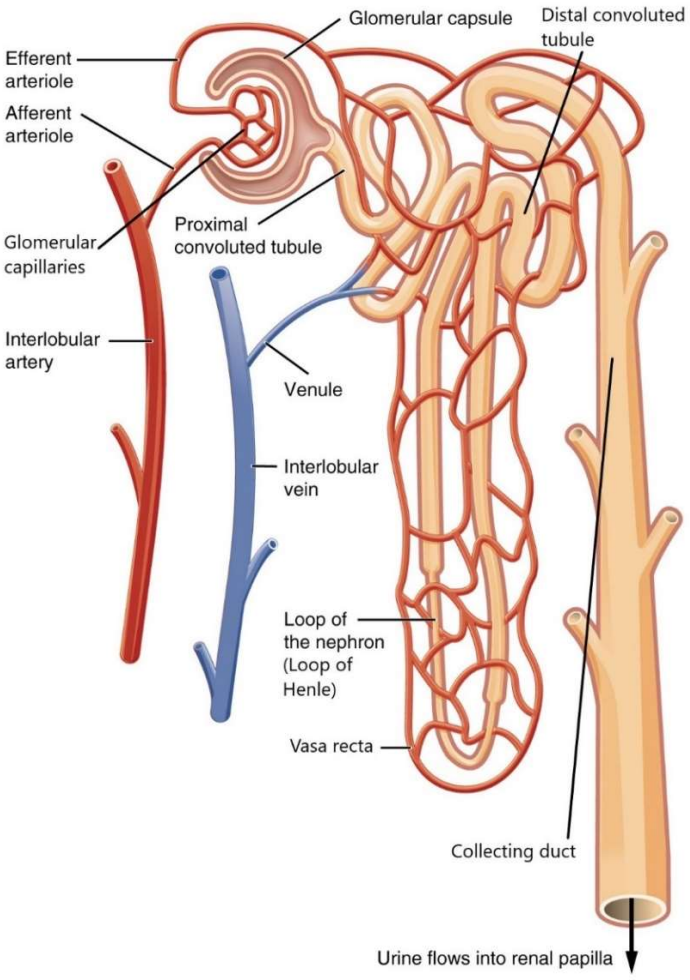

Figure 1.2: The Nephron
Adapted from OpenStax (2016)[60] on a Creative Commons Attribution 4.0 International License. Download for free at http://cnx.org/contents/14fb4ad7-39a1-4eee-ab6e-3ef2482e3e22@8.24

1.2.2 Mouse Kidney Anatomy

Information for this section was provided by Delaney et al[61] unless otherwise referenced.

The kidneys of mice show several similarities to human kidneys in structure and function: two kidneys drain urine via their respective ureters to a single pelvic bladder. However, differences do exist. Mice of different strains show variation in kidney size. The mouse kidney is unilobar and has a single papilla which reaches into the pelvis and ureter instead of the multipapillar, multilobar kidney of humans. Rodents predominantly have long nephron loops which aid in the production of a highly concentrated urine.

1.3 Kidney Excretory Physiology

Information for this section was provided by Bailey et al[55] unless otherwise referenced.

1.3.1 Kidney Perfusion

In the adult human, the two kidneys receive blood at around 1200 mL/min (25% of cardiac output) via the renal arteries[62]. Equally, mice kidneys received ~25% of cardiac output[61]. The renal arteries enter at the hilum and divide along each of the 6-8 lobes of the human kidney as interlobar arteries[60]. These traverse the medulla to the cortex. At the cortex they divide into the arcuate arteries which run parallel to the cortico-medullary junction. These branch to form the interlobular arteries which traverse the cortex to form the afferent arterioles that feed the glomeruli. Importantly, none of this arterial blood yet feeds the medulla: all perfusion to the deep matter of the kidney is post-glomerular. After the glomerulus, the efferent arterioles form the vasa recta capillary bed. This descends from the cortex back into the medulla. This organisation creates a relative hypoxia in the medulla[2]. The vasa recta capillaries return to the cortex to form the venous drainage of the kidneys mirroring the arterial supply: interlobular, arcuate, interlobar, and renal vein.

The ability of the kidneys to clear waste is dependent on renal perfusion in two ways. It provides the hydrostatic pressure to drive GFR and supplies the oxygen and glucose for aerobic respiration required by the tubule for active solute transport. Systemic blood pressure can change for several physiological and pathological reasons: diurnal variation, eating, fluid intake, exercise, environmental temperature, sweating, stress, stimulants (e.g., caffeine), pain, bleeding, diarrhoea, infection, and inflammation amongst others. As such the kidney must function across as large a range of perfusing blood pressures as possible to maintain GFR. This is achieved by autoregulation of the intraglomerular pressure via constriction or relaxation of the afferent arteriole. The afferent arteriole is constricted by two adenosine triphosphate (ATP) dependent mechanisms: myogenic reflex and

tubuloglomerular feedback. If the blood pressure becomes elevated, the walls of the arterioles supplying the glomerulus become stretched leading to depolarisation of the smooth muscle cells and constriction of the blood vessel. Equally, elevated blood pressure will lead to increased sodium chloride delivery to the macula densa in the distal tubule leading to constriction of these vessels. This allows intraglomerular pressure to remain consistent through a range of 80 mmHg to 180 mmHg systolic blood pressures and is able to respond within seconds.

1.3.2 Formation of Urine

The major physiological mechanism by which the kidneys act is the formation of urine by the nephrons. Blood perfuses the branching vasculature of the two kidneys until reaching specialised, selectively permeable capillary beds known as glomeruli (Figure 1.3). In humans, an average of one million glomeruli exists in each healthy kidney and all are formed prior to birth. The glomeruli act as filters and allow the passive movement of small, non-negatively charged, non-globular, and deformable solutes into the urinary space under osmotic and hydrostatic pressure[63,64]. This solution is known as the ultrafiltrate. The ultrafiltrate then passes through the tubule: an epithelial tube which tailors the ultrafiltrate composition via primary and secondary active transport. Reabsorption of important amino-acids, glucose, proteins, water, electrolytes, and bicarbonate as well as the secretion of hydrogen ions, weak organic acids and bases occurs here. Following this process, the ultrafiltrate is known as urine. Multiple tubules then drain into a collecting duct where urine acidification and further concentration occurs. The final urine contains urea, creatinine, creatine, uric acid, hippurate, ammonia, pigmented products of blood breakdown, very small quantities of organic molecules (glucose, ketone bodies, protein, amino-acids), electrolytes, and water[65,66]. The collecting ducts empty into the renal minor calyces which merge to form the major calyces and then the renal pelvis - all are collecting chambers for urine. The urine then flows out of the kidney via the ureter to the bladder where it is stored and later voided.

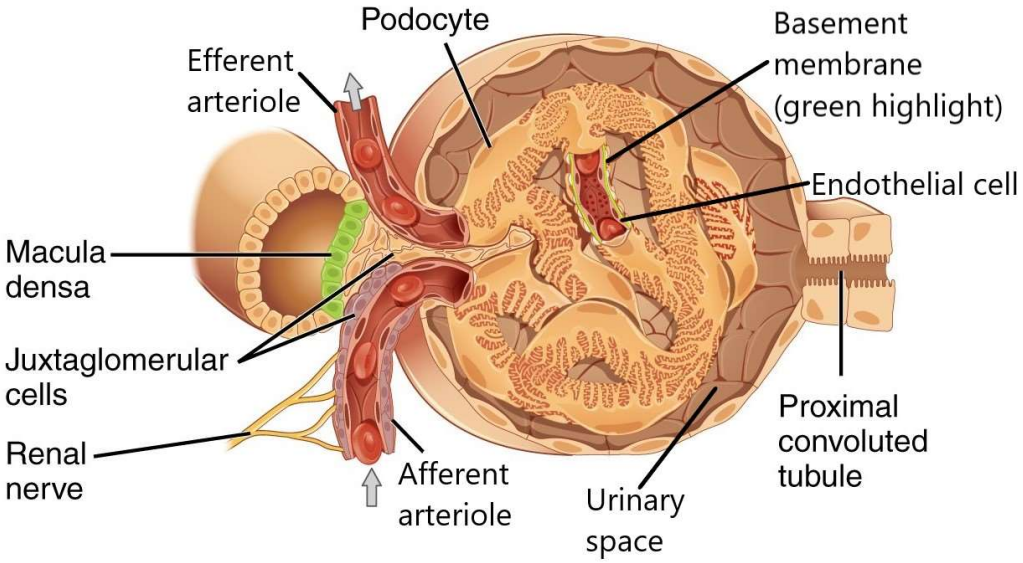

Figure 1.3: The Glomerulus
Adapted from OpenStax (2016)[60] on a Creative Commons Attribution 4.0 International License. Download for free at http://cnx.org/contents/14fb4ad7-39a1-4eee-ab6e-3ef2482e3e22@8.24

1.3.2.1 Glomerular Filtration

The glomerulus acts as a sieve via its highly specialised structure (Figure 1.3). This filter is created by the capillary endothelium covered by a basement membrane and then a layer of interdigitated podocyte cells. Beyond this is a surrounding urinary space enclosed by a parietal epithelium. This space leads to a draining tubule. The fenestrae of the capillary endothelium, the protein matrix of the glomerular basement membrane, and the interdigitated podocyte cell foot processes create a charge, size, and shape selective filter between the intravascular and urinary space.

The solution that is formed by what passes through is known as the ultrafiltrate. In health, the ultrafiltrate contains no solute with a molecular radius larger than 4 nm, no significantly negatively charged molecules, and tends to exclude spherico-globular proteins in molecular radius range 2-4 nm but may allow linear or deformable proteins of that size[63]. The purpose is to prevent the loss of cells and larger proteins from the blood, while allowing metabolic waste to pass into the urinary space. Movement across the filter is passive and produced by hydrostatic and oncotic pressure with the rate further dictated by the available glomerular surface area (adjustable by the contraction of mesangial cells) and glomerular hydraulic conductivity.

GFR correlates with the mass of functioning kidney tissue and is associated with the non-excretory functions of the kidney[30,31]. It provides valuable information to diagnose renal disease, prognosticate renal or cardiovascular complications, and plan treatments[67]. In

humans, GFR is reported as the volume of plasma filtered per time per body surface area. In health, this is around 120 mL/min/1.73m^2 [68]. The adjustment for body surface area standardizes the GFR for different kidney sizes which correlate with body size[31]. In mice, GFR is commonly reported by weight rather than body surface area and is around 10 µL/min/g body weight but varies significantly with strain and gender[69].

1.3.2.2 Tubular Secretion

The ultrafiltrate passes from the urinary space of the glomerulus to the tubule: a tube consisting of a single layer of epithelial cells on a basement membrane. Between these cells are linking proteins forming the selectively permeable "tight junction"[70]. Small solutes may be transported via the tight junction but the majority of solutes are transported transcellularly via transporter proteins. The tubules facilitate the secretion of waste from the blood to the filtrate via both primary and secondary active transport. The tubular cells express many different transmembrane transporter proteins at their basolateral (interstitial, nearest the blood) and apical (luminal, filtrate) surfaces. The proximal tubular cells (PTCs) are important in the renal clearance of drugs and toxins that do not easily undergo glomerular filtration. This includes protein-bound and charged compounds[71–75].

Aerobic metabolism is key to tubular secretory function in the PTCs. Here, glycolysis is limited and ATP production is dependent on oxidative phosphorylation[2]. Additionally, the partial pressure of oxygen delivered to the PTCs is low due to their post-glomerular blood supply[2]. This makes the tubular cells and tubular function particularly susceptible to hypoxia and IRI.

1.3.2.2.1 Proximal Tubular Secretion

Organic anion uptake by the PTCs is performed by the organic anion transporter (OAT) proteins at the basolateral surface via secondary active transport. This is facilitated by the basolateral sodium–potassium pump (Na^+K^+ATPase). ATP provided by the numerous mitochondria present in PTCs power the primary active transport of intracellular sodium into the interstitium via this pump. The sodium gradient created is utilised by the solute carrier (SLC) family 13 member 3 (SLC13A3) co-transporter protein. This results in the uptake of α-ketoglutarate (αKG) into the PTCs[71,73]. αKG is then exchanged for organic anions by OAT 1 and 3. OAT 1 and 3 transport many anionic drugs including acyclovir, furosemide, and ibuprofen[73]. The mechanism by which OAT 2 functions is less clear though it appears to facilitate the efflux of glutamate, an abundant intracellular amino acid, in exchange for organic anions including the drugs bumetanide, erythromycin, and ranitidine[71,73,76]. In humans, OAT 2 is additionally expressed at the apical surface and may contribute to organic

anion secretion into the filtrate[77]. Transmission after uptake to the apical surface may be partially via vesicles[78]. Organic anion secretion into the filtrate at the apical surface is facilitated by ATP-binding cassette (ABC) transporters: ABCB1, ABCC4, and ABCG2[73]. As their name suggests, this is via primary active transport. OAT 4 and 10 are localised at the apical surface of PTCs in humans and play a more complex role in organic anion handling by performing both secretion and reabsorption[73].

Organic cation uptake by the PTCs at the basolateral surface is via facilitated diffusion down the electrochemical gradient or organic cation transporter (OCT) 2[71,73,78]. Transmission after uptake to the apical surface is via endosomes[78]. Organic cation secretion into the filtrate at the apical surface occurs via primary active transport at ABCB1 transporter or proton exchange via SLC47A1 or SLC47A2 isoform transporters[71,73]. This proton exchange is facilitated by the sodium gradient provided by the basolateral Na^+K^+ATPase which enables the sodium–hydrogen antiporter secretion of hydrogen ions at the PTCs apical surface[79].

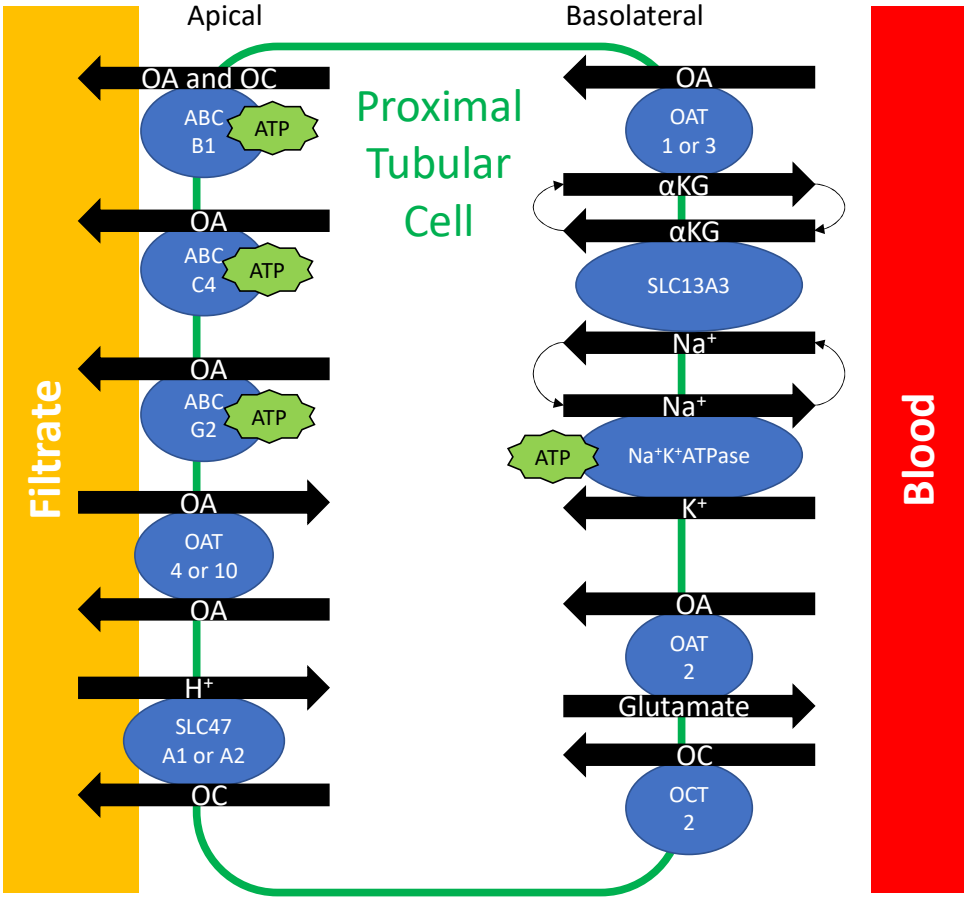

Figure 1.4: Proximal Tubular Secretion of Organic Anions and Cations via Transmembrane Transporters
OA (Organic Anion), OC (Organic Cation), OAT (Organic Anion Transporter), OCT (Organic Cation Transporter), Na^+K^+ATPase (sodium–potassium adenosine triphosphatase pump), SLC13A3 (solute carrier family 13 member 3 co-transporter protein), ABC (ATP-binding cassette transporters), αKG (α-ketoglutarate), Na^+ (Sodium), K^+ (Potassium), ATP (adenosine triphosphate), SLC (Solute Carrier).

1.3.2.2.2 Collecting Duct Secretion

Secretion of potassium occurs in the principal cells through renal outer medullary potassium ion channels. This is facilitated by the electrochemical gradient created by the basolateral Na^+K^+ATPase. Secretion of H^+ and bicarbonate occurs in the intercalated cells. H^+ATPase and H^+K^+ATPase secrete H^+, while SLC26A4 secrets bicarbonate.

1.3.2.3 Tubular Reabsorption

Tubular reabsorption describes many processes driven by numerous transporter proteins and mechanisms in different locations along the tubule.

The proximal tubule is the primary site of tubular reabsorption. To aid this, the tubular epithelial cells have microvilli to increase surface area and many mitochondria to provide ATP for active transport. 50% of filtered sodium is reabsorbed at the proximal convoluted tubule and a further 15% at the proximal straight tubule. In health, 100% of glucose and amino acids are full reabsorbed here. Phosphate and citrate are also reabsorbed. This reabsorption is facilitated by co-transporters with sodium that are enabled by the intracellular sodium gradient created by the basolateral Na^+K^+ATPase. The Na^+H^+ antiporter secrets H+ into the lumen that facilitates bicarbonate reabsorption. Chloride is exchanged with formate/oxylate. Potassium reabsorption occurs passively at the tight junction via the electrochemical gradient[80]. Calcium reabsorption is similar[81,82]. Bicarbonate reabsorption occurs via the active secretion of hydrogen ions into the filtrate which reacts with HCO_3^- to form CO_2 and H_2O in the filtrate which can diffuse back into the tubular epithelial cells. Finally, filtered proteins are taken up by the receptors megalin and cubilin via endocytosis[83].

1.3.2.4 Urine Concentration

The loop of Henle creates a counter current system to reabsorb water. The descending limb is highly water permeable while poorly ion permeable. The ascending limb is highly ion permeable and progresses from poorly water permeable to water impermeable. This results in a highly osmolar inner medulla and a much lower osmolarity in the outer cortex that maximises water and solute extraction. This results in 20% of total water reabsorption.

Under antidiuretic hormone (ADH) mediation, the collecting duct handles most of the water reabsorption via aquaporins. These transcellular proteins facilitate the transport of water between cells. Antidiuretic hormone is released under the influence of osmoreceptors in the hypothalamus, arterial baroreceptors, and atrial stretch receptors. ADH binds to V2 receptors that produce cyclic adenosine monophosphate generation and cell membrane insertion of aquaporins.

1.4 Measuring Renal Excretory Functions

Renal function can be measured in several ways. Techniques utilise either endogenously produced or administered exogenous markers. The quantification of these markers may be measured in blood samples, in urine samples, in a combination of blood and urine samples, by a transcutaneous optical device, or by different imaging modalities. Labels of the markers may be required for detection, and these may be radioactive or fluorescent.

Imaging offers the distinct benefit of providing split renal function: the contribution of each kidney to the total function of all renal mass. This split renal function may be in absolute units or a relative percentage contribution of each kidney to global function. In clinical practice, this assists in the identification of unilateral renal disease and in assessing the suitability of live kidney donors. In preclinical experiments, it facilitates the assessment of renal function where a unilateral injury has been applied by providing an internal control. This is particularly useful in discerning functional impairment specific to the intervention, from functional impairment due to overall poor health e.g., dehydration.

1.4.1 Measuring Glomerular Filtration

GFR is "the rate at which substances are filtered from the blood of the glomeruli into the glomerular capsules of the nephrons"[84]. GFR measurement relies on the quantification of an ideal filtration marker. An ideal marker is freely filtered at the glomerulus, is unaffected by tubular secretion and reabsorption, is not toxic, is free in the plasma (not bound to proteins), is only renally excreted, and is not metabolised[85,86]. There is no endogenous marker that fits these criteria as yet described. Where an ideal GFR marker is applied, GFR is equal to urinary clearance as calculated by Equation 1.1[31].

$$C = \frac{U \times V}{P}$$

Equation 1.1: Urinary Clearance
C (Clearance of the substance), U (Urine concentration of the substance), V (Urine flow rate), P (Average plasma concentration of a substance)

The measurement of GFR can be achieved without measuring urinary marker concentration by the calculation of marker clearance from the blood alone. Multiple timed blood samples are taken followed by the application of a two compartment model: the first decay being the dispersal of the marker through its volume of distribution plus clearance and the second decay being the clearance alone[31].

The gold standard marker for GFR is the exogenous agent inulin. Inulin is a fructan-type polysaccharide with a molecular weight between 972 and 5200 Da (depending on the degree of polymerisation) and is obtained from plants[87–89]. The discovery of inulin as a GFR marker is credited to Shannon and Smith, and Richards et al[88,90]. The absence of inulin in the urine of aglomerular fish, the independence of inulin clearance rate from its plasma concentration, and the unimpaired clearance in the presence of glucose transport blockade were used as supporting evidence that inulin is a GFR marker[91]. Micropuncture studies later confirmed this[91–93]. The gold standard method of using inulin to measure GFR is unwieldy due to poor marker solubility, the need for a continuous intravenous infusion , the acquisition of multiple strictly timed samples of blood and urine, the requirement for oral water loading, and the preference for urinary catheterisation[89]. Inulin is also expensive and poorly available. While bolus methods of inulin clearance exist, changing plasma concentrations can result in errors when calculating an average plasma concentration[31]. Due to the poor solubility of inulin, there has been interest in the use of sinistrin. Sinistrin is a fructan-type polysaccharide like inulin with a molecular weight between 2000 and 6000 Da. Sinistrin is also obtained from plants, meaning it is also expensive and less available[94]. Both inulin and sinistrin have been labelled with fluorescein isothiocyanate (FITC). This fluorescent label allows smaller doses of these markers to be detected in urine and blood samples as well as enabling the measurement of marker clearance using a transcutaneous optical device[69,95–98]. FITC maximally absorbs at 495 nm and emits at 519 nm.

Pyrazine and derivatives, with and without polyethylene glycol, undergo a mixture of glomerular filtration and tubular secretion and have also had their clearance measured by a transcutaneous optical device[99–101]. These absorb light maximally in the blue region of the visible spectrum and emit maximally in the green region – similar to FITC.

2-hydroxylpropyl-β-cyclodextrin and 2-hydroxylpropyl-γ-cyclodextrin are cyclical oligosaccharides that are hydrophilic, minimally protein bound, and when intravenously administered are rapidly excreted by the kidneys[101,102]. By binding these to fluorophores (heptamethine cyanine dyes or FITC) their clearance can be measured by high performance liquid chromatography or transcutaneous optical device[102,103]. Cyclodextrins are easily synthesized and relatively inexpensive. 2-hydroxylpropyl-β-cyclodextrin bound to the heptamethine NIR dye ABZWCY has shown characteristics desirable in a GFR marker: minimal plasma protein binding (3.7%), significant urinary recovery (97% after 24 hours), no evidence of tubular secretion, and no cytotoxicity[102]. The use of a NIR dye improves on

fluorescein labelled compounds by reducing interference from autofluorescence when detected by a transcutaneous optical device.

Iothalamate is an organic compound containing three iodine molecules that was originally purposed as a radiocontrast agent[104]. It is water-soluble, does not undergo metabolism, is 9.6% protein bound, is cleared by glomerular filtration, and is inexpensive[67,105,106]. However, there is evidence to suggest some degree of tubular secretion of iothalamate and as such it can overestimate GFR[107]. It can be detected by a scintillation counter/spectrometer through radiolabelling (where the compound contains iodine 125), or through high performance liquid chromatography or mass spectrophotometry[31]. Similar to iothalamate, iohexol is an iodine containing organic compound originally purposed as an x-ray contrast agent. Detection is commonly via high performance liquid chromatography but can also be via x-ray fluorescence or computed tomography (CT) to deliver split renal function[67,108,109]. However, imaging techniques requires larger doses and increase radiation exposure[110]. Unlike iothalamate, iohexol underestimates GFR when compared to inulin which may be due to tubular reabsorption[111]. Other iodine containing contrast agents, including iopamidol and ioversol, have been used to measure single kidney GFR in CT[112–115].

Ethylenediaminetetraacetic acid (EDTA) and its analogue diethylenetriaminepentaacetic acid (DTPA) are chelating agents that can be labelled with radioactive isotopes to measure GFR. Both have been labelled with Technetium-99m (Tc-99m) but this is only routine for DTPA[116]. Tc-99m DTPA provides a similar estimation of GFR as iohexol[117]. Tc-99m benefits from being detectable by a gamma camera meaning split renal function can be determined by scintigraphy or single photon emission computed tomography (SPECT). EDTA is more commonly labelled with chromium 51. Chromium 51 EDTA can measure GFR via x-ray fluorescence or high performance liquid chromatography and this also provides a similar GFR estimation to iohexol[118]. DTPA has also been labelled with europium and detected via fluorescence to measure its glomerular filtration[119]. Labelling with gadolinium has facilitated measurement of DTPA clearance and single kidney GFR calculation via DCE magnetic resonance imaging (MRI)[120]. A number of chelation agents in combination with gadolinium have been examined for this purpose including tetraxetan (DOTA), DO3A-butrol, and the DTPA derivative BOPTA[120,121]. The choice of kinetic model applied to DCE MRI has been noted to produce significantly different GFR results[120,122]. The use of gadolinium based MRI GFR estimation is limited by the risk of the fatal complication nephrogenic systemic fibrosis in patients with a low GFR, and ongoing concerns about reliability and accuracy[120,123].

1.4.2 Estimating Glomerular Filtration Rate

Creatinine estimated GFR (eGFR) is the current routine method of assessing renal function in the clinical environment. Creatinine is a 113 Da amino acid derivative produced by muscle catabolism[31]. A single blood test is taken to measure the concentration of serum creatinine and an equation applied to calculate the eGFR. This benefits from the fact that creatinine is produced endogenously and at a steady rate meaning a single sample can be taken without any preparation.

There are several drawbacks to eGFR in the clinical setting. As creatinine production is different from person to person, adjustments for weight, sex, and race are made in the different eGFR formulas (MDRD, Cockcroft-Gault, CKD-EPI). This leads to some formulas being more accurate estimators than others depending on the patient and clinical context[31,124]. However, these formulas may not entirely compensate for all clinical conditions that affect creatinine production, concentration, and excretion. Cirrhosis, malnutrition, haemodilution from intra-venous fluids, competition for tubular secretion sites by drugs are some examples of this[3]. Furthermore, 10% of creatinine undergoes active tubular secretion in humans making it a less than ideal GFR marker[85,125]. This is even more impactful in mice where 35-50% of creatinine undergoes tubular secretion[126]. Categorising the severity of AKI requires assessment of the change of creatinine (a pre- and a post-injury measurement) which is often not available[3]. The rise in creatinine is slow compared to the timing of injury and the change in GFR: it takes time for creatinine to accumulate following the reduction in filtration meaning acute changes in GFR will not be seen in the eGFR for 2-3 days[127,128]. eGFR via creatinine is most accurate where GFR is 20-60 mL/min/1.73m^2 making it less sensitive to early deteriorations in renal function[129].

Cystatin C is a 120 amino acid, non-glycosylated protein that is significantly larger than creatinine (13,359 Da) and is produced by all nucleated cells at a constant rate[31,129,130]. It is freely filtered by the glomerulus, undergoes near total reabsorption by the PTCs where it is metabolised[130]. It can also be used to estimate GFR and has shown some benefits over creatinine. Unlike creatinine, cystatin C is unimpacted by dietary protein and can detect changes in GFR as early as 70-90 mL/min/1.73m^2 [129]. Cystatin C has a shorter half-life than creatinine and detects changes in GFR faster than creatinine[129]. However, cystatin C is impacted by extra-renal parameters including thyroid function, steroids, cancer, inflammation, cardiovascular disease, and a small amount of extra-renal elimination[31,129]. Equations using cystatin C have not been demonstrated to be more precise in estimation of GFR than creatinine based equations[1].

1.4.3 Measuring Tubular Secretion

TSR is the rate at which a marker is transported from the peritubular blood to the filtrate via the PTCs. The focus on the PTCs derives from their importance in the renal excretion of drugs and uraemic toxins too large or protein bound for filtration[73,131,132]. The potential benefits of measuring TSR would be the diagnosis of tubular specific renal disease, tailoring drug dosing schedules, and to provide greater insight into CKD and ESRF residual function[71]. Despite the significant rate of injury to the tubules in AKI and their greater sensitivity to commonly observed hypoxic-hypoperfusive insult AKI aetiology, clinical practice does not routinely utilise measures of tubular function nor injury[2]. Additionally, GFR is a poor estimator of a number of protein-bound uraemic toxins[133]. This may explain why the tolerance of a low GFR varies between individuals. These toxins are tubularly secreted and associated with symptoms of ESRF, cardiac disease, and tissue calcification[131,134].

An ideal marker of TSR would not be cleared by glomerular filtration or any extra-renal elimination. It would not undergo metabolism and be excreted unchanged in the urine. It would also be non-toxic. Finally, due to the potential for competitive inhibition between different compounds for transporters, an ideal marker would have a high transporter affinity and short half-life[132]. Unlike GFR, TSR has no standardised measure or marker[135–137].

Endogenous markers that have been examined to measure TSR include hippurate, indoxyl sulphate, p-cresol sulphate, cinnamoylglycine, pyridoxic acid, isovalerylglycine, tiglylglycine, kynurenic acid, and xanthosine[137–139]. These compounds may be produced by the metabolism of human cells (e.g., hippurate) or by gut bacteria (e.g., indoxyl sulphate), are frequently protein-bound, and are poorly filtered by the glomerulus and dialysis[134]. A number of these markers have been shown to have different clearance rates from para-amino hippuric acid, a marker of renal plasma flow, increasing their potential specificity for tubular secretion[140]. However, a small study of 33 CKD patients suggested that GFR, TSR measured by eight endogenous compounds, and the clearance of two drugs that undergo tubular secretion were similar[138].

Dimercaptosuccinic acid (DMSA) labelled with Tc-99m has been used in scintigraphy and SPECT to measure uptake by the PTCs. DMSA reaches the PTCs by both glomerular filtration with megalin/cubulin facilitated reabsorption and by peritubular OAT 3-mediated uptake[141–144]. It is then broken down into mixed disulphides of cysteine[141]. While it is used to measure tubular health and split renal function, it does not measure TSR[145,146]. Mercaptoacetyltriglycine (MAG3) can also be labelled with Tc-99m and undergoes tubular

secretion via OAT1 and OAT3 uptake, and ABCC2 and ABCC4 transporter secretion into the filtrate[144]. The dynamic clearance of MAG3 and its specificity for the PTCs enables DCE imaging e.g., SPECT to measure TSR[147,148]. It has been theorised that MAG3 could be labelled with gadolinium which would facilitate estimation of TSR by DCE MRI albeit with the limitation of its use in those with a lower GFR due to the risk of nephrogenic systemic fibrosis[149].

1.4.4 Considerations for Measuring Renal Excretory Function in Mice

In the preclinical setting, using blood samples to serially measure GFR or TSR in small lab animals is undesirable[126,150–152]. Mice have a low total blood volume available and repeated sampling negatively impacts the wellbeing of the mouse. Furthermore, removing blood volume for sampling may itself impact renal function and injury by a reduction in circulating volume and haemoglobin. Even where blood samples are taken, the most commonly measured endogenous marker (creatinine) is unspecific for GFR in mice undergoing significant tubular secretion[126]. Collection of urine via metabolic cage adds further potential stress for the mice due to lone caging and an uncomfortable environment as well as evidence of altered physiology including a rise in urinary creatinine over time[153].

The use of optical transcutaneous devices (TD) to measure the global clearance of fluorescent markers in rats and mice have shown the potential to longitudinally measure GFR[94,96,97,154–157]. In combination with FITC-sinistrin this has been shown reliable and reproducible across different mouse strains and ages[156]. The method utilises the detection of fluorescence in the skin by a device that is taped to a shaved portion of the animal. The signal is then fit with a compartment model to calculate GFR[98]. This method benefits from minimal anaesthesia time for the animals allowing the clearance of the agent to be measured mainly while conscious. This is important as anaesthetic agents have been associated with changes in renal function[158–161]. While FITC labelled compounds are potentially impacted by autofluorescence, there are NIR dye labels that can be used instead[102]. A potential disadvantage of TD measurement is that the detector can become saturated which results in a loss of data points and may lead to inaccurate fitting of the compartment model. Also, the TD may become inadvertently detached also resulting in a loss of data.

Using imaging in preclinical experiments to measure renal function offers unique benefits. First, it allows the quantification of the functions of each individual kidney. This allows for the detection of any baseline discrepancy between left and right kidney function[162,163] as well as creating an internal control kidney where a unilateral injury model is implemented. As the

mouse surgical model of IRI is less stable and subject to potential variability, the internal control kidney helps maintain the relevance of each result[164]. It also allows the specific degree of injury due to the intervention and the specific degree of recovery due to the treatment to be examined rather than any additional factors that may occur and affect kidney function e.g., dehydration. It may also highlight compensation and crosstalk between the kidneys[34,165]. Second, imaging allows for the assessment of renal volumes including total kidney volume, cortex volume, and medulla volume, which are factors in renal function, health, and disease[166,167]. Finally, specific acquisition sequences can be used to assess perfusion, oxygenation, inflammation, microstructure, and fibrosis[168–172]. There are specific challenges using imaging to measure renal function in small animals such as mice. First, a high enough spatial resolution is required to define the borders of the structures of interest. This can be particularly challenging for measuring the time activity curve of the blood vessels which are required for most kinetic GFR models. Secondly, continuous anaesthesia is required which can itself alter renal function or protect against IRI[158–160]. Thirdly, the respiration of the animal will lead to movement that requires either respiratory gated imaging resulting in a potential loss of temporal resolution, or image averaging resulting in a blurring of the image. Finally, animal throughput is relatively low with regards to tomographic techniques.

1.5 Multispectral Optoacoustic Tomography

MSOT is a type of photoacoustic (also known as optoacoustic) imaging technique. Photoacoustic imaging is based on the photoacoustic effect discovered by Alexander Graham Bell: a portion of modulated light energy that is absorbed by a material may be emitted as a sound wave.

MSOT utilises a tuneable laser to deliver nanosecond pulses of electromagnetic radiation in the NIR range. This is absorbed by the sample resulting in a thermoelastic expansion and generation of ultrasound that is then detected by an array of piezoelectric sensors arranged around the subject[173]. The acoustic signals are coupled from the subject to the sensors by a water bath and ultrasound gel. There is an associated safe temperature rise in the millikelvin range[174]. The amplitude of the returned ultrasound is proportional to the number of photons absorbed where material is homogenous: qualitative, semi-quantitative, and quantitative measurements can be taken[175]. Measuring multiple wavelengths followed by the application of a multispectral unmixing algorithms allows measurement of haemoglobin, oxyhaemoglobin, melanin, lipids, collagen, genetically encoded chromophores, small molecule dyes, and nanoparticles (metallic, polymer, carbon)[169,173,176].

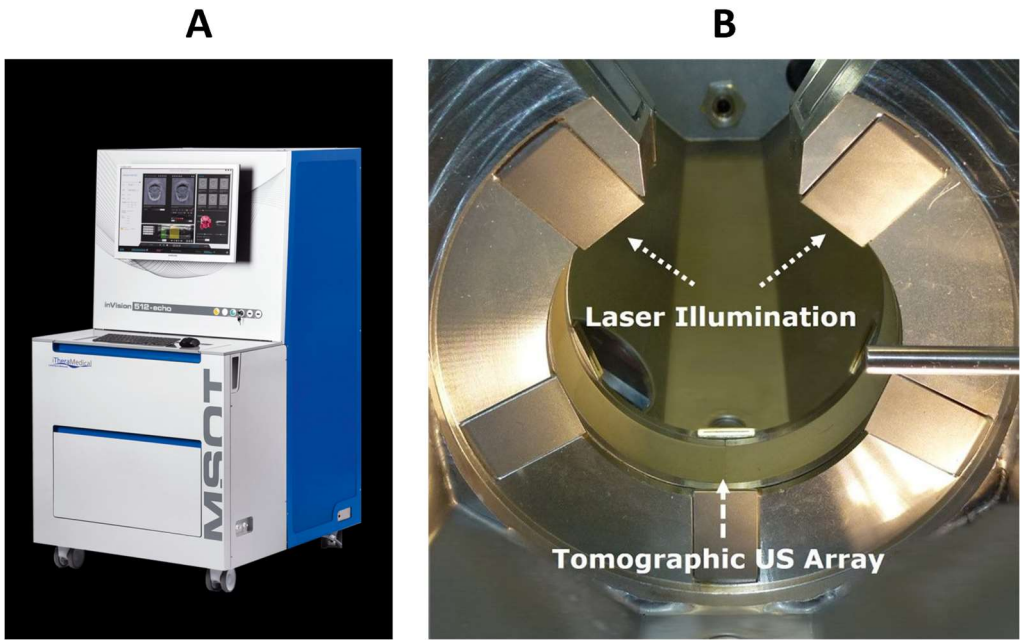

Figure 1.5: MSOT inVision 256 Preclinical Imaging Device from iThera Medical
Adapted from ithera-medical.com[177]. A. External view. B. Internal view of imaging array.

Due to its ability to detect numerous NIR absorbing compounds, MSOT has the theoretical potential to simultaneously measure renal perfusion, glomerular filtration, tubular secretion, tubular reabsorption, biomarkers via activatable probes, and regenerative cell biodistribution[176,178–180]. Measuring different physiological processes depends on identifying an appropriate contrast agent that undergoes that process.

An ideal photoacoustic contrast agent has a high extinction coefficient, has a low fluorescence quantum yield, has a unique NIR absorbance spectrum, is nontoxic, and is photostable. The preference for a low fluorescence quantum yield is because once light energy is absorbed it may be converted to light or heat. The more energy that is converted to heat the more ultrasound is produced[181]. As such it is more efficient to have probes with a low fluorescence quantum yield when trying to generate a photoacoustic signal. However, many current fluorophores are still translatable to MSOT.

MSOT has a high temporal resolution (0.1 seconds) while simultaneously delivering a high spatial resolution (~100 µm)[182]. It can simultaneously provide anatomical and functional data: positron emission tomography, SPECT, and fluorescence imaging lack anatomical data while planar x-ray and CT have a lower temporal resolution[183]. MSOT suffers less from photon scattering than pure optical imaging by 2-3 orders of magnitude[174,184]. Scattering is where the photons are forced from their straight trajectory by material nonuniformities or particle collisions[184]. MSOT achieves this by detecting the return of sound rather than light.

This facilitates a greater imaging resolution at depth[173–175]. MSOT can image at a depth of around 4 centimeters[173–175,185,186]. The imaging depth achievable by MSOT makes it suitable for visualising whole mice and small rats, but direct translation of entire abdominal tomographic photoacoustics into humans is improbable. Instead, handheld photoacoustic probes have been utilised to image the skin, muscles, superficial bowel (patients with low adiposity), superficial vasculature, and breast in humans[169,186–192]. Renal transplants in patients with low adiposity may potentially be imaged this way. Photoacoustic probes may also be used intraoperatively for deeper tissues or externally for extracted organs planned for transplant[169]. MSOT benefits from the varied optical absorbance of tissues and administered agents, resulting in high levels of contrast when compared to pure ultrasound imaging[174,175]. In MSOT, intrinsic contrast is dominated by blood (haemoglobin and oxyhaemoglobin), but fat and bone also provide contrast[193]. MSOT inherits the molecular specificity and good safety profile (non-destructive and non-ionizing) of optical imaging[174,184].

Quantification is an area of ongoing research in MSOT and photoacoustic imaging generally. While qualitative and semi-quantitative images are easily achieved in MSOT, fully quantitative measurements are more taxing[175]. Local light energy distribution (fluence) varies throughout samples: both due to depth and heterogenous absorbance. A reduction in the amount of light delivered to a point will result in a reduced amount of photoacoustic signal produced per unit of absorber. Animals show a great deal of heterogeneity in their absorbance of NIR light. This problem is further increased following the administration of a dynamic contrast agent leading to the variation of fluence throughout the time course of the imaging. In order to provide an absolute quantification of an absorber, knowledge of and modelling for fluence in the sample is required[173,175,194]. Models using the delta-Eddington approximation of the radiative transfer equation have been explored for this purpose and require further validation[194,195]. Kinetic models using the normalised time activity curves of two regions of interest have been implemented in an attempt to eliminate the need for fluence correction, but they produce parameters that are scaled by two regions rather than an absolute result[196]. Fluence mapping has been achieved by diffuse optical tomography in phantoms but this is limited by a lesser depth than possible by photoacoustic imaging[197]. Fluence mapping has also been achieved by concurrent ultrasound imaging where a camera measures ultrasonically modulated light[198]. Unfortunately, this process has only been performed in adynamic imaging and acquisition of the fluence map is slow (530 mm^2 is imaged in 29 minutes)[198]. While the returned ultrasound waves also are heterogeneous in

their transmission through the sample, this is reportedly less impactful than optical absorbance heterogeneity[199].

MSOT of rodents is more easily executed with an inhaled, rather than injected, anaesthetic. This means that anaesthesia can be titrated to achieve a respiratory rate that suits the imaging protocol. Measured images can be averaged and timed to a respiratory rate (e.g., 10 frames per second, 1 breath per second) as an attempt to compensate for respiratory movement. Isoflurane also allows a continuous level of anaesthetic to be supplied throughout the procedure, potentially creating a more stable animal physiology. As mentioned previously, some reports find that isoflurane may have a potentially renal protective effect and may alter GFR[158–161]. Furthermore, general anaesthesia[200] and specifically isoflurane[201,202] can influence haemoglobin levels and vasodilation. As blood is a significant element of an animal's endogenous photoacoustic contrast in the NIR range this may affect image quantification.

The reliability of MSOT is impacted by the skill of the operator. The ability to position animals, maintain their physiology (temperature, respiratory rate), and motion (anaesthesia level and respiration) are limiting factors[203]. A study which measured coefficient of variation in phantom and mouse MSOT imaging showed that user experience was a major factor on signal reproducibility – in addition to sample rotation, and removal on the animal from the water bath between acquisitions[204]. It was also noted that creation of regions of interest is somewhat subjective.

1.6 Measuring Renal Function and Injury with Multispectral Optoacoustic Tomography

MSOT has been used in many preclinical experiments to measure renal anatomy, health, injury, and function. Dima et al have shown anatomical correlation between MSOT acquired images and cryo-section in mice[205]. Large organs and their boundaries are shown clearly including the kidney, spleen, liver, and spine. Cheng et al have developed an MSOT detectable activatable contrast agent that activates in the presence of γ-glutamyl transferase in acute kidney injury[206].

MSOT has been used to measure renal perfusion. Yang et al demonstrated a reduction in haemoglobin and oxygenation of the kidneys in mice after caecal ligation and puncture as a model of septic AKI[207]. This was associated with a reduced perfusion as detected by transonic flowmeter. Indocyanine Green (ICG) is a protein-bound NIR dye that is entirely excreted in the bile[208,209]. It has been used in MSOT to image the renal vasculature[180]. Buehler et al were

able to demonstrate the renal arteries and parenchymal presence of ICG but no signal in the renal pelvis[180].

MSOT has been used to measure renal excretion most frequently via the contrast agent IRDye 800CW. This NIR dye has been shown to be cleared by the kidneys in mice and rats[210,211]. Taruttis et al confirmed this by a combination of MSOT and cryo-slice[210]. A number of model-free measurements have been applied to quantify the renal clearance of this marker[155,157,207,212]. These model-free measurements have been shown to correlate with histological glomerular damage and blood urea nitrogen in a model of Adriamycin nephropathy[157,212]. In surgical IRI[155] and septic AKI[207] model-free measurements of IRDye 800CW have also shown significant decline. Jiang et al have used a renally clearable glutathione-coated gold nanocluster to measure single kidney GFR in MSOT in health and a surgical model of ureteric obstruction[183].

1.7 Summary and Thesis Aims

Kidney disease is a growing health care emergency carrying high levels of morbidity, mortality, and cost. While preclinical animal experiments have limitations, they remain the best way to examine kidney injury and novel treatments in the organism as a whole. There are opportunities to improve the accuracy of injury models and treatments tested in this way. MSOT offers a rapid, safe, and flexible way of imaging the kidneys and their excretory functions: glomerular filtration and tubular secretion. However, inexpensive and easily synthesised contrast agents for MSOT that specifically undergo each of these functions are yet to be identified. Additionally, the best model or metric to quantify the clearance of contrast agents in MSOT are yet to be characterised.

The main aims of this thesis were to:

1. Characterise two potential NIR dyes for their suitability to be detected in MSOT to measure GFR and TSR
2. Compare the adequacy of model-free and pharmacokinetic models of these dyes in MSOT to quantify GFR and TSR in health and IRI
3. Compare MSOT clearance of these dyes to more commonly used measures of renal health and injury: sinistrin clearance, DMSA uptake, and histology

2 Methods

2.1 Preparation of Dye Solutions and Probenecid

This work was performed under a laminar-flow hood. Unless otherwise specified, compounds were dissolved in sterile 1X Dulbecco's Phosphate Buffered Saline (Sigma, UK) and thoroughly mixed by vortex. Solutions were passed through 0.2 µm sterile filters (Sartorius, Germany) and stored in microfuge tubes at -20°C and wrapped in tin foil. Probenecid (water soluble, P36400) was purchased from Invitrogen, USA. ABZWCY-HPβCD and STAR FLUOR 770 Acid were provided by our collaborators at Cyanagen, Italy. IRDye 800CW Carboxylate was purchased from LI-COR, USA. Indocyanine green was purchased from Cayman Chemical, USA and dissolved in 100% Dimethyl Sulfoxide (Sigma, UK) then diluted to 1.55% DMSO with sterile 1X Dulbecco's Phosphate Buffered Saline (Sigma, UK).

2.2 Plasma Protein Binding of Dyes

The examination of dye plasma protein binding was kindly performed by Yinuo Xie under the supervision of Norbert Gretz at the University of Heidelberg, Germany.

A dye-protein solution was made by the incubation of 250 µL of 200 µM dye in 1X phosphate buffered saline (PBS) with 1 mL of human plasma (provided by Karen Bieback, University of Heidelberg, Germany) in lithium-heparin for 24 hours at 37°C. A control-protein solution of 250 µL 1X PBS was created in the same way.

Dye-protein or control-protein solutions were placed in the inner chamber of a fast micro equilibrium dialyzer (Quik PREP, Harvard Apparatus, USA) while 1 mL 1X PBS was placed in the outer chamber. This was performed in triplicate. Dialysis was allowed for 24 hours at room temperature on a roller mixer. 100 µL from each chamber were then pipetted to a 96-well plate in triplicate. Absorption was measured by spectroscopy (Spark 10M microplate reader, Tecan, Austria). An equation based on the Lambert-Beer law was used to calculate the degree of protein binding (Equation 3.1).

2.3 Photospectra Measurements

Photospectra of dyes in either 1X PBS or 10% bovine serum albumin (BSA) were measured by the FLUOstar Omega microplate reader (BMG LABTECH, France) in flat bottomed polystyrene "costar" 96-well microplates (Corning, USA). Automatic path correction was applied and a volume of 100 µL was used. A separate set of control wells containing the solvents (PBS or BSA) were measured and their absorbance was subtracted from the

absorbance of the dye wells. Wavelengths from 680 to 900 nm were measured in steps of 1 nm.

2.4 Agar Phantom Creation

Tissue mimicking, scattering (μ's = 5 cm^{-1}), non-absorbing phantoms of 2 cm diameter were made by the previously published method[194,213,214]. The light scattering property, which is similar to living tissue, is provided by intralipid (a lipid emulsion from soybeans). A mould was made by cutting off the front of a 20 mL, 2 cm diameter syringe off. 1.03 mL of 20% intralipid (Sigma-Aldrich, USA) was warmed in a water bath at 60°C. Separately, 0.75 g of agar (Sigma, UK) was added to 50 mL of distilled water and heated until boiling in a microwave. The warmed intralipid was added to the hot agar and stirred, then poured into the mould. Two straws of 4 mm bore (Stephensons, UK) were inserted before the solution could set and positioned using tape. These created cavities for insertions of test absorbers later. The phantoms were allowed to set at room temperature for one hour.

2.5 Animals

All animal work was carried out by Home Office Personal Licence holders under the Home Office Project Licence numbers 70/8741 and PP3076489 with approval from the University of Liverpool Animal Welfare and Ethics Review Board. B6 Albino mice (B6N-Tyrc-Brd/BrdCrCrl), a coisogenic mutant of the C57BL/6 strain, were used from the University of Liverpool colony. Mice were housed in individually ventilated GM500 cages with access to food and water ad libitum. A 12-hour light/dark cycle was implemented. Daily checks of animal wellbeing were made and, following surgical intervention, a daily post-operative checklist completed to confirm animal welfare and suitability to remain in the experiment.

2.6 Multispectral Optoacoustic Tomography

All Multispectral Optoacoustic Tomography (MSOT) was performed using the inVision 256-TF (iThera Medical, Germany). Images were reconstructed in viewMSOT 4.0.1.34 software (iThera Medical, Germany) using the BP 4.0 pre-set. Reconstruction field of view was set to 25 mm (75 μm resolution). Clear, non-absorbing ultrasound gel (Barclay-Swann, UK) was applied to both phantoms and mice for imaging. Both mice and phantoms were imaged in MSOT by their placement in the supplied animal holder.

2.6.1 MSOT Phantom Imaging

Phantom inserts were contained within sealed, clear, minimally absorbent straws (Stephensons, UK).

2.6.1.1 Photoacoustic Spectrum MSOT Phantom Acquisition

Agar phantoms containing two inserts were imaged. One insert contained a solution of the dye in 1X PBS or 10% BSA. A second control insert contained the solvent alone (PBS or BSA). The photoacoustic signal of the control straw was subtracted from the photoacoustic signal of the dye straw. The agar phantom was imaged at a water bath temperature of 25°C. Three frames per wavelength imaged were averaged. 45 wavelengths were measured from 680 to 900 nm in steps of 5 nm.

2.6.1.2 Concentration versus Photoacoustic Signal MSOT Phantom Acquisition

Agar phantoms containing two inserts were imaged. One insert contained a solution of the dye in 1X PBS. A second control insert contained the PBS alone. The photoacoustic signal of the control straw was subtracted from the photoacoustic signal of the dye straw. Seven concentrations were measured for each dye (1, 5, 10, 15, 20, 25, 30 µM). The agar phantom was imaged at a water bath temperature of 25°C. Three frames per wavelength imaged were averaged. Measurements were repeated in five positions along the phantom and averaged. 1 wavelength was measured at the peak photoacoustic signal for that dye (700 nm for ABZWCY-HPβCD, 770 nm for STAR FLUOR 770 Acid, and 775 nm for IRDye 800CW).

2.6.1.3 Continuous MSOT Phantom Acquisition

Agar phantoms containing separate inserts of 30 µM ABZWCY-HPβCD, STAR FLUOR 770 Acid, or IRDye 800CW in 1X PBS were imaged. The agar phantoms were imaged in a water bath at 34°C. Photoacoustic signal was measured continuously at a single stage position. The MSOT laser was set near the dyes' peak photoacoustic signal (700 nm for ABZWCY-HPβCD, 770 nm for STAR FLUOR 770 Acid, and 770 nm for IRDye 800CW). Laser emission was 0.1 Hz. Frames were not averaged.

2.6.2 MSOT Animal Imaging

24 hours prior to imaging, fur was removed with clippers and depilatory cream (Veet Hair Removal Cream 8336076, RB Healthcare, UK) under isoflurane (1-3%) and oxygen (1 L/min) anaesthetic. On imaging day, animals were anaesthetised with isoflurane (1-3%) and oxygen (1 L/min) via a nose cone on a heated mat. The isoflurane dose was titrated to produce a respiratory rate of 1 Hz.

Where the administration of intravenous agents was required, a 30-gauge needle attached to fine bore 0.28 mm polyethylene sterile tubing (Smiths Medical 800/100/100, Fisher Scientific, UK) cut to a length of 33 cm and flushed with 0.9% sterile saline was inserted into the tail vein.

The mouse was placed in the MSOT mouse holder (supine for kidney imaging, prone for gallbladder imaging) with a thin layer of clear non-absorbing ultrasound gel applied (Barclay-Swann, UK). The holder was transferred into the water bath previously heated to 34°C. The mouse was allowed to equilibrate to the water bath temperature for 15 minutes before imaging was started.

2.6.3 MSOT Liver and Gallbladder Imaging

Following 15 minutes acclimatisation to the MSOT water bath, mice were imaged continuously at a single position for 33 minutes with an intravenous injection of 20 nmol of dye (ABZWCY-HPβCD, STAR FLUOR 770 Acid, or ICG) in 100 µL 0.9% sterile saline at 3 minutes. The plane for imaging was selected using the built in Anatomy Atlas in the viewMSOT software (iThera Medical, Germany). Mice were imaged at two wavelengths: 900 nm and the peak MSOT absorbance of each contrast agent (700 nm for ABZWCY-HPβCD, 770 nm for STAR FLUOR 770 Acid, and 800 nm for indocyanine green). 10 frames were taken per wavelength and averaged giving a temporal resolution of 2 seconds. The differencing unmixing method was applied to reconstructions to quantify the dyes.

2.6.4 MSOT Renal Volume Imaging and Measurement

Following 15 minutes acclimatisation to the MSOT water bath, mice were imaged from above the upper renal pole to below the lower renal pole in 1 mm steps at 850 nm. 10 frames were acquired per stage position and averaged. After image reconstruction, viewMSOT software was used in “Orthogonal View” mode and a region of interest was drawn around the kidney at each slice. From this, the organ volume was calculated by the viewMSOT software.

2.6.5 MSOT Renal Dye Imaging

Following 15 minutes acclimatisation to the MSOT water bath, mice were imaged continuously at a single position for up to 40 minutes with intravenous injection of a dye at 3 minutes. ABZWCY-HPβCD was administered at 30 mg/100 g body weight at a concentration of 150 mg/mL in 0.9% sterile saline. IRDye 800CW and STAR FLUOR 770 Acid were administered as 20 nmol in 100 µL. The imaging plane was selected visually by identification of the renal hila in MSOT at 850 nm.

In experiments where two wavelengths were measured, mice were imaged at 850 nm and the peak absorbance of the relevant contrast agent (700 nm for ABZWCY-HPβCD, 775 nm for IRDye 800CW). 10 frames were measured per wavelength and averaged giving a temporal resolution of 2 seconds. The differencing unmixing method was applied to reconstructions to quantify the dyes.

In experiments where one wavelength was measured, mice were imaged at the peak absorbance of the relevant contrast agent (700 nm for ABZWCY-HPβCD, 770 nm for STAR FLUOR 770 Acid). 10 frames were measured per wavelength and averaged giving a temporal resolution of 1 second. Time-lapse processing in viewMSOT software was used to quantify the change in dye concentration. A frame 5 seconds before injection was subtracted from the photoacoustic signal as the "zero point".

Following reconstruction, regions of interest (ROIs) were drawn for the renal cortex, renal medulla, renal pelvis, aorta, vena cava, and an apparent spinal blood vessel (Figure 2.1). The ROIs for the renal cortex and medulla were drawn in the dorsal aspect to limit interference from the spleen and liver. The boundary of the renal medulla was identified by a medial segment internal to the cortex which was where the initial flash of contrast was identified. MSOT does not provide contrast to differentiate cortex and medulla and these region labels should be interpreted with caution. The boundary of the spinal blood vessel was identified by a significant peak of contrast immediately following the peak in the aorta.

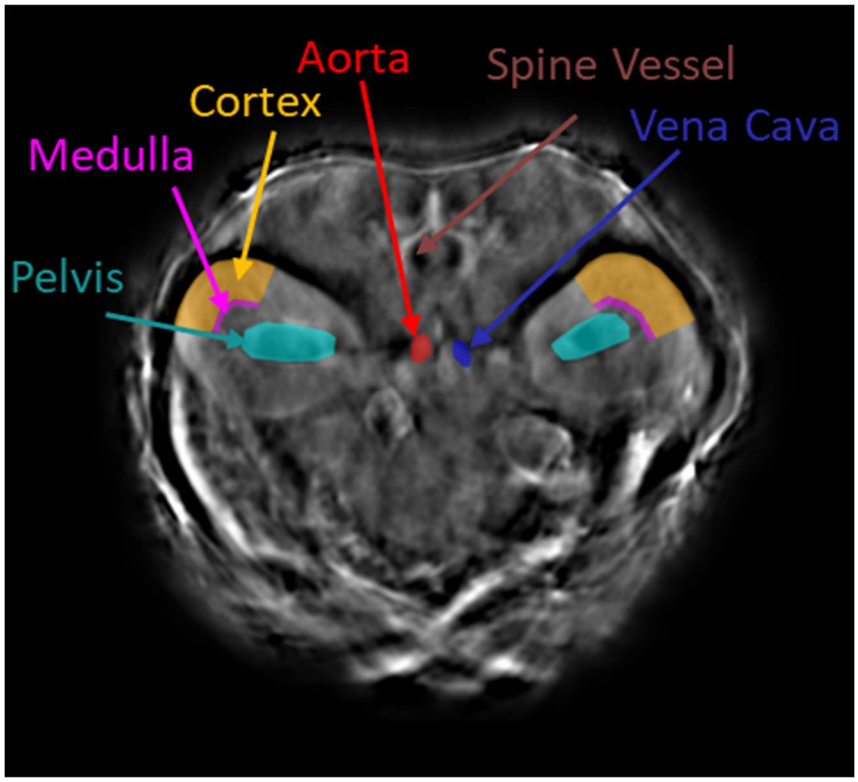

Figure 2.1: MSOT Regions of Interest in Renal Imaging

2.6.6 MSOT Vascular Haemoglobin and Oxygenation Imaging and Measurement

Following 15 minutes acclimatisation to the MSOT water bath, mice were imaged at five wavelengths: 700, 730, 760, 800, and 850 nm. This was measured before any contrast agent

was administered. 10 frames were measured and averaged. After image reconstruction, images were multispectrally unmixed for haemoglobin and oxyhaemoglobin using the linear regression algorithm (viewMSOT, iThera Medical, Germany). Multispectral unmixing algorithms use the total measured spectrum of a region and regression to estimate the relative quantities of multiple absorbers in that region by their a priori spectra. Regions of interest representing the aorta, vena cava, and spinal blood vessel were copied from the dye imaging scan.

2.7 Fluorescence Organ Imaging

All fluorescence Imaging was performed in the IVIS Spectrum In Vivo Imaging System (Perkin-Elmer, USA). The filter pair was selected using the IVIS imaging wizard after providing the peak optical absorbance and emission wavelengths of the dye in question. Epi-illumination was applied. Following MSOT, organs were harvested after schedule 1 cervical dislocation cull of mice. Urine was aspirated from the bladder by 0.5 mL insulin syringe and placed in a microfuge tube.

2.8 Statistical Analysis, Normalisation and Mathematical Model Fitting

2.8.1 Statistics

All statical tests were performed in Graphpad Prism 9.4.0 (Graphpad Software, USA). Paired T tests assume a gaussian distribution and are reported with two-tailed P values. Bland-Altman plots were calculated as the difference of A – B vs the average. Correlation Pearson r are reported with two-tailed P values. Confidence intervals and confidence bands are expressed at the 95% confidence limits. Statistical significance is abbreviated as follows:

ns P >0.05

* P ≤0.05

** P ≤0.01

*** P ≤0.001

**** P ≤0.0001

2.8.2 Normalisation Plots

Plots that were normalised are expressed so that largest value in each data set is 100% or 1.0 and the value of 0 is 0% or 0.0.

2.8.3 Calculation of Cortex Half-life

Graphpad prism 9.4.0 (Graphpad Software, USA) was used to fit the built-in one-phase exponential decay model (Equation 2.1) in the least squares sense to the first five minutes of cortex photoacoustic signal. Cortex half-life was calculated as the natural logarithm of 2 divided by the decay constant (K).

$$Y = (Y0 - P) * \exp(-K * T) + P$$

Equation 2.1: One-phase exponential decay
P (Plateau), T (Time), K (Decay constant), Y0 (Starting Signal)

2.8.4 Fitting of Mathematical Models and Calculation of MSOT Metrics

Matlab R2020a (MathWorks, USA) was used to calculate:

- area under the curve ratio (cumtrapz function)
- T^{MAX} and T^{MAX} delay (max function)
- Baumann-Rudin model (ode15s, lsqcurvefit, multistart functions)
- Patlak-Rutland model and Modified Patlak-Rutland model (cftool, cumtrapz functions)

Baumann-Rudin model (Equation 4.1) clearance was calculated by applying a smoothing spline to cortex data to create a fit object that was passed to the ordinary differential equation solver ode15s via the fit function lsqcurvefit. This fit the manually selected medulla or pelvis uptake phase in the least squares sense. A global minimum was found using the multistart function and 50 start points. The solved k_{cl} per second was multiplied by 60 and averaged over the two kidneys.

Patlak-Rutland (Equation 4.2) and Modified Patlak-Rutland (Equation 4.4) fits used a 1-degree polynomial fit with bisquare robust fitting and manual exclusion of data points after the initial renal accumulation phase. The integral of the blood was found by the cumtrapz function. Single kidney glomerular filtration rate was calculated by the slope of the polynomial fit multiplied by 0.5 (1 minus the assumed haematocrit) multiplied by the kidney volume measured in MSOT.

2.9 Transcutaneous Fluorescein Isothiocyanate-sinistrin Measurements and Global GFR Calculation

Mice were anaesthetised by isoflurane (1-3%) and oxygen (1 L/min). A small portion of fur at the dorsum near the loin was shaved and depilated (Veet Hair Removal Cream, RB

Healthcare, UK). The adhesive transcutaneous device (MB mini, Medibeacon, Germany) was applied to this region and 3 minutes of baseline readings were recorded. At 3 minutes, 75 µg/g body weight fluorescein isothiocyanate-sinistrin (FITC-sinistrin) was given by intravenous injection in the tail vein. Following this, mice were recovered from anaesthesia in individual cages. The devices were removed after 90 minutes. FITC-sinistrin curve data was analysed in MB Studio 2 (Medibeacon, Germany) using the 3-compartment fit. A global glomerular filtration rate was calculated from FITC-sinistrin half-life via Equation 2.2[97,156].

$$GFR(\mu L/min) = \frac{14620}{FSHL(\min)} \times 0.01 \times BW(g)$$

Equation 2.2: Calculation of a Global GFR from Transcutaneous Device Detected FITC-sinistrin Half-life
GFR (Glomerular filtration rate), FSHL (FITC-sinistrin half-life), BW (body weight).

2.10 Ischaemia Reperfusion Surgery

Ischaemia reperfusion surgery was performed by Dr Rachel Harwood (University of Liverpool). This method follows her optimised, published technique[155,215].

All surgical procedures were performed in specialised animal theatre. Sterile gloves, gowns, masks, and drapes were used. Mice were anaesthetised by isoflurane (1-3%) and oxygen (1 L/min). Mice received analgesia in the form of subcutaneous buprenorphine (1 mg/kg body weight). In addition to this, subcutaneous saline (0.5 mL) and Baytril (70 µL of 10% w/v) was administered. Baytril is Enrofloxacin, a fluoroquinolone antibiotic that is used here prophylactically against wound infection. Surgery was performed on heat pad with feedback from a rectal thermometer to maintain body temperature at 37°C (Far Infrared Warming Pads, Physiosuite, Kent Scientific, UK). Mice were shaved dorsally (if not already) and prepared with iodine surgical wash. At the loin, the skin then the muscle was incised using a scalpel. Abdominal pressure was applied to externalise the kidney via the incision. Forceps were used to expose the kidney blood vessels via blunt dissection. A vascular clamp (Schwartz, Interfocus, Linton) was applied across the vessels at the hilum so that a loss of perfusion was visibly identified. A timer was started, and the vascular clamp was removed after either 27.5 or 40 minutes. Reperfusion was confirmed visually. The kidney was gently pushed back into the abdominal cavity by wet cotton bud (sterile saline). Muscle then skin was sutured with braided absorbable 6/0 suture (cliniSorb, CliniSut sutures, UK). Mice were then recovered from anaesthesia in a 32°C heat box for 30 minutes.

2.11 Single-Photon Emission Computed Tomography

This work was performed by Dr Jack Sharkey and Dr Rachel Harwood (University of Liverpool).

Radioactive compounds were handled behind lead bricks and screens. They were transported in a lead-lined containers. 1 mg dimercaptosuccinic acid (DMSA, Renocis, Curium, UK) was combined with technetium-99m (Tc-99m) that was eluted from a molybdenum 99 generator (Curium, UK). Renocis was labelled with Tc-99m that produced an activity of 3.7 GBq per 5 mL. While anaesthetised with isoflurane and oxygen, a dose of 12 MBq Tc-99m DMSA in 0.9% saline was given to mice by intravenous injection via the tail vein. Mice were then recovered in individual cages.

After four hours mice were anaesthetised again by isoflurane and oxygen. A single-photon emission computed tomography scan was performed in Molecubes Imaging System (Molecubes NV, Belgium). Images were reconstructed in VivoQuant (Invicro, USA). Radioactivity was measured in each kidney by a hand drawn region of interest. Split renal function was calculated as the radioactivity of the right injured kidney divided by the sum of radioactivity of both kidneys.

2.12 Histological Assessment of Kidney Injury

Histological processing and assessment were performed by Professor Lorenzo Ressel and Ms Andreea Luchian at the Veterinary Histopathology Laboratory, Leahurst Campus, University of Liverpool, UK.

Kidneys were collected following schedule 1 cull by cervical dislocation. Kidneys were fixed in 10% formalin and stored at 4°C. Samples were dehydrated by increasing ethanol concentrations (70, 85, 96, 100%), cleared with xylene, infiltrated with wax, and embedded in paraffin blocks. 4 µm sections were cut and mounted to glass slides and stored at 60°C for 45 minutes.

Haematoxylin and eosin (H&E, TCS Biosciences Ltd, UK) staining was used to count fibroblasts. Sections were dewaxed in xylene for 5 minutes, rehydrated through descending grades of ethanol (100, 96, 85, 70%) then distilled water. Sections were then stained with haematoxylin (Mayer's Haemalum) for 5 minutes then rinsed with tap water for 5 minutes. Then sections were stained with eosin for 2 minutes. Then sections are dehydrated three times with 96% ethanol then three times with 100% ethanol for 1 minute each. Then two further immersions in xylene. Sections were mounted in DPX.

Periodic Acid-Schiff (PAS) staining was performed to highlight the tubular brush border and basement membrane. PAS was used for injury scoring features of tubular damage (tubular regeneration, casts, necrosis, and inflammation). For PAS staining, sections were dewaxed and rehydrated as above then stained for 10 minutes in 0.5% periodic acid (50% w/v aqueous periodic acid, TCS Biosciences Ltd, UK) and then rinsed with distilled water. Sections were then exposed to Schiff reagent (Solmedia Ltd, UK) for 30 minutes and then washed with tap water for 10 minutes. Then sections were stained with haematoxylin (Mayer's Haemalum) for 2 minutes and rinsed in tap water for 5 minutes. Dehydration with ethanol, immersion in xylene, and mounting was performed as for H&E protocol.

2.12.1 Tubular Injury Score

On PAS-stained sections, ten fields of view (10x objective) were selected at random on a single, central section of kidney. The percentage field of view occupied by regenerating tubules, inflammation, tubular dilatation, and casts/necrosis was estimated by two assessors and scored as follows:

Field of View Percentage	Score
0%	0
1-25%	1
26-50%	2
51-75%	3
75-100%	4

The scores across the ten fields of view were averaged to give a final score in each category.

2.12.2 Fibroblast Score

On H&E-stained sections, five fields of view (10x objective) were selected at random on a single, central section of kidney. The number of rows of fibroblasts and the number of clusters of fibroblasts were counted. The number of fibroblast rows per cluster was averaged across the five fields of view.

3 Characterisation of Near-Infrared Dyes for the Assessment of Renal Function using Multispectral Optoacoustic Tomography

3.1 Introduction

Multispectral optoacoustic tomography (MSOT) has the potential to measure glomerular filtration and tubular secretion noninvasively and longitudinally. This requires the identification of appropriate contrast agents that undergo these processes. The measurement of glomerular filtration rate (GFR) is highly desirable as it represents the amount of functioning kidney tissue[31]. Also, a decrease in GFR is associated with a decline in tubular, metabolic, and endocrine functions of the kidney[30,31]. Measuring tubular secretion is attractive as a number of pathologies are known to primarily affect the tubules[71]. Also, tubular secretion is a significant clearance route for drug excretion, and plays an important role in the metabolic complications of chronic kidney disease[71,137]. Measuring these separate processes would facilitate greater understanding of renal function, injury, and recovery. Using dynamic contrast enhanced (DCE) imaging to measure these processes provides separate quantification of left and right kidney function which can be leveraged to provide an internal control in unilateral injury model experiments.

Jiang et al have estimated single kidney GFR with MSOT by measuring the renal clearance of a gold nanoparticle, $Au_{25}(SG)_{18}$, in combination with a Patlak-Rutland model[183]. This was examined in both healthy mice and following a surgical injury model of unilateral ureteral obstruction. However, alternative contrast agents for measuring GFR in MSOT are worth exploring as gold nanoparticles have a higher theoretical risk of toxicity, show poor biodegradability, and are relatively expensive[216–218].

There is no gold standard method to measure tubular secretion rate (TSR) despite a number of markers having been considered[135–137]. In imaging, tubular secretion has been measured by renal scintigraphy using technetium-99m (Tc-99m) labelled mercaptoacetyltriglycine (MAG3)[144]. The literature does not provide evidence of attempts to measure tubular secretion by MSOT.

Small-molecule organic near-Infrared (NIR) dyes show potential benefits over gold nanoparticles in MSOT. They are associated with low toxicity, high biocompatibility, and rapid clearance[176,216]. They can show a variety of ionic charges and different degrees of

protein binding that results in their potential clearance by different excretory routes in vivo including glomerular filtration and tubular secretion.

Several publications have used preclinical MSOT to assess renal clearance by measuring the kinetics of the NIR dye IRDye 800CW[155,157,207,210,219–223]. The tissue distribution of IRDye 800CW in rodents is primarily in the kidneys and urine, but it is also present in the liver and other organs[224]. The specificity of IRDye 800CW for assessing renal function is in question due to its high levels of plasma protein binding (41%)[157] and evidence of the dye in the extrahepatic bile ducts of live rodents after intravenous administration[225]. As such, the renal kinetics of IRDye 800CW are described in terms of the time to peak concentration or area under the curve[157,219]. IRDye 800CW cannot be used to calculate GFR due to its significant protein binding.

Therefore, identification of suitable NIR dyes to measure GFR and TSR by MSOT are required. Ideally these dyes would yield high intensity photoacoustic signal following absorbance of NIR light, be photostable under normal MSOT imaging conditions, be excreted unchanged in the urine, and be specifically cleared by either glomerular filtration or tubular secretion. They would not be cleared by non-kidney elimination nor be metabolised. It would also be beneficial if their photoacoustic spectra were unique to allow accurate multispectral unmixing from native and administered absorbers in MSOT.

3.1.1 ABZWCY-HPβCD: MSOT Glomerular Filtration Marker Candidate

ABZWCY-HPβCD has shown great potential as a marker of GFR in rodents[102], but it has not previously been examined in MSOT. ABZWCY-HPβCD is a zwitterionic heptamethine cyanine NIR dye bound to 2-hydroxylpropyl-β-cyclodextrin with a peak optical absorbance of 705 nm and a molecular weight of 2,466 Da[101,102]. Huang et al have shown that ABZWCY-HPβCD has low plasma protein binding (3.7%), has high levels of urinary recovery (97% after 24 hours), does not undergo tubular secretion, and is not cytotoxic on incubation with human proximal tubular cells[102]. The urinary recovery of ABZWCY-HPβCD compares favourably with $Au_{25}(SG)_{18}$ (70% after 24 hours)[183].

3.1.2 STAR FLUOR 770 Acid: MSOT Tubular Secretion Marker Candidate

STAR FLUOR 770 Acid is a commercially available, water soluble, cyanine NIR dye with a peak optical absorbance of 774 nm, a molecular weight of 1,160 Da, and is produced by Cyanagen, Italy[226]. It has a net negative charge owing to two sulfonate groups. Due to the anionic charge, it may undergo tubular secretion by organic anion transporter (OAT) proteins in the proximal tubule. The negative charge of STAR FLUOR 770 Acid also reduces the likelihood

that it is filtered by the glomerulus where the glycocalyx and the basement membrane contain fixed, negatively charged molecules that repel other negatively charged molecules. STAR FLUOR 770 Acid has not previously been examined in MSOT, nor has it been assessed in terms of routes of clearance.

3.1.3 Objectives

This chapter aims to assess the suitability of these two NIR dyes for the measurement by MSOT of GFR (ABZWCY-HPβCD) or TSR (STAR FLUOR 770 Acid). The objectives of this chapter were to:

1. Characterise the optical and photoacoustic spectra of the two dyes
2. Determine the relationship between dye concentration and photoacoustic signal intensity
3. Examine the photostability of the dyes in normal MSOT imaging conditions
4. Compare the renal kinetics of ABZWCY-HPβCD to IRDye 800CW in mice
5. Asses the degree of protein binding of STAR FLUOR 770 Acid
6. Assess for biliary excretion of the two dyes
7. Assess for changes in spectral properties of STAR FLUOR 770 Acid after renal excretion

3.2 Results

3.2.1 Optical and Photoacoustic Spectra of ABZWCY-HPβCD and STAR FLUOR 770 Acid

The photoacoustic spectra of both dyes were measured to find which wavelength yielded the greatest intensity of photoacoustic signal to facilitate the highest signal sensitivity when later measured in single wavelength DCE MSOT. This was examined with and without bovine serum albumin (BSA) as proteins can alter the spectral properties of NIR dyes[227]. These were compared to optical absorbance spectra to investigate whether there was any difference.

The optical absorbance of solutions of the two dyes in either phosphate buffered saline (PBS), or 10% bovine serum albumin (BSA) were measured using a microplate reader; the photoacoustic spectrum was measured in an agar phantom using MSOT. The optical and photoacoustic spectra of the solvents (PBS and BSA) were measured in the same way and subtracted from the dye-containing samples to find the spectrum of the dye alone.

3.2.1.1 ABZWCY-HPβCD Spectra

Optical and photoacoustic spectra of ABZWCY-HPβCD are largely identical in PBS (Figure 3.1A). There is a slight suggestion of a left-shift in the peak (695 nm from 705 nm) and a broader absorbance curve from the photoacoustic spectrum.

The presence of BSA does not greatly change the optical absorbance nor the photoacoustic spectrum of ABZWCY-HPβCD (Figure 3.1B&C). There is a slightly broader photoacoustic spectrum where BSA has been added (Figure 3.1C)

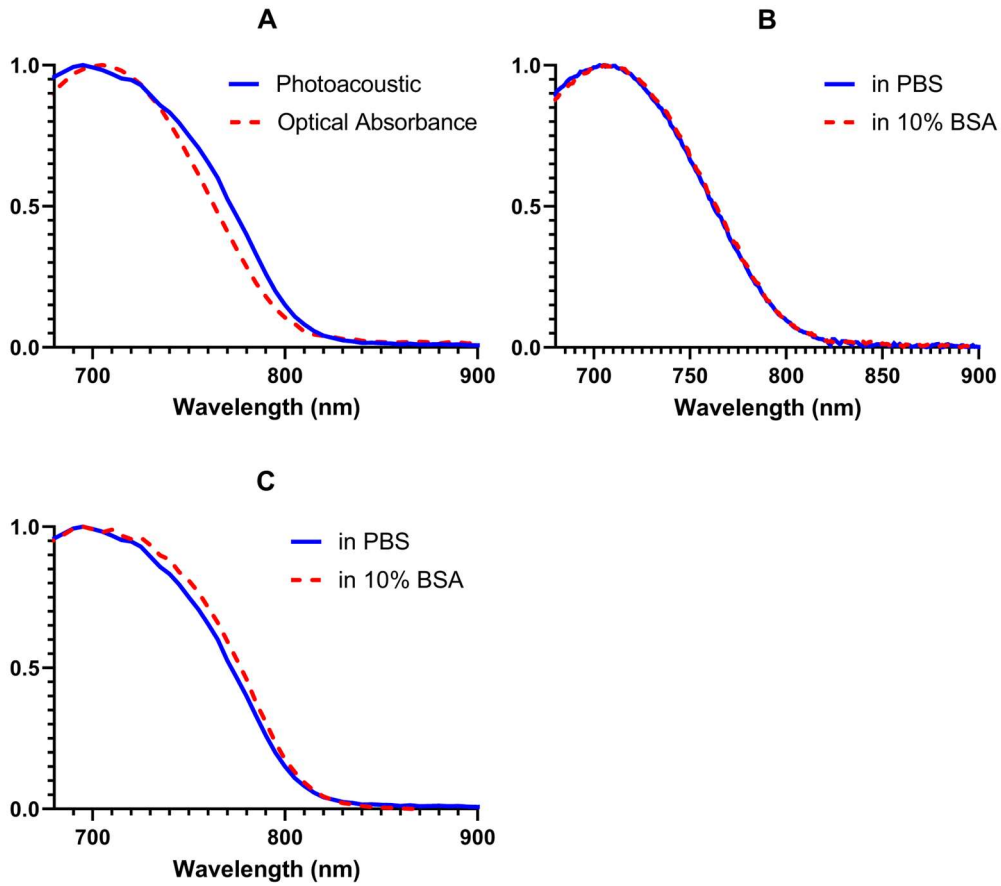

Figure 3.1: Normalised Spectra of ABZWCY-HPβCD.
A. Spectral analysis of 20 µM ABZWCY-HPβCD in PBS: photoacoustic spectrum measured in agar phantom in MSOT, and optical absorbance measured in microplate reader. B. Optical absorbance of 20 µM ABZWCY-HPβCD dissolved in PBS with or without 10% BSA measured with a microplate reader. C. Photoacoustic spectra of 20 µM ABZWCY-HPβCD dissolved in PBS with or without 10% BSA as inserts in agar phantom. PBS (Phosphate Buffered Saline), BSA (Bovine Serum Albumin)

3.2.1.2 STAR FLUOR 770 Acid Spectra

Solutions of STAR FLUOR 770 Acid were measured in the same way as ABZWCY-HPβCD. STAR FLUOR 770 Acid in PBS showed a similar peak in both optical absorbance and photoacoustic spectra at 770 nm. However, the photoacoustic spectrum showed a broader absorbance curve and an elevated left shoulder compared with optical absorbance (Figure 3.2A).

The addition of BSA shifted the optical absorbance peak from 770 nm to 786 nm but the overall spectral shape remained the same (Figure 3.2B).

A spectral shift to the right was also seen in the photoacoustic spectrum after the addition of BSA (Figure 3.2C). However, this shift was far less pronounced than seen in the optical spectra. The peak photoacoustic intensity shifted from 770 nm to 775 nm.

Both dyes show similar photoacoustic spectra with and without BSA. ABZWCY-HPβCD shows greater spectral similarity between its photoacoustic and optical absorbance spectra than STAR FLUOR 770 Acid does.

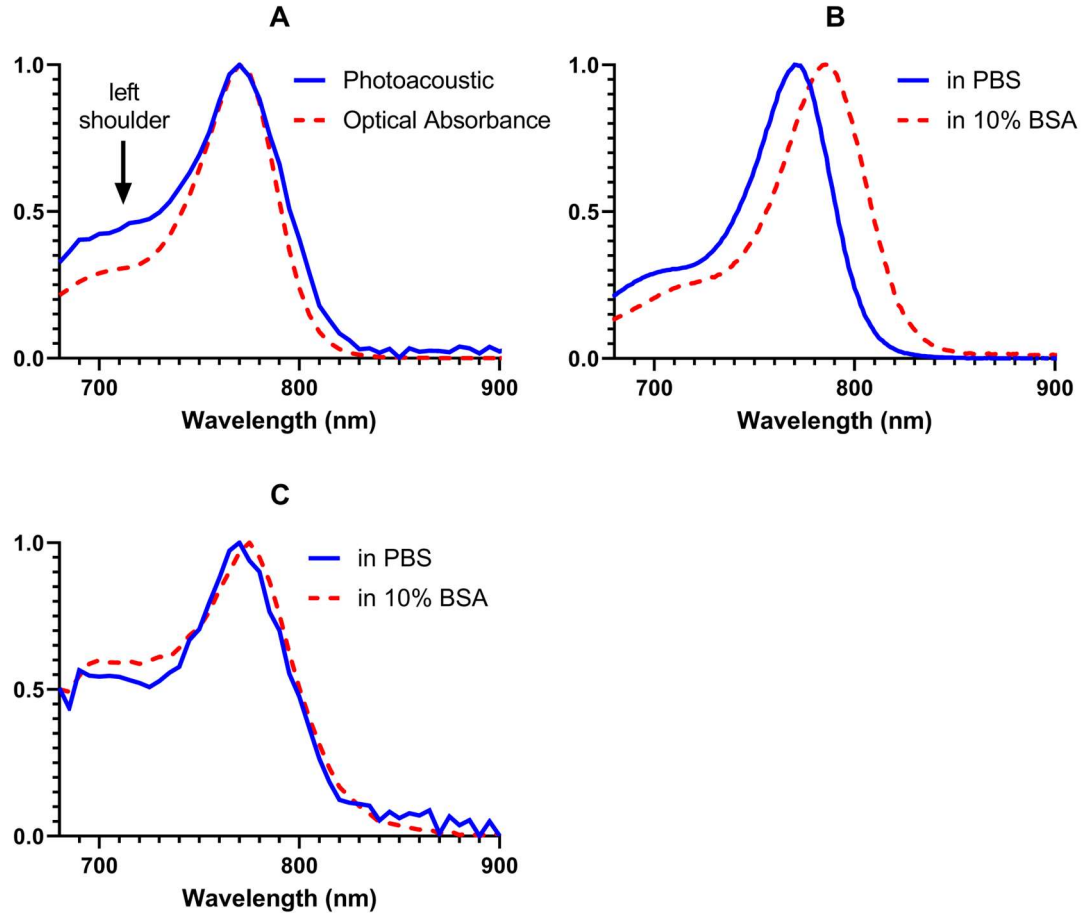

Figure 3.2: Normalised Spectra of STAR FLUOR 770 Acid.
A. 20 µM STAR FLUOR 770 Acid in PBS: comparing photoacoustic spectrum measured in agar phantom in MSOT and optical absorbance measured in microplate reader. B. Microplate reader measured optical absorbance of 20 µM STAR FLUOR 770 Acid dissolved in PBS with or without 10% BSA. C. MSOT measured photoacoustic spectra of 20 µM STAR FLUOR 770 Acid dissolved in PBS with or without 10% BSA as agar phantom inserts. PBS (Phosphate Buffered Saline), BSA (Bovine Serum Albumin).

3.2.2 Photoacoustic Signal Intensity of NIR Dyes at Different Concentrations

The relationship between photoacoustic signal intensity and concentration of our two candidate NIR dyes was examined so that parametric models that use marker concentration

as an input could later be applied (chapter 4). Comparison was made with IRDye 800CW to examine the relative photoacoustic signal yield.

Solutions of each dye were imaged in an agar phantom by MSOT at seven concentrations. Photoacoustic intensity was measured at the peak MSOT absorbance of each dye. Absorbance of a PBS control insert was subtracted to find the photoacoustic yield of the dye alone. All three dyes appears to show a loosely linear relationship between concentration and photoacoustic signal (Figure 3.3).

Simple linear regression shows STAR FLUOR 770 Acid has a lower photoacoustic signal per µM (Figure 3.3B, slope = 14.42) than both ABZWCY-HPβCD (Figure 3.3A, slope = 27.86) and IRDye 800CW (Figure 3.3C, slope = 30.53).

IRDye 800CW shows some suggestion of a drop off in photoacoustic signal at concentrations above 20 µM (Figure 3.3C).

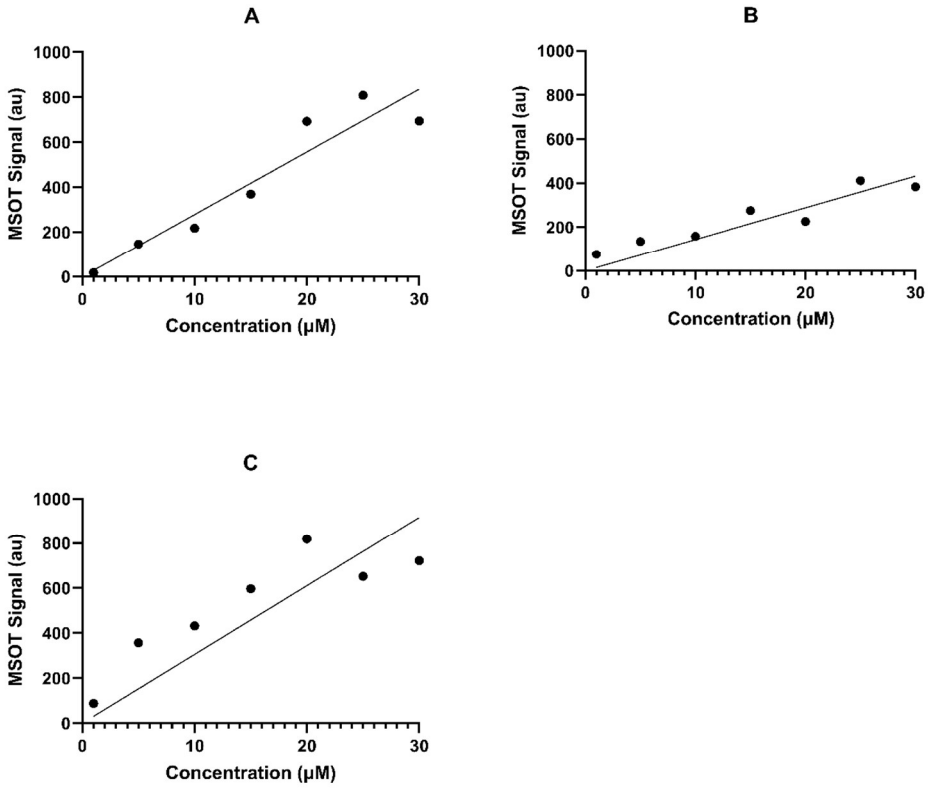

Figure 3.3: Concentration versus Photoacoustic Signal of NIR Dyes in Agar Phantom.
Dyes were measured at their peak photoacoustic absorbance in MSOT. A. ABZWCY-HPβCD measured at 700 nm. B. STAR FLUOR 770 Acid meaured at 770 nm. C. IRDye 800CW measured at 775 nm.
Solid lines are a simple linear regression fit.

3.2.3 Change in Photoacoustic Signal of NIR Dyes with Prolonged MSOT Imaging

As NIR dyes are known to undergo photodegradation[228–230], we examined whether there was evidence of a change in photoacoustic intensity with continual NIR laser irradiation in MSOT. This is important because a change in photoacoustic intensity should reflect changes in concentration that are due to clearance rather than break down.

Solutions of each dye were imaged in an agar phantom by MSOT at their peak photoacoustic absorbance wavelength at 34°C. to mimick mouse imaging conditions that would be used in DCE MSOT.

Figure 3.4 shows that all three dyes produce less photoacoutic signal through time in these conditions. The photoacoustic signal of IRDye 800CW declines the most rapidly. Photoacoustic signal decay was largely similar for the first 5 minutes for all three dyes, and similar for ABZWCY-HPβCD and STAR FLUOR 770 Acid for the first 12 minutes of imaging.

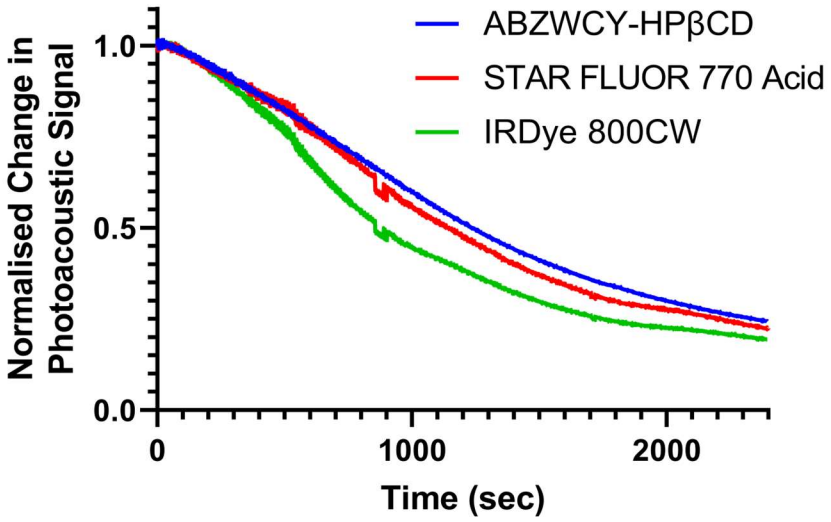

Figure 3.4: Change in Photoacoustic Signal of NIR Dyes with Continuous MSOT Imaging.
Agar Phantoms with 30 µM NIR dye in PBS insert imaged at 34°C and at 700 nm (ABZWCY-HPβCD) or 770 nm (STAR FLUOR 770 Acid and IRDye 800CW) with a temporal resolution of 0.1 seconds. PBS (Phosphate Buffered Saline).

3.2.4 Comparing the Renal Kinetics of ABZWCY-HPβCD and IRDye 800CW in Mice

As IRDye 800CW is the most used contrast agent for assessing renal function in MSOT, and ABZWCY-HPβCD has previously shown favourable characteristics as a GFR marker, we compared these dyes in mice using DCE MSOT. We hypothesised that a difference in their clearance would confirm the renal excretion of IRDye 800CW as not being solely via filtration.

Four mice were imaged on two occasions, four days apart in MSOT. An intravenous injection of either ABZWCY-HPβCD or IRDye 800CW was given during imaging. The initial 5 minutes of MSOT signal intensity in the right renal cortex was fit with a one-phase exponential decay to calcualte the half-life.

Goodness of fit for the one-phase exponential decay was acceptable showing a mean R^2 of 0.8945 (Table 3.1). Examples of the cortex curves and the fitting with a one-phase exponential decay can be seen in Figure 3.5A&C.

The mean half-life in the renal cortex for IRDye 800CW was 82.9 seconds and for ABZWCY-HPβCD was 108.6 seconds (Figure 3.5B). A paired t test showed a mean half-life difference of 25.7 seconds (95% CI 18.6 to 32.7 seconds) which was significant (P = 0.0014).

Peak photoacoustic signal in the renal cortex was significantly higher for ABZWCY-HPβCD than IRDye 800CW (Figure 3.5D, P = 0.0178) with a mean difference of 63.95 au/pixel (95% CI 20.98 to 106.9 au/pixel). This was despite IRDye 800CW showing greater photoacoustic signal per µM than ABZWCY-HPβCD in the MSOT phantom experiments (Figure 3.3).

Table 3.1: Goodness of fit for one-phase exponential decay fits of renal cortex in MSOT

Mouse	R^2 for ABZWCY-HPβCD	R^2 for IRDye 800CW
1	0.9603	0.9255
2	0.9112	0.9176
3	0.9748	0.8856
4	0.9187	0.6626
Mean	0.9413	0.8478

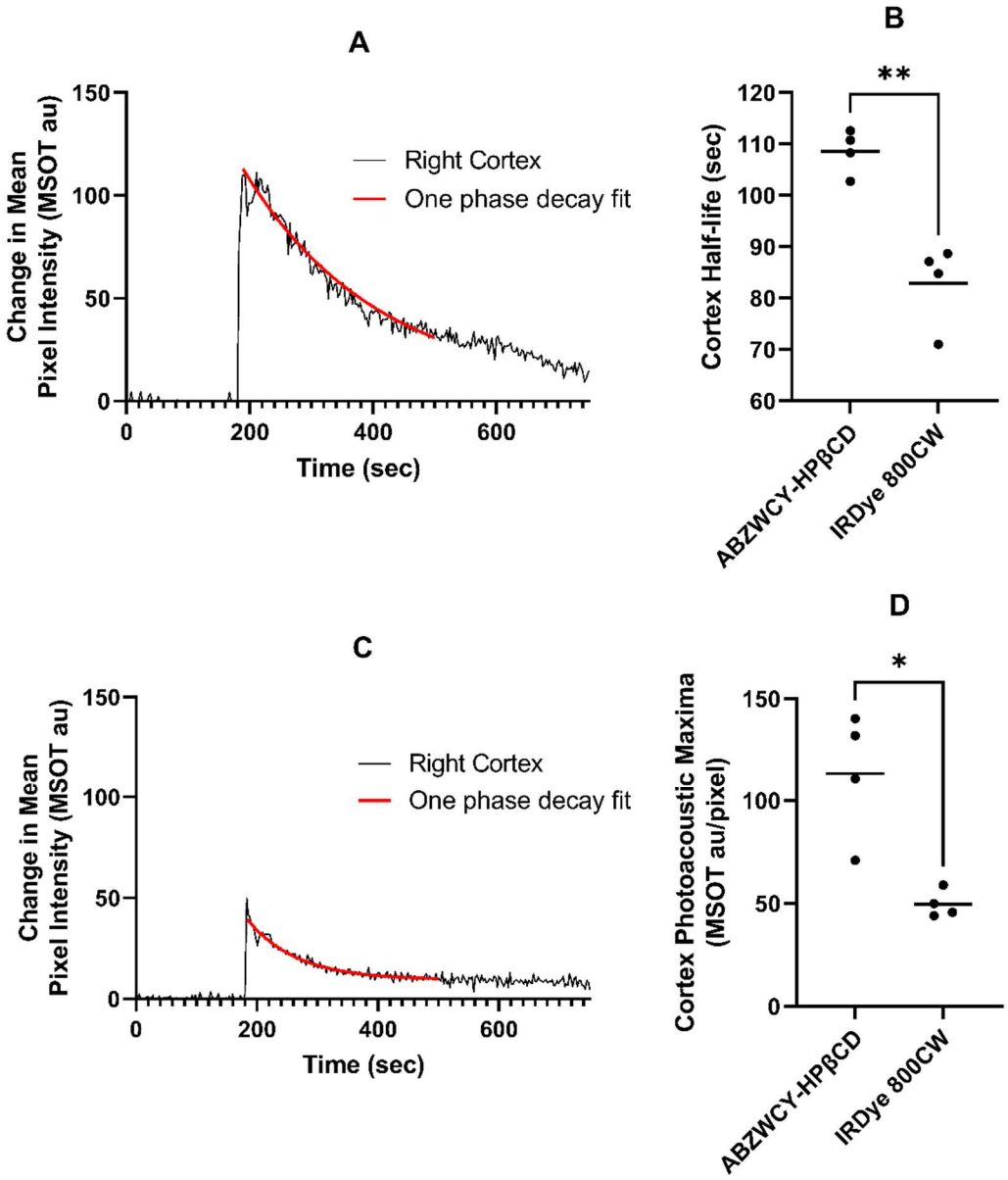

Figure 3.5: Comparing Renal Cortex Kinetics of ABZWCY-HPβCD and IRDye 800CW.
A. Typical one-phase exponential decay fit of ABZWCY-HPβCD. B. Half-life of both dyes measured in the right renal cortex (P=0.001392). C. Typical one-phase exponential decay fit of IRDye 800CW. D. Maximum photoacoustic signal of both dyes measured in the right renal cortex (P=0.0178).
Horizontal lines are the mean.

In summary, IRDye 800CW has shown a more rapid decline and a lower peak photoacoustic intensity than ABZWCY-HPβCD in the renal cortex when measured by MSOT.

3.2.5 Plasma Protein Binding of STAR FLUOR 770 Acid

As plasma protein binding may be advantageous in a tubular secretion marker[71,72,231], the degree of plasma protein binding of STAR FLUOR 770 Acid was examined by our collaborators, Yinuo Xie and Dr Norbert Gretz, at the University of Heidelberg, Germany.

Fast Micro Equilibrium Dialysis of dye in PBS with human plasma was performed. The degree of protein binding was calculated by measuring the absorbance of the dialysate and using Equation 3.1. The mean plasma protein binding was 47.17% (Figure 3.6).

$$PPB\% = \frac{(A[PD] - A[PC]) - (A[SD] - A[SC])}{(A[PD] - A[PC]) + (A[SD] - A[SC])} \times 100\%$$

Equation 3.1: Plasma Protein Binding Percentage
PPB (plasma protein binding), A (absorbance), PD (plasma with dye, undialysed portion), PC (plasma control), SD (saline with dye, dialysed portion), SC (saline control).

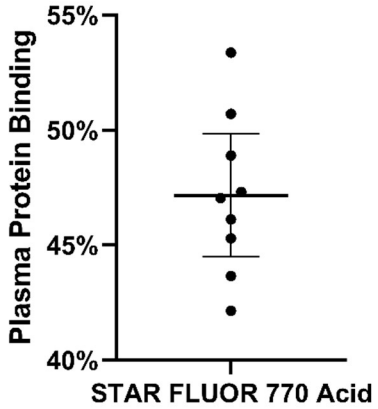

Figure 3.6: Plasma Protein Binding of STAR FLUOR 770 Acid by Micro-Equilibrium Dialysis.
Mean 47.17% (95% CI, 44.51 to 49.84%). Performed by Yinuo Xie, University of Heidelberg, Germany. Bars are the standard deviation.

3.2.6 Biliary Excretion of NIR Dyes

As both an ideal marker of tubular secretion and glomerular filtration should not show any extra-renal clearance, we investigated if there was any evidence of biliary clearance of our two candidate dyes. These were compared against the NIR dye Indocyanine Green (ICG) that is entirely excreted in the bile[208,209].

Seven mice underwent MSOT imaging of their liver and gallbladder with intravenous injection of either ICG (three mice), ABZWCY-HPβCD (two mice), or STAR FLUOR 770 Acid (two mice). Organs were collected post-mortem, and urine was aspirated from the bladder. Tissue and urine fluorescence was quantified by IVIS Spectrum fluorescence imager (Figure 3.8).

MSOT (Figure 3.7) was able to detect ICG accumulating in the gallbladder in all three cases. MSOT showed minimal uptake in the region of the gallbladder for mice that received ABZWCY-HPβCD. Finally, MSOT demonstrated mice receiving STAR FLUOR 770 Acid had

greater signal in the region of the gallbladder than those receiving ABZWCY-HPβCD but less than those receiving ICG. The gallbladder provided little photoacoustic contrast natively.

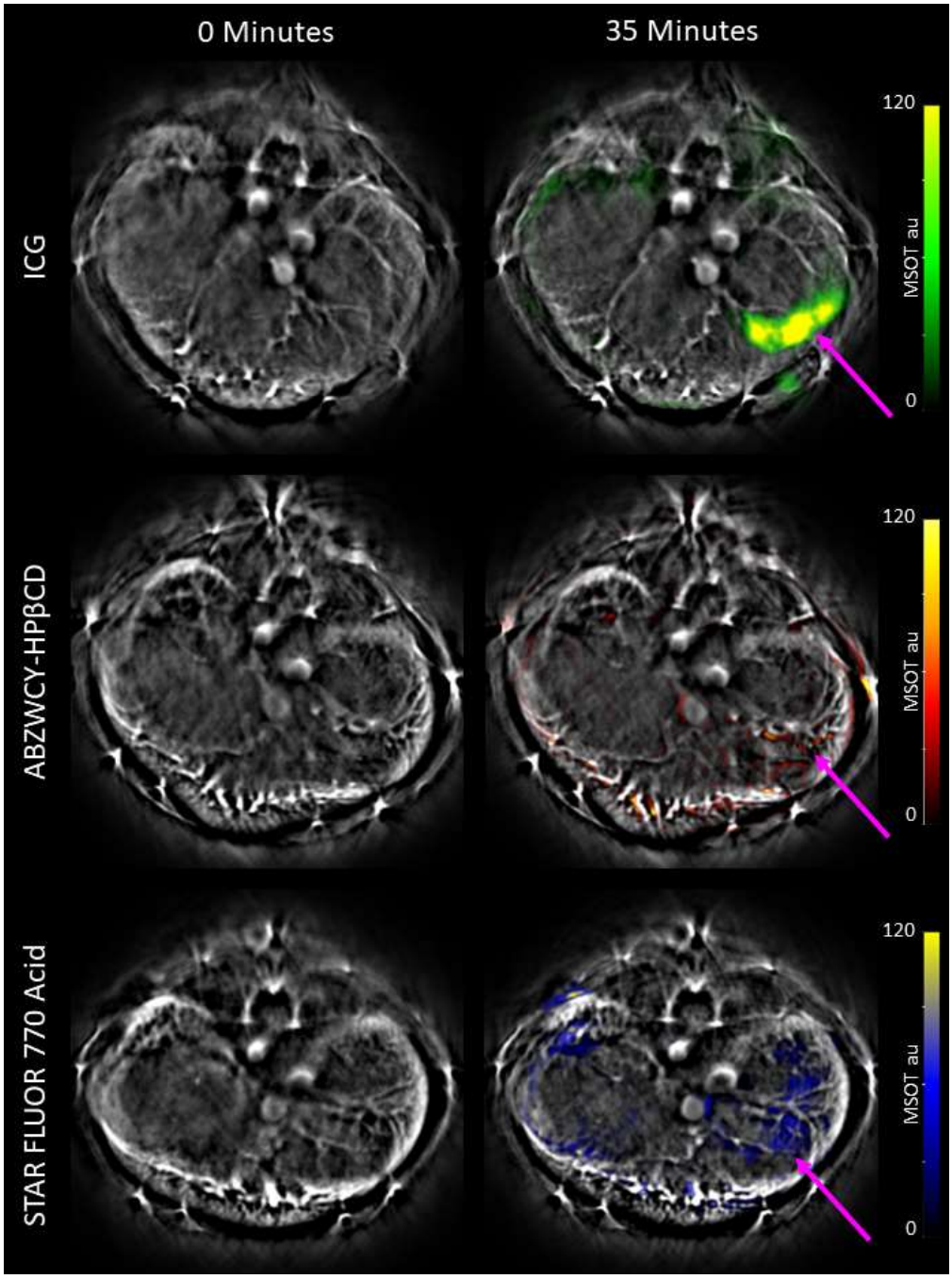

Figure 3.7: MSOT Imaging of Liver and Gallbladder after 20 nmol NIR Dye Administration.
Magenta arrow indicating approximate location of the gallbladder. ICG (Indocyanine Green). Colour coding of the scales is arbitrary.

Fluorescence images of ex-vivo organs (Figure 3.8) revealed mice receiving ICG had signal predominantly in the liver and gallbladder, while no signal was detected in the urine. In contrast, Mice receiving ABZWCY-HPβCD had signal predominantly in the kidneys and urine

with little signal from the gallbladder. Finally, mice receiving STAR FLUOR 770 Acid showed signal in all four tissues.

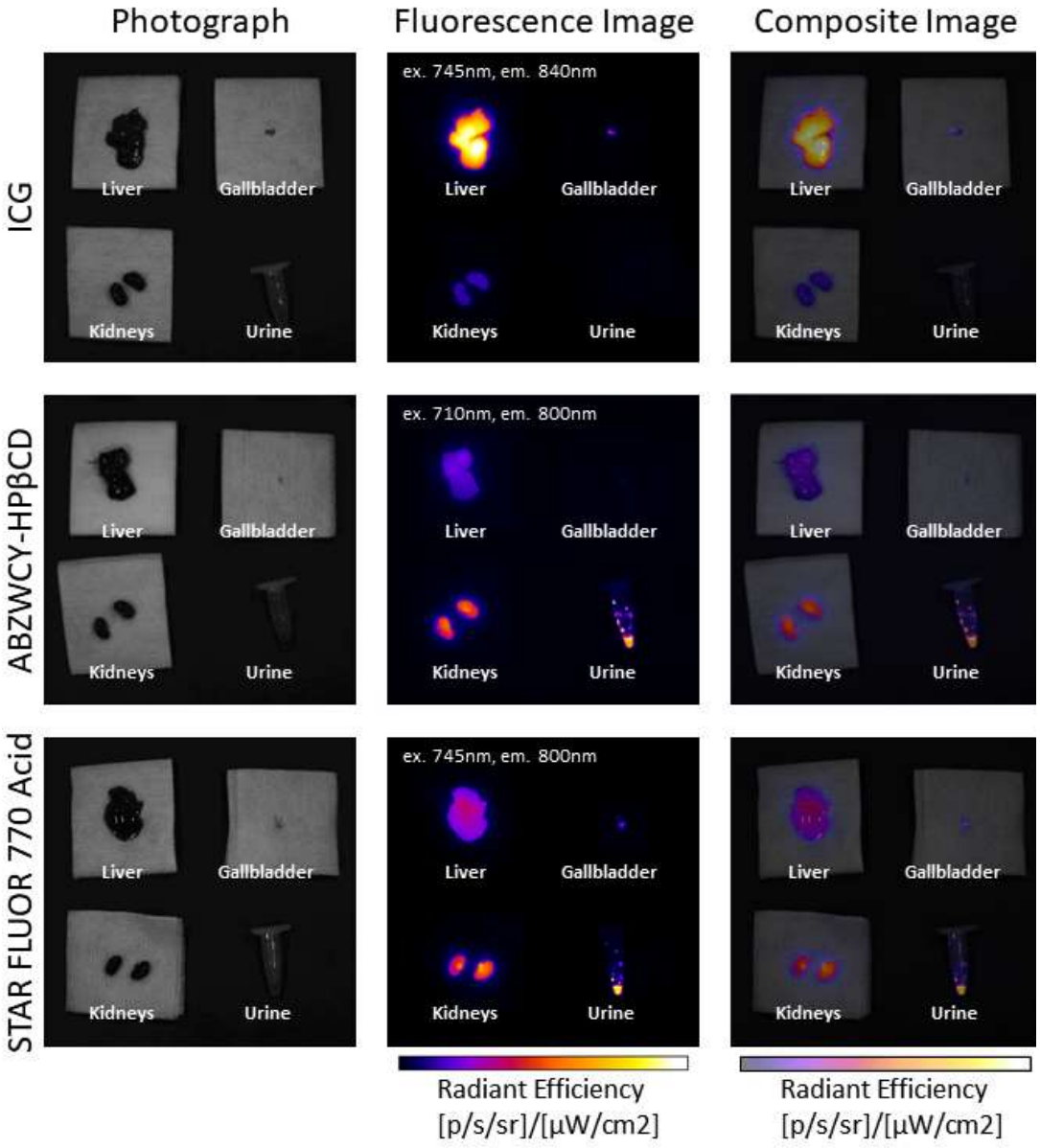

Figure 3.8: Fluorescence Imaging of Organs and Urine following Intravenous Injection of 20 nmol NIR Dyes. ICG (Indocyanine Green), [p/s/sr]/[µW/cm^2] ([photons per second per steradian] per [microwatt per cm^2])

3.2.7 Photospectrum of STAR FLUOR 770 Acid Following Renal Excretion

An ideal tubular secretion marker should be excreted unchanged in the urine and undergo no metabolism. We examined the photospectra of urine after the administration of STAR FLUOR 770 Acid to investigate for evidence of metabolites and changes in optical absorbance of the dye.

Four mice had their bladder aspirated for urine following the intravenous injection of either 20 nmol STAR FLUOR 770 Acid (three mice) or PBS (one mouse). The photospectrum of urine was measured in a microplate reader (Figure 3.9) and showed that the spectral properties of STAR FLUOR 770 Acid remained unchanged (Figure 3.9B) after in vivo administration and renal excretion. No additional spectral peaks were identified to suggest the excretion of additional NIR absorbent metabolites.

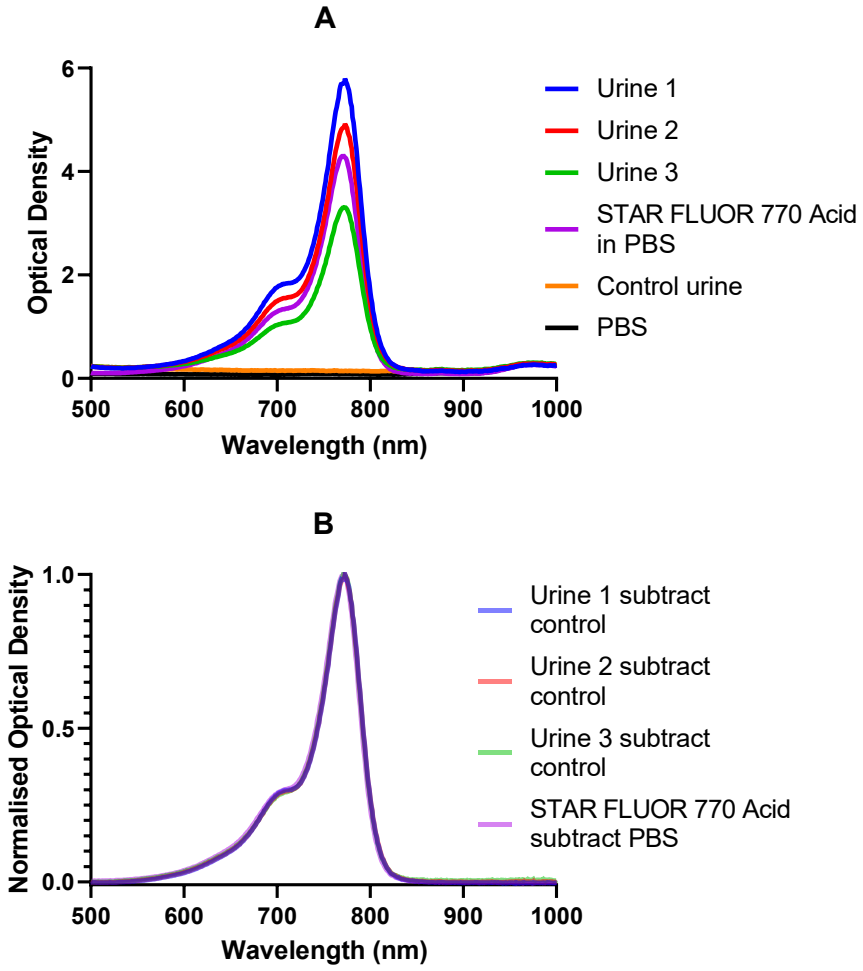

Figure 3.9: Optical Absorbance Spectrum of Urine following IV Injection of 20 nmol STAR FLUOR 770 Acid. A. Absolute absorbance of samples and controls. B. Normalised absorbance of samples subtracting control urine. PBS (phosphate buffered saline).

3.3 Discussion

Here we report on several experiments aiming to characterise ABZWCY-HPβCD and STAR FLUOR 770 Acid and their potential to specifically image and quantify the renal excretory functions of live mice in MSOT.

3.3.1 ABZWCY-HPβCD and STAR FLUOR 770 Acid are Suitable MSOT Contrast Agents

Both dyes have shown absorbance in the NIR spectrum and the capacity to produce ultrasound waves when irradiated by NIR laser in MSOT.

Optical absorbance spectra and photoacoustic spectra for ABZWCY-HPβCD are largely similar and unchanged by the presence of BSA. This is likely attributable to the previously reported low protein binding (3.7%) of ABZWCY-HPβCD[102]. STAR FLUOR 770 Acid shows an optical spectral shift in the presence of BSA that is less pronounced in photoacoustic spectra when measured in MSOT. The binding of cyanine dyes to albumin and other serum proteins can alter their spectral properties including their fluorescence quantum yield and peak absorbance[227]. Additionally, photoacoustic spectra can differ significantly from optical absorbance[232]. As such, the spectral nature of a dye should be examined under environmental conditions that are similar to those in vivo.

In chapters 4 and 5, the DCE MSOT performed measures a single wavelength continuously to maximise temporal resolution. However, for any future multispectral unmixing of these dyes in vivo, spectral analysis should be performed to select the best wavelengths that would facilitate unmixing from native absorbers e.g., haemoglobin. Theoretically, the sharper, more defined spectral peak of STAR FLUOR 770 Acid may lend itself better to multispectral unmixing than the broader photoacoustic spectrum of ABZWCY-HPβCD.

ABZWCY-HPβCD produces a more intense photoacoustic signal in MSOT phantom than STAR FLUOR 770 Acid at similar concentrations. ABZWCY-HPβCD has a fluorescence quantum yield of 3.2%, STAR FLUOR 770 Acid has a fluorescence quantum yield of 10%, while that of IRDye 800CW is 9%[102,226,233]. A lower fluorescence quantum yield can be associated with a higher photoacoustic yield as this potentially means a greater proportion of absorbed light energy is converted to heat and ultrasound waves rather than emitted light[176]. This is a potential advantage for ABZWCY-HPβCD use in MSOT. However, the efficiency with which an absorber converts heat to an expansion related pressure change is also important[234] and may explain the relatively high photoacoustic signal produced by IRDye 800CW despite having a similar fluorescence quantum yield to STAR FLUOR 770 Acid. Finally, none of the three dyes show a perfectly linear relationship between concentration and photoacoustic signal (Figure 3.3). This variation across concentrations may relate to differences in phantom positioning and acoustic coupling between scans. In between imaging each concentration, the phantom is removed from the MSOT holder to insert the next straw containing a different concentration.

The amount of ultrasound gel applied, the rotation, and the position in the MSOT water bath is not identical and may result in these discrepancies.

Both ABZWCY-HPβCD and STAR FLUOR 770 Acid show a decline in the intensity of photoacoustic signal produced with continuous imaging in MSOT. NIR cyanine dyes are known to undergo photodegradation by oxidative cleavage[228–230]. Continual exposure to the MSOT laser could be causing photodegradation and lead to the loss of photoacoustic signal. This is an important consideration for our planned application as a loss of signal over time could be interpreted as the dye being cleared. As such, any assessment of the kinetics of these dyes in MSOT should either use a small time-course of data where degradation is least impactful or compare two or more regions where degradation can be assumed to be similar.

3.3.2 ABZWCY-HPβCD Renal Clearance is Significantly Different from IRDye 800CW in MSOT

IRDye 800CW is the most frequently used NIR dye to examine renal excretory function in MSOT[155,157,207,210,219–223]. However, significant protein binding[157] and evidence of biliary excretion[225] mean the clearance of IRDye 800CW is not renal specific and is not an appropriate marker to use to measure GFR. In contrast, ABZWCY-HPβCD has shown good potential as a GFR marker[102].

Here we have measured the kidney cortex NIR dye half-life by fitting a one-phase exponential decay to the first five minutes of MSOT photoacoustic signal. This was chosen as the decay in photoacoustic signal in phantom experiments were similar during the first five minutes for ABZWCY-HPβCD and IRDye 800CW (Figure 3.4). The difference between the renal cortex half-life of the two dyes is significant and suggests they are being cleared by different mechanisms. The more rapid decay of IRDye 800CW suggests either additional clearance routes from the circulation (e.g., biliary) and/or a larger volume of extravascular distribution. Alongside the evidence provided by Tanaka et al[225]. This suggests IRDye 800CW is less suitable to assess renal function specifically.

A one-phase exponential decay fit of cortex photoacoustic intensity achieved a good R^2 with both dyes in most cases. However, one mouse receiving IRDye 800CW did not fit well with this model (Table 3.1). Certainly, more than one decay process is happening during this time. These include, but are not limited to, the mixing of the dye through the blood, the excretion of the dye from the mouse, and equilibrium of the intravascular and extravascular concentrations of dye. As such, a one-phase exponential decay fit is a significant

oversimplification. Further work to develop more accurate models of renal clearance of dyes in MSOT are presented in chapters 4 and 5.

The more intense peak photoacoustic signal seen with ABZWCY-HPβCD than IRDye 800CW in the cortex suggests ABZWCY-HPβCD has greater renal delivery and specificity. IRDye 800CW has a more intense photoacoustic signal per µM in MSOT phantom (Figure 3.3). If a similar concentration of both dyes were delivered to the kidney, we would expect to see a more intense photoacoustic signal with IRDye 800CW. As a more intense kidney signal is seen with ABZWCY-HPβCD, it suggests that greater amounts of this dye are being delivered to the kidney rather than to other tissues of the mouse. This provides further evidence that IRDye 800CW is undergoing clearance by additional routes and/or has a greater volume of distribution than ABZWCY-HPβCD.

3.3.3 STAR FLUOR 770 Acid Shows Significant Protein Binding and Biliary Excretion

Our collaborators, Prof. Norbert Gretz's group, at the University of Heidelberg, Germany have shown significant protein binding of STAR FLUOR 770 Acid (Figure 3.6) that is similar to what is seen with IRDye 800CW[157]. This suggest routes other than glomerular filtration are likely to contribute to its clearance.

Given the biliary excretion of IRDye 800CW[225], we investigated if there was evidence of biliary excretion of STAR FLUOR 770 Acid using both MSOT and fluorescence imager. MSOT can image the gallbladder and absorbers cleared through biliary excretion as evidenced by our positive control, ICG (Figure 3.7). However, the gallbladder provides minimal native contrast in MSOT. As such, being certain that the gallbladder is in-plane prior to delivery of intravenous contrast agent is challenging. Our approach of using the anatomical atlas built into the viewMSOT software (iThera, Germany) to locate the gallbladder appears to be successful with our positive controls. Definitive evidence of STAR FLUOR 770 Acid accumulating in the gallbladder in MSOT was less convincing. While a greater signal at the site of the gallbladder is seen compared with our negative control (ABZWCY-HPβCD), the signal at this site is similar to other regions across the liver. It is possible that the gallbladder was partially or fully out of plane. It is also possible that smaller quantities of STAR FLUOR 770 Acid are excreted by the biliary system than ICG.

Fluorescence imaging showed more convincing evidence of biliary excretion of STAR FLUOR 770 Acid than MSOT (Figure 3.8). The presence of signal in the gallbladder following STAR FLUOR 770 Acid injection that was absent in the negative control (ABZWCY-HPβCD) provides a strong argument that this STAR FLUOR 770 Acid is partially cleared by the liver.

Biliary clearance of STAR FLUOR 770 Acid makes the marker less specific for kidney function and may impair its suitability for this purpose. For example, any inadvertent injury to the liver during delivery of an injury model may result in outliers and misleading results. Even where direct injury has not occurred, liver hypoperfusion may result in liver injury and impaired function. Hypotension, upper abdominal surgery, and anaesthesia are all associated with reduce liver blood flow[235]. Additionally, any applied therapy to be investigated had the theoretical potential to alter liver excretion or function and potentially impair the assessment of renal health by this marker.

3.3.4 STAR FLUOR 770 Acid Spectral Properties Do Not Appear to Change Following Renal Clearance

The optical spectrum of STAR FLUOR 770 acid following in vivo intravenous administration and renal excretion was identical to dye that had not been injected (Figure 3.9). This suggests that STAR FLUOR 770 Acid reaching the urine is molecularly unchanged. No additional spectral peaks were identified to suggest NIR absorbing urine excreted metabolites were generated. Due to concurrent biliary excretion of STAR FLUOR 770 Acid, the collected urine cannot be used to assess what percentage of the injected dose is recoverable intact after animal administration. Further work to directly collect bile and urine following administration of STAR FLUOR 770 Acid could be performed to measure the portion of injected dye excreted unchanged.

3.4 Conclusions

ABZWCY-HPβCD has shown that it is detectable in MSOT, has no evidence of biliary excretion, and shows significantly different renal kinetics and renal specificity when compared to the current renal MSOT NIR dye standard, IRDye 800CW. ABZWCY-HPβCD has the potential to measure single kidney GFR in MSOT due to the dye's high urinary recovery, low protein binding, and absence of tubular secretion[102]. This is further examined in chapter 4.

STAR FLUOR 770 Acid is also detectable in MSOT, but it is not exclusively cleared by the kidney as it has shown evidence of biliary excretion. It also has a lower photoacoustic yield than IRDye 800CW. However, the renally excreted portion is spectrally unchanged and may undergo tubular secretion which is further explored in chapter 5.

4 Measurement of Glomerular Filtration Rate in Multispectral Optoacoustic Tomography

4.1 Introduction

Renal excretory function has been measured in dynamic contrast enhanced (DCE) multispectral optoacoustic tomography (MSOT) using IRDye 800CW[155,157,207,210,219–223]. These studies have used a number of different model-free measures and exponential fits to quantify this process (Figure 4.1):

- T^{MAX}: The time from injection of a contrast agent to the peak in the renal cortex[155]
- T^{MAX} Delay: The time between the peak in the renal cortex and the peak in the renal pelvis[157,207,221]
- AUC C:P: The ratio between area under the curve in the renal cortex and the renal pelvis[219,220]
- One-phase exponential decay and half-life of the renal cortex signal[157,220]
- Bi- and Tri-Exponential fits of the renal cortex[155]

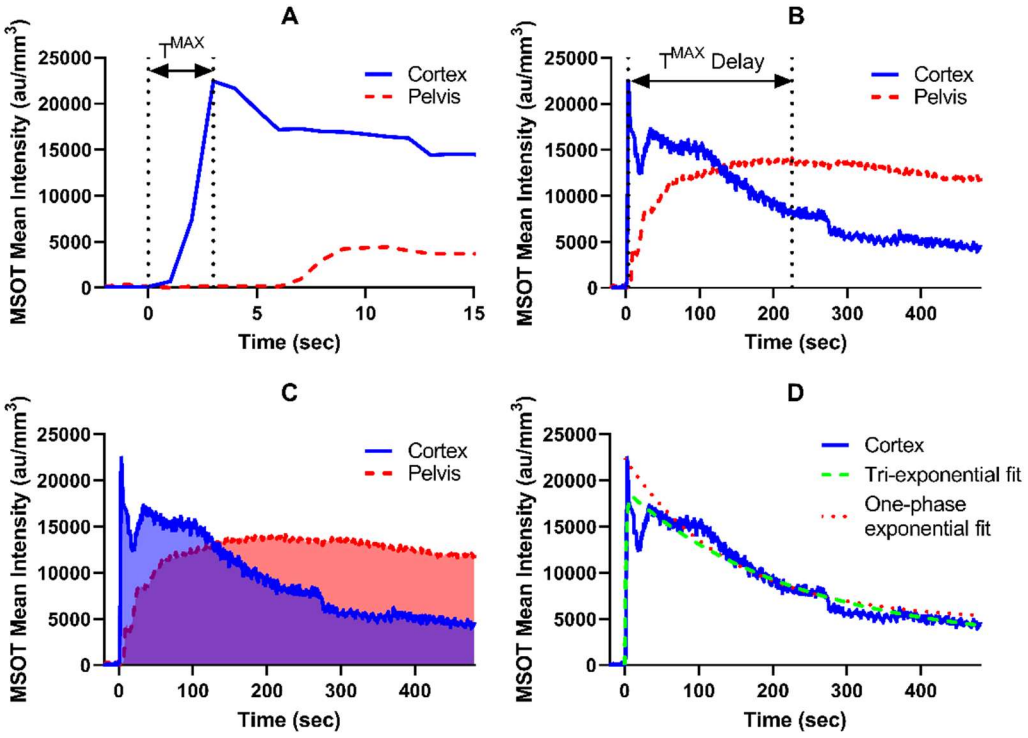

Figure 4.1: Examples of model-free measures and exponential fits applied to renal DCE MSOT.
A. T^{MAX}, the time between injection and the peak in the renal cortex. B. T^{MAX} delay, the time between the peak in the renal cortex and the peak in the renal pelvis. C. Ratio of the area under the curve between the pelvis and cortex. D. Exponential decay fits.

These studies have shown correlation between model-free measurements and kidney injury in models of ischaemia reperfusion injury (IRI)[155], diabetic kidney disease[221], septic acute kidney injury[207], and primary focal segmental glomerulosclerosis[157,219].

However, these model-free measurements do have limitations. Harwood et al note that the renal pelvis is not always easily visualised following ischaemia reperfusion injury (IRI) surgery due to the altered anatomy, sutures, and postoperative oedema[155]. This makes T^{MAX} Delay and AUC C:P measurements difficult. Sharkey et al noted that renal cortex did not fit a one-phase exponential decay and did not show a pelvis peak following Adriamycin induced injury impeding measurements of cortex half-life and T^{MAX} Delay respectively[219]. While T^{MAX} has been identified as one of the most easily measured and consistent parameters, it may represent perfusion and vascular health of the kidney rather than clearance functions specifically[155]. While multiple phase exponential fits can describe the data, deciding which coefficient specifically represents clearance and avoiding multiple solutions that fit equally well poses a challenge. Another limitation is signal noise. The peak in the renal cortex or renal pelvis may or may not be clearly defined. Additional peaks may be created by noise in the signal. While smoothing methods can be applied to attempt to address this issue, they may introduce their own bias and a choice of smoothing method or model may produce different results for model-free measurements requiring individual validation. Importantly, none of these model-free measurements are typically used in clinical practice to assess renal function. This potentially impacts the translation of results using these metrics to the clinical setting.

Glomerular Filtration Rate (GFR) is the current clinical gold standard measurement of renal function as it correlates with the amount of functioning renal tissue and the ability of the kidneys to maintain fluid and electrolyte homeostasis, produce hormones, and clear nitrogenous waste[30,31]. A decrease in global GFR may be because of the loss of a number of functioning nephrons e.g., a local infarction, or may be due to a reduction in the GFR of all individual nephrons e.g., whole kidney hypoperfusion following systemic haemorrhage.

DCE imaging modalities have been used to measure GFR. These include magnetic resonance imaging (MRI)[122,236–238], computed tomography (CT)[112,239,240], and scintigraphy[241–244]. This approach has the distinct benefit of measuring both left and right kidney GFR individually. This is described as single kidney glomerular filtration rate (SK-GFR). In healthy humans, left and right kidneys do not have equal excretory function: The difference between left and right GFR can be as large as 10%[162,163]. In preclinical experiments, awareness of any baseline

discrepancy between left and right kidney is important where a unilateral injury model is applied: injury to a dominant kidney may produce a significantly different result to an injury applied to the nondominant kidney. Tracking left and right kidney functions separately also benefits unilateral injury model work by providing an internal control kidney. This allows for a change in function and recovery to be better attributed to the intervention rather than other variables.

DCE imaging requires the application of a pharmacokinetic (PK) model to measure GFR[238]. The majority of PK GFR models require measurement of the blood concentration through time which is known as the arterial input function (AIF)[122,238,245]. The AIF can be measured either by repeated blood sampling or during DCE imaging. As mice have a small total blood volume, an imaged AIF is preferred. An imaged AIF can either be directly measured by a region of interest (ROI) draw at a blood vessel, or deduced using a reference tissue and knowledge of the contrast agents exchange perameters[245–247].

4.1.1 Baumann-Rudin Model

The Baumann-Rudin (BR) model is a simple kinetic model that does not require an AIF (Figure 4.2A, Equation 4.1)[122,248–250]. It describes the transport of the contrast agent from the cortex to the medulla or the pelvis. It was first described in DCE MRI[250] where it has shown a good correlation with GFR calculated by inulin clearance in rodents[251].

$$\frac{\mathrm{dm}}{\mathrm{dt}} = k_{cl} \times c$$

Equation 4.1: Baumann-Rudin Model
m (kidney medulla or pelvis concentration), t (time), k_{cl} (clearance constant), c (kidney cortex concentration)

4.1.2 Patlak-Rutland Model

The Patlak-Rutland (PR) model is a graphical, two compartment, AIF dependent, unidirectional kinetic model (Figure 4.2B, Equation 4.2)[240,252–254]. It is used in a number of tomography imaging modalities to measure GFR as volume of plasma cleared per time per volume of kidney[122,236,239]. With knowledge of each kidney's volume, a global GFR and SK-GFR can be calculated. As the PR equation (Equation 4.2) takes the form of the equation of a straight line (Equation 4.3), a plot of $\frac{c(t)}{b(t)}$ against $\frac{\int_0^t b(\tau)d\tau}{b(t)}$ fit with linear regression finds the GFR (the slope) and the fractional vascular volume (FVV, the intercept).

$$\frac{c(t)}{b(t)} = \frac{v_b}{v} + \frac{GFR}{v} \times \frac{\int_0^t b(\tau)d\tau}{b(t)}$$

Equation 4.2: Patlak-Rutland Model
t or τ (time), c (kidney cortex concentration), b (blood concentration), v (volume of kidney), v_b (blood compartment volume of the kidney)

$$y = intercept + slope \times x$$

Equation 4.3: Straight Line Equation

One of the requirements of the PR model is that the irreversible compartment (the tubular compartment when applied to the kidney) shows negligible outward flow of contrast. This means that the model can only be applied during the uptake phase where dye is still rapidly accumulating in the kidney and tubular outflow is minimal.

Jiang et al published on the use of the PR model in DCE MSOT using gold nanoparticles in health and a model or ureteric obstruction[183]. They were able to correlate a global GFR calculated by FITC-inulin clearance with the DCE MSOT GFR.

4.1.3 Modified Patlak-Rutland Model

Additionally, we have developed a modified version of the PR model (MPR, Figure 4.2C, Equation 4.4). Due to the rapid renal cortex outflow seen with ABZWCY-HPβCD, application of a standard PR model is limited by a short uptake phase. The MPR model compensates for this by using the renal pelvis where the uptake phase lasts for several minutes. As the renal pelvis is avascular, the term that represents the fractional vascular volume is absent.

$$\frac{p(t)}{b(t)} = \frac{GFR}{v} \times \frac{\int b(t)dt}{b(t)}$$

Equation 4.4: Modified Patlak-Rutland Model
t (time), p (kidney pelvis concentration), b (blood concentration), GFR (glomerular filtration rate), v (volume of the kidney)

4.1.4 Objectives

This chapter aims to use ABZWCY-HPβCD, the previously validated GFR marker, in MSOT to measure SK-GFR of mice in health and IRI using the BR, PR, and MPR models. We have assessed two sites for an imaged AIF in DCE MSOT: the aorta and a spinal blood vessel. The examined PK models are:

1. Baumann-Rudin (BR)
2. Patlak-Rutland with aorta AIF (PRa)

3. Patlak-Rutland with spinal blood vessel AIF (PRs)
4. Modified Patlak-Rutland with spinal blood vessel AIF (MPRs)

Correlation is made with a global GFR calculated using a transcutaneous device (TD) that measures the clearance of FITC-sinistrin[96,97,156]. The previously described model-free measurements of T^{MAX}, T^{MAX} Delay, and AUC C:P will be examined for their ability to describe ABZWCY-HPβCD kinetics and to look for correlation with the global GFR calculated by FITC-sinistrin.

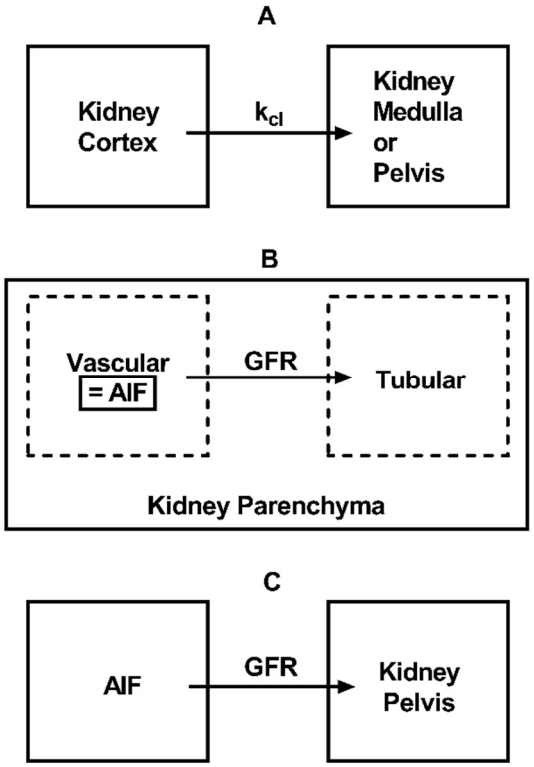

Figure 4.2: Schematics of Pharmacokinetic Models of GFR.
A. Bauman-Rudin. B. Patlak-Rutland. C. Modified Patlak-Rutland. Solid lines represent a measured region of interest. Dotted lines represent compartments deduced by the model. Arterial Input Function (AIF) is a measured blood vessel e.g., aorta. Glomerular Filtration Rate (GFR), Clearance Constant (k_{cl}).

4.2 Animal Experiment Design

In the first animal experiment, seven male C57BL/6 albino mice aged 8-11 weeks were examined. FITC-sinistrin clearance was quantified by TD to measure a global GFR. Following this, mice were imaged with MSOT to measure kidney volume and ABZWCY-HPβCD clearance.

In a second experiment, ten male B6 albino mice aged 8-11 weeks underwent examination. 27.5-minute surgical IRI was performed: five mice received bilateral IRI while five received

unilateral IRI. Mice had their TD GFR and MSOT ABZWCY-HPβCD clearance measured on three occasions: baseline, post-op day 1, and post-op day 3.

4.3 Results

4.3.1 FITC-sinistrin Photoacoustic Signal

To assess whether FITC-sinistrin produces photoacoustic signal, an MSOT phantom containing an insert of FITC-sinistrin was imaged in MSOT. This was important to ensure that FITC-sinistrin would not interfere in the measurement of the clearance of ABZWCY-HPβCD in MSOT.

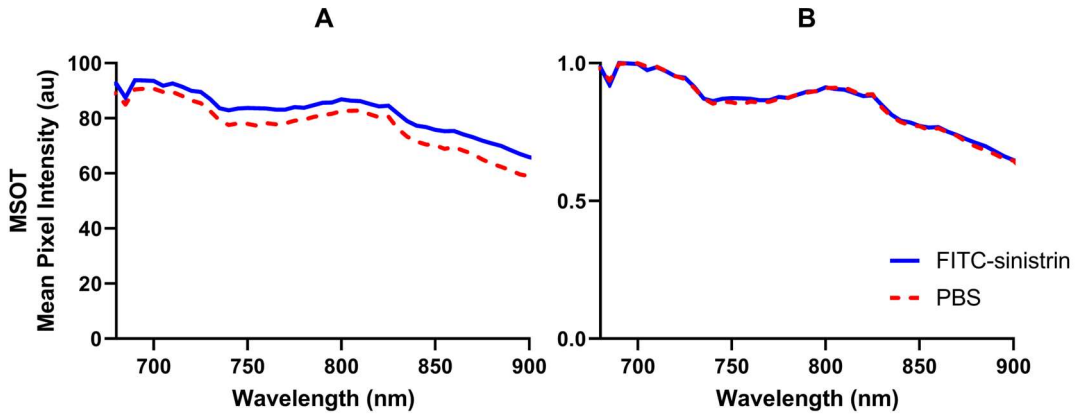

Figure 4.3: Photoacoustic Spectrum of FITC-sinistrin.
A. Comparing photoacoustic spectrum of 2.41 mg/mL FITC-sinistrin (the approximate peak blood concentration after administration to mice) and PBS in agar phantom in MSOT. B. Normalised photoacoustic spectrum of the same. PBS (Phosphate Buffered Saline), FITC (Fluorescein Isothiocyanate).

FITC-sinistrin produces no significant signal in MSOT phantom with NIR excitation wavelengths (Figure 4.3). The normalised photoacoustic spectrum of FITC-sinistrin in PBS was identical to the control (PBS) insert (Figure 4.3B). The slight difference in absolute quantification of photoacoustic signal between FITC-sinistrin and PBS (Figure 4.3A) can be attributed to slight differences in the position of inserts within the phantom and the phantom within the water bath.

4.3.2 Distribution of ABZWCY-HPβCD in DCE MSOT

A typical example of DCE MSOT measured ABZWCY-HPβCD distribution after intravenous administration in mice is shown in Figure 4.4. The dye rapidly peaks in the aorta and vena cava (Figure 4.4B). During this time, the renal vasculature and spinal blood vessels are also highlighted. After this the renal cortex shows accumulation (Figure 4.4C). Finally, the dye moves to the renal pelvis (Figure 4.4D). This is associated with some dye in the skin and soft tissues.

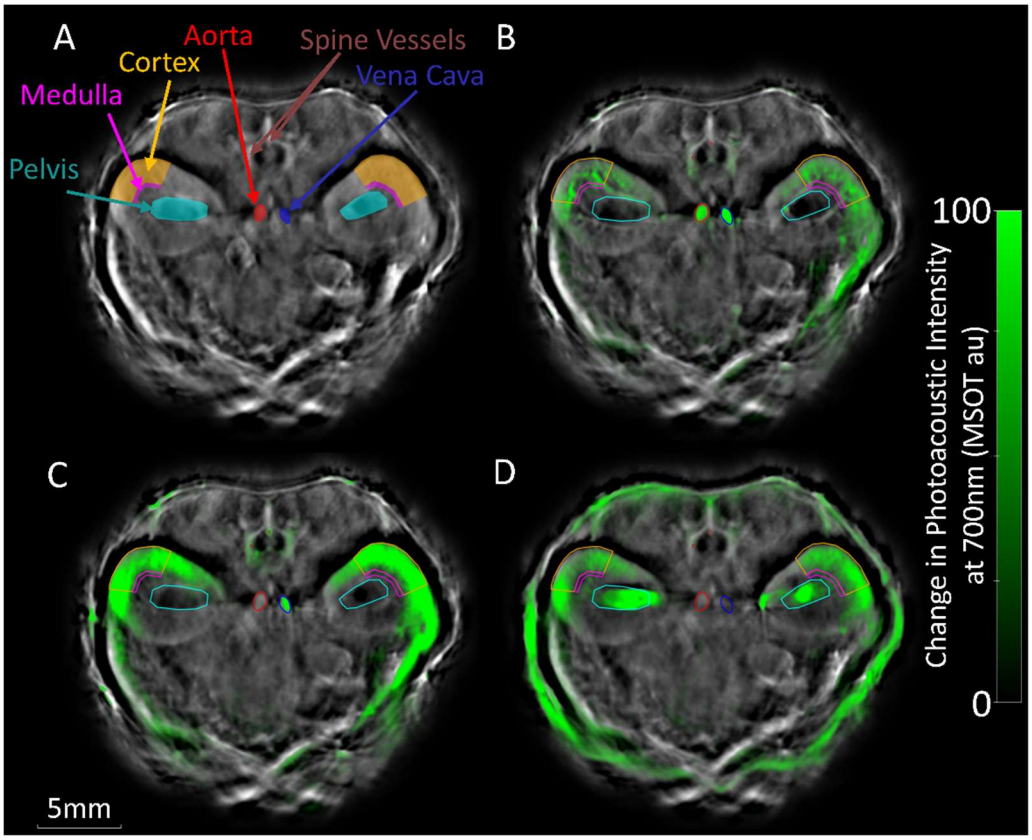

Figure 4.4: Typical ABZWCY-HPβCD Distribution after IV administration measured by DCE MSOT.
A. Regions of interest measured for models. B. Vascular peak. C. Renal cortex Peak. D. Renal pelvis peak.

4.3.3 Baumann-Rudin Model in ABZWCY-HPβCD DCE MSOT

The BR model was applied to all 17 mice using a numerical ordinary differential equation solver in MATLAB. The MSOT clearance of ABZWCY-HPβCD was measured in regions of interest that represent the kidney medulla or the kidney pelvis as the receiving compartment, as well as the kidney cortex (Figure 4.4A). These were compared with a global GFR calculated by TD measured FITC-sinistrin clearance.

The BR medulla method showed a loose linear correlation between k_{cl} and TD GFR with several outliers (Figure 4.5A). Pearson r showed wide confidence intervals (0.2898 to 0.7490) but did show statistical significance (P = 0.0003).

The BR pelvis method also showed a linear correlation but with narrower confidence intervals (0.3963 to 0.7974) and fewer outliers particularly amongst animals following IRI surgery (Figure 4.5B). The pelvis method also shows a more favourable Pearson r (0.6384, P = <0.0001) than the medulla method (0.5611, P = 0.0003).

Simple linear regression did not provide an R^2 suggestive of a good fit in either case: medulla method R^2 = 0.3148, pelvis method R^2 = 0.4075).

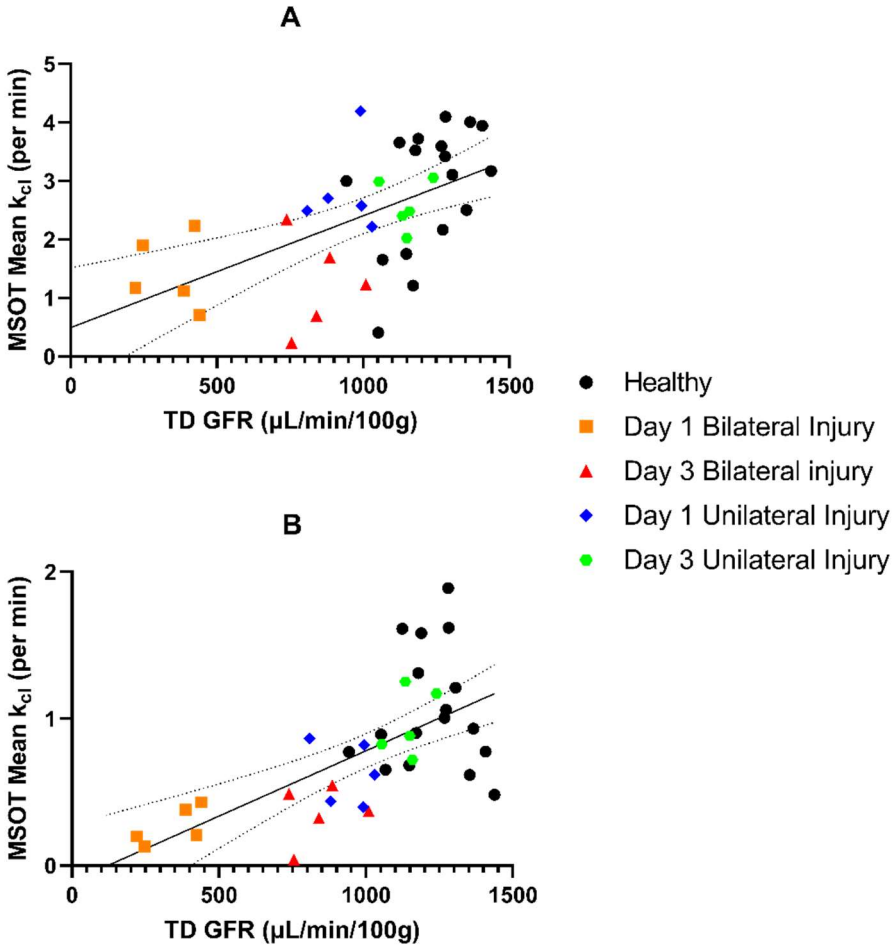

Figure 4.5: Correlation of MSOT ABZWCY-HPβCD Baumann Rudin k_{cl} and Transcutaneous Device GFR.
A. Medulla receiving compartment, Pearson r = 0.5611 (CI 0.2898 to 0.7490), P = 0.0003. B. Pelvis receiving compartment, Pearson r = 0.6384 (CI 0.3963 to 0.7974), P = <0.0001. k_{cl} (clearance constant), TD (transcutaneous device), GFR (glomerular filtration rate), CI (confidence intervals). Solid line is a simple linear regression fit; dotted lines are the 95% confidence bands. Global MSOT k_{cl} calculated as a mean of left and right kidney k_{cl}.

4.3.4 Arterial Input Function in Dynamic Contrast Enhanced Multispectral Optoacoustic Tomography

4.3.4.1 The Aorta

To investigate whether the aorta would be a suitable site for an imaged AIF, a region of interest was drawn around the aorta and the photoacoustic signal intensity over time was measured. The pre-injection signal was subtracted to calculate the change in signal.

In all cases, a signal below pre-injection levels was seen immediately after an initial peak in the aorta (Figure 4.6). Over the course of the imaging session, the signal slowly drifts back to baseline. This “negative” signal significantly impacts our ability to use the aorta as an AIF as a negative concentration of dye is a physical impossibility. I believe this is due to the depth

of the aorta and the reduced light delivery there on accumulation of dye in the periphery (see section 4.4.2).

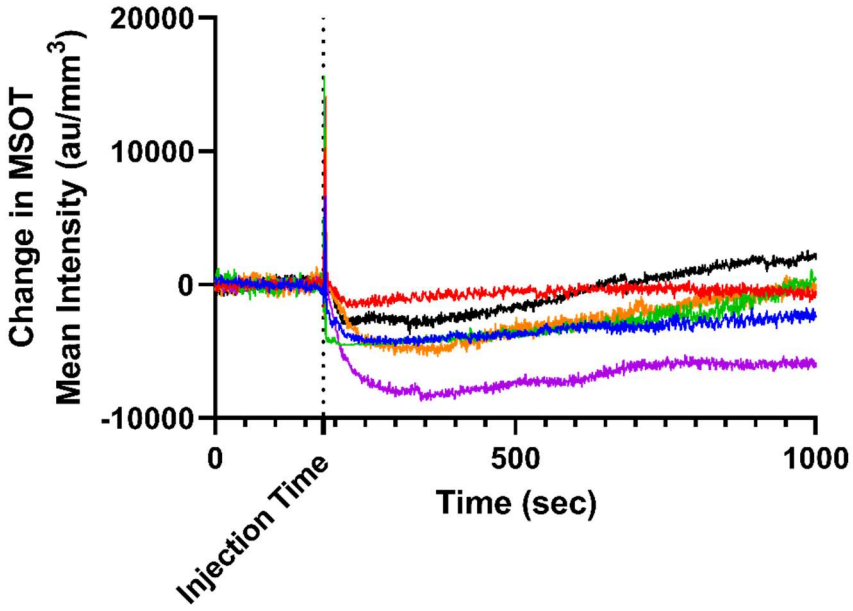

Figure 4.6: Examples of the Change in Mouse Aorta Photoacoustic Signal Following Injection of ABZWCY-HPβCD.
Each coloured line represents a different mouse. Time of injection of contrast marked by dotted line.

4.3.4.2 Spinal Blood Vessel

To assess whether a more superficial blood vessel would make a suitable AIF in DCE MSOT, we attempted to measure a point in the spine consistent with a blood vessel. A ~0.2 mm diameter circular region of interest was drawn in the spine where a hyperintense signal was seen in the frames immediately following contrast injection. The change in photoacoustic signal intensity over time was measured in the same way as the aorta.

In an attempt to confirm this site was consistent with a blood vessel, photoacoustic signal was measured at multiple wavelengths (700, 730, 760, 800, 850 nm) prior to contrast injection. Then multispectral unmixing algorithms were applied to quantify haemoglobin, oxyhaemoglobin, and haemoglobin saturation. The concentrations of these absorbers within the spine blood vessel region of interest were compared with the aorta and vena cava.

A typical example of the photoacoustic time activity curves for the aorta and spinal blood vessel is shown in Figure 4.7 and typical images, in Figure 4.8. The change in photoacoustic signal over time in the apparent spinal blood vessel did not show any dip below pre-injection

signal in any cases. These curves showed a peak immediately after the aorta followed by an apparent multi-phase exponential decay.

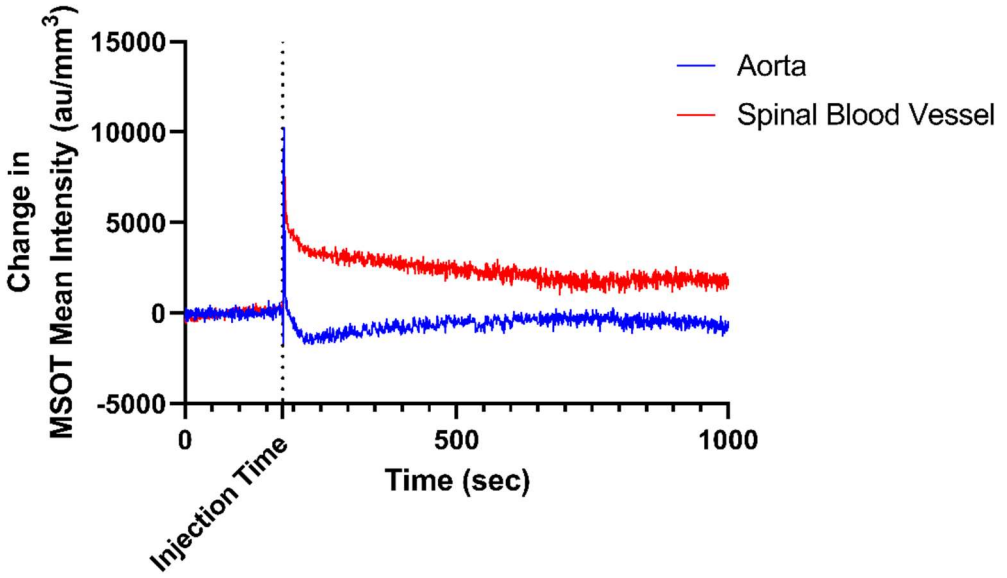

Figure 4.7: Example comparing Aorta and Spinal Blood Vessel Photoacoustic Signal Following Injection of ABZWCY-HPβCD.
Time of injection of contrast marked by dotted line.

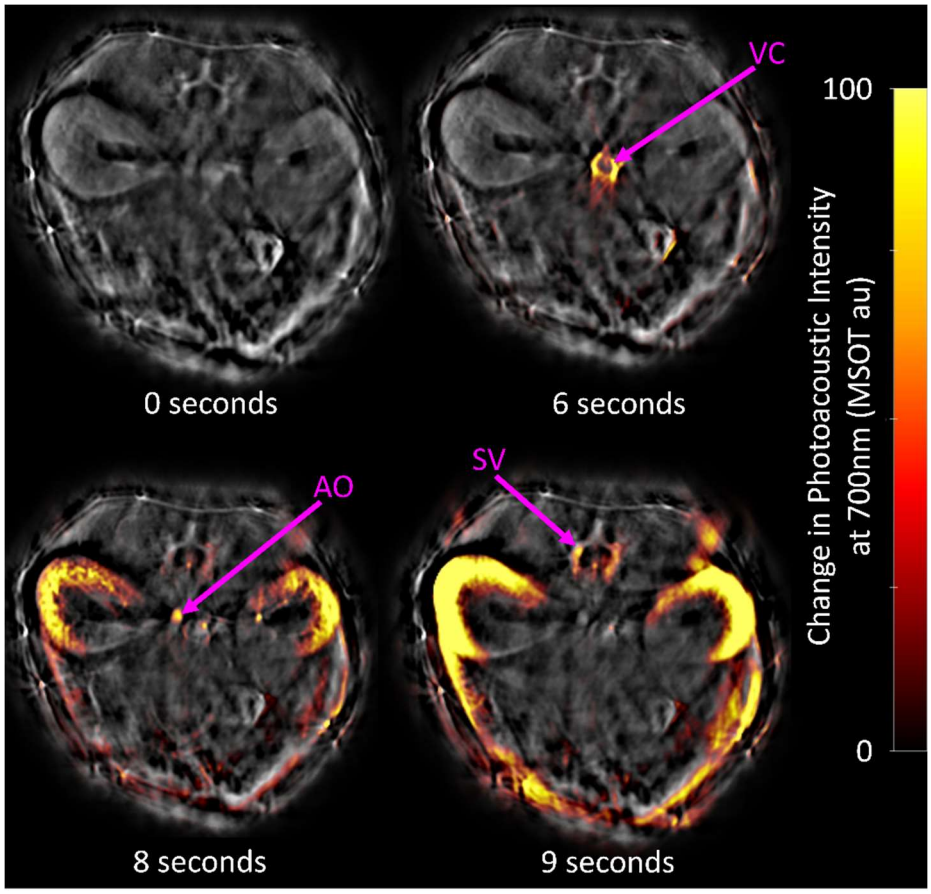

Figure 4.8: Location of Blood Vessels on DCE MSOT after Intravenous ABZWCY-HPβCD.
Vena Cava (VC), Aorta (AO) and Spinal Blood Vessel (SV) shown at peak signal.

Multispectral unmixing of the three blood vessels (spinal, aorta, and vena cava) revealed that the quantification of oxygenated haemoglobin (HbO_2) and oxygen saturation of haemoglobin (mSO2) for the spinal blood vessel was between that measured in the aorta and the vena cava (Figure 4.9). However, the mean quantification of deoxyhaemoglobin was higher in the spinal vessel than both the aorta and vena cava. The aorta and spinal vessel showed no significant difference in their quantification of HbO_2 ($P = 0.1519$) and a significant difference in Hb ($P = 0.0055$). However, mSO_2 was significantly different between the aorta and spinal vessel ($P = 0.0047$).

4.3.5 Uptake Phase of ABZWCY-HPβCD in the Renal Cortex and Pelvis

The PR model doesn't account for the flow of dye from the tubules to the renal pelvis and bladder (Figure 4.2B). As such, a requirement of the model is to fit only the uptake phase of the contrast in the kidney. ABZWCY-HPβCD has previously shown a significantly short uptake phase in the renal cortex (Figure 3.5A).

Figure 4.10A shows that the initial uptake in the renal cortex (α1) occurs after 3 seconds. While there is a smaller increase that some may consider to be part of the uptake phase (Figure 4.10A α2), this is dramatically earlier than what Jiang et al[183] saw with their renally cleared gold nanoparticle, $Au_{25}(SG)_{18}$. The renal pelvis shows a longer uptake phase with ABZWCY-HPβCD (Figure 4.10B).

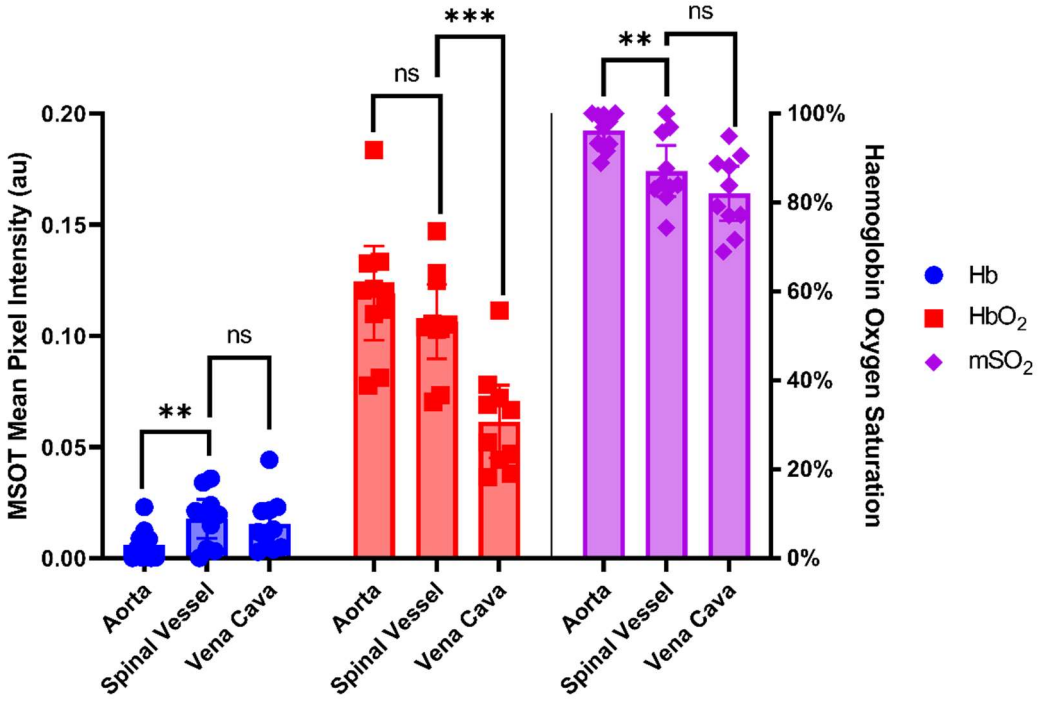

Figure 4.9: MSOT Unmixing for Deoxyhaemoglobin, Oxyhaemoglobin, and Haemoglobin Oxygen Saturation in the Spinal Blood Vessel, Aorta, and Vena Cava of Mice.
Hb (Deoxyhaemoglobin), HbO_2 (Oxyhaemoglobin), mSO_2 (Haemoglobin Oxygen Saturation). ns P >0.05, * P ≤0.05, ** P ≤0.01, *** P ≤0.001, **** P ≤0.0001. Bars are the standard deviation.

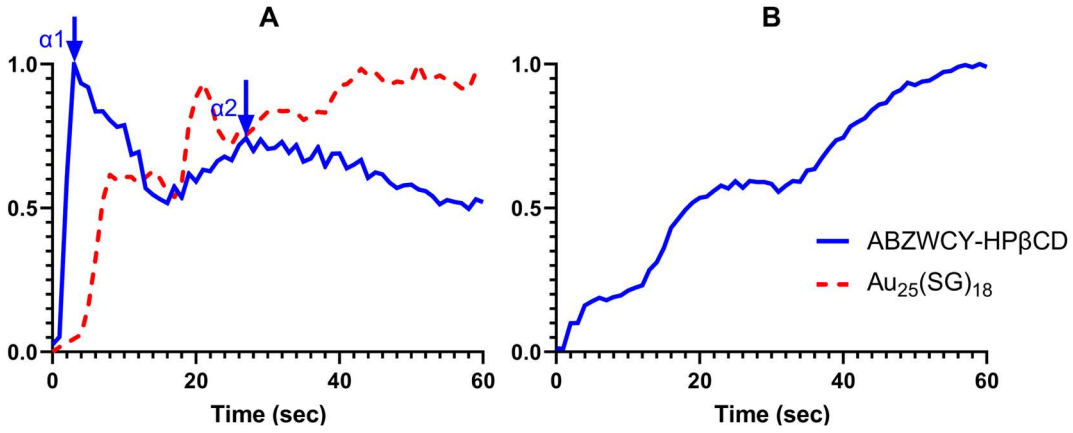

Figure 4.10: Comparing the Kidney Uptake Phase of ABZWCY-HPβCD and $Au_{25}(SG)_{18}$ in MSOT.
A. Normalised change in concentration measured in the kidney cortex. B. Normalised change in concentration measured in the kidney pelvis. α1: End of greater uptake phase for ABZWCY-HPβCD. α2: End of lesser uptake phase for ABZWCY-HPβCD. $Au_{25}(SG)_{18}$ plot adapted from Jiang, X et al. Photoacoustic Imaging of Nanoparticle Transport in the Kidneys at High Temporal Resolution. Angew Chem Int Ed Engl 58, 5994–6000 (2019).

4.3.6 Patlak-Rutland and Modified Patlak-Rutland Models in ABZWCY-HPβCD DCE MSOT

To assess which PR model variant was provided the best approximation of GFR, the PRa, PRs and MPRs models were applied to 7 healthy mice to calculate an ABZWCY-HPβCD DCE MSOT derived Global GFR. This global GFR was calculated by the sum of the two SK-GFRs which were derived from the product of the GFR per minute per volume of the kidney, the volume of the kidney, and 0.5 (1 minus the haematocrit). This was compared with a global GFR calculated by TD measured FITC-sinistrin clearance. Typical examples of time activity curves for each model and their associated PR or MPR plot can be seen in Figure 4.11. In the PRa model, the b(t) value for the PR plot was changed to zero where the aorta signal was negative.

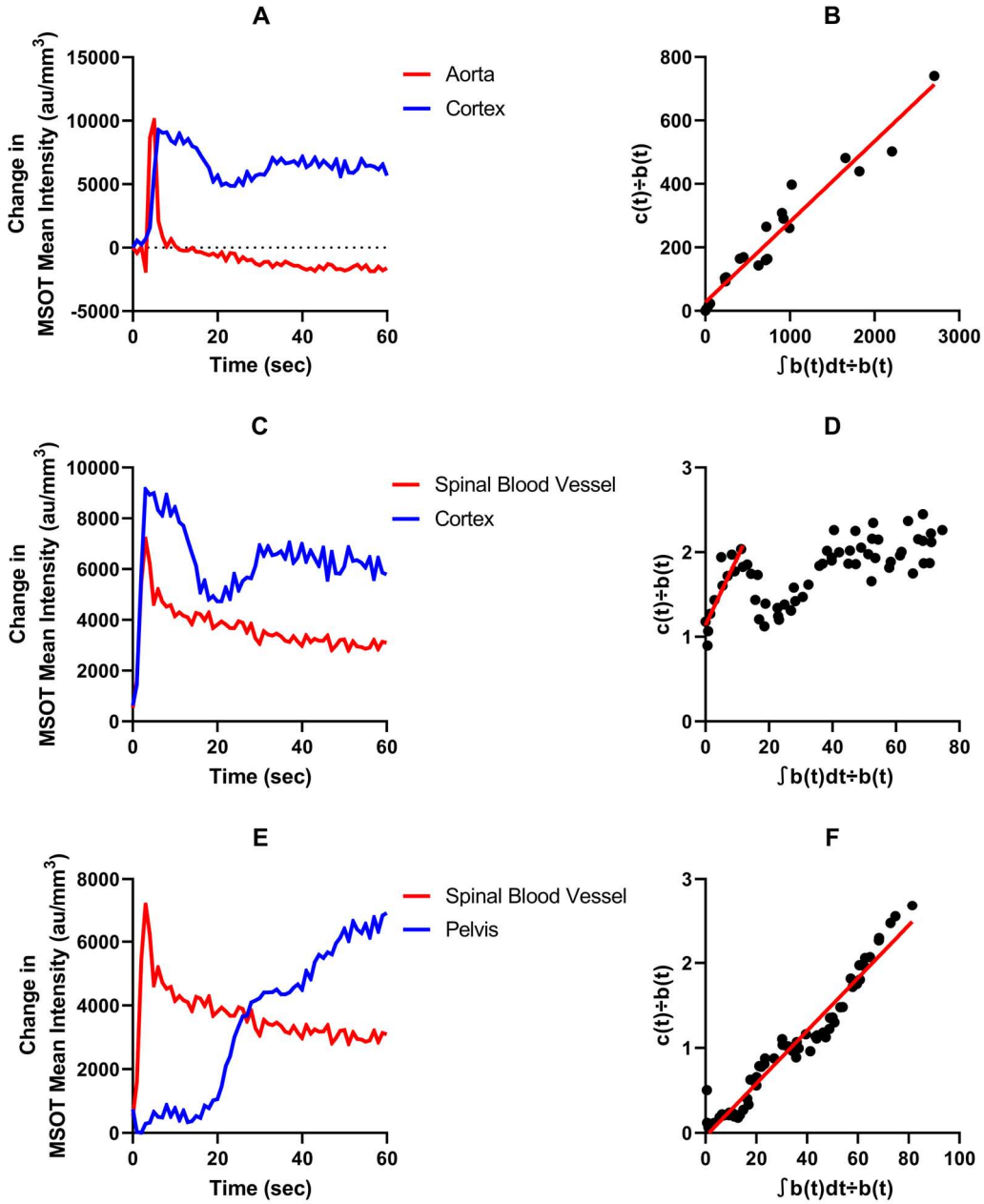

Figure 4.11: Typical Examples of Time Activity Curves in ABZWCY-HPβCD DCE MSOT and Associated PR and MPR Plots.
A. Time activity curve for ROIs applied to PR model with aorta AIF. B. PR plot for A. C. Time activity curve for ROIs applied to PR model with spinal blood vessel AIF. D.PR plot for C. E. Time activity curve for ROIs applied to MPR model with spinal blood vessel AIF. F. MPR plot for E. PR (Patlak-Rutland), MPR (Modified Patlak-Rutland), DCE (Dynamic Contrast Enhanced), MSOT (Multispectral Optoacoustic Tomography), ROI (region of interest).

Figure 4.12 shows how DCE MSOT derived GFRs using each PR model and ABZWCY-HPβCD compare with TD derived GFRs using FITC-sinistrin. PRa dramatically overestimates GFR, PRs overestimates GFR in most cases, and MPRs modestly overestimates GFR (Figure 4.12A). Both the use of the spinal blood vessel as the AIF and the longer uptake phase seen in the pelvis appears to benefit the MPRs model.

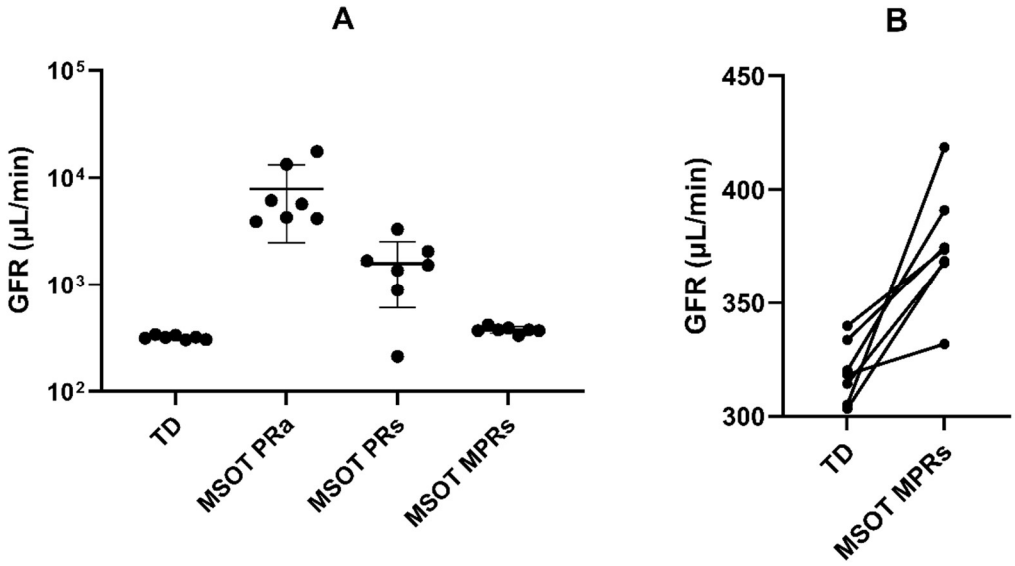

Figure 4.12: Different PR models of DCE MSOT GFR versus TD GFR in Healthy Mice
A. Three models of ABZWCY-HPβCD DCE MSOT derived GFR compared to FITC-sinistrin TD GFR. B. TD GFR versus DCE MSOT GFR MPRs model. TD (Transcutaneous Device), PR (Patlak-Rutland), PRa (Patlak-Rutland model with aorta arterial input function), PRs (Patlak-Rutland model with spinal blood vessel arterial input function), MPRs (Modified Patlak-Rutland model with spinal blood vessel arterial input function), DCE (Dynamic Contrast Enhanced), MSOT (Multispectral Optoacoustic Tomography). Bars are the standard deviation.

4.3.7 Modified Patlak-Rutland Model in Health and Ischaemia Reperfusion Injury

The MPRs model was applied to all 17 mice and investigated for correlation with TD GFR in health and following IRI.

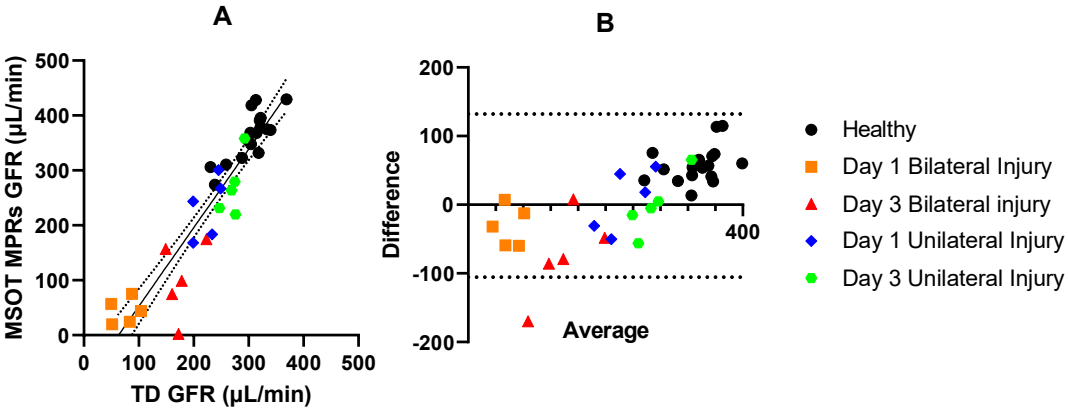

Figure 4.13: Correlation between MSOT MPRs GFR and TD GFR.
A. TD versus PRMs, Pearson r = 0.9296 (CI 0.8665-0.9634, R^2 0.8641). B. Bland-Altman plot of A.
TD (Transcutaneous Device), MPRs (Modified Patlak-Rutland with spinal blood vessel AIF). Solid line is a simple linear regression fit. Dotted lines are the 95% confidence bands. Dashed lines are 95% Limits of Agreement.

Global GFR calculated by MPRs ABZWCY-HPβCD DCE MSOT showed good correlation with FITC-sinistrin TD GFR across a range of GFRs with a Pearson r of 0.9296 (P = <0.0001, Figure 4.13A). 95% confidence intervals were significantly narrower (0.8655 – 0.9634) than those

seen with the BR model pelvis method. Only one distinctive outlier could be identified in the day 3 bilateral injury group.

Bland-Altman plot showed that the MPRs method overestimates GFR in healthy mice while underestimating GFR following IRI (Figure 4.13B). However, the 95% limits of agreement are wide (105.6 – 132.2) meaning an error of around 100 uL/minute in the GFR can be expected.

4.3.8 Modified Patlak-Rutland in Unilateral Ischaemia Reperfusion Injury

To find whether the MPRs model was able to detect differences in renal function between two kidneys in a model of unilateral IRI, SK-GFR was calculated using the MPRs model for mice receiving both the bilateral and unilateral IRI. These were compared and tested for statistical difference between left and right SK-GFR.

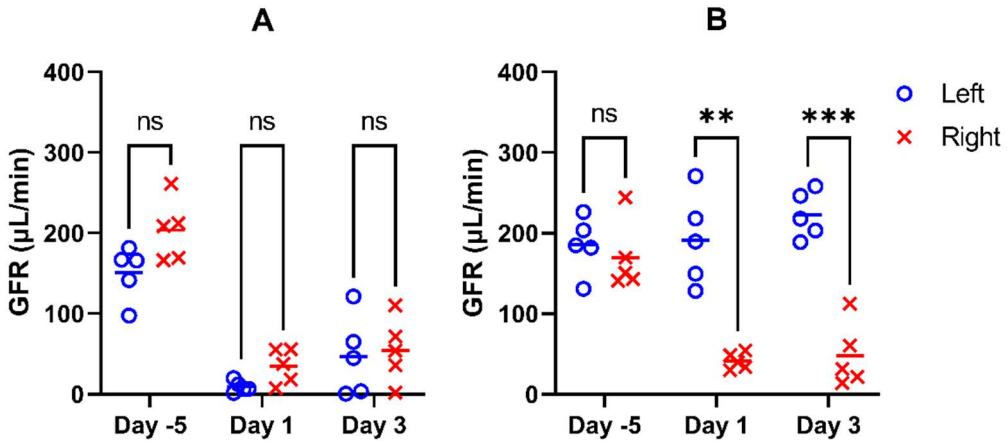

Figure 4.14: MSOT Modified Patlak Single Kidney GFR in Ischaemia Reperfusion Injury.
A. Bilateral injury. B. Unilateral injury (Day 1 P = 0.004636, Day 3 P = 0.000867). Horizontal line is the mean.

At baseline, the right kidney SK-GFR was moderately higher than the left SK-GFR in the bilateral injury group (Figure 4.14A). However, this was not significant. On day 1 post injury the GFR of both kidneys dropped similarly with the right kidney function remaining slightly higher than left in the bilateral injury group. Day 3 saw some recovery. There was no statistical difference between left and right SK-GFR at any point in the bilateral injury group.

In the unilateral injury group, the left kidney SK-GFR was mildly higher than the right kidney though this was not significant (Figure 4.14B). On day 1 and 3 post injury the right kidney was significantly impaired while the left kidney function remained similar. There was a statistical difference between left and right after injury on both injury days (Day 1 P = 0.004636, Day 3 P = 0.000867).

This shows that the MPRs model is able to detect impaired filtration following a 27.5 minute surgical unilateral IRI and able to discriminate the injured and uninjured kidneys.

4.3.9 Model-free Measurements of ABZWCY-HPβCD DCE MSOT

4.3.9.1 Model-free Measures in Bilateral Injury

MSOT T^{MAX}, T^{MAX} Delay, and AUC C:P ratio were measured for the five animals receiving bilateral IRI using the raw data acquired without smoothing. As global GFR declines significantly following bilateral IRI surgery, we examine whether these model-free measurements can track this impairment.

The group of mice receiving bilateral IRI showed a significant decline in TD GFR on both day 1 and day 3 following injury (Figure 4.15A). Renal function was most impaired on day 1 with some recovery on day 3.

Mean T^{MAX} appeared unchanged on day 1 following injury. On day 3, most of the animals showed an increase in the T^{MAX}. However, two animals appeared to have no change in their T^{MAX}. Neither post injury day showed significant differences in T^{MAX} from pre-injury.

Mean T^{MAX} Delay increased both on day 1 and 3 post injury (Figure 4.15C). While this wasn't significant by paired t test on day 1, it was significant on day 3 post injury ($P = 0.0396$). The two animals that had the worst T^{MAX} delay on day 1 showed recovery on day 3, while the three mice with a better T^{MAX} delay on day 1 continued to worsen on day 3.

AUC C:P ratio dropped on both day 1 and 3 post injury and showed statistical significance $P = 0.0132$ and 0.0313, respectively (Figure 4.15D). Baseline AUC C:P showed a large range which narrowed significantly in injury. P values were not comparable to those seen with TD GFR. However, AUC C:P ratio did mirror the partial recovery seen on day 3 with TD GFR.

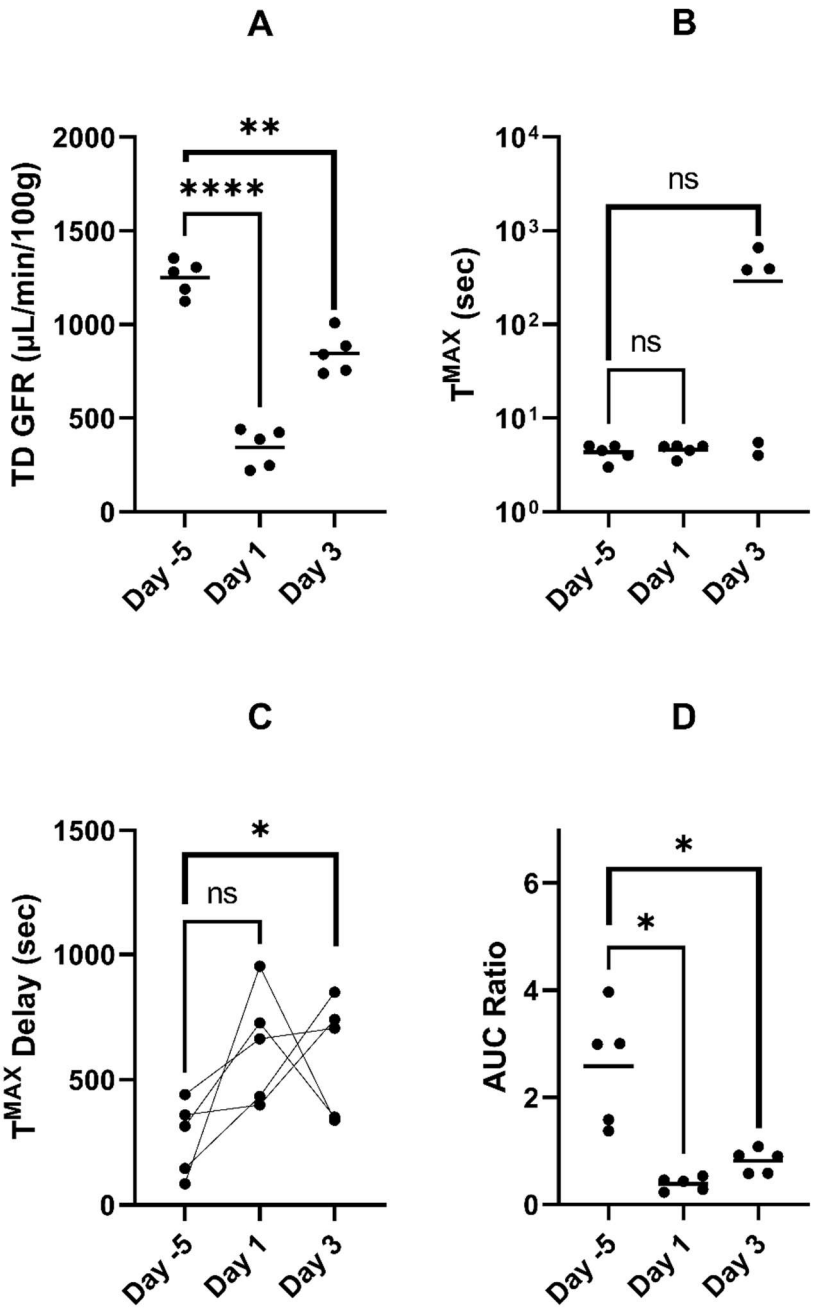

Figure 4.15: Transcutaneous Device GFR and MSOT ABZWCY-HPβCD Renal Model-free Measures Following Bilateral Ischaemia Reperfusion Injury.
A. Transcutaneous Device GFR. B. MSOT TMAX. C. MSOT TMAX Delay. D. MSOT Area Under the Curve (AUC) Cortex to Pelvis Ratio. ns P >0.05, * P ≤0.05, ** P ≤0.01, *** P ≤0.001, **** P ≤0.0001. Horizontal line is the mean.

4.3.9.2 Model-free Measures in Unilateral Injury

MSOT TMAX, TMAX Delay, and AUC C:P ratio were measured for the five animals receiving unilateral IRI using the raw data acquired without smoothing. As a major benefit of measuring renal clearance by imaging is individually measuring each kidneys contribution, we examine whether these model-free measurements can discern a kidney receiving a 27.5-minute IRI surgery from the internal control.

TD GFR dropped significantly on day 1 post unilateral IRI, P = 0.0066 (Figure 4.16A). The GFR lost was less than that seen with a bilateral injury. Like in bilateral injury, a recovery was seen on day 3.

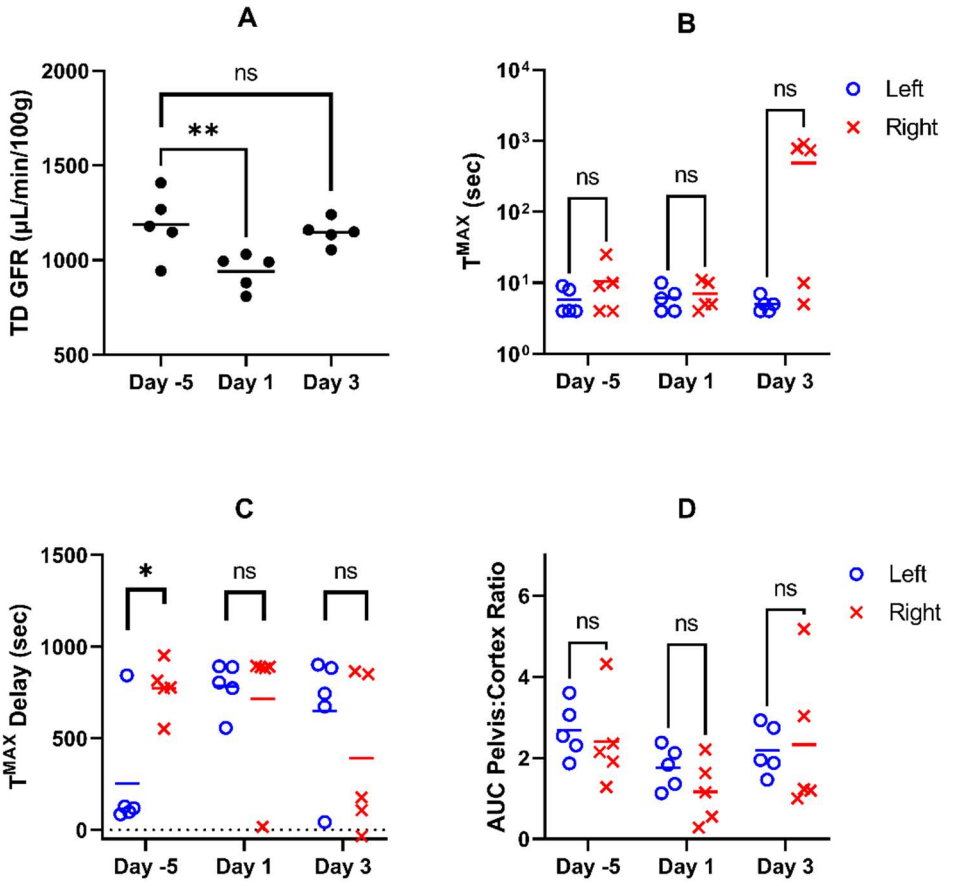

Figure 4.16: MSOT ABZWCY-HPβCD Renal Model-free Measurements Following Right-sided Unilateral Ischaemia Reperfusion Injury and Transcutaneous Device GFR.
A. Transcutaneous Device (TD) GFR. B. MSOT TMAX. C. MSOT TMAX Delay. D. MSOT Area Under the Curve (AUC) Pelvis to Cortex Ratio. ns P >0.05, * P ≤0.05, ** P ≤0.01, *** P ≤0.001, **** P ≤0.0001. Horizontal line is the mean.

T^{MAX} was similar between the left and right kidney at baseline and day 1 post injury (Figure 4.16B). There was no significant difference identified between left and right kidney. However, day 3 showed a large increase in T^{MAX} for three of the five mice.

T^{MAX} Delay showed a significant difference between the left and right kidney at baseline (Figure 4.16C). This was not present following unilateral injury. Indeed, the T^{MAX} Delay in the right kidney only improved following injury.

AUC C:P ratio of the right kidney dropped day 1 post injury (Figure 4.16D). The AUC C:P ratio also dropped in the control kidney. Both showed recovery day 3 post injury. Statistical difference between left and right kidney was not identified by the AUC C:P ratio.

In summary, model-free measurements do not show statistical difference in unilateral injury despite TD GFR showing a significant drop on day 1 post injury. However, trends in bilateral injury appear best captured by the AUC C:P ratio out of these model-free measurements.

4.3.9.3 Model-free Measurement Correlation with TD GFR

We examined whether model-free measurements of ABZWCY-HPβCD DCE MSOT could be used to track changes in filtration rate. Mean model-free measures were examined for correlation with TD GFR in animals who underwent bilateral or unilateral IRI.

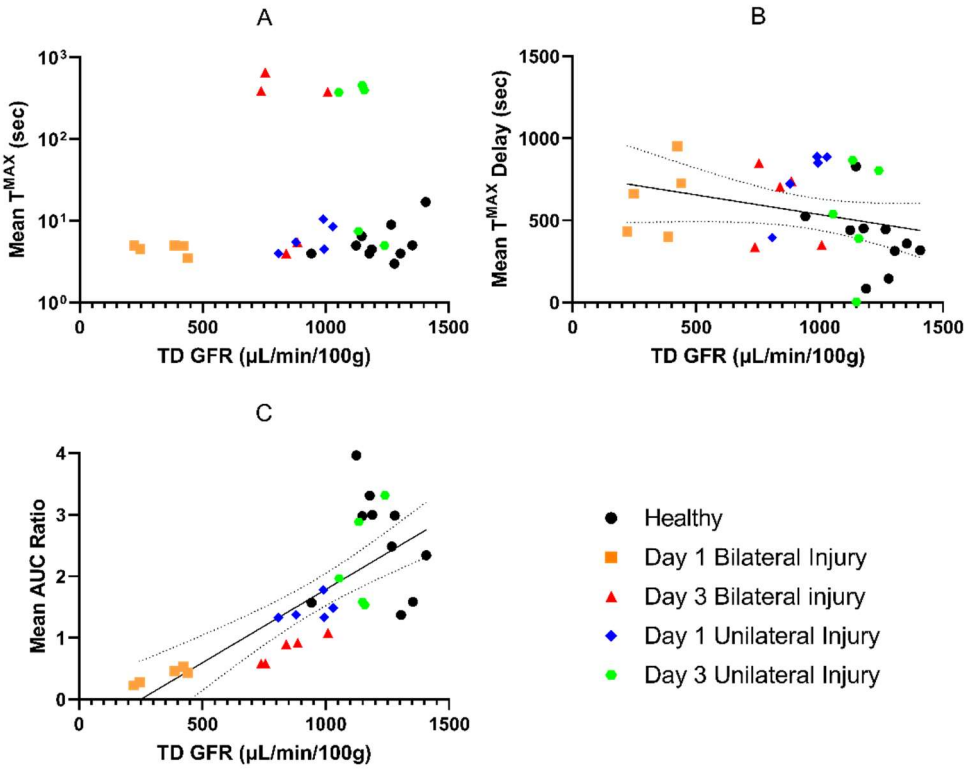

Figure 4.17: Model-free Measurements versus TD GFR in IRI
A. T^{MAX} (Pearson r = 0.01366, CI -0.3483 to 0.3721, R^2 = 0.0001867). B. T^{MAX} Delay (Pearson r = -0.2998, CI -0.5957 to 0.06784, R^2 = 0.08986). C. AUC C:P Ratio (Pearson r = 0.7523, CI 0.5378 to 0.8753, R^2 = 0.5660). Solid line is a simple linear regression fit; dotted lines are the 95% confidence bands.

Mean T^{MAX} showed poor correlation with TD GFR with a Pearson r that is close to zero and several distinct outliers (Figure 4.17A).

Mean T^{MAX} Delay showed some negative correlation with TD GFR (Figure 4.17B). This is consistent with our expectation that the time between the peak in the pelvis and cortex to increase as filtration decreases. While Pearson r =-0.2998, the confidence intervals were wide and extended above zero (-0.5957 to 0.06784). Numerous data points exist outside of the confidence bands. This suggests a large spread of data that makes the metric less helpful for tracking changes in filtration.

Mean AUC C:P ratio showed a positive correlation with a Pearson r = 0.7523 (Figure 4.17C). Confidence intervals were narrower than for the other two metrics (CI 0.5378 to 0.8753). Additionally, the correlation showed statistical significance (P = <0.0001).

4.4 Discussion

Here we report on three PK models of filtration and three model-free measurements of DCE MSOT using the GFR marker ABZWCY-HPβCD. These metrics are assessed for their potential to estimate a global GFR and discern unilateral injury from internal control kidney.

4.4.1 Baumann-Rudin Model Tracks Filtration Best When Using the Pelvis

The first publication reporting on the BR model in DCE MRI examined both the outer medulla and inner medulla/pelvis ROIs[250]. We have measured the BR model in MSOT using both the medulla and the pelvis as the receiving compartment. The pelvis method correlated better with GFR measured by TD.

Both the pelvis and medulla ROIs were manually selected. The renal pelvis provides good native contrast against the renal parenchyma in MSOT[180,210]. This means that the borders for ROI creation are easily identified. Creation of the medulla ROI was less certain as the border between the cortex and the medulla using the native MSOT contrast is much lower. Instead, the border of the medulla was defined following the administration of ABZWCY-HPβCD. A frame was identified where the initial flash of contrast in the kidney edge was brightest which defined the cortex ROI borders. A small region interior to this, but external to the pelvis, defined the medulla ROI borders. This may explain why the BR medulla method was less consistent. The medulla ROI may have been contaminated with varying amounts of cortex. A higher cortex contamination of the medulla ROI will lead to a false high k_{cl}. As the borders of the pelvis are more defined, ROI contamination is far less likely in the BR pelvis method.

While MRI can differentiate the cortex from the medulla, the segmentation of the kidneys into subregions remains an area of ongoing research[255,256]. The review of Zöllner et al highlights a number of techniques to achieve MRI sub-segmentation that both do and do not

require a contrast agent[256]. Sub-segmentation of the kidneys in MSOT is less explored. Lui et al used a 12-wavelength acquisition and a 2 or 3 Gaussian-curve fit of the corresponding histogram to separate renal cortex, medulla, and cysts[257]. This was compared with histology. However, the animal group was small, and further validation of such a technique should be made. The BR model in MSOT may be further improved by automatic sub-segmentation to reduce ROI contamination.

4.4.2 An Apparent Spinal Blood Vessel Provides a More Realistic AIF Than the Aorta in ABZWCY-HPβCD DCE MSOT

While blood sampling is considered the gold standard AIF measurement[238], mice have small blood volumes meaning repeated sampling can lead to poor animal welfare and hypotension impairing GFR results. As such, an imaged AIF is preferred in small animal DCE imaging.

On ABZWCY-HPβCD administration in MSOT, a region of interest drawn at the aorta shows an initial peak in photoacoustic signal followed by a fall below pre-injection levels. The "negative" signal makes the use of the aorta ROI as an AIF impractical because a negative signal would represent a negative concentration of dye which is a physical impossibility. This phenomenon is not present in the apparent spinal blood vessel ROI.

MSOT is a semi-quantitative imaging technique. The intensity of photoacoustic signal generated is the result of the amount of delivered light, the efficiency with which the absorber converts heats to a pressure related expansion, the concentration of the absorber, and the acoustic coupling[194]. The amount of light delivered to a point is dependent on the points depth as well as the absorbance and scattering of the light in the tissues superficial to this[258].

The aorta is a deep structure near the centre of the mouse cross section when imaged at the level of the renal hila. As such, it is susceptible to a reduction in light delivered particularly as absorbance increases in the periphery of the mouse. We suspect that the increasing concentrations of ABZWCY-HPβCD in the periphery of the animal and the associated increase in the absorbance of light means significantly less light can be delivered to the aorta. The result is a significantly lower than pre-injection photoacoustic signal. This hypothesis is supported by the progressive return to baseline over the course of the imaging session. As ABZCY-HPβCD is cleared from the animal the peripheral absorbance of light reduces and an increasing amount of light can reach the aorta.

The spinal blood vessel is significantly more superficial than the aorta. This means that depth related reductions in light delivery are potentially less impactful. There is less overlying tissue to facilitate the accumulation of ABZWCY-HPβCD, increase peripheral absorbance, and reduce light transmission to this structure. This may explain why the spinal blood vessel does not show “negative” signal.

The spinal blood vessel is also at a similar depth to the kidneys. This makes the amount of delivered light potentially more comparable between the spine and the kidneys. This may explain why models using the spinal blood vessel as an AIF more closely approximate GFR.

Algorithms that can account for the delivery of light to different points in the sample (light fluence models) are in development and are a requirement to transform MSOT from a semi-quantitative modality to a fully quantitative technique[194,259,260].

4.4.3 Renal Cortex ABZWCY-HPβCD Outflow is Rapid

ABZWCY-HPβCD signal in the cortex begins to drop six to ten seconds after injection. While a second less intense peak is frequently seen in the 40 seconds following the first peak, the general trajectory of the signal is downward. This means that the uptake phase in the cortex is relatively short.

A short uptake phase in the renal cortex impairs the application of a standard PR model. This model does not account for the outflow of marker from the irreversible compartment. The initial increase in the cortex is likely more representative of the dye in the vascular compartment of the kidney. The dye that has been filtered into the tubules has no opportunity to accumulate in the cortex ROI because outflow rate is so high. This leads to the overestimation of GFR by the PRa and PRs models.

Small molecule NIR dyes are known to be quickly excreted and frequently are cleared by the kidneys[176,216]. As such, a rapid outflow of ABZWCY-HPβCD is in keeping with this. The fast clearance of small molecule NIR dyes may contribute to their lower risk of toxicity.

4.4.4 A Modified Patlak-Rutland Model Tracks Global GFR

We have shown that the MPRs model using ABZWCY-HPβCD DCE MSOT can approximate GFR in health and following surgical IRI. It more closely tracks global GFR than the BR model and the model-free measurements of T^{MAX}, T^{MAX} Delay, and AUC C:P ratio. The MPRs model more closely estimates GFR than the PRs model. This is likely because the uptake phase of ABZWCY-HPβCD in the renal pelvis is significantly longer than in the renal cortex.

The MPRs model overestimates the GFR in healthy animals and underestimates the GFR following injury. The 95% limits of agreement are ±118.9 µL/min. As a comparison, DCE MRI has shown both overestimation and underestimation of GFR depending on the model and acquisition used where the PR model underestimates the GFR[120,122,261–263]. Bokacheva et al showed a 50% underestimation using DCE MRI and a PR model in humans compared with diethylene-triamine-pentaacetate clearance[122]. Zöllner et al showed a significant underestimation and wide 95% limits of agreement (±2500 µL/min) when comparing a two compartment model with DCE MRI GFR and FITC-sinistrin GFR in rats[264]. Also, this two compartment model was previously shown to produce higher GFR estimates than a PR model[265]. DCT CT PR models have also been shown to underestimate GFR in pigs[113]. Interestingly, we saw an overestimation with a PR model in DCE MSOT which may relate to the more rapid tubular outflow of NIR dyes compared with gadolinium, iopamidol, or nanoparticles.

Following IRI, identification of the renal pelvis is more challenging due to oedema, sutures, and changes in positioning of the kidneys[155]. We have also noted a reduction in the native contrast between the renal parenchyma and the renal cortex following IRI. It is possible that the renal pelvis was partially out of plane during imaging. This could lead to less accurate quantifications of ABZWCY-HPβCD in this region and an underestimation of GFR.

Also, the rate at which ABZWCY-HPβCD moves through the tubules is likely reduced following IRI. The pelvis is not the site of filtration. In distinction from the standard PR method, the MPRs model relies on the rapid outflow of dye from the cortex to the pelvis to make the tubule to pelvis transit time negligible and the calculated rate representative of GFR. However, as evidenced by a decrease in the BR pelvis model K_{cl}, the transit time from the cortex and pelvis is prolonged following IRI. As the flow through the tubules is reduced in injury, the tubule to pelvis transit time may no longer be insignificant.

Furthermore, the amount of ABZWCY-HPβCD accumulating in the renal pelvis would be significantly lower in injury and such a low concentration in the renal pelvis may be less detectable by MSOT leading to an underestimation of GFR.

4.4.5 A Modified Patlak-Rutland Model is More Sensitive for Unilateral Injury than Model-free Measurements

The MPRs model was able to detect a significant difference between the injured and uninjured kidney in a unilateral 27.5-minute IRI. Model-free measurements did not return a

significant difference. The greater sensitivity of the MPRs model to detect these changes gives it a distinct advantage over the model-free measurements for tracking renal function.

TD global GFR only detected a significant difference on day 1 post unilateral injury. The MPRs model showed an increase in the mean SK-GFR of the uninjured kidney on day 3. This compensatory increase in the control kidney may explain why the TD global GFR has normalised on day 3.

Contralateral kidney compensation is seen in models of unilateral nephrectomy in rodents where there is an increase in renal blood flow in the remaining kidney[266–268]. Changes in renal blood flow occur within 15 minutes and an increase in SK-GFR occurs as soon as 48-hours following nephrectomy[267,268]. Acute SK-GFR compensation following nephrectomy appears to be driven by a reduced production of renin, reduced stimulation of angiotensin II type 1 receptors, and increased renal blood flow produced by decreased intra-renal vascular resistance[267].

However, IRI is associated with an upregulation of angiotensin II type 1 receptors with a maintained production of renin[269]. This achieves a higher SK-GFR by increasing intraglomerular pressure. Angiotensin II type 1 antagonism has been shown to reduce progression to CKD after IRI induced AKI independent of systemic blood pressure control[270]. We did not measure renin–angiotensin–aldosterone system (RAAS) products nor blood pressure, but this would be a valuable area of investigation. There may be an association between MSOT MPRs detected contralateral filtration compensation, changes in RAAS products, systemic blood pressure, and intra-renal vascular resistance.

4.4.6 Model-free Measurements May Be Impacted by Acquisition and Contrast Agent

It is important to note that direct comparison of these experiments with other papers exploring renal DCE MSOT is difficult. First, these other publications utilise IRDye 800CW [155,157,207,210,219–223]. We have shown in chapter 3 that the MSOT measured kinetics of ABZWCY-HPβCD differ from IRDye 800CW. The faster signal decay and the sharper peaks seen in the kidney with IRDye 800CW may be better suited to measuring T^{MAX} and T^{MAX} Delay.

Secondly, these papers have measured multiple wavelengths: two[155,219,220], five[210,223], six[222], and seven[157,207,221]. Our experiments have measured a single wavelength to maximise temporal resolution. This was to facilitate capturing rapid changes in the concentration of the dye in the blood compartment in order to provide an accurate AIF. However, the

potential for signal drift due to changes in the concentration of non-dye absorbers may lead to changes in the timing of the peaks. AUC C:P ratio, PR models, and MPR models will be less susceptible to this where drift is equally present in all regions and compartments as this leads to the drift cancelling itself out.

Finally, these publications have used different reconstruction software including different reconstruction and spectral unmixing algorithms. The impact that these different tools have in this injury setting with these contrast agents has not been explored.

4.5 Conclusions

The MPRs model has shown the ability to measure GFR in DCE MSOT, sensitively track unilateral injury, and has greater utility than model-free measurements. Unfortunately, it remains dependent on identification of the renal pelvis which is more challenging following IRI surgery.

The semi-quantitative nature of MSOT and the impact of light fluence has shown that the aorta is currently an unsuitable AIF until fluence correction algorithms are further developed. The rapid outflow of ABZWCY-HPβCD from the cortex has shown a standard PR model overestimates GFR.

5 Measurements of Tubular Health in Multispectral Optoacoustic Tomography

5.1 Introduction

Tubular function and health are not routinely measured in clinical practice despite their physiological significance[71].

The proximal tubules are responsible for the active secretion of organic acids, organic bases, and hydrogen ions via transmembrane transporter proteins[55,73]. They are important in the clearance of drugs and uraemic toxins – particularly where substrates are protein-bound or charged which impairs their glomerular filtration[71–75]. The expression of different transporter proteins on the apical and basolateral surface of the proximal tubular cells (PTCs) results in a complicated clearance pathway from blood to urine.

PTCs are reliant on aerobic metabolism to perform their clearance functions and are laden with mitochondria to provide the adenosine triphosphate (ATP) required[55]. This ATP facilitates clearance directly and indirectly. ATP powers the sodium–potassium pump (Na^+K^+ATPase) at the basolateral surface of the PTCs. This increases the interstitial space sodium concentration which is required for solute carrier (SLC) family 13 member 3 (SLC13A3) to co-transport α-ketoglutarate (αKG) into the PTCs[71,73]. αKG facilitates organic anion transporter (OAT) 1 and 3 at the basolateral surface to transport organic anions into the PTCs[71]. Then, ATP directly facilitates apical secretion of organic anions into the filtrate via the ATP-binding cassette (ABC) transporters: ABCB1, ABCC4, and ABCG2[73]. Furthermore, the sodium gradient provided by the basolateral Na^+K^+ATPase facilitates the sodium–hydrogen antiporter secretion of hydrogen ions at the PTCs apical surface[79]. This luminal hydrogen then enables the transport of organic cations into the filtrate by the SLC family 22 and 47 transporters: SLC22A4, SLC47A1, and SLC47A2[73,271].

Kidney ischaemia reperfusion injury (IRI) results in tubular injury[272]. This primarily affects the proximal tubule and medullary thick ascending limb of the loop of Henle[2]. These energy demanding segments of the nephron exist where the partial pressure of oxygen is low[55,273]. This relatively hypoxic state is worsened by any cause of hypoperfusion. Hypoxia results in reduced ATP and nitric oxide production and increased reactive oxygen species and intracellular calcium[2,273]. This results in vascular, endoplasmic reticulum, and mitochondrial dysfunction[274], activating an inflammatory response via cytokines (TNF-α, IL-1, IFN-γ), neutrophils, monocytes, dendritic cells, and macrophages[275]. Ultimately, tubular cell

apoptosis leads to sloughing of cells into the lumen that bind with Tamm-Horsfall protein forming casts and tubular obstruction. Remaining tubular cells can display cytoskeletal damage and translocation of Na^+K^+ATPase from the basolateral to apical membrane, leading to increased sodium delivery to the macula densa and vasoconstriction of the glomerular afferent arteriole via tubuloglomerular feedback[2].

While the histology of a renal biopsy can describe tubular health, this is an invasive procedure with significant associated complications. There is no standard marker that can be used to measure tubular secretion rate (TSR) in a similar manner to what is established with glomerular filtration rate (GFR)[135–137].

In imaging, both scintigraphy and single photon emission computed tomography (SPECT) have been used to assess tubular health via two different Technetium-99m (Tc-99m) labelled contrast agents. Dimercaptosuccinic acid (DMSA) is a more than 50% protein bound acid with a molecular mass of 182 Da[141,142,276,277]. It is taken up by the PTCs with a long retention time. Due to this, imaging is performed as a static scan at a set time interval after administration. It is eventually metabolised to mixed disulphides of cysteine in the kidney[141]. There is evidence of both megalin/cubulin-mediated tubular reabsorption following glomerular filtration and OAT3-mediated basolateral peritubular uptake of DMSA into the PTCs[141–144]. It can be used to assess renal cortical structure and split renal function[145,146]. Mercaptoacetyltriglycine (MAG3) is a 77-85% protein bound triamide mercaptide with a molecular mass of 263 Da[106,278,279]. It is excreted by tubular secretion via OAT1 and OAT3 uptake at the basolateral side, and ABCC2 and ABCC4 secretion on the apical side[144]. In human, Tc-99m-MAG3 is cleared at 321 mL/min/1.73m^2 [147]. In contrast to DMSA, MAG3 is imaged dynamically.

The Centre for Preclinical Imaging at the University of Liverpool houses a Molecubes SPECT scanner (MOLECUBES NV, Belgium), but this instrument is limited by a 1-minute temporal resolution; as such it is less suitable for measuring MAG3 clearance where a temporal resolution of 2 to 15 seconds is commonly required[147,280–282]. If an AIF dependent model were to be compared between MSOT and SPECT, a temporal resolution approaching 1 second would be desirable[245]. While MAG3 and DMSA differ in their acquisition parameters, the split renal function that they measure produces similar results, differing by just 0.1%[283]. As such, the focus here was on the use of SPECT DMSA.

5.1.1 Objectives

This chapter aims to use dynamic contrast enhanced (DCE) MSOT measured clearance of STAR FLUOR 770 Acid to assess tubular function and injury. First, the clearance of STAR FLUOR 770 Acid is measured with and without the OAT blocking drug probenecid. This will assess whether STAR FLUOR 770 Acid is partially cleared by tubular secretion.

Second, the MSOT clearance of STAR FLUOR 770 Acid is measured in a model of unilateral IRI. Correlation with SPECT measured Tc-99m DMSA uptake and histological evidence of tubular injury is examined. Further comparison is made with the MSOT measured clearance of ABZWCY-HPβCD.

5.2 Results

5.2.1 Clearance of STAR FLUOR 770 Acid with and without Organic Anion Transporter Blockade

The clearance of both STAR FLUOR 770 Acid and ABZWCY-HPβCD was measured in MSOT with and without intra-peritoneal probenecid. ABZWCY-HPβCD acts as the negative control. Mice were imaged first without probenecid and then four days later with probenecid. Mice were in two groups and received probenecid either at a high (150 mg/kg) or low (50 mg/kg) dose on the second imaging day. The change in mean photoacoustic intensity was measured in the renal cortex and pelvis.

Representative examples of cortex time activity curves are seen in Figure 5.1. ABZWCY-HPβCD did not show any notable difference in time activity curves with either dose of probenecid. STAR FLUOR 770 Acid showed visually different cortex time activity curves where a high dose of probenecid was given. There was a progressive, slow increase in MSOT intensity after an initial sharp peak. This slow increase was not seen in the absence of probenecid. Also, a slower signal decay was seen where high dose probenecid was administered. STAR FLUOR 770 Acid did not show any observable differences in cortex time activity curves with low dose probenecid.

Representative examples of pelvis time activity curves are seen in Figure 5.2. ABZWCY-HPβCD did not show any observable differences in the pelvis time activity curves with either dose of probenecid. STAR FLUOR 770 Acid showed a slowed uptake in the renal pelvis where high dose probenecid was given. Figure 5.3 shows the individual pelvis time activity curves for each mouse given STAR FLUOR 770 Acid and high dose probenecid. All show a reduced uptake rate. This was not present in mice receiving low dose probenecid (Figure 5.4).

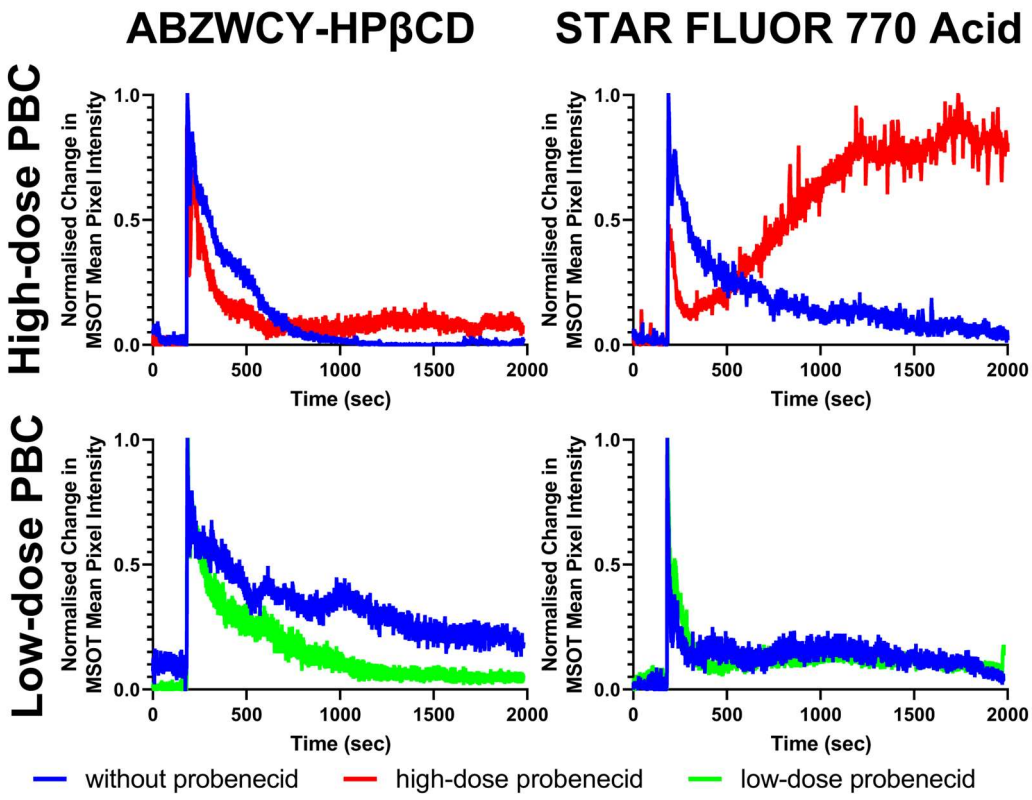

Figure 5.1: Example MSOT Cortex Time Activity Curves of ABZWCY-HPβCD and STAR FLUOR 770 Acid with and without Probenecid.

High dose probenecid = 150 mg/kg. Low-dose probenecid =50 mg/kg. PBC (Probenecid).

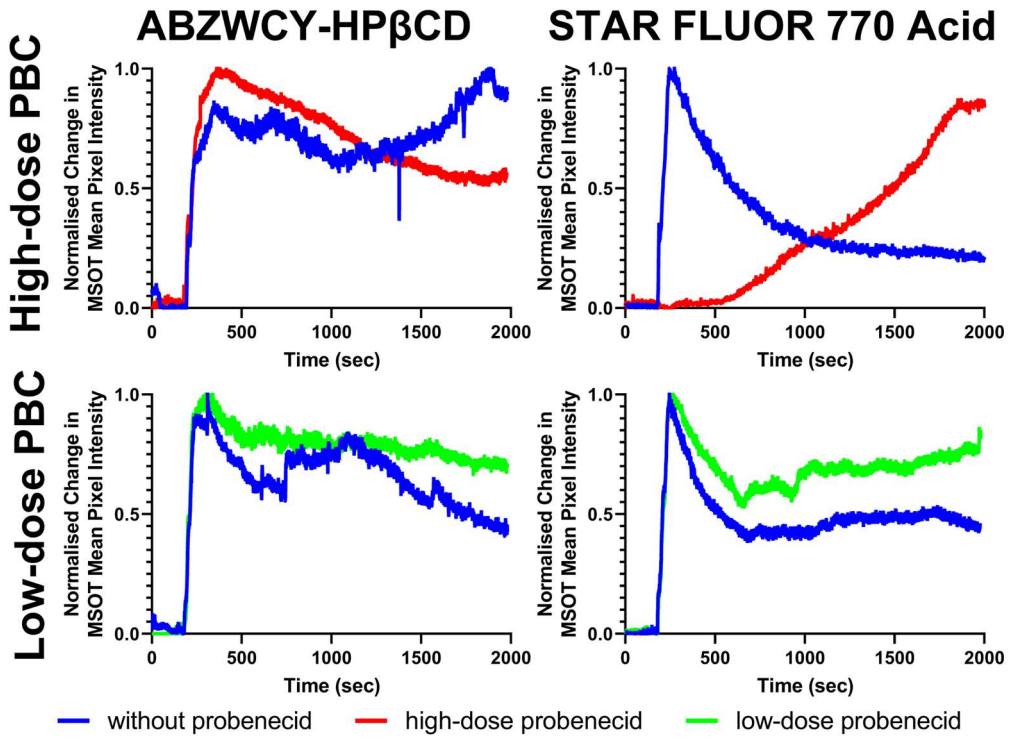

Figure 5.2: Example MSOT Pelvis Time Activity Curves of ABZWCY-HPβCD and STAR FLUOR 770 Acid with and without Probenecid.

High dose probenecid = 150 mg/kg. Low-dose probenecid =50 mg/kg. PBC (Probenecid).

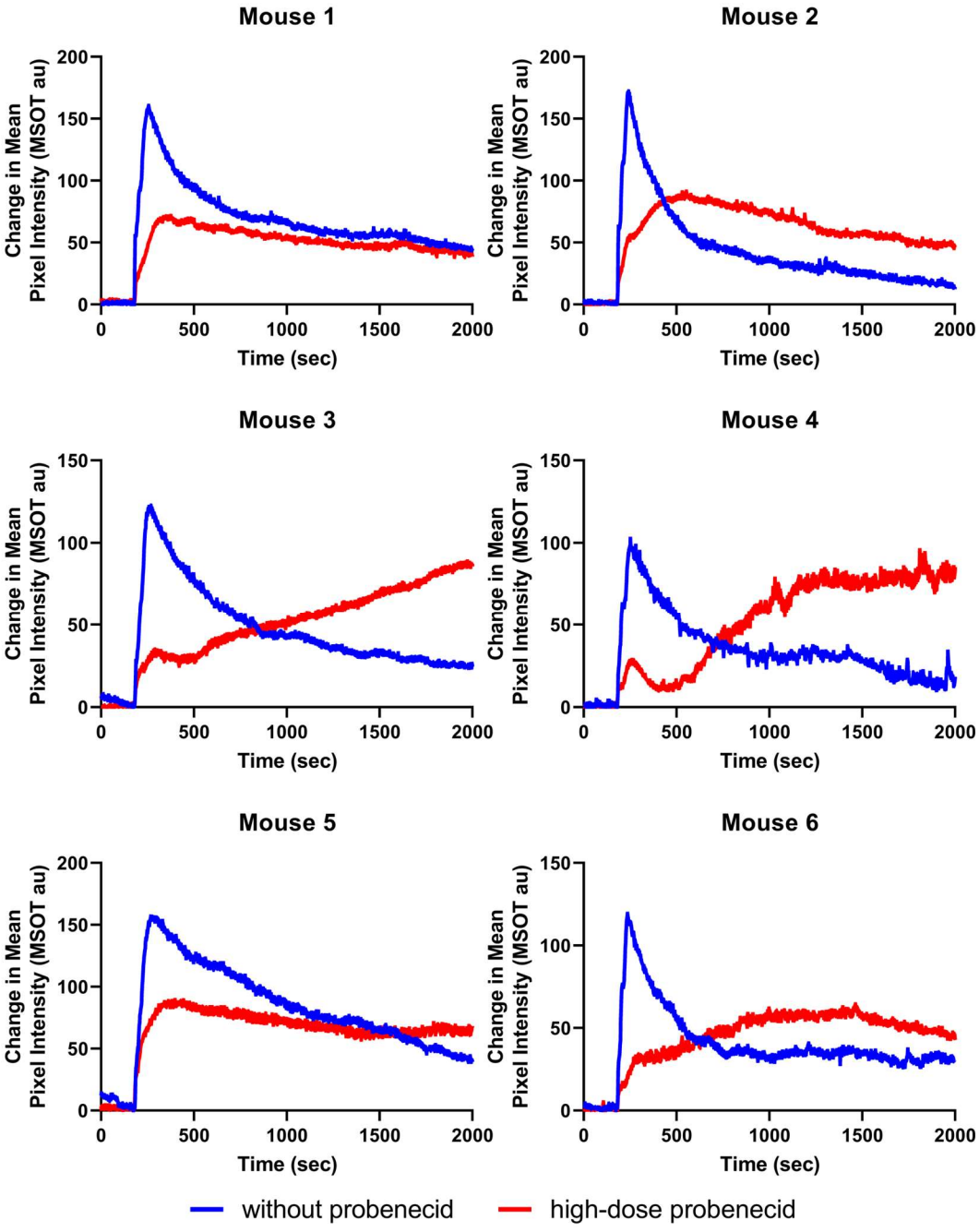

Figure 5.3: MSOT STAR FLUOR 770 Acid in the Right Renal Pelvis with and without High Dose Probenecid
High dose probenecid = 150 mg/kg. PBC (Probenecid).

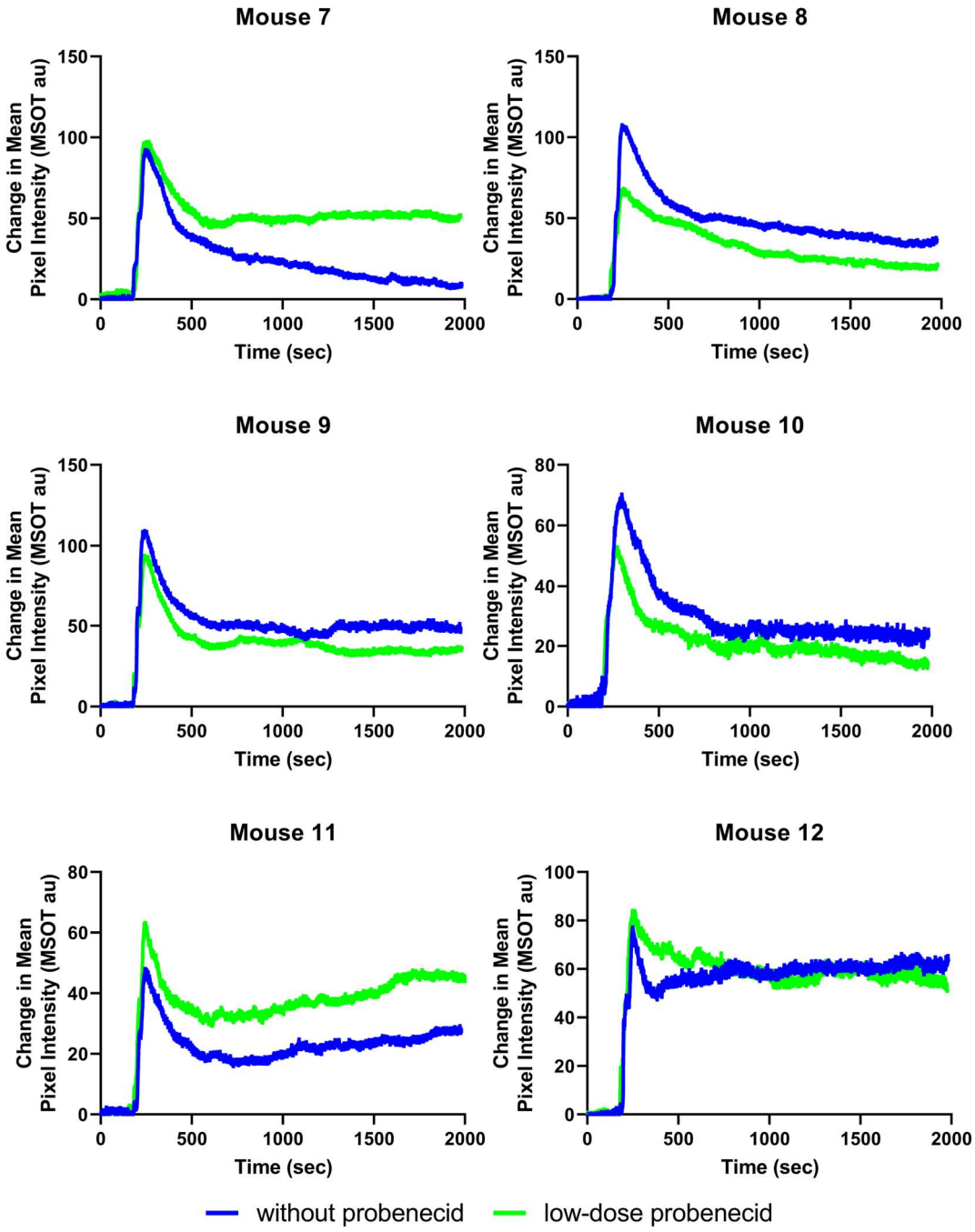

Figure 5.4: MSOT STAR FLUOR 770 Acid in the Right Renal Pelvis with and without Low Dose Probenecid
Low dose probenecid = 50 mg/kg. PBC (Probenecid).

5.2.2 MSOT Clearance and DMSA Uptake Following Severe Unilateral IRI

Ten mice underwent 40-minute right-sided unilateral surgical IRI along with MSOT and SPECT imaging prior to surgery then twice weekly for three weeks after injury. They were divided in two groups for MSOT: five received STAR FLUOR 770 Acid and five received ABZWCY-HPβCD. SPECT renal function was expressed as the percentage contribution of the right kidney to total kidney function, also known as split renal function. MSOT renal function was

calculated by the area under the curve cortex:pelvis ratio (AUC C:P ratio) and the MPRs method (4.1.3 Modified Patlak-Rutland Model) as well as expressed as split renal function for both the AUC C:P ratio and MPRs methods.

5.2.2.1 STAR FLUOR 770 Acid Clearance Following Severe IRI

Following a 40-minute unilateral IRI, STAR FLUOR 770 Acid AUC C:P ratio dropped significantly in the injured kidney with some apparent compensation in the control kidney (Figure 5.5A). There was a significant statistical difference between left and right kidney on day 1 post operation with P = 0.007. Following this the right kidney appeared to show some recovery in AUC C:P ratio. The standard deviation appeared to be particularly wide on days 8 and 12.

The mean MPRs clearance of STAR FLUOR 770 Acid was significantly higher before injury (525 µL/min, Figure 5.5B) compared to GFR calculated by measuring FITC-sinistrin clearance with the transcutaneous device in healthy animals (chapter 4, 305 µL/min). STAR FLUOR 770 Acid MPRs showed a decrease in the IRI kidney following injury. The difference between injured and control kidney was significant on day 1 and 8. Additionally, near statistical significance was seen at day 5.

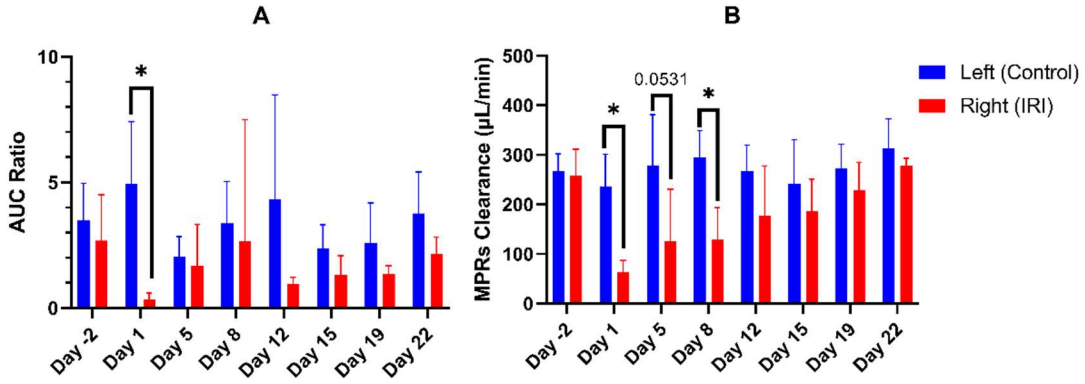

Figure 5.5: MSOT STAR FLUOR 770 Acid following Severe Unilateral IRI.
A. Area under the curve (AUC) cortex:pelvis ratio. B. MPRs clearance. MPRs (Modified Patlak-Rutland model with spine blood vessel AIF). ns P >0.05, * P ≤0.05, ** P ≤0.01, *** P ≤0.001, **** P ≤0.0001. Bars are standard deviation.

5.2.2.2 ABZWCY-HPβCD Clearance Following Severe IRI

Following a 40-minute unilateral IRI, the AUC C:P ratio of ABZWCY-HPβCD, which is exclusively filtered, dropped significantly in the injured kidney and showed a milder drop in the control kidney compared to baseline (Figure 5.6A). This was significant on day 1 post injury (P = 0.012898). AUC C:P ratio progressively recovered in the injured kidney over the course of imaging, while the control kidney remained largely similar.

The mean baseline MPRs GFR of ABZWCY-HPβCD was 350 µL/min which is similar to the GFR measured in Chapter 4 both by transcutaneous device (FITC-sinistrin clearance) and MSOT (ABZWCY-HPβCD clearance). Statistical significance between injured and control kidney was present from day 1 to 12. The injured kidney MPRs GFR recovered from day 1 through the course of the imaging period being similar to pre-injury levels at day 19.

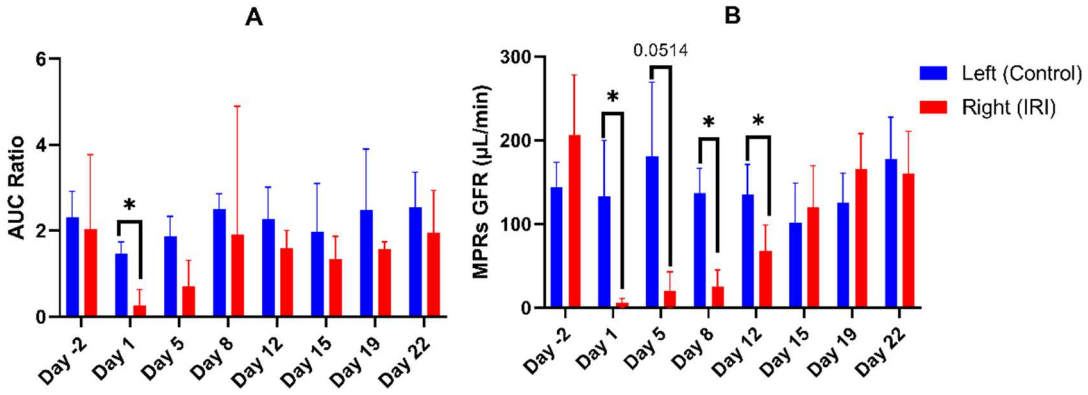

Figure 5.6: MSOT ABZWCY-HPβCD following Severe Unilateral IRI.
A. Area under the curve (AUC) cortex:pelvis ratio. B. MPRs GFR. MPRs (Modified Patlak-Rutland model with spine blood vessel AIF). ns P >0.05, * P ≤0.05, ** P ≤0.01, *** P ≤0.001, **** P ≤0.0001. Bars are standard deviation.

5.2.2.3 STAR FLUOR 770 Acid versus DMSA Uptake

Figure 5.7 shows representative example images of a single mouse in SPECT (DMSA) and MSOT (STAR FLUOR 770 Acid) at each imaging time point. The MSOT images shown are at the time of the cortex peak in the uninjured kidney. Decreased DMSA uptake can be seen in the injured right kidney which progresses over the study period. Decreased STAR FLUOR 770 Acid signal can be seen in the injured right kidney which shows some recovery towards the end of the study.

When examined as split renal function, MSOT STAR FLUOR 770 shows an initial drop immediately after injury with progressive recovery to baseline by both AUC C:P ratio (Figure 5.8A) and MPRs clearance (Figure 5.8C). The initial drop is more pronounced when measured by the AUC C:P ratio method. In contrast, SPECT DMSA uptake declines after injury but to a lesser extent and then continues to decline through the imaging period without evidence of recovery (Figure 5.8A&C).

Split renal function measured by SPECT DMSA uptake does not appear to show correlation with split renal function measured by MSOT STAR FLUOR 770 Acid whether using AUC C:P ratio (Pearson r = -0.03044, Figure 5.8B) or MPRs clearance (Pearson r = -0.03161, Figure 5.8D).

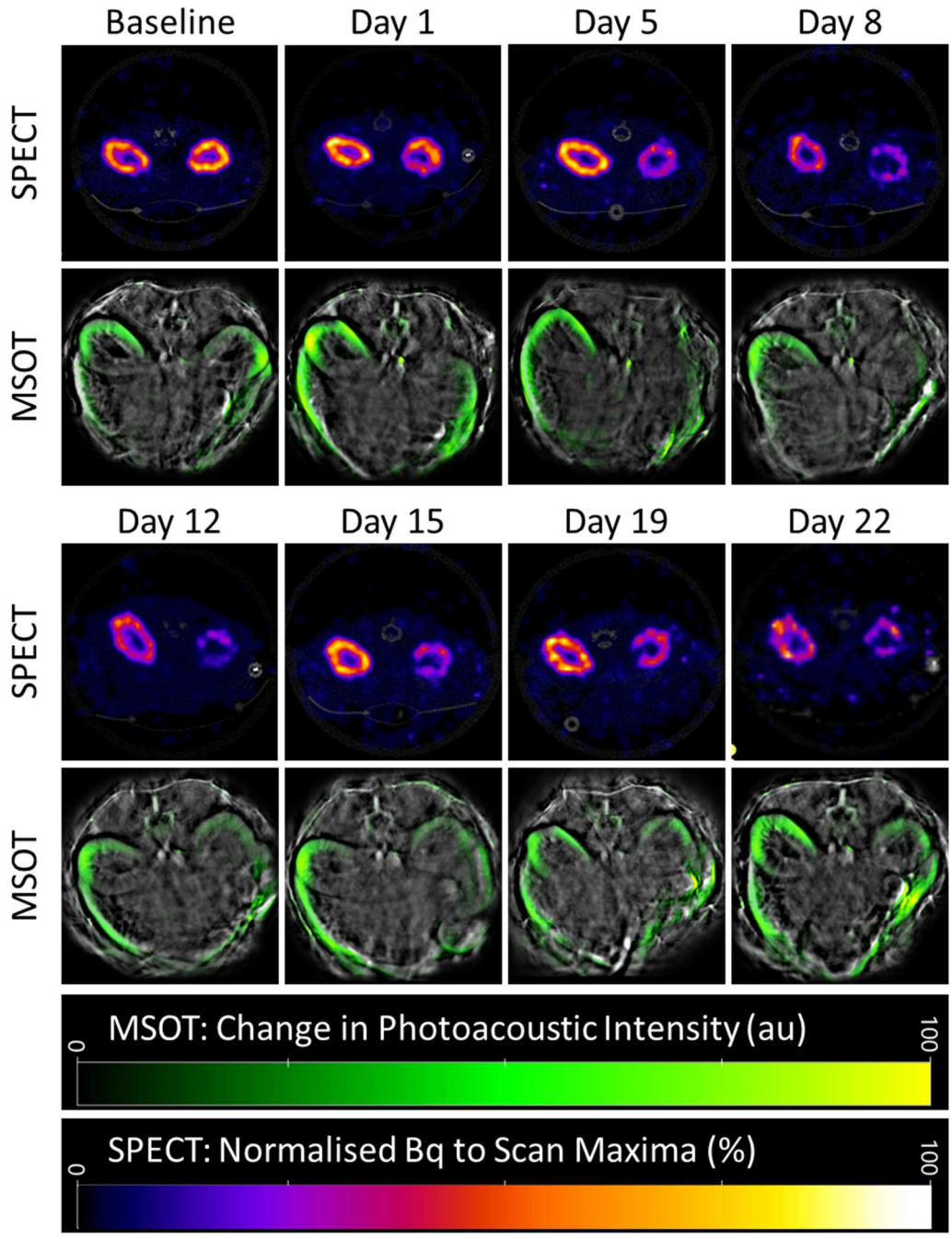

Figure 5.7: Example Images of SPECT DMSA and MSOT STAR FLUOR 770 Acid following Unilateral Right-sided IRI

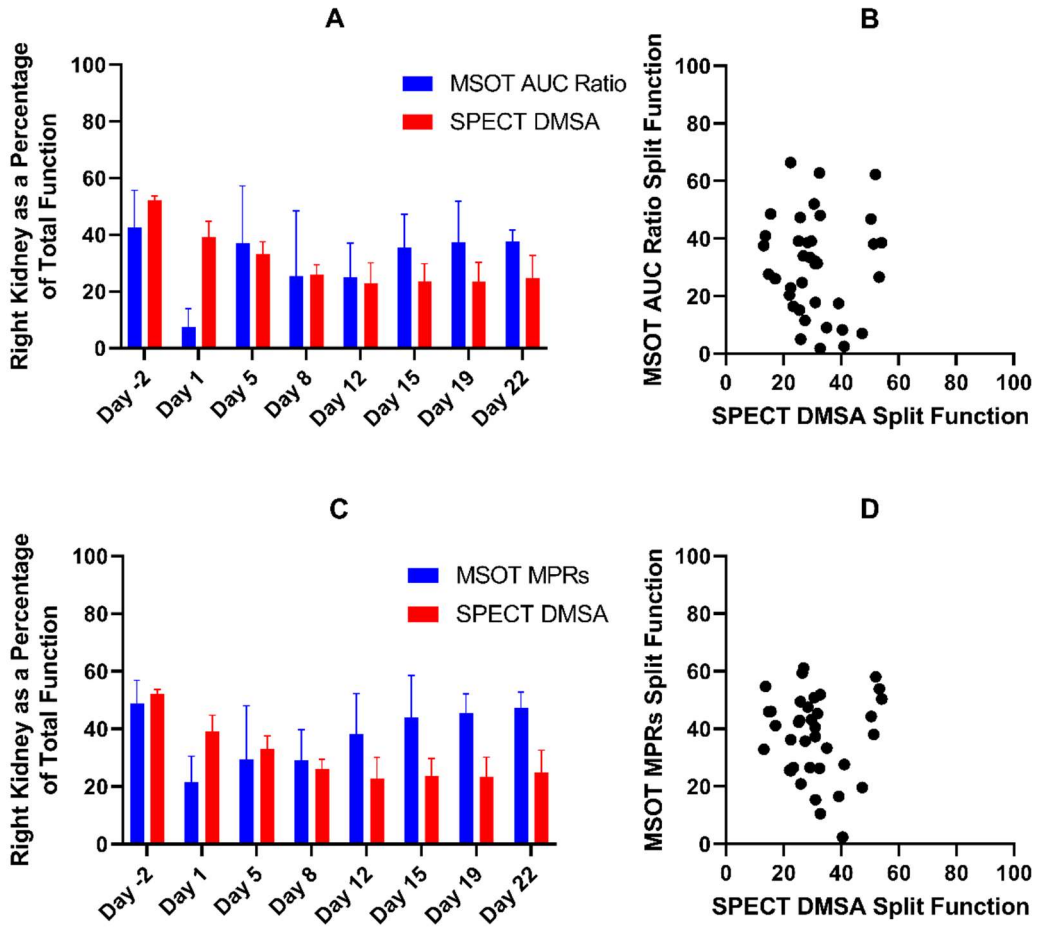

Figure 5.8: Split Renal Function by MSOT STAR FLUOR 770 Acid and SPECT DMSA following Severe Unilateral IRI.

A. MSOT AUC C:P ratio vs SPECT DMSA. B. Correlation of MSOT AUC C:P ratio vs SPECT DMSA. Pearson r = -0.03044 (CI -0.3510 to 0.2965, P = 0.8581). C. MSOT MPRs vs SPECT DMSA. D. Correlation of MSOT MPRs vs SPECT DMSA. Pearson r = -0.03161 (CI -0.3520 to 0.2954, P = 0.8527). AUC (Area under the curve). MPRs (Modified Patlak-Rutland model with spinal blood AIF). SPECT (Single-photon emission computed tomography). DMSA (Dimercaptosuccinic acid).

5.2.2.4 ABZWCY-HPβCD versus DMSA Uptake

Figure 5.9 shows representative example images of a single mouse in SPECT (DMSA) and MSOT (ABZWCY-HPβCD) at each imaging time point. The MSOT images shown are at the time of the cortex peak in the uninjured kidney. Again, decreased DMSA uptake can be seen in the injured right kidney which progresses over the study period. ABZWCY-HPβCD signal in the right kidney is decreased after injury and then shows some recovery in the following imaging sessions.

Split function examined by ABZWCY-HPβCD follows a similar pattern to STAR FLUOR 770 Acid: An initial drop following injury followed by progressive recovery to baseline (Figure 5.10A&C). Initial injury appears more severe when measured by MPRs split function (Figure 5.10C).

Split renal function measured by MSOT ABZWCY-HPβCD does not correlate with SPECT DMSA split renal function whether measured by AUC C:P ratio (Pearson r = -0.1780, Figure 5.10B) or MPRs GFR (Pearson r = -0.1207, Figure 5.10D).

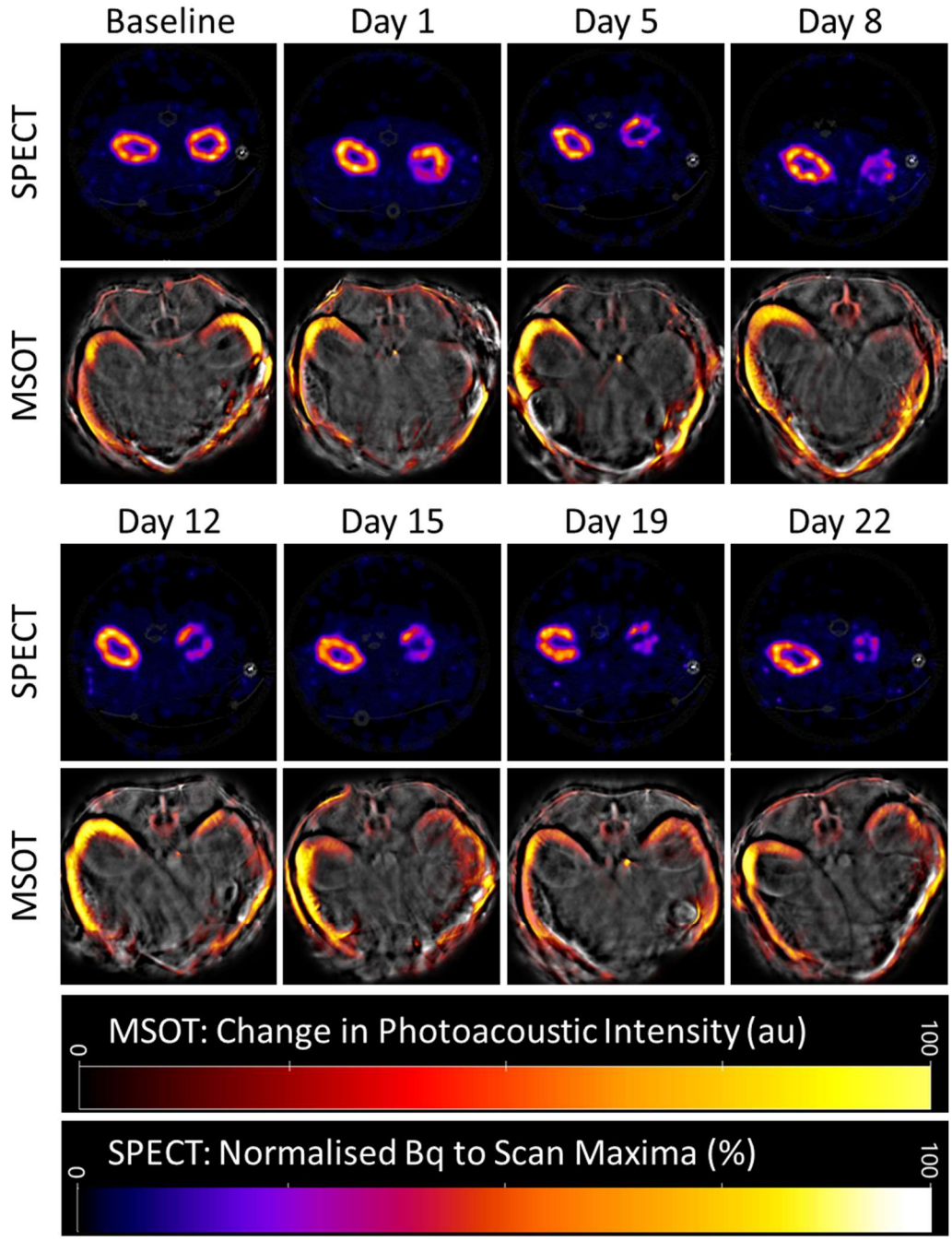

Figure 5.9: Example Images of SPECT DMSA and MSOT ABZWCY-HPβCD following Unilateral Right-sided IRI

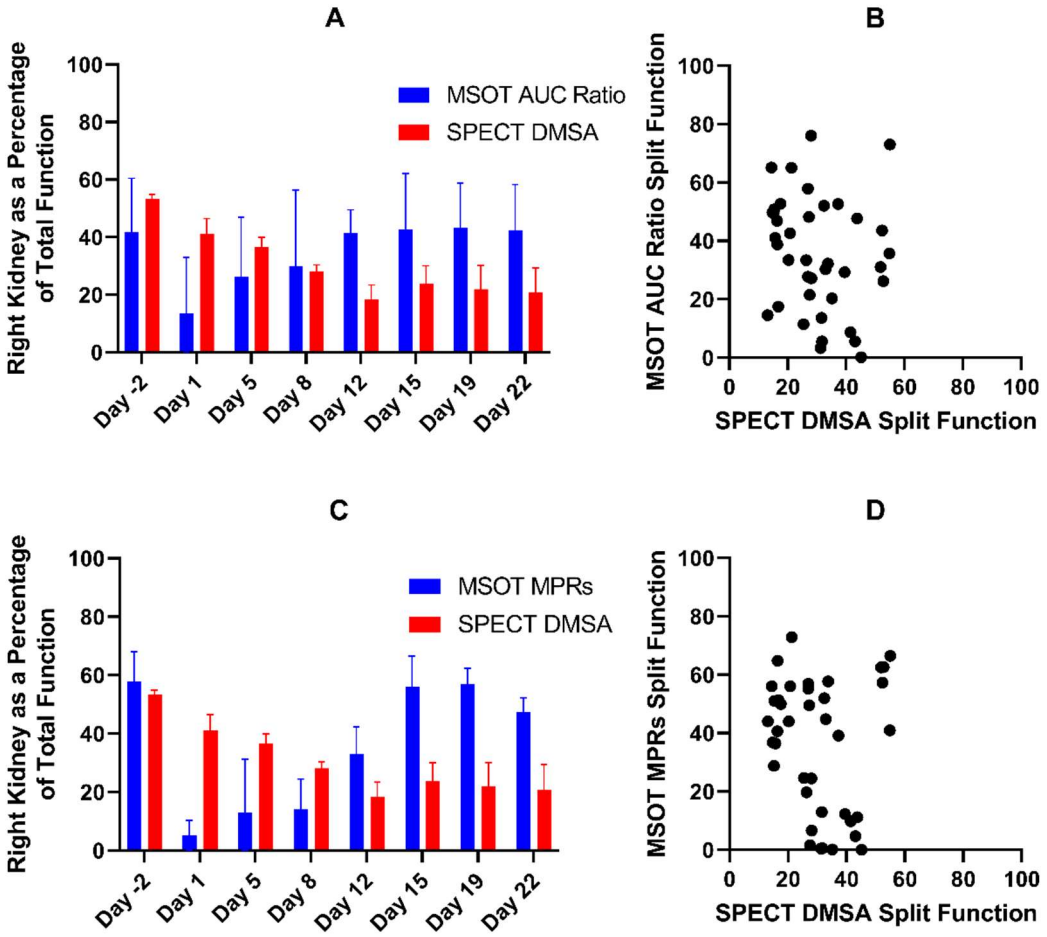

Figure 5.10: Split Renal Function by MSOT ABZWCY-HPβCD and SPECT DMSA following Severe Unilateral IRI. A. MSOT AUC C:P ratio vs SPECT DMSA. B. Correlation of MSOT AUC C:P ratio vs SPECT DMSA. Pearson r = -0.1780 (CI -0.4673 to 0.1457, P = 0.2784). C. MSOT MPRs vs SPECT DMSA. D. Correlation of MSOT MPRs vs SPECT DMSA. Pearson r = -0.1207 (CI -0.4202 to 0.2025, P = 0.4642). AUC (Area under the curve). MPRs (Modified Patlak-Rutland model with spinal blood AIF). SPECT (Single-photon emission computed tomography). DMSA (Dimercaptosuccinic acid).

5.2.2.5 Comparing MSOT Split Renal Function by ABZWCY-HPβCD and STAR FLUOR 770 Acid

Split renal function by MPRs measured using ABZWCY-HPβCD and STAR FLUOR 770 Acid was similar following severe unilateral IRI (Figure 5.11). Both show an immediate drop following IRI with progressive recovery to baseline. A significant difference is seen on day 1 post injury with split function MPRs with ABZWCY-HPβCD showing a much greater decline from baseline than with STAR FLUOR 770 Acid (P = 0.007898). Split function MPRs with ABZWCY-HPβCD was statistically greater than with STAR FLUOR 770 Acid on day 19 (P = 0.023010).

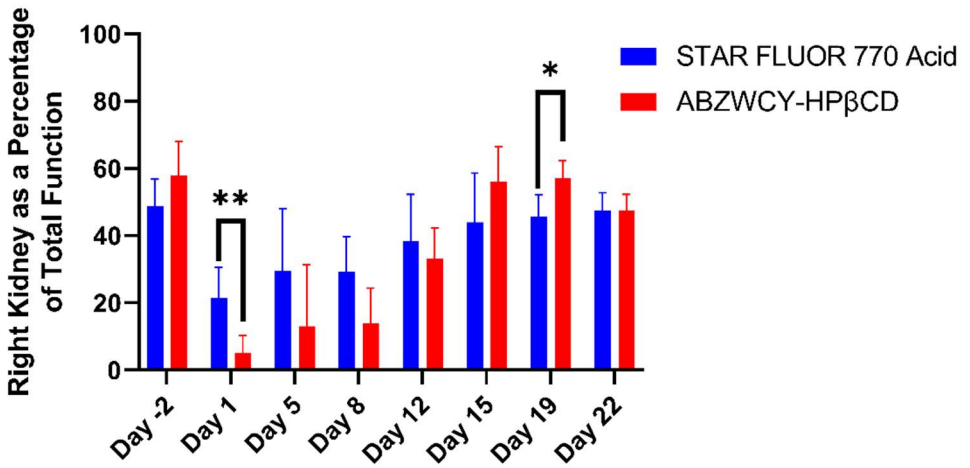

Figure 5.11: Comparing MSOT STAR FLUOR 770 Acid and MSOT ABZWCY-HPβCD MPRs Split Renal Function following Severe Unilateral IRI.
MPRs (Modified Patlak-Rutland model with spinal blood AIF). ns P >0.05, * P ≤0.05, ** P ≤0.01, *** P ≤0.001, **** P ≤0.0001. Bars are standard deviation.

5.2.3 Comparing Tubular Injury Histology with MSOT and SPECT

Eight mice from the SPECT and MSOT unilateral IRI experiment (section 5.2.2) were sacrificed and their kidneys collected following the final imaging session (day 22 post injury): four from the group receiving STAR FLUOR 770 Acid and four from the group receiving ABZWCY-HPβCD. The histology of the collected kidneys was examined by Professor Lorenzo Ressel and Ms Andreea Luchian at the Leahurst Campus Veterinary Histopathology Laboratory. Both the left control kidney and right clamped kidney were analysed. They were assessed for fibroblast deposition and scored for tubular damage. Tubular injury histology was compared with MSOT MPRs data due to the greater accuracy and sensitivity for injury this method has shown in our work. Histology was also compared with SPECT DMSA uptake.

5.2.3.1 Tubular Injury Following Ischaemia Reperfusion and Longitudinal MSOT and SPECT

Tubular injury was scored in four categories from 0 to 4 where 0 was no damage and 4 was severe damage. These scores were obtained by estimating the percentage of the field of view occupied by regenerating tubules, inflammation, tubular dilatation, and casts/necrosis by two assessors and as follows:

Field of View Percentage	Score
0%	0
1-25%	1
26-50%	2
51-75%	3
75-100%	4

Scores in each category were averaged over ten fields of view chosen at random. A maximum total injury score of 16 was possible where the four categories were added together. Examples of features scored on histological assessment are seen in Figure 5.12.

Mice in both the STAR FLUOR 770 Acid group (Figure 5.13) and the ABZWCY-HPβCD group (Figure 5.14) showed evidence of tubular injury by all four histology parameters and by total tubular injury score in the clamped kidney on day 22. The control kidney was generally free of evidence of tubular injury in both dye groups.

When comparing the clamped kidney between the two dye groups, the degree of histological injury was similar (Figure 5.15). Multiple paired T-tests did not reveal any statically significant difference in the clamped kidneys between the two dye groups at any imaging time point in any of the four histology parameters or their total tubular injury score.

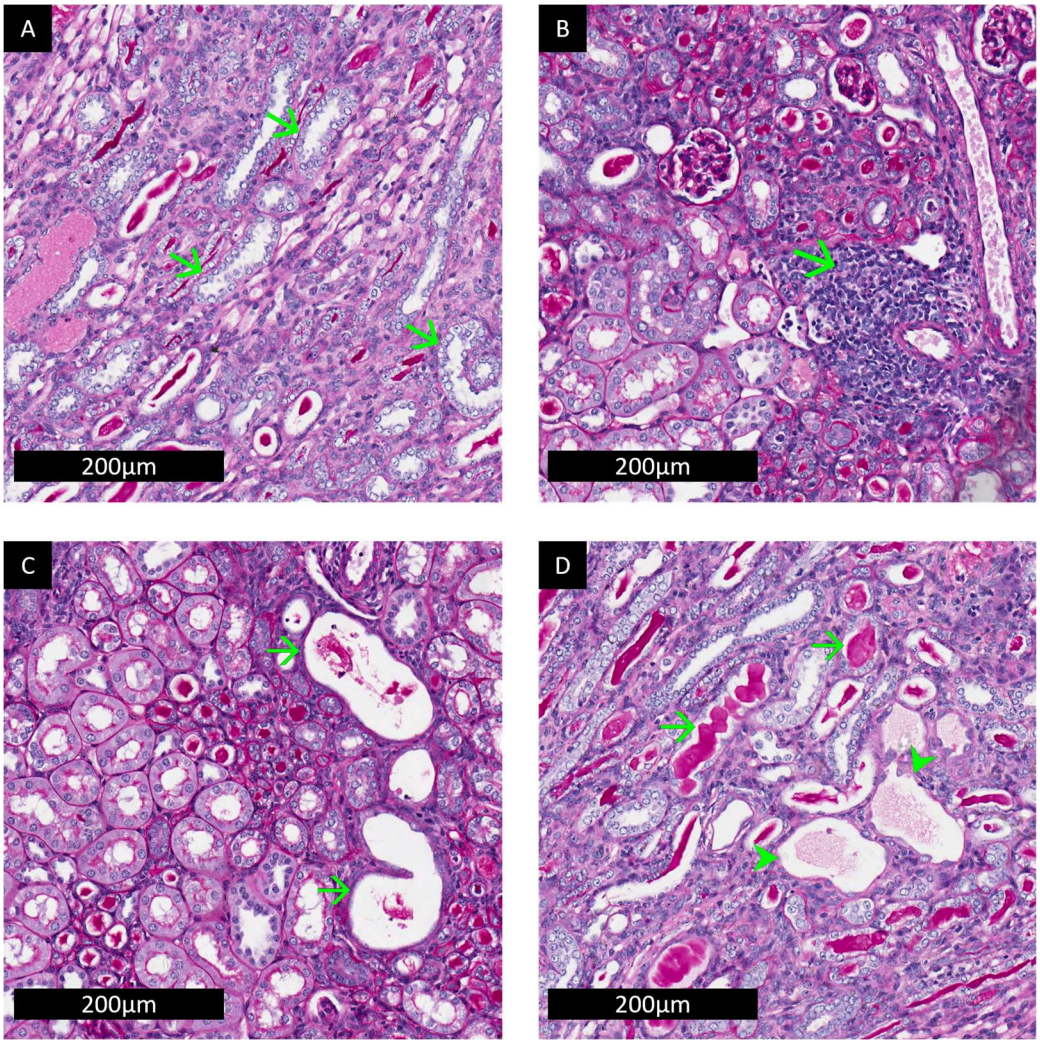

Figure 5.12: Examples of Tubular Injury Features Scored at Histology (Periodic Acid-Schiff Stain).
A. Regenerating tubules (green arrows). B. Inflammation (green arrow). C. Tubular dilatation (green arrows). D. Tubular casts (green arrows) and tubular necrosis (green arrow heads).

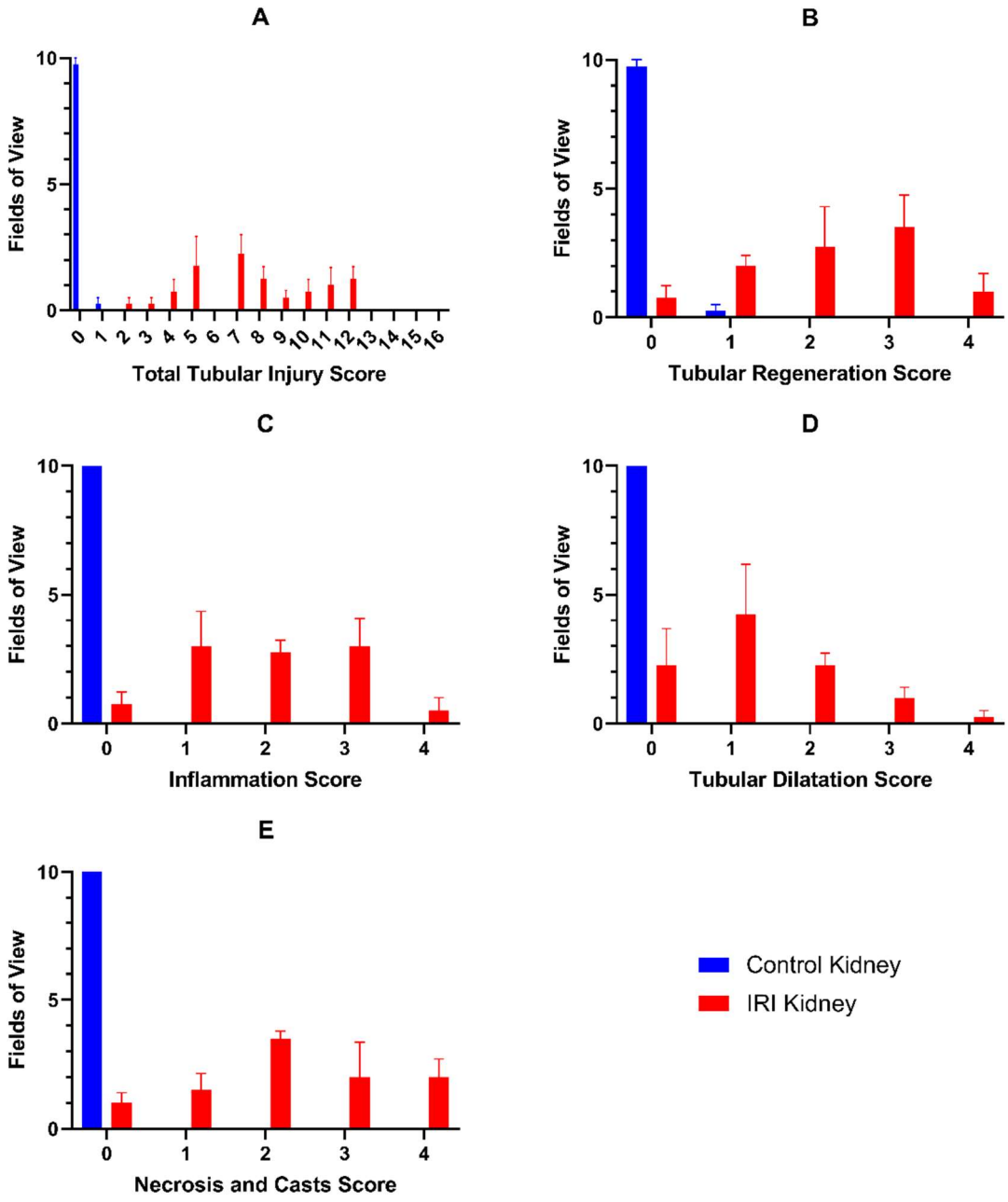

Figure 5.13: Mean Histological Tubular Injury Scores following Ischaemia Reperfusion Injury and Longitudinal MSOT with STAR FLUOR 770 Acid.

Mean of four mice - each contributing one IRI and one control kidney. A. Total tubular injury score. B. Tubular regeneration score. C. Inflammation score. D. Tubular dilatation score. E. Necrosis and casts score. Bars are the mean. Error bars are the standard error of the mean. IRI (Ischaemia reperfusion injury).

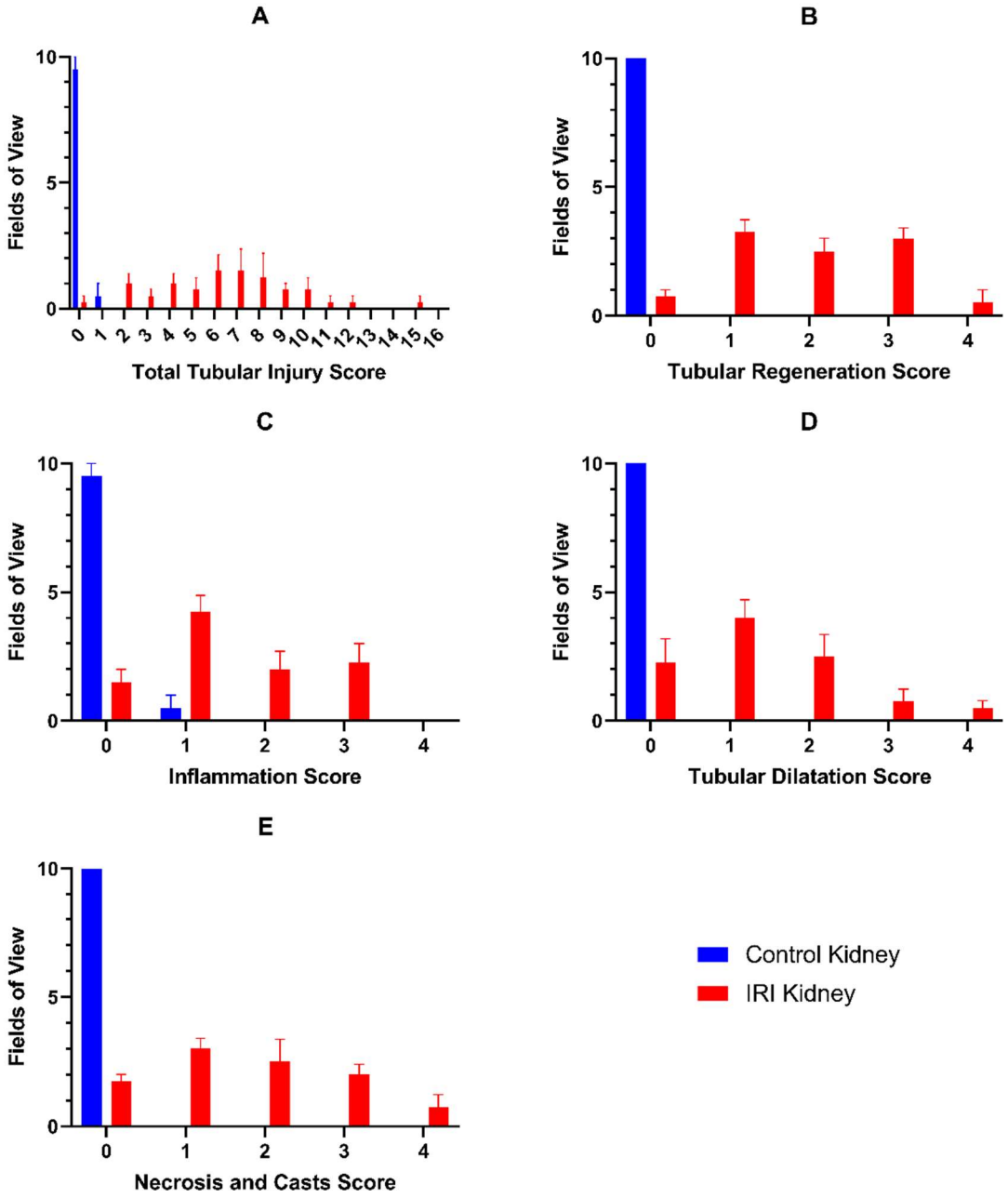

Figure 5.14: Mean Histological Tubular Injury Scores following Ischaemia Reperfusion Injury and Longitudinal MSOT with ABZWCY-HPβCD.
Mean of four mice - each contributing one IRI and one control kidney. A. Total tubular injury score. B. Tubular regeneration score. C. Inflammation score. D. Tubular dilatation score. E. Necrosis and casts score. Bars are the mean. Error bars are the standard error of the mean. IRI (Ischaemia reperfusion injury).

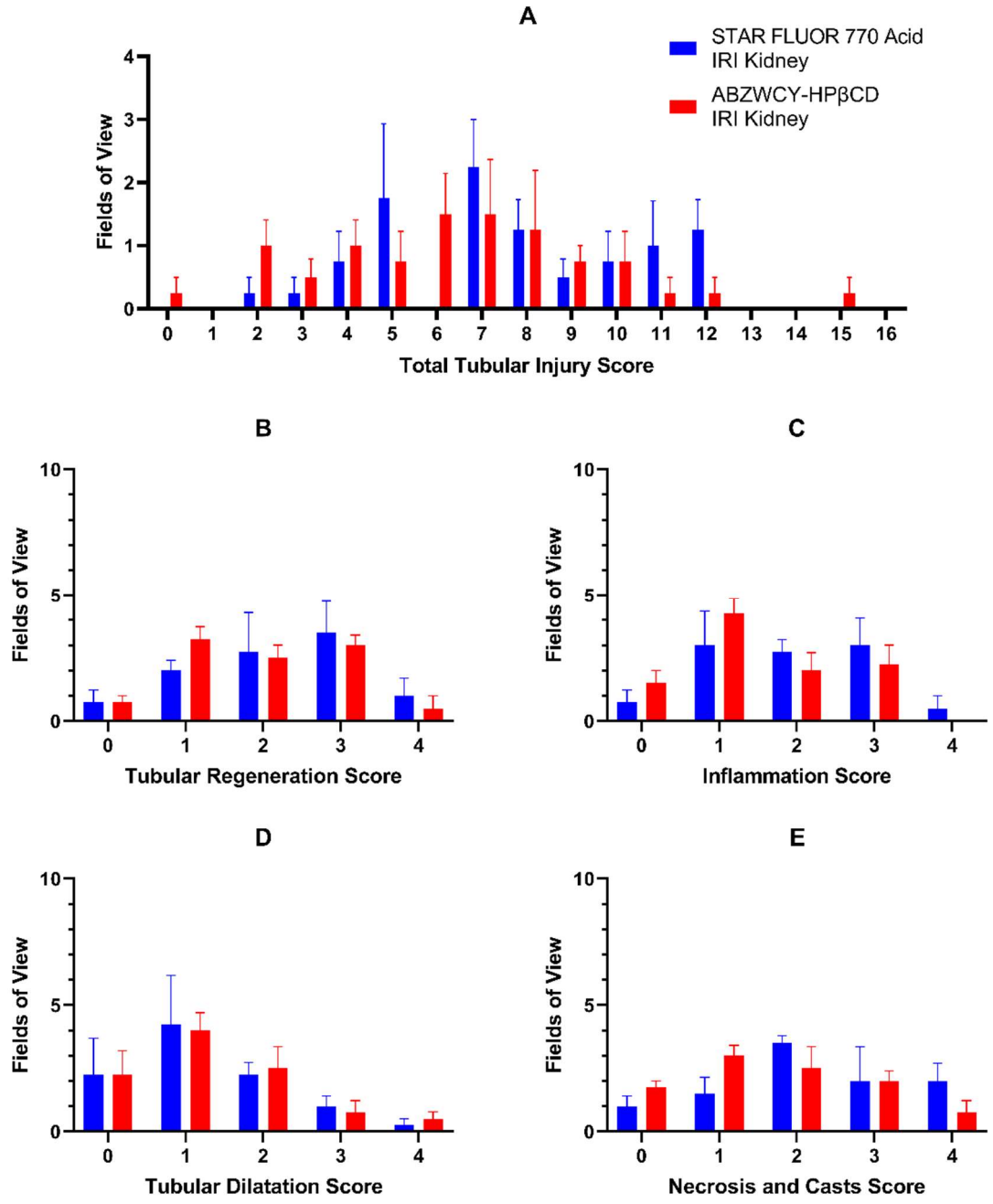

Figure 5.15: Comparing Mean Histological Tubular Injury Scores between Longitudinal MSOT with STAR FLUOR 770 Acid or ABZWCY-HPβCD following Ischaemia Reperfusion Injury
A. Total tubular injury score. B. Tubular regeneration score. C. Inflammation score. D. Tubular dilatation score. E. Necrosis and casts score. Bars are the mean. Error bars are the standard error of the mean. IRI (Ischaemia reperfusion injury).

5.2.3.2 Tubular Injury Score Compared with Day 1 Imaging

Impaired DCE MSOT MPRs STAR FLUOR 770 Acid clearance day 1 post IRI was associated with an increase in all four histological scores (Figure 5.16). This was similar when expressed as split renal function (Figure 5.17).

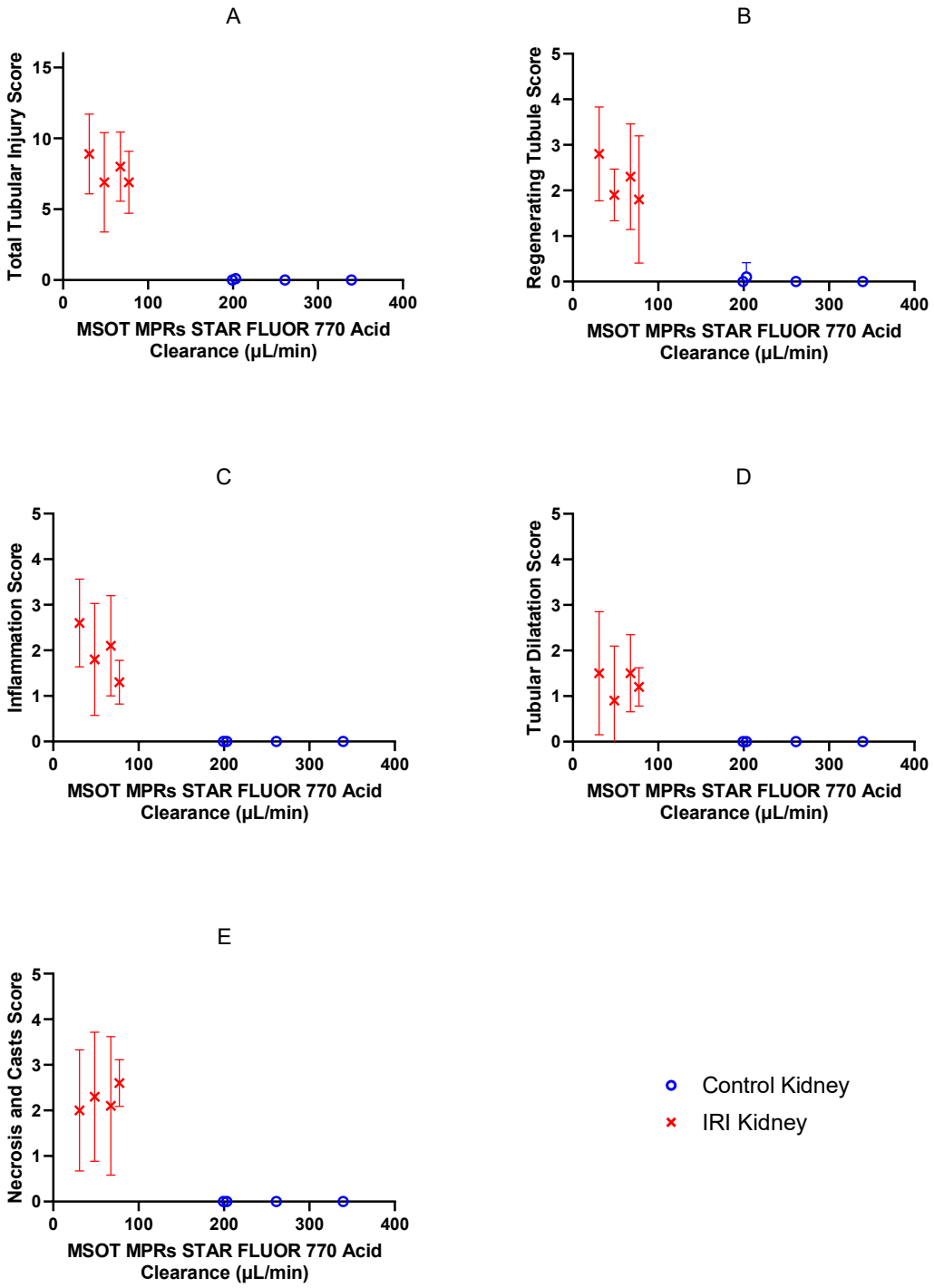

Figure 5.16: Day 1 post IRI DCE MSOT STAR FLUOR 770 Acid Clearance versus Histological Tubular Injury Scores

The MSOT clearance of STAR FLUOR 770 Acid using the MPRs model versus A. Total tubular injury score. B. Tubular regeneration score. C. Inflammation score. D. Tubular dilatation score. E. Necrosis and casts score. Error bars are the standard deviation. IRI (Ischaemia reperfusion injury), MPRs (Modified Patlak-Rutland method with spinal blood vessel AIF).

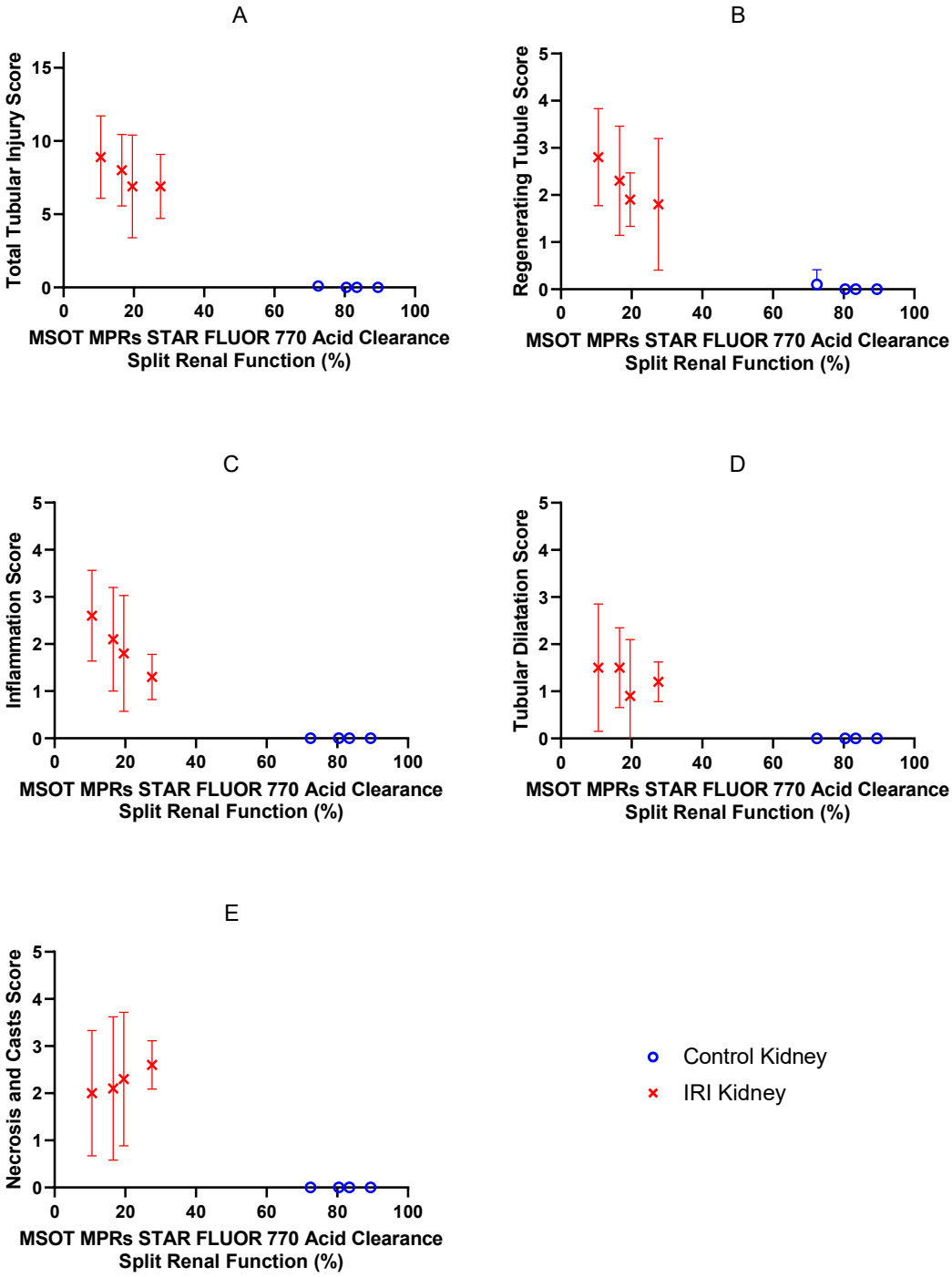

Figure 5.17: Day 1 post IRI DCE MSOT STAR FLUOR 770 Acid Split Renal Function versus Histological Tubular Injury Scores

The MSOT clearance of STAR FLUOR 770 Acid using the MPRs model as split renal function versus A. Total tubular injury score. B. Tubular regeneration score. C. Inflammation score. D. Tubular dilatation score. E. Necrosis and casts score. Error bars are the standard deviation. IRI (Ischaemia reperfusion injury), MPRs (Modified Patlak-Rutland method with spinal blood vessel AIF).

DCE MSOT MPRs ABZWCY-HPβCD GFR day 1 post IRI was also associated with an increase in tubular injury scores in the IRI kidney (Figure 5.18). While the histological injury was not

higher, the ABZWCY-HPβCD GFR was lower than the STAR FLUOR 770 Acid clearance rate in both in the IRI and control kidneys. Split renal function calculated by MSOT MPRs ABZWCY-HPβCD GFR shows a more dramatic difference between the two kidneys than is seen with STAR FLUOR 770 Acid (Figure 5.19).

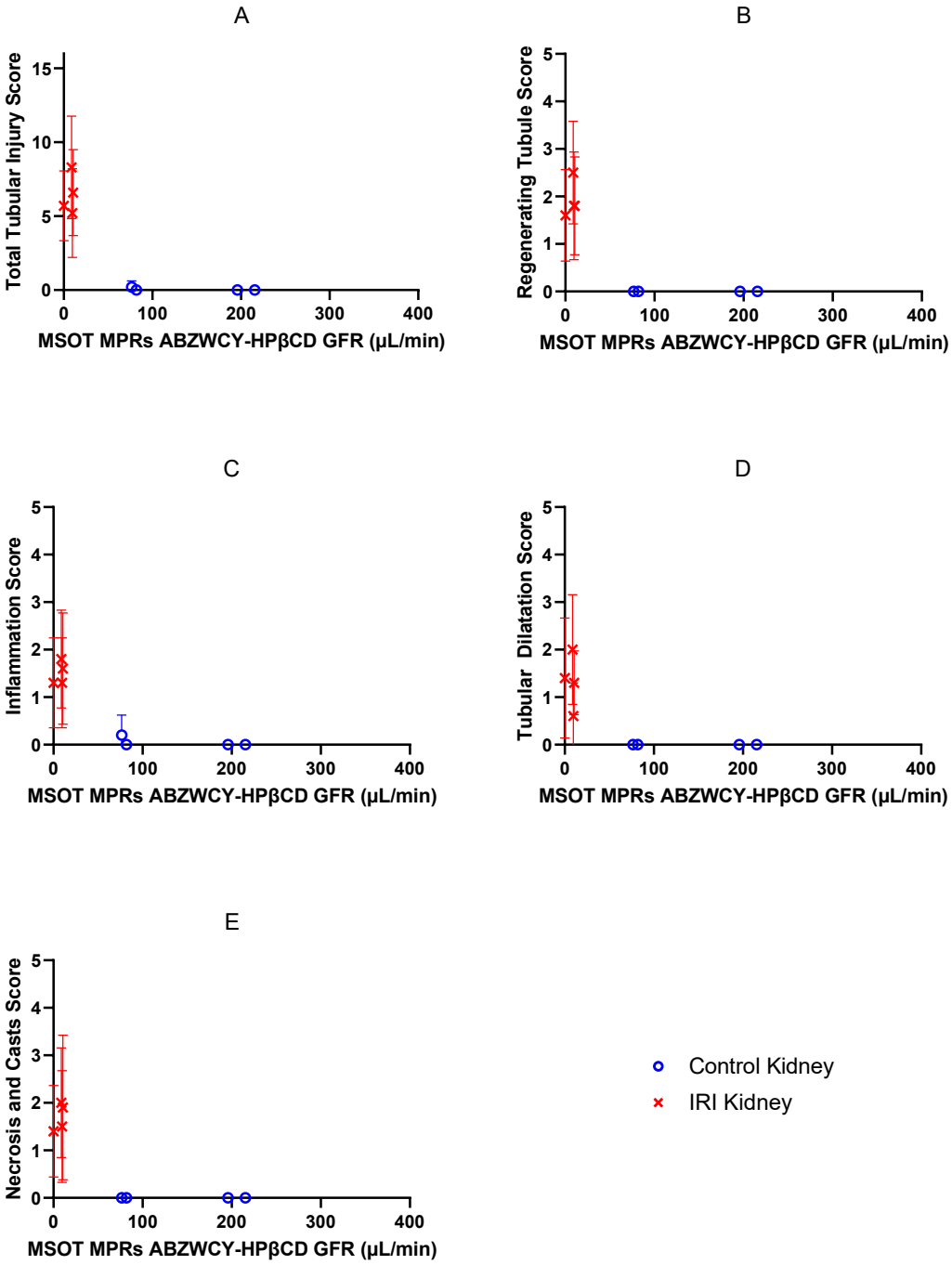

Figure 5.18: Day 1 post IRI DCE MSOT ABZWCY-HPβCD GFR versus Histological Tubular Injury Scores
The MSOT GFR of ABZWCY-HPβCD using the MPRs model versus A. Total tubular injury score. B. Tubular regeneration score. C. Inflammation score. D. Tubular dilatation score. E. Necrosis and casts score. Error bars are the standard deviation. IRI (Ischaemia reperfusion injury), MPRs (Modified Patlak-Rutland method with spinal blood vessel AIF).

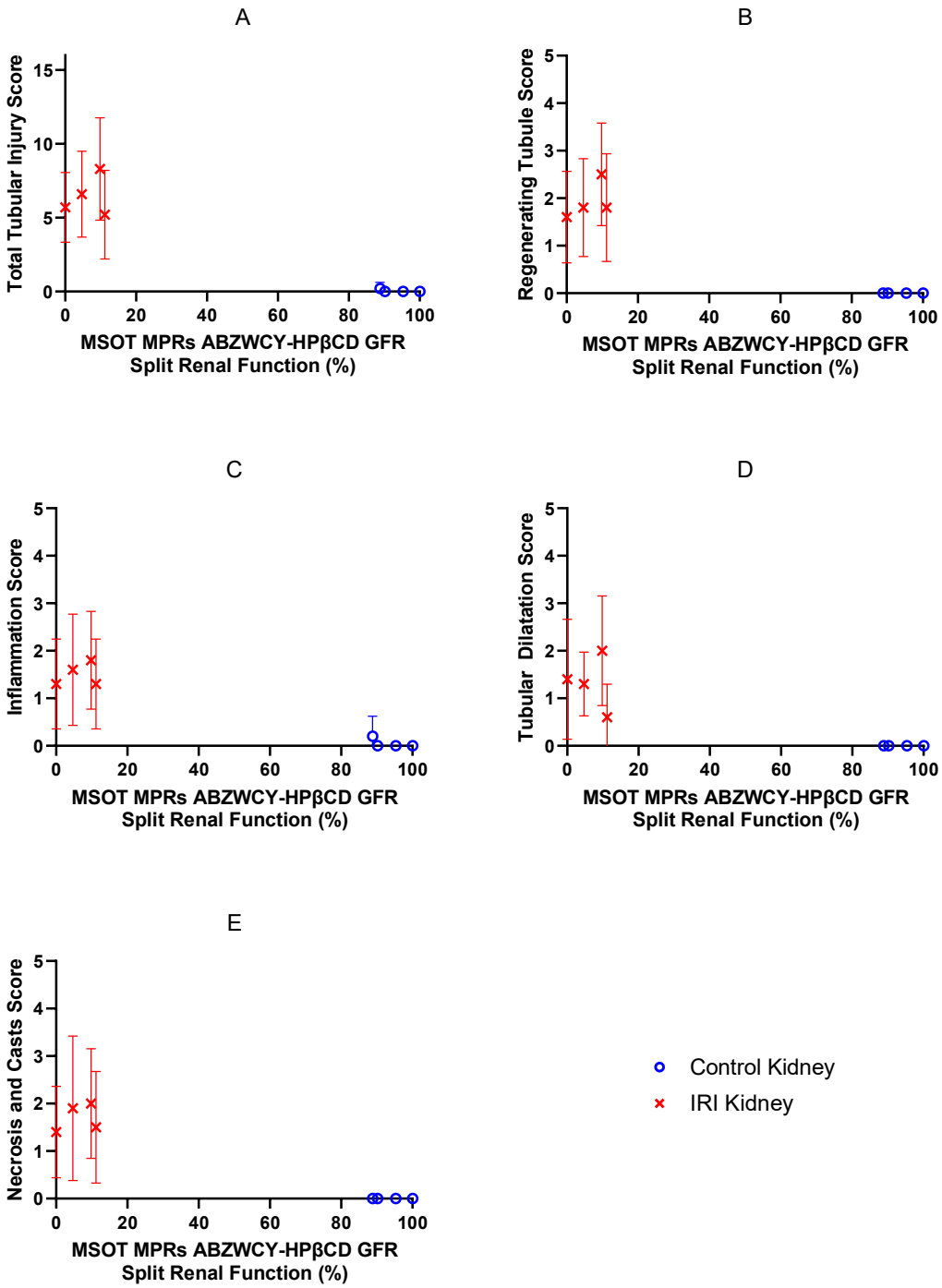

Figure 5.19: Day 1 post IRI DCE MSOT ABZWCY-HPβCD Split Renal Function versus Histological Tubular Injury Scores

The MSOT clearance of ABZWCY-HPβCD using the MPRs model as split renal function versus A. Total tubular injury score. B. Tubular regeneration score. C. Inflammation score. D. Tubular dilatation score. E. Necrosis and casts score. Error bars are the standard deviation. IRI (Ischaemia reperfusion injury), MPRs (Modified Patlak-Rutland method with spinal blood vessel AIF).

Split renal function measured by SPECT DMSA on day 1 shows a less dramatic difference between the injured and control kidney compared to MSOT with both ABZWCY-HPβCD and

STAR FLUOR 770 Acid (Figure 5.20). However, there remains an association between DMSA uptake and all four histology scores and the total tubular injury score.

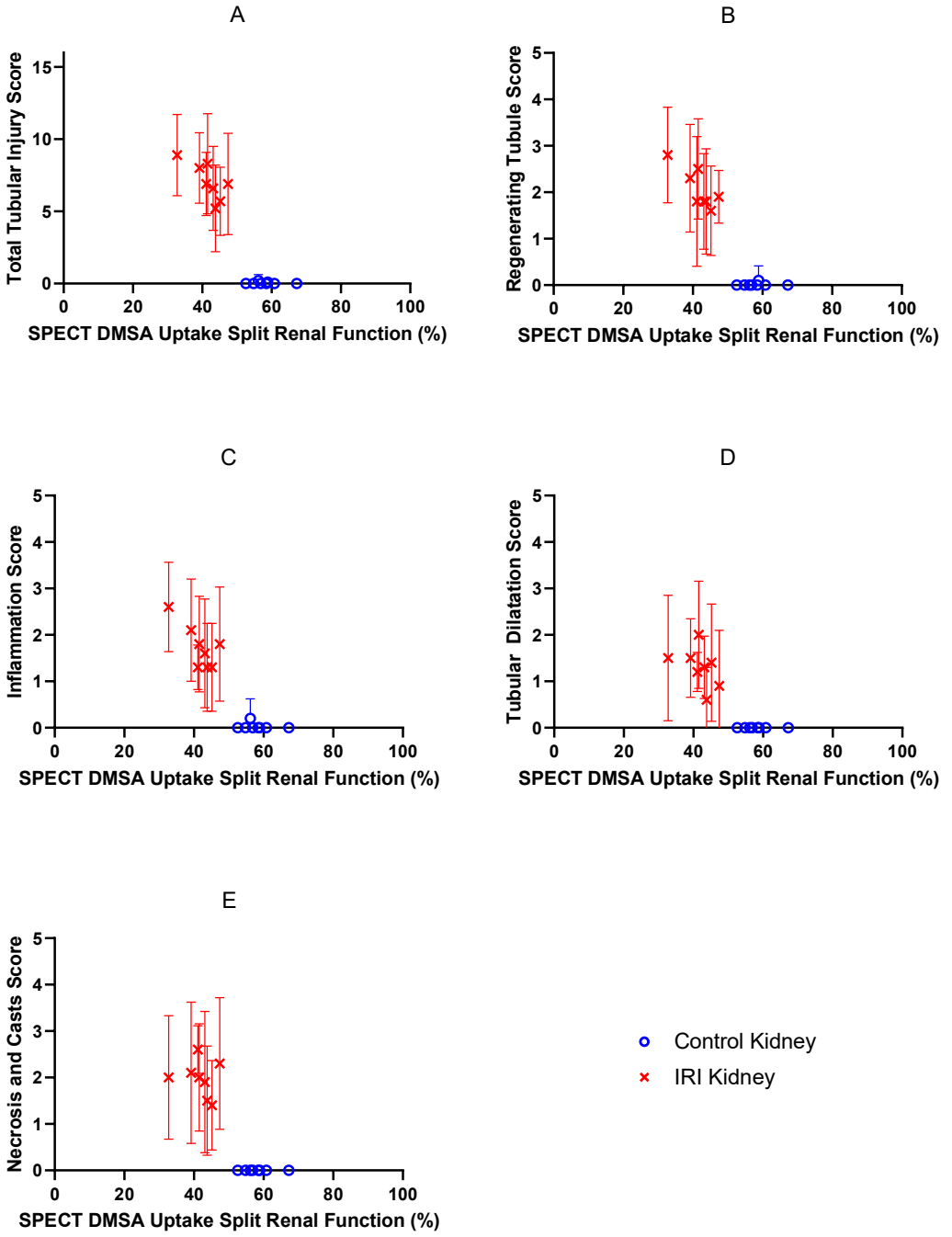

Figure 5.20: Day 1 post IRI SPECT DMSA Uptake Split Renal Function versus Histological Tubular Injury Scores The uptake of DMSA measured via SPECT versus A. Total tubular injury score. B. Tubular regeneration score. C. Inflammation score. D. Tubular dilatation score. E. Necrosis and casts score. Error bars are the standard deviation. IRI (Ischaemia reperfusion injury), MPRs (Modified Patlak-Rutland method with spinal blood vessel AIF), SPECT (Single-photon emission computed tomography).

5.2.3.3 Tubular Injury Score Compared with Day 22 Imaging

Unlike day 1, renal function measured with MSOT on day 22 shows a poor association with tubular injury scores. STAR FLUOR 770 Acid clearance (Figure 5.21), STAR FLUOR 770 Acid split renal function (Figure 5.22), ABZWCY-HPβCD GFR (Figure 5.23), and ABZWCY-HPβCD split renal function (Figure 5.24) all show a functional recovery in the IRI kidney despite evidence of tubular injury by histological scoring. In contrast, SPECT DMSA uptake split renal function on day 22 shows a more defined association with all histological injury scores (Figure 5.25).

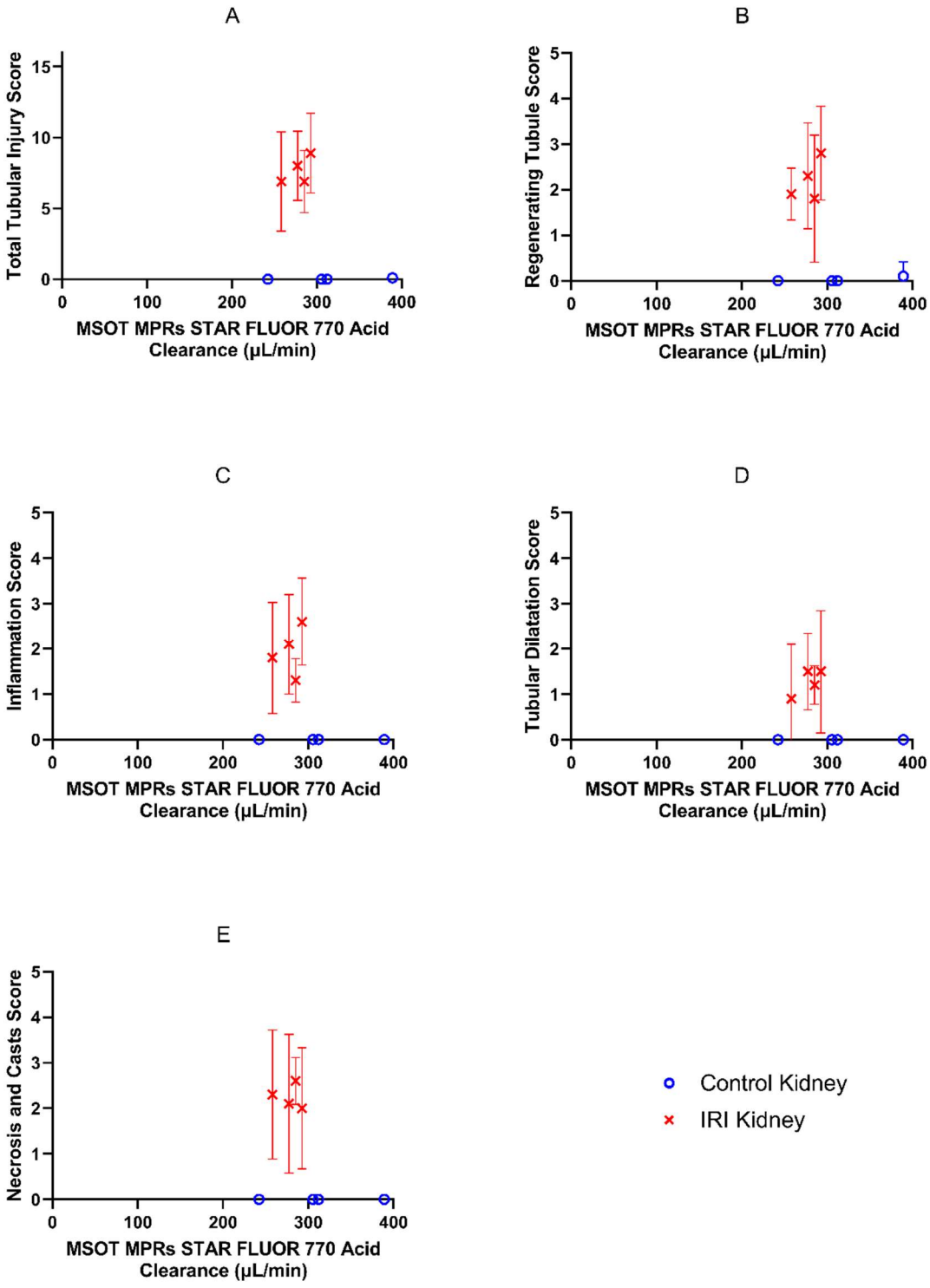

Figure 5.21: Day 22 post IRI DCE MSOT STAR FLUOR 770 Acid Clearance versus Histological Tubular Injury Scores

The MSOT clearance of STAR FLUOR 770 Acid using the MPRs model versus A. Total tubular injury score. B. Tubular regeneration score. C. Inflammation score. D. Tubular dilatation score. E. Necrosis and casts score. Error bars are the standard deviation. IRI (Ischaemia reperfusion injury), MPRs (Modified Patlak-Rutland method with spinal blood vessel AIF).

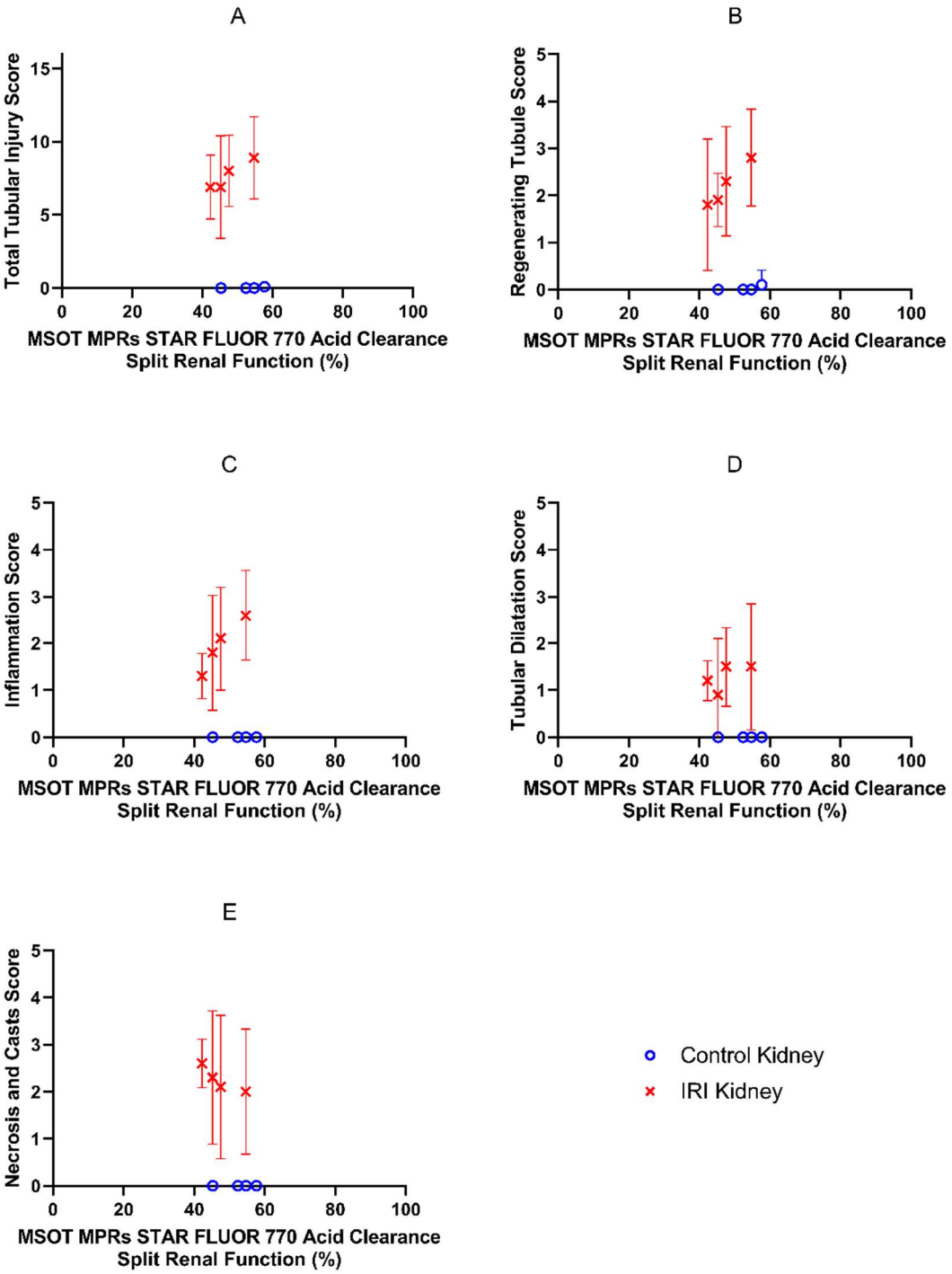

Figure 5.22: Day 22 post IRI DCE MSOT STAR FLUOR 770 Acid Split Renal Function versus Histological Tubular Injury Scores

The MSOT clearance of STAR FLUOR 770 Acid using the MPRs model as split renal function versus A. Total tubular injury score. B. Tubular regeneration score. C. Inflammation score. D. Tubular dilatation score. E. Necrosis and casts score. Error bars are the standard deviation. IRI (Ischaemia reperfusion injury), MPRs (Modified Patlak-Rutland method with spinal blood vessel AIF).

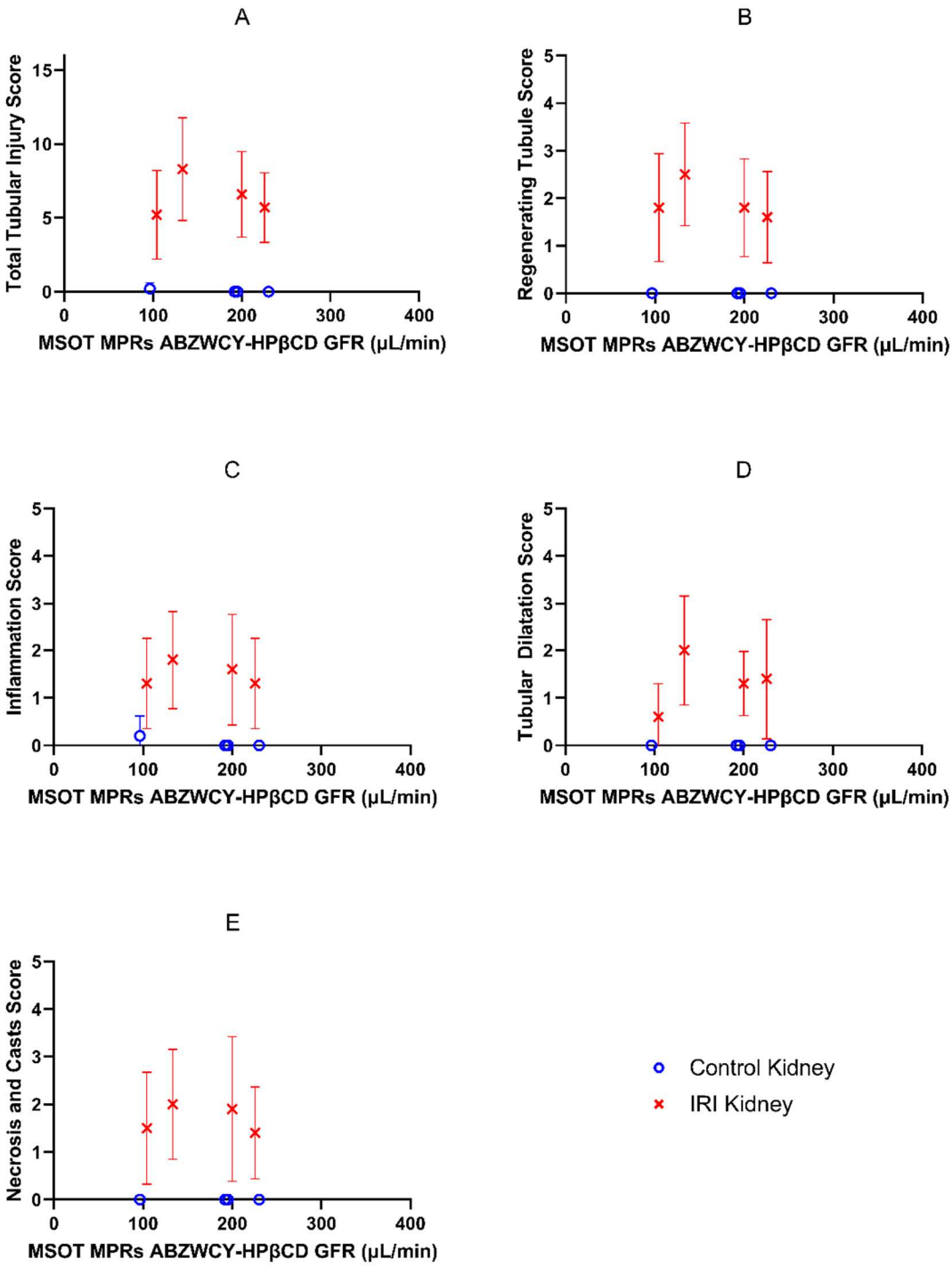

Figure 5.23: Day 22 post IRI DCE MSOT ABZWCY-HPβCD GFR versus Histological Tubular Injury Scores
The MSOT GFR of ABZWCY-HPβCD using the MPRs model versus A. Total tubular injury score. B. Tubular regeneration score. C. Inflammation score. D. Tubular dilatation score. E. Necrosis and casts score. Error bars are the standard deviation. IRI (Ischaemia reperfusion injury), MPRs (Modified Patlak-Rutland method with spinal blood vessel AIF).

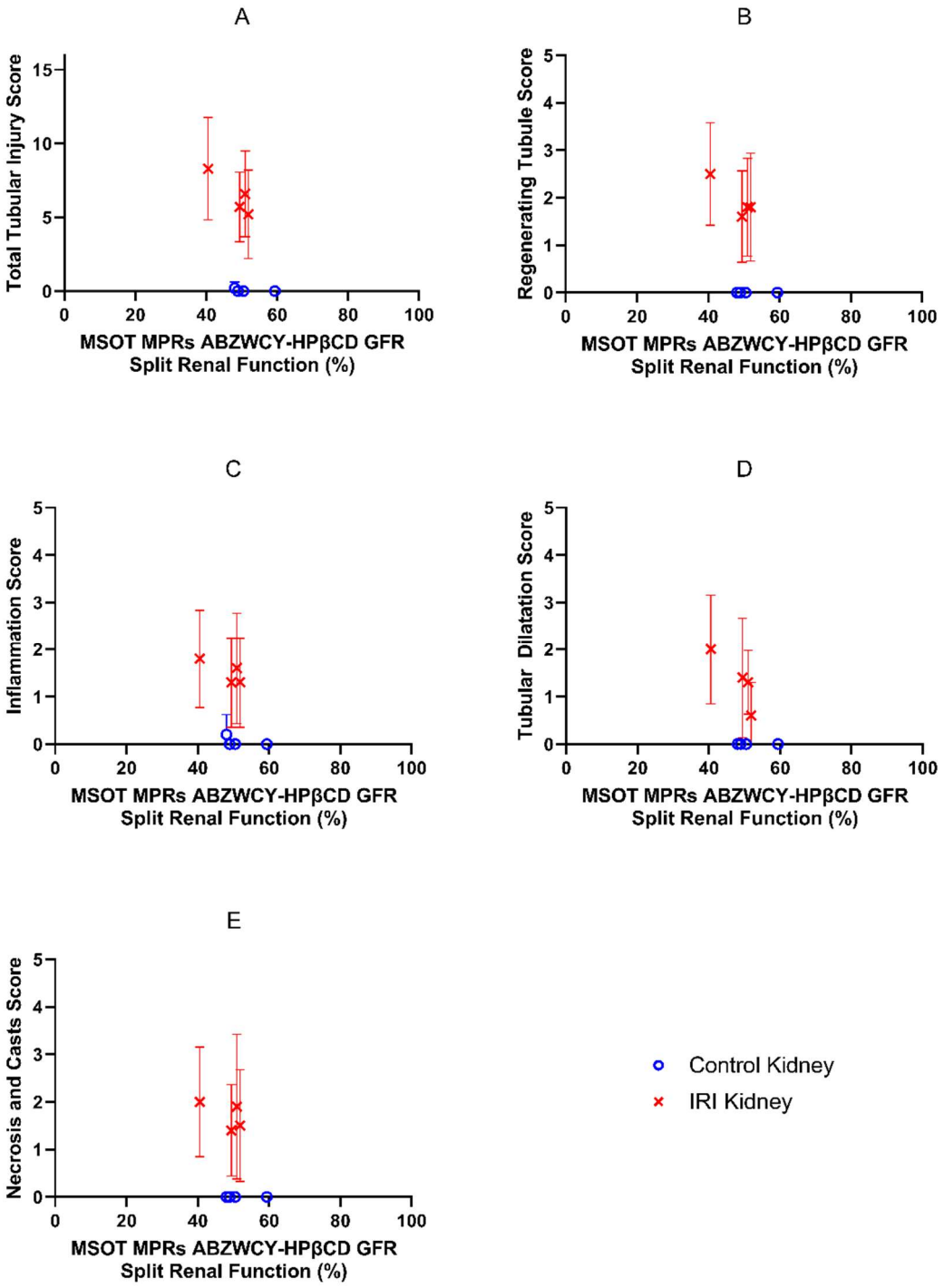

Figure 5.24: Day 22 post IRI DCE MSOT ABZWCY-HPβCD Split Renal Function versus Histological Tubular Injury Scores

The MSOT clearance of ABZWCY-HPβCD using the MPRs model as split renal function versus A. Total tubular injury score. B. Tubular regeneration score. C. Inflammation score. D. Tubular dilatation score. E. Necrosis and casts score. Error bars are the standard deviation. IRI (Ischaemia reperfusion injury), MPRs (Modified Patlak-Rutland method with spinal blood vessel AIF).

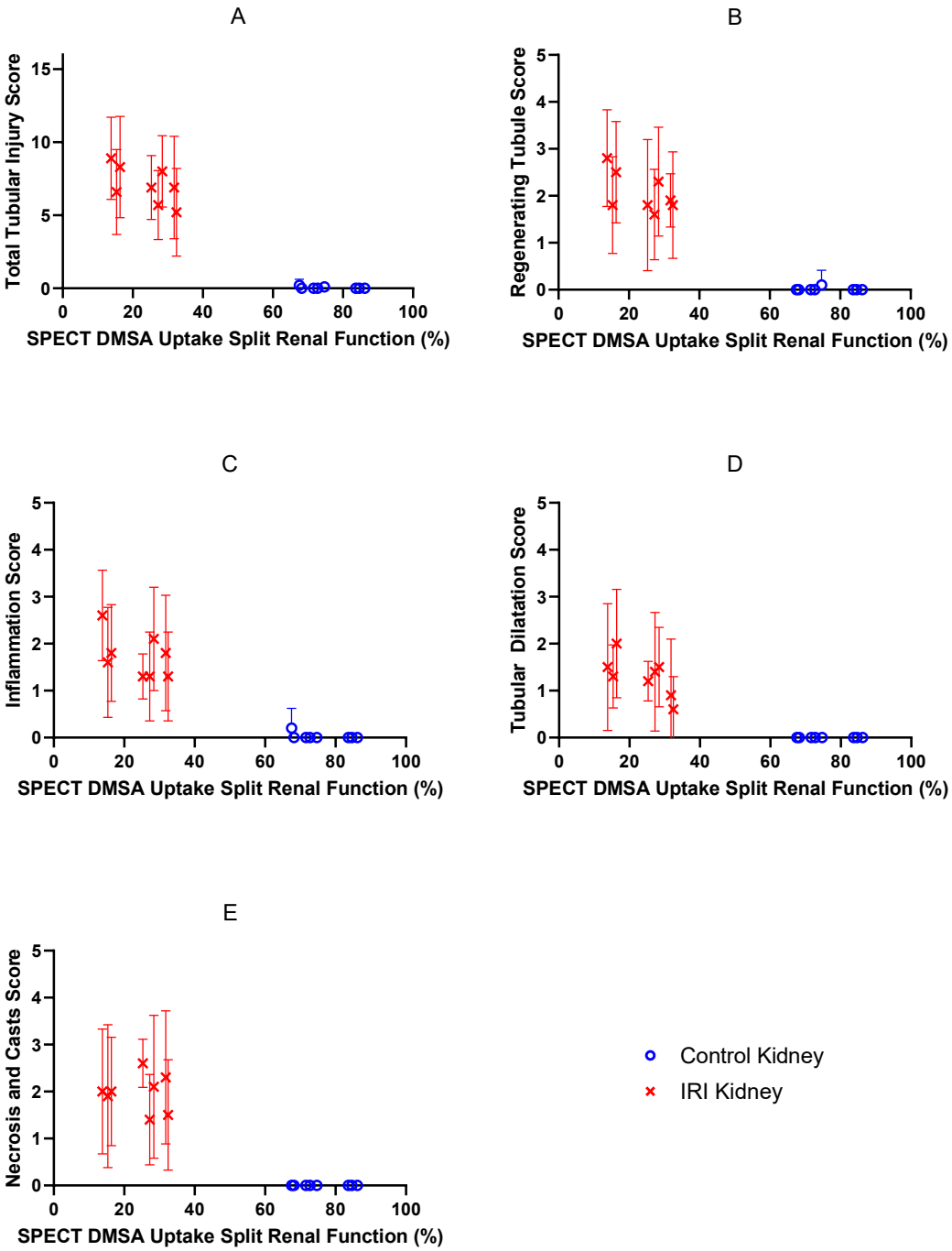

Figure 5.25: Day 22 post IRI SPECT DMSA Uptake Split Renal Function versus Histological Tubular Injury Scores
The uptake of DMSA measured via SPECT versus A. Total tubular injury score. B. Tubular regeneration score. C. Inflammation score. D. Tubular dilatation score. E. Necrosis and casts score. Error bars are the standard deviation. IRI (Ischaemia reperfusion injury), MPRs (Modified Patlak-Rutland method with spinal blood vessel AIF), SPECT (Single-photon emission computed tomography).

5.2.3.4 Fibroblast Deposition

Rows of fibroblasts and the number of fibroblast clusters were counted across five fields of view chosen at random. The mean number of fibroblast rows per cluster was calculated and

compared to SPECT DMSA split renal function, DCE MSOT MPRs STAR FLUOR 770 Acid clearance, and DCE MSOT MPRs ABZWCY-HPβCD GFR. Comparison was made with imaging derived renal functions at day 1 and 22 post IRI.

All imaging techniques showed some inverse association with the degree of fibroblast deposition (Figure 5.26).

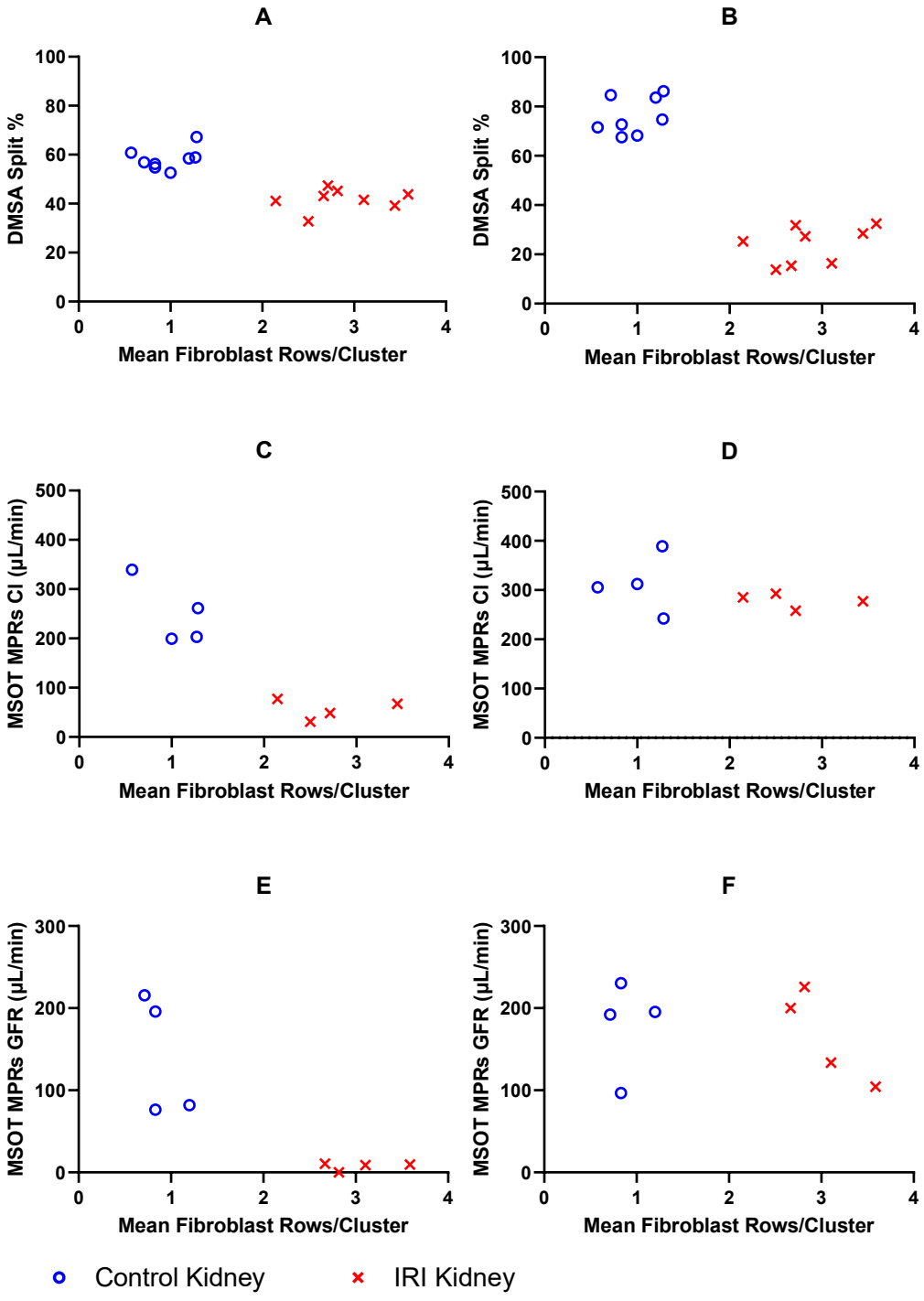

Figure 5.26: Comparing Image Derived Renal Function and Fibroblast Deposition.
A. Day 1 post IRI SPECT DMSA split renal function versus fibroblast deposition. B. Day 22 post IRI SPECT DMSA split renal function versus fibroblast deposition. C. Day 1 post IRI DCE MSOT STAR FLUOR 770 Acid clearance versus fibroblast deposition. D. Day 22 post IRI DCE MSOT STAR FLUOR 770 Acid clearance versus fibroblast deposition. E. Day 1 post IRI DCE MSOT ABZWCY-HPβCD GFR versus fibroblast deposition. F. Day 22 post IRI DCE MSOT ABZWCY-HPβCD GFR versus fibroblast deposition. Cl (Clearance), GFR (Glomerular Filtration Rate), MPRs (Modified Patlak-Rutland method with spinal blood vessel AIF).

5.3 Discussion

This chapter assessed the suitability of STAR FLUOR 770 Acid as a tubular secretion marker and DCE MSOT to measure tubular injury and split renal function via the clearance of STAR FLUOR 770 Acid in severe unilateral IRI.

5.3.1 Renal Excretion of STAR FLUOR 770 Acid is Impaired by Probenecid

Probenecid is an anionic, water insoluble drug and inhibitor of OAT1 and 3[284,285]. It has an inhibition constant between 4.41 and 12.1 µM for OAT1 and 4.41 and 29.8 µM for OAT3[286]. It was originally developed to assist in the retention of penicillin (that was in limited supply) by reducing its renal clearance meaning that lower doses could be used to achieve the same clinical effect[287]. Probenecid is itself a substrate of OATs and inhibition has previously been reported as competitive[285,288–293]. However, probenecid has also been shown in higher concentrations to impair mitochondrial production of ATP[294]. PTCs are dependent on ATP to perform tubular secretion either directly or indirectly[55]. ATP in PTCs powers Na^+K^+ATPase that provides the sodium gradient required for the functioning of OAT1 and 3 at the basolateral surface[55,71,73]. ATP also directly powers apical tubular secretion via ABCB1, ABCC4, and ABCG2[55,71,73]. Probenecid has been shown to inhibit secretion of cations[295,296] which may be explained by impaired mitochondrial ATP production rather than competitive inhibition[294].

We hypothesised that STAR FLUOR 770 Acid is handled by the PTC OAT proteins because it is negatively charged and partially protein bound. Both the protein binding and charged nature make renal clearance via filtration less likely[71]. Here we have shown that high doses of probenecid impair the renal clearance of STAR FLUOR 770 Acid but not ABZWCY-HPβCD. Given ABZWCY-HPβCD has already shown favourable characteristics as a GFR marker, it does not appear that high doses of probenecid are impairing glomerular filtration in these mice. It is probable that the PTCs play a role in the urinary clearance of STAR FLUOR 770 Acid due to the impaired delivery to the renal pelvis and abnormal cortex time activity curves seen when administered with high dose probenecid.

The mechanism underlying this may be via competitive inhibition of OATs or impaired overall tubular function due to reduced mitochondrial production of ATP. In humans, Maeda et al showed 1500 mg of oral probenecid completely inhibits the tubular secretion of benzylpenicillin, while 750 mg completely inhibits adefovir[297]. These provided a weight based dose of <30 mg/kg and <15 mg/kg, respectively. This is far lower than either dose applied in our studies. As low dose probenecid does not impair the renal clearance of STAR FLUOR 770

Acid and such a dose is large enough to impair the OAT transport of other substrates, it seems more probable that an overall tubular impairment by reduced production of ATP is the mechanism. An alternative explanation could be that STAR FLUOR 770 Acid has a far higher affinity for OATs that requires a larger dose of probenecid to be overcome. Further experiments looking at the relative affinity and inhibition constants of probenecid and STAR FLUOR 770 Acid in models of PTCs would clarify this.

While 150 mg/kg probenecid is a large dose, it has been used at this level for the purposes of blocking tubular secretion in rodent studies[298–303]. Interestingly, where it has been examined in models of PTC injury (paracetamol and aristolochic acid nephropathy), 150 mg/kg probenecid and higher is reported to protect against tubular histological damage and renal impairment (elevated serum creatinine and urea)[300,302,304]. Here it has been shown that 150 mg/kg probenecid did not alter the MSOT renal time activity curves of ABZWCY-HPβCD. This suggests that GFR was not impaired, and that renal perfusion was likely maintained within the bounds of autoregulation. As such the impaired renal excretion of STAR FLUOR 770 Acid with this dose appears attributable to impaired tubular secretion rather than an alternative effect of the probenecid.

Probenecid has been shown to impair the clearance of some anionic drugs by impairing their hepatic metabolism[305,306]. However, if this were the mechanism impairing the clearance of STAR FLUOR 770 Acid we would expect the blood concentration of the dye to be higher for longer resulting in an increased availability for the secretion of the dye into the urine. This would result in a more rapid increase in the pelvis MSOT signal with probenecid which was not observed.

5.3.2 STAR FLUOR 770 Acid Clearance Rate is Faster than Glomerular Filtration Rate in Healthy Mice

The average plasma clearance rate of STAR FLUOR 770 Acid in healthy mice measured by the MSOT MPRs model was 525.3 µL/min (464.4 to 578.9 µL/min). This was significantly more rapid than what was seen with ABZWCY-HPβCD (average 305.2 µL/min; range 279.7 to 488.0 µL/min) and what is seen by measuring GFR using FITC-inulin clearance in mice[69]. This more rapid clearance rate is consistent with markers of tubular secretion or markers that undergo both glomerular filtration and tubular secretion[71]. STAR FLUOR 770 Acid may potentially undergo both glomerular filtration and tubular secretion or just tubular secretion alone.

Para-aminohippuric acid (PAH) is an organic anion that is cleared by both tubular secretion and filtration and used to measure renal plasma flow[307]. The clearance of this marker

significantly outpaces GFR[140]. Tc-99m MAG3 also shows a higher clearance rate than GFR while being cleared by tubular secretion[147]. A number of candidate endogenous tubular secretion markers have been shown in humans to undergo more rapid clearance than GFR markers without significant correlation with renal plasma flow[140]. The variation in rates of clearance of these markers may relate to their affinity for the range of different receptors on the basolateral and apical PTCs, and the degree of marker protein binding.

5.3.3 SPECT DMSA Split Renal Function is Significantly Different from MSOT STAR FLUOR 770 Acid Split Renal Function

As SPECT DMSA is an adynamic functional imaging technique, it is not the ideal candidate for direct comparison with DCE MSOT using STAR FLUOR 770 Acid. This is because we cannot apply the same quantification models to the two techniques. However, SPECT DMSA has been shown to represent structural injury of the tubular tissues and a good approximation of split renal function[145,146,283,308]. Additional work comparing DCE MSOT STAR FLUOR 770 Acid to DCE SPECT MAG3 clearance would be of benefit to potentially allow the same clearance quantification models to be applied to each imaging technique for a fairer assessment.

We failed to identify a correlation between split renal function measured by SPECT DMSA and MSOT STAR FLUOR 770 Acid clearance using either the MPRs model or AUC C:P ratio. STAR FLUOR 770 Acid clearance showed progressive recovery to baseline after IRI. In contrast, SPECT DMSA uptake showed progressive decline. Impaired STAR FLUOR 770 Acid clearance appears to be associated with acute injury whereas impaired SPECT DMSA uptake appears to be associated with chronic injury.

This could be explained by a difference in the transcellular proteins responsible for the renal kinetics of these two markers. DMSA is taken up by the PTCs both on the apical and basolateral surface[141–143]. The basolateral uptake of DMSA is believed to be via OAT3 and the sodium-dependent dicarboxylate transporter (NaDC3)[144,309]. The apical uptake of DMSA via megalin/cubilin facilitated endocytosis appears particularly significant in mice with a knockout model showing a 90% reduction in DMSA uptake[143]. The uptake and secretion of STAR FLUOR 770 Acid by the PTCs is unknown. However, several potential routes may be implicated in the PTC uptake (OAT1, OAT2, OATP4C1) and secretion (ABCB1, OAT4, OAT10, ABCG2, ABCC4) of STAR FLUOR 770 Acid[73]. Given its rapid clearance rate, it seems likely that the urinary excretion of STAR FLUOR 770 Acid may be via multiple transcellular transporter proteins.

A review by Fauncher et al highlights the fact that the expression of transmembrane transporter protein expression varies following IRI[310]. At the basolateral surface, OAT1 and 3 mRNA and protein expression decrease as early as 6 hours following IRI and completely recover by 72 hours[311–313]. Interestingly, Zhang et al found evidence of upregulation of OAT1 and 3 following IRI[314]. Also, protein expression of Na^+K^+ATPase is significantly reduced following IRI[311,314,315]. Na^+K^+ATPase is important for maintaining the sodium gradient that facilitates αKG transport that is in turn exchanged for organic anions by OATs. At the apical surface of PTCs, ABCB1 and ABCC4 expression is increased following IRI, while ABCG2 is decreased[311,316]. If the protein handling of STAR FLUOR 770 Acid differs significantly from DMSA we can expect the split renal function to be different between the two techniques.

Additionally, both of our quantification methods for DCE MSOT feature the renal pelvis, while quantification of SPECT DMSA is limited to the cortex. This is significant as downstream transit of the filtrate through the renal tubules and collecting ducts may be impaired to different degrees following IRI. A potential cause of this could be sloughing of tubular epithelial cells and cast formation following injury that can lead to intratubular obstruction[2]. It is possible that impaired delivery of STAR FLUOR 770 Acid to the pelvis following IRI may be partly due to decreased filtrate flow rather than a decrease in active tubular secretion.

5.3.4 MSOT STAR FLUOR 770 Acid Clearance Recovers Despite Evidence of Persistent Histological Tubular Injury

Due to the tubules' dependence on aerobic respiration, the tubulointerstitium is the characteristic site of impact following IRI[317]. The features of IRI in the tubulointerstitium include the loss of the brush border, thickened basal membrane, inflammation, cast formation, necrosis, and haemorrhage[318].

Proliferation and activation of fibroblasts is a key step in the pathophysiology of CKD[319]. As well as producing the interstitial matrix components that facilitate collagen deposition, fibroblasts release chemokines that attract macrophages with the potential to exacerbate fibrosis[320,321]. Tubulointerstitial fibrosis brings about tissue destruction and loss of renal function[322]. Activated fibroblasts can persist beyond the initial insult leading to ongoing damage[322,323].

Here it was found that unilateral severe IRI surgery induced an increased number of fibroblasts compared with the control kidney. Split SPECT DMSA uptake showed an association with this both immediately following injury and 3 weeks later. This was far more pronounced at day 22. However, this comes with the caveat that each kidney is expressed as

its contribution to the total function rather than an absolute measure. As such, any reduction in the function of the injured kidney will produce an increase in the healthy kidney's percentage contribution even if the absolute contribution of that kidney is unchanged. This is a potential limitation of using SPECT to measure renal function. Producing an absolute measurement by SPECT Tc-99m DMSA that can be monitored chronically is more challenging[324]. First, the Molybdenum-99 generator from which Tc-99m is eluted decays over time and reduced radioactivity per volume occurs[215]. Due to the intravenous volume injection limitations for the wellbeing of animals this can lead to underdosing. Second, the loss of radioactivity to the needle, cannula, and syringe can also result in a variable dose being delivered. Nuclear medicine can be impacted by technical issues that impair absolute uptake measurements e.g., scatter[325]. However, this might be considered in the same category as fluence is for MSOT. Finally, Durand et al show that the absence of measuring an AIF in standard DMSA imaging can result in an overestimation of the function of the contralateral control kidney in a unilateral injury model where absolute measurements are used[325]. The overall reduction in uptake results in an increased blood concentration overtime facilitating greater uptake in the uninjured kidney.

DCE MSOT MPRs does not have this issue and an absolute measurement can be tracked over multiple imaging sessions. Impaired STAR FLUOR 770 Acid clearance showed an association with elevated tubular injury scores and with fibroblast deposition day 1 post IRI. Further work to measure different degrees of injury and impaired clearance rates against the degree of fibroblast deposition would be of value to assess whether there is a correlation between early reduced STAR FLUOR 770 Acid clearance and fibrosis.

However, neither STAR FLUOR 770 Acid clearance nor ABZWCY-HPβCD GFR measured by MSOT on day 22 show association with fibroblast deposition. The association with tubular injury scores is also lost. The renal excretion of both markers had significantly recovered towards the end of the 3 weeks. Following IRI, OAT expression can normalise by day 3[312], Na^+K^+ATPase expression can normalise by day 6[314], and the expression of ABC transporters can normalise by day 14[316]. Given the potential for transmembrane protein expression to have been restored, secretion of markers by these proteins may also normalise despite ongoing histological evidence of injury. Additionally, the upregulation of ABC transporters may deliver compensatory mechanisms to maintain homeostasis that potentially result in the maintained clearance of STAR FLUOR 770 Acid[310,326].

Finally, it is important to note that there is no evidence of tubular injury in the control kidney following multiple administration of ABZWCY-HPβCD or STAR FLUOR 770 Acid. Neither dye appears to be toxic to tubular cells or the kidney with chronic use in mice. Additionally, glomerular injury by these dyes appears unlikely given the maintained MSOT MPRs GFR in the control kidney at the end of the experiment.

5.4 Conclusion

STAR FLUOR 770 Acid appears to be partially secreted by the PTCs. This is evidenced by its impaired clearance in the presence of probenecid and its clearance rate being more rapid than GFR. It is uncertain which OATs or ABC transporters are involved. Further work to examine which transporters facilitate the renal excretion of these markers is desirable.

DCE MSOT MPRs clearance of STAR FLUOR 770 Acid and ABZWCY-HPβCD differs significantly from SPECT DMSA uptake imaging. This may relate to the greater specificity of DMSA for tubular injury or a difference in the group of transmembrane proteins handling each marker. DCE MSOT MPRs clearance of STAR FLUOR 770 Acid day 1 post IRI is associated with histological signs of tubular injury and fibroblast deposition at day 22 following injury.

6 Discussion

This work aimed to use dynamic contrast enhanced (DCE) multispectral optoacoustic tomography (MSOT) to assess the excretory functions of the mouse kidney. The near-infrared (NIR) dyes ABZWCY-HPβCD and STAR FLUOR 770 Acid were used in an attempt to quantify glomerular filtration rate (GFR) and tubular secretion rate (TSR) in MSOT. Different model-free and pharmacokinetic models were examined for their suitability in this purpose.

6.1 ABZWCY-HPβCD Shows Significantly Different Clearance than IRDye 800CW in MSOT

ABZWCY-HPβCD has not previously been measured by MSOT. We have demonstrated the ability of MSOT to detect this dye both in phantoms and mice. Our experiments have shown ABZWCY-HPβCD clears slower from the renal cortex than IRDye 800CW in MSOT with a higher peak concentration (Figure 3.5). We have also found evidence of more rapid photodegradation of IRDye 800CW under normal MSOT animal imaging conditions (Figure 3.4). IRDye 800CW has previously been shown to have a plasma protein binding of 41%[157]. IRDye 800CW is also cleared by the biliary system[224,225]. The different cortex kinetics in MSOT, high protein binding, and biliary clearance of IRDye 800CW provide evidence that it is less specific for renal function than ABZWCY-HPβCD and that it is an unsuitable GFR marker.

IRDye 800CW has been used multiple times to assess renal function in DCE MSOT[155,157,207,210,219–223]. There is good evidence that this dye is at least partially cleared by the kidneys[210,211] and its measurement by model-free parameters has been correlated with renal injury[155,157,207,212]. However, the greater specificity of ABZWCY-HPβCD for renal clearance has the potential the improve the accuracy of DCE MSOT for measuring renal excretory function. ABZWCY-HPβCD is a suitable GFR marker due to lack of biliary clearance (Figure 3.8) as well as the previously described low protein binding, lack of tubular secretion, and high levels of urinary recovery[102]. Our finding of a slower cortex clearance of ABZWCY-HPβCD compared with IRDye 800CW supports ABZWCY-HPβCD as a pure GFR marker. As IRDye 800CW undergoes additional clearance routes we expect its clearance to be faster.

Our comparison of IRDye 800CW and ABZWCY-HPβCD was limited to healthy mice. A direct comparison of the two dyes and their MSOT clearance kinetics in different injury models could be considered. This might identify whether there is greater correlation with renal injury when using one of the two dyes. A comparison between IRDye 800CW and STAR FLUOR 770 Acid may also be of interest given the similar levels of protein binding and evidence of biliary clearance.

6.2 DCE MSOT Can Quantify Renal Excretory Function via NIR Dyes Despite its Semiquantitative Nature

It has been shown that DCE MSOT using ABZWCY-HPβCD and a modified Patlak-Rutland model (MPRs) using a spinal blood vessel as the arterial input function (AIF) correlates well with GFR calculated using FITC-sinistrin and a transcutaneous device (Figure 4.13). We have also demonstrated that this method in combination with STAR FLUOR 770 Acid produces a more rapid clearance rate than is seen with ABZWCY-HPβCD (Figure 5.5 and Figure 5.6) which is expected of a dye that has additional clearance routes (biliary, tubular secretion). This provides preclinical researchers with the opportunity to measure single kidney GFR and, potentially, TSR at a simultaneously high spatial and temporal resolution without ionising radiation. This facilitates greater understanding of injury and recovery in unilateral injury models via an internal control kidney.

MSOT and other forms of photoacoustic imaging are semiquantitative techniques if corrections for the local distribution of light energy (fluence) are not applied[173,175,194]. We have shown evidence of the impact of fluence in DCE MSOT using ABZWCY-HPβCD particularly affecting the aorta (Figure 4.6). This deep region of interest (ROI) appears to suffer impaired light delivery as ABZWCY-HPβCD accumulates in the periphery of the mouse as evidenced by post-injection photoacoustic signal dropping below pre-injection levels. It is theoretically possible that the presence of ABZWCY-HPβCD somehow impairs the 700 nm light absorbance by or alters the acoustic quantum yield of other native absorbers in the blood. Additional work looking for any change in the optical and photoacoustic spectral properties of ABZWCY-HPβCD in the presence of blood may help to remove this as a possibility.

Jiang et al did not report any issue with the aorta as the AIF using their renally cleared gold nanoparticles to measure single kidney GFR in DCE MSOT via a standard Patlak-Rutland (PR) model[183]. They do not report any attempt to perform fluence correction and describe using the linear relationship between concentration and photoacoustic signal in phantoms to calculate nanoparticle concentration from MSOT imaging. The lack of fluence impact may be due to the different natures of the contrast agents. ABZWCY-HPβCD may show greater peripheral accumulation increasing its chances of impairing light delivery to the deep tissues. It may also show lower photoacoustic signal generation at lower concentrations than the gold nanoparticles and so is less detectable at this depth of imaging.

Certainly, the aorta is an unreliable AIF for a standard PR model in the DCE MSOT protocol described here. This might be addressed in a number of ways. Fluence correction methods including models of radiative transfer[194,195] and experimental quantification of fluence[197,198] could be used to turn MSOT into a fully quantitative imaging system. Unfortunately, fluence models need further development and validation. Experimental methods of fluence correction are limited by acquisition speed and depth which would neither meet the temporal resolution requirements of DCE MSOT nor reach the aorta. A population-based AIF or tissue reference AIF could be developed for ABZWCY-HPβCD in DCE MSOT to estimate the aorta concentrations instead of directly measuring them[245,246,327–329]. While fluence-independent models could be used, they would not provide an absolute measure of GFR and would not be any better suited to addressing the negative signal seen in the aorta ROI[196]. Another option is to use an AIF free model. However, our examination of the Baumann-Rudin (BR) model did not reveal a convincing correlation (Figure 4.5).

A limitation of the MPRs model is the uncertainty that the ROI selected for the spinal blood vessel is a blood vessel. Due to the size of the mice and the imaging resolution achievable by MSOT these regions of interest were only a few pixels. These ROIs may include other tissues such as bone. However, we have evidence that the level of haemoglobin and oxygen saturation in these ROIs are similar to other blood vessels, suggesting that the ROIs selected were likely to be spinal blood vessels (Figure 4.9).

The use of the pelvis in the MPRs model also leads to uncertainty where a surgical ischaemia reperfusion injury (IRI) has been implemented. The native contrast between the pelvis and the kidney is lost. This is most prominent on day 1 post IRI. Also, the anatomy is deranged following IRI meaning that the pelvis of one or both kidneys may be partially in plane or fully out of plane. This may lead to an underestimation of clearance using this method in IRI. However, due to the more rapid transit of NIR dyes through the kidney the uptake phase in the cortex appears too short for PR methods. Further work looking at models using a system of ordinary differential equations that describe tubular outflow of filtrate may accommodate the use of the cortex for estimation of single kidney GFR and TSR.

6.3 Pharmacokinetic Models Offer Benefits Over Model-free Measurements in DCE MSOT

Our results show that single kidney GFR measured by DCE MSOT using ABZWCY-HPβCD and the MPRs model showed significant differences between the control and injured kidney in a unilateral model of IRI, and a similar decrease in a bilateral injury (Figure 4.14). In contrast,

model-free measurements did not show a significant difference between the left and right kidney following a unilateral IRI (Figure 4.16). Of the model-free measurements, only the area under the curve ratio showed a correlation with GFR measured by FITC-sinistrin clearance using a transcutaneous device (Figure 4.17). DCE MSOT ABZWCY-HPβCD MPRs also offers the benefit of calculating a GFR. This is important because GFR is the gold standard measurement of renal health and function and is widely used or estimated in clinical practice. The model-free measures described here are not commonly used in clinical practice.

Model-free measurements are how DCE MSOT using IRDye 800CW is frequently reported and have been correlated with renal disease[155,157,207,219,221]. While our results have suggested these metrics are less consistent than our pharmacokinetic models, it is important to consider the different methodologies used.

First, IRDye 800CW has a more rapid clearance than ABZWCY-HPβCD. This appears to produce a sharper peak particularly in the cortex, but also the pelvis[157,207,219]. These sharper peaks make T^{MAX} and T^{MAX} delay more consistent and more resistant to signal noise. Sharkey et al note that the pelvis peak is lost following acute Adriamycin-induced injury despite using IRDye 800CW[219]. In the current study, it was often found that on day 1 post severe IRI, very low levels and slow accumulation of ABZWCY-HPβCD was observed in the pelvis with the highest levels at the end of the imaging duration. These dynamics impair the use of T^{MAX} Delay.

Second, these reports measured multiple wavelengths: two[155,219,220], five[210,223], six[222], and seven[157,207,221] and used multispectral unmixing algorithms to quantify IRDye 800CW. To facilitate our pharmacokinetic modelling, we measured a single wavelength to maximise our temporal resolution with the aim being a more accurately imaged AIF. Using multiple wavelengths may have increased the specificity for detecting IRDye 800CW, reducing noise and any underlying signal drift. This may improve the accuracy of model-free measurements by producing more reliable peaks for T^{MAX} and T^{MAX} Delay. Underlying signal drifts are unlikely to affect area under the curve ratio or pharmacokinetic models where drift is equal in the multiple measured ROIs.

6.4 STAR FLUOR 770 Acid Requires Further Assessment as a Tubular Secretion Marker

We have successfully measured STAR FLUOR 770 Acid and its renal clearance in DCE MSOT which has not previously been examined. We have shown evidence supporting STAR FLUOR

770 Acid as a tubular secretion marker: its clearance is more rapid than GFR (Figure 5.5 and Figure 5.6) and it is impaired by a high dose of probenecid while ABZWCY-HPβCD clearance is not (Figure 5.1, Figure 5.2, and Figure 5.3). However, its MSOT measured clearance recovers following IRI while DMSA uptake continues to deteriorate (Figure 5.8) and histological features of tubular injury persist (Figure 5.13). It also shows evidence of biliary clearance (Figure 3.8).

The probenecid impaired clearance of STAR FLUOR 770 Acid suggests at least partial handling by the proximal tubular cells (PTCs). This may be due to competitive inhibition of the organic anionic transporter (OAT) proteins on the basolateral surface or impaired mitochondrial ATP production limiting the function of both OATs and ATP-binding cassette (ABC) transporter proteins on the apical surface of the PTCs[284,285,288–291,293,294]. OATs are indirectly reliant on ATP while ABC transporters are directly reliant on ATP. However, renal clearance of STAR FLUOR 770 Acid may not be exclusively via secretion. It seems possible that the unbound portion of STAR FLUOR 770 Acid undergoes glomerular filtration. While the 47% protein binding of STAR FLUOR 770 Acid (Figure 3.6) is similar to DMSA[277], accumulation of DMSA in the PTCs via basolateral uptake and apical reabsorption is extensive[141]. This likely contributes to the specificity of DMSA for the PTCs. It is unlikely STAR FLUOR 770 Acid undergoes that level of PTC accumulation given the delivery of dye we have identified in the renal pelvis. The protein binding of STAR FLUOR 770 Acid is considerably less than MAG3 (>77%)[106,278,279]. The role of the glomerular basement membrane as a charge barrier is debated[330–332]. Harvey et al have shown that a knockout model of reduced heparan sulphate proteoglycans expression in the basement membrane did not result in a leak of negatively charged albumin (66,000 Da) or carboxymethyl Ficoll-70 (60,000 Da)[333]. Their filtration is most likely prevented by their size. Smaller anionic proteins than albumin have been shown to have higher filtration fractions e.g., myoglobin[334]. Anions with a molecular radius 57% that of albumin are 100% filtered[332]. STAR FLUOR 770 Acid is less than 2% the mass of albumin (1,160 Da). It seems likely that the unbound STAR FLUOR 770 Acid has a small enough molecular radius to allow glomerular filtration. Further work to measure this would be useful.

A limitation of this work was the use of the adynamic imaging of DMSA uptake due to the technical limitations of our equipment. Experiments to directly compare STAR FLUOR 770 Acid kinetics with those of MAG3 would be of benefit as MAG3 is a dynamically cleared, specific marker of tubular secretion[144]. This would potentially facilitate the application of identical models to MSOT and SPECT data for better comparison. Roberts et al have shown a deterioration in Tc-99m MAG3 metrics (T^{MAX}, percentage uptake of injected dose, the ratio

between the counts at peak and 10 minutes) measured via scintigraphy in the acute phase post IRI (5 hours to 48 hours)[282]. Theirs was a model of unilateral IRI with contralateral nephrectomy in C57BL/6 mice. Tubular injury was confirmed by histology. Their findings mirror the acute decline we saw with STAR FLUOR 770 Acid. Harrler et al have shown that a 40 minute surgical model of unilateral IRI in severe combined immunodeficient (SCID) mice produced a reduction in scintigraphy using Tc-99m MAG3 fractional uptake rate (FUR) on day 8 post IRI that showed signs of recovery on day 14[281]. However, FUR had not normalised on day 14 and the difference from baseline remained significant. Histology confirmed tubular dilatation and cytoplasmic degeneration but no inflammatory changes in the IRI kidney. The lack of inflammatory changes was attributed to the use of SCID mice. Herrler et al separately reported a persistent reduced peak and impaired excretion of MAG3 in a 45-minute IRI at day 18 in BALB/c mice[335]. DCE MSOT STAR FLUOR 770 MPRs clearance and AUC C:P ratio improved significantly before day 14 suggesting STAR FLUOR 770 Acid is a less specific tubular function marker than MAG3. However, there are experimental differences including the strain of mouse and the quantification parameter of tubular secretion (though both FUR and MPRs have grounding in the PR model). An alternative explanation may be that STAR FLUOR 770 Acid undergoes tubular secretion by a greater number of transporters than MAG3. Similar to STAR FLUOR 770 Acid, MAG3 also undergoes a degree of biliary excretion so this feature may not limit a marker's ability to measure tubular function[336–338].

STAR FLUOR 770 Acid may have a greater affinity for OAT and ABC transporters than the uraemic toxins produced following injury. This means they would not impair STAR FLUOR 770 Acid clearance leading to an apparent earlier recovery. Experiments looking at the expression levels of these transporters correlated with changes in clearance of STAR FLUOR 770 Acid may help clarify this.

6.5 Future Work

The use of the MSOT MPRs model with ABZWCY-HPβCD to measure GFR should be further validated in other animal models of kidney injury including septic and drug-induced acute tubular necrosis. The MPRs GFR model may be better suited here, as these injury models do not cause significant anatomical aberrations the way surgical models can, and the renal pelvis will not risk being out of plane. However, the benefit of an internal control kidney in unilateral injury will be lost. It is important that the GFR measurement is accurate in all circumstances. The technique should also be examined by several different operators to assess the degree of variation. Given the potential kidney protective effects of isoflurane, it would also be interesting to investigate whether different anaesthetic agents change the

clearance of ABZWCY-HPβCD in MSOT. Finally, comparisons should be made with other methods of calculating GFR in mice including the direct measurement of inulin clearance.

To improve on the precision of DCE MSOT to measure GFR and TSR, further technical work is required. Fully quantitative MSOT can be delivered via the optimisation of retrospectively applied fluence correction algorithms. This is an important step in improving the accuracy of pharmacokinetic models applied to DCE MSOT data. There has been promising work using equations of radiative transfer and these have been used to improve quantification of absorbers at depth in MSOT. Further validation of this work to apply these correction algorithms where fluence changes over the time course of imaging secondary to a dynamically distributed contrast agent will allow the use of the aorta as an AIF and further improve the reliability of the pelvis signal.

Renal DCE MSOT might be additionally improved by the development of more slowly cleared NIR dyes. This would allow the application of a PR model to the cortex rather than the pelvis which would be beneficial in surgical injury models. Finally, the development or discovery of a NIR absorber that is definitively handled by tubular secretion would create the opportunity for rapidly measured, safe, single kidney TSR measurements. There is even the potential to concurrently administer a GFR and TSR agent to determine these functions simultaneously via multispectral unmixing. Again, dyes with a slower kinetic profile would be advantageous to allow multiple wavelengths to be measured while maintaining an appropriate temporal resolution to apply AIF dependant models.

Further experimental work looking at fibrosis in the preclinical setting will be of great value. It would be exciting to compare histological evidence of fibrosis with the ability of MSOT to estimate collagen deposition. This could be compared with magnetic resonance imaging techniques for assessing kidney fibrosis. The reversal of fibrosis and the restoration of functional renal tissue is of substantial clinical importance and the ability to examine novel anti-fibrotic therapies longitudinally in the preclinical setting will help deliver this.

6.6 Conclusion

In conclusion, DCE MSOT provides a safe, fast, radiation-free method to measure single kidney GFR in preclinical experiments at a high spatial and temporal resolution despite its semiquantitative nature. Pharmacokinetic models offer distinct benefits over model-free measurements. Further work to implement fluence correction models will improve the accuracy of this method.

STAR FLUOR 770 Acid is not a specific tubular secretion marker and further work to ascertain to what extent it is filtered by the glomerulus and what transmembrane proteins handle its tubular clearance is of value. Measurement of TSR by DCE MSOT is feasible but requires a marker specific to that process.

7 References

1. Kidney Disease: Improving Global Outcomes (KDIGO) Acute Kidney Injury Work Group. KDIGO clinical practice guideline for acute kidney injury. *Kidney Int Suppl* **2**, 1–138 (2012).
2. Heseley, L. & Ashley Jefferson, J. Pathophysiology and Etiology of Acute Kidney Injury. in *Comprehensive Clinical Nephrology* (Elsevier, 2019).
3. Rewa, O. & Bagshaw, S. M. Acute kidney injury—epidemiology, outcomes and economics. *Nat. Rev. Nephrol.* **10**, 193–207 (2014).
4. Lameire, N., Van Biesen, W. & Vanholder, R. The changing epidemiology of acute renal failure. *Nat. Clin. Pract. Nephrol.* **2**, 364–377 (2006).
5. Srisawat, N. & Kellum, J. A. Acute kidney injury: definition, epidemiology, and outcome. *Curr. Opin. Crit. Care* **17**, 548–555 (2011).
6. Pannu, N. & Tonelli, M. Epidemiology and Prognostic Impact of Acute Kidney Injury. in *Comprehensive Clinical Nephrology* (Elsevier, 2019).
7. Susantitaphong, P. *et al.* World Incidence of AKI: A Meta-Analysis. *Clin. J. Am. Soc. Nephrol.* **8**, 1482–1493 (2013).
8. Zeng, X., McMahon, G. M., Brunelli, S. M., Bates, D. W. & Waikar, S. S. Incidence, Outcomes, and Comparisons across Definitions of AKI in Hospitalized Individuals. *Clin. J. Am. Soc. Nephrol.* **9**, 12–20 (2014).
9. Coca, S. G., Singanamala, S. & Parikh, C. R. Chronic kidney disease after acute kidney injury: a systematic review and meta-analysis. *Kidney Int.* **81**, 442–448 (2012).
10. Horne, K. L., Packington, R., Monaghan, J., Reilly, T. & Selby, N. M. Three-year outcomes after acute kidney injury: results of a prospective parallel group cohort study. *BMJ Open* **7**, e015316 (2017).
11. Kerr, M., Bedford, M., Matthews, B. & O'Donoghue, D. The economic impact of acute kidney injury in England. *Nephrol. Dial. Transplant.* **29**, 1362–1368 (2014).

12. Kolhe, N. V., Eldehni, M. T., Selby, N. M. & McIntyre, C. W. The Reimbursement and Cost of Acute Kidney Injury: A UK Hospital Perspective. *Nephron Clin. Pract.* **126**, 51–56 (2014).

13. Mistry, H., Abdelaziz, T. S. & Thomas, M. A Prospective Micro-costing Pilot Study of the Health Economic Costs of Acute Kidney Injury. *Kidney Int. Rep.* **3**, 1285–1293 (2018).

14. Abubakar, I. I., Tillmann, T. & Banerjee, A. Global, regional, and national age-sex specific all-cause and cause-specific mortality for 240 causes of death, 1990-2013: a systematic analysis for the Global Burden of Disease Study 2013. *Lancet* **385**, 117–171 (2015).

15. Xie, Y. *et al.* Analysis of the Global Burden of Disease study highlights the global, regional, and national trends of chronic kidney disease epidemiology from 1990 to 2016. *Kidney Int* **94**, 567–581 (2018).

16. Fogo, A. B. Mechanisms of progression of chronic kidney disease. *Pediatr. Nephrol.* **22**, 2011–2022 (2007).

17. Wu, V.-C. *et al.* Acute-on-chronic kidney injury at hospital discharge is associated with long-term dialysis and mortality. *Kidney Int.* **80**, 1222–1230 (2011).

18. Liyanage, T. *et al.* Worldwide access to treatment for end-stage kidney disease: a systematic review. *The Lancet* **385**, 1975–1982 (2015).

19. Baboolal, K. *et al.* The cost of renal dialysis in a UK setting—a multicentre study. *Nephrol. Dial. Transplant.* **23**, 1982–1989 (2008).

20. Department of Health. *National Service Framework for Renal Services. Part One: Dialysis and Transplantation*. (DoH, 2004).

21. Levy, J., Brown, E. & Lawrence, A. Haemodialysis. in *Oxford Handbook of Dialysis* 71–194 (Oxford University Press).

22. Levy, J., Brown, E. & Lawrence, A. Peritoneal Dialysis. in *Oxford Handbook of Dialysis* 71–194 (Oxford University Press).

23. Selby, N. M. & Kazmi, I. Peritoneal dialysis has optimal intradialytic hemodynamics and preserves residual renal function: Why isn't it better than hemodialysis? *Semin. Dial.* **32**, 3–8 (2019).

24. Port, F. K., Wolfe, R. A., Mauger, E. A., Berling, D. P. & Jiang, K. Comparison of survival probabilities for dialysis patients vs cadaveric renal transplant recipients. *Jama* **270**, 1339–1343 (1993).

25. Oniscu, G. C., Brown, H. & Forsythe, J. L. Impact of cadaveric renal transplantation on survival in patients listed for transplantation. *J. Am. Soc. Nephrol.* **16**, 1859–1865 (2005).

26. Laupacis, A. *et al.* A study of the quality of life and cost-utility of renal transplantation. *Kidney Int* **50**, 235–242 (1996).

27. NHS Blood and Transplant. *Organ and Tissue Donation and Transplantation Activity Report 2020/21*. https://nhsbtdbe.blob.core.windows.net/umbraco-assets-corp/23461/activity-report-2020-2021.pdf (2021).

28. Steddon, S., Ashman, N., Chesser, A. & Cunningham, J. Transplantation. in *Oxford Handbook of Nephrology and Hypertension* (Oxford University Press).

29. A. O. Phillips & Steve Riley. Structure and function of the kidney. in *Oxford Textbook of Medicine* (Oxford University Press, 2012).

30. Inker, L. A. & Perrone, R. Assessment of kidney function. https://www.uptodate.com/contents/assessment-of-kidney-function (2019).

31. Inker, L. & Levey, A. Assessment of Glomerular Filtration Rate. in *Comprehensive Clinical Nephrology* (Elsevier, 2019).

32. Levey, A. & Inker, L. Definition and staging of chronic kidney disease in adults. https://www.uptodate.com/contents/definition-and-staging-of-chronic-kidney-disease-in-adults (2018).

33. Bonventre, J. V. & Yang, L. Cellular pathophysiology of ischemic acute kidney injury. *J. Clin. Invest.* **121**, 4210–4221 (2011).

34. Li, X., Hassoun, H. T., Santora, R. & Rabb, H. Organ crosstalk: the role of the kidney. *Curr. Opin. Crit. Care* **15**, 481–487 (2009).

35. Ferenbach, D. A. & Bonventre, J. V. Mechanisms of maladaptive repair after AKI leading to accelerated kidney ageing and CKD. *Nat. Rev. Nephrol.* **11**, 264 (2015).

36. Sharfuddin, A. A. & Molitoris, B. A. Pathophysiology of ischemic acute kidney injury. *Nat. Rev. Nephrol.* **7**, 189–200 (2011).

37. Bellomo, R., Kellum, J. A. & Ronco, C. Acute kidney injury. *The Lancet* **380**, 756–766 (2012).

38. Van Norman, G. A. Limitations of Animal Studies for Predicting Toxicity in Clinical Trials. *JACC Basic Transl. Sci.* **5**, 387–397 (2020).

39. Van Norman, G. A. Limitations of Animal Studies for Predicting Toxicity in Clinical Trials. *JACC Basic Transl. Sci.* **4**, 845–854 (2019).

40. Menon, M. C., Chuang, P. Y. & He, C. J. The glomerular filtration barrier: components and crosstalk. *Int. J. Nephrol.* **2012**, (2012).

41. Taylor, A. *et al.* Multimodal Imaging Techniques Show Differences in Homing Capacity Between Mesenchymal Stromal Cells and Macrophages in Mouse Renal Injury Models. *Mol. Imaging Biol.* **22**, 904–913 (2020).

42. Amadeo, F. *et al.* Mesenchymal stromal cells: what have we learned so far about their therapeutic potential and mechanisms of action? *Emerg. Top. Life Sci.* **5**, 549–562 (2021).

43. Burt, T. *et al.* Phase 0/microdosing approaches: time for mainstream application in drug development? *Nat. Rev. Drug Discov.* **19**, 801–818 (2020).

44. Our strategy | NC3Rs. https://www.nc3rs.org.uk/who-we-are/our-strategy.

45. Malek, M. & Nematbakhsh, M. Renal ischemia/reperfusion injury; from pathophysiology to treatment. *J. Ren. Inj. Prev.* **4**, 20–27 (2015).

46. Carden, D. L. & Granger, D. N. Pathophysiology of ischaemia–reperfusion injury. *J Pathol* 12 (2000).

47. Definition, classification, etiology, and pathophysiology of shock in adults - UpToDate. https://www.uptodate.com/contents/definition-classification-etiology-and-pathophysiology-of-shock-in-adults.

48. Morath, C. & Zeier, M. Chronic Allograft Injury. in *Comprehensive Clinical Nephrology* (Elsevier, 2019).

49. Singh, A. P. *et al.* Animal models of acute renal failure. *Pharmacol. Rep.* **64**, 31–44 (2012).

50. Heyman, S. N., Lieberthal, W., Rogiers, P. & Bonventre, J. V. Animal models of acute tubular necrosis. *Curr. Opin. Crit. Care* **8**, 526–534 (2002).

51. Lieberthal, W. & Nigam, S. K. Acute renal failure. II. Experimental models of acute renal failure: imperfect but indispensable. *Am. J. Physiol.-Ren. Physiol.* **278**, F1–F12 (2000).

52. Doi, K., Leelahavanichkul, A., Yuen, P. S. T. & Star, R. A. Animal models of sepsis and sepsis-induced kidney injury. *J. Clin. Invest.* **119**, 2868–2878 (2009).

53. Wan, L. *et al.* Pathophysiology of septic acute kidney injury: What do we really know? *Crit. Care Med.* **36**, S198 (2008).

54. Kriz, W. & Elger, M. Renal Anatomy. in *Comprehensive Clinical Nephrology* (Elsevier, 2019).

55. Bailey, M. & Unwin, R. Renal Physiology. in *Comprehensive Clinical Nephrology* (Elsevier, 2019).

56. Bertram, J. F., Douglas-Denton, R. N., Diouf, B., Hughson, M. D. & Hoy, W. E. Human nephron number: implications for health and disease. *Pediatr. Nephrol.* **26**, 1529–1533 (2011).

57. Charlton, J. R., Baldelomar, E. J., Hyatt, D. M. & Bennett, K. M. Nephron number and its determinants: a 2020 update. *Pediatr. Nephrol.* **36**, 797–807 (2021).

58. Zeisberg, M. & Kalluri, R. Physiology of the Renal Interstitium. *Clin. J. Am. Soc. Nephrol.* **10**, 1831–1840 (2015).

59. Teteris, S. A., Engel, D. R. & Kurts, C. Homeostatic and pathogenic role of renal dendritic cells. *Kidney Int.* **80**, 139–145 (2011).

60. OpenStax CNX. Gross Anatomy of the Kidney. in *OpenStax, Anatomy & Physiology* (OpenStax, 2016).

61. Delaney, M. A., Kowalewska, J. & Treuting, P. M. 16 - Urinary System. in *Comparative Anatomy and Histology (Second Edition)* (eds. Treuting, P. M., Dintzis, S. M. & Montine, K. S.) 275–301 (Academic Press, 2018). doi:10.1016/B978-0-12-802900-8.00016-6.

62. O'Neill, P., Dornan, T. & Denning, D. Renal disease, and fluid-electrolyte and acid-base balance. in *Master Medicine: Medicine* (2008).

63. Blouch, K. *et al.* Molecular configuration and glomerular size selectivity in healthy and nephrotic humans. *Am. J. Physiol.-Ren. Physiol.* **273**, F430–F437 (1997).

64. Venturoli, D. & Rippe, B. Ficoll and dextran vs. globular proteins as probes for testing glomerular permselectivity: effects of molecular size, shape, charge, and deformability. *Am. J. Physiol.-Ren. Physiol.* **288**, F605–F613 (2005).

65. The Editors of Encyclopaedia Britannica. Urine. *Encyclopædia Britannica* https://www.britannica.com/science/urine (2019).

66. Baig, A. Biochemical Composition of Normal Urine. *Nat. Preced.* (2011) doi:10.1038/npre.2011.6595.1.

67. Stevens, L. A. & Levey, A. S. Measured GFR as a confirmatory test for estimated GFR. *J. Am. Soc. Nephrol.* **20**, 2305–2313 (2009).

68. Heaf, J. G. The origin of the 1·73-m2 body surface area normalization: problems and implications: Origin of body surface area normalization. *Clin. Physiol. Funct. Imaging* **27**, 135–137 (2007).

69. Qi, Z. *et al.* Serial determination of glomerular filtration rate in conscious mice using FITC-inulin clearance. *Am. J. Physiol.-Ren. Physiol.* **286**, F590–F596 (2004).

70. Hou, J. The kidney tight junction (Review). *Int. J. Mol. Med.* **34**, 1451–1457 (2014).

71. Wang, K. & Kestenbaum, B. Proximal Tubular Secretory Clearance: A Neglected Partner of Kidney Function. *Clin. J. Am. Soc. Nephrol.* **13**, 1291–1296 (2018).

72. van der Made, T. K. *et al.* Quantitative Translation of Microfluidic Transporter in Vitro Data to in Vivo Reveals Impaired Albumin-Facilitated Indoxyl Sulfate Secretion in Chronic Kidney Disease. *Mol. Pharm.* **16**, 4551–4562 (2019).

73. Koepsell, H. The SLC22 family with transporters of organic cations, anions and zwitterions. *Mol. Aspects Med.* **34**, 413–435 (2013).

74. Motohashi, H. & Inui, K. Organic cation transporter OCTs (SLC22) and MATEs (SLC47) in the human kidney. *AAPS J.* **15**, 581–588 (2013).

75. Hsueh, C.-H. *et al.* Identification and Quantitative Assessment of Uremic Solutes as Inhibitors of Renal Organic Anion Transporters, OAT1 and OAT3. *Mol. Pharm.* **13**, 3130–3140 (2016).

76. Fork, C. *et al.* OAT2 catalyses efflux of glutamate and uptake of orotic acid. *Biochem. J.* **436**, 305–312 (2011).

77. Shen, H. *et al.* Characterization of Organic Anion Transporter 2 (SLC22A7): A Highly Efficient Transporter for Creatinine and Species-Dependent Renal Tubular Expression. *Drug Metab. Dispos.* **43**, 984–993 (2015).

78. Pritchard, J. B. & Miller, D. S. Renal secretion of organic anions and cations. *Kidney Int.* **49**, 1649–1654 (1996).

79. Mahnensmith, R. L. & Aronson, P. S. The plasma membrane sodium-hydrogen exchanger and its role in physiological and pathophysiological processes. *Circ. Res.* **56**, 773–788 (1985).

80. Palmer, B. F. Regulation of Potassium Homeostasis. *Clin. J. Am. Soc. Nephrol. CJASN* **10**, 1050–1060 (2015).

81. Blaine, J., Chonchol, M. & Levi, M. Renal control of calcium, phosphate, and magnesium homeostasis. *Clin. J. Am. Soc. Nephrol. CJASN* **10**, 1257–1272 (2015).

82. Felsenfeld, A., Rodriguez, M. & Levine, B. New insights in regulation of calcium homeostasis. *Curr. Opin. Nephrol. Hypertens.* **22**, 371–376 (2013).

83. Nielsen, R., Christensen, E. I. & Birn, H. Megalin and cubilin in proximal tubule protein reabsorption: from experimental models to human disease. *Kidney Int.* **89**, 58–67 (2016).

84. Martin, E. Glomerular Filtration Rate. in *Concise Medical Dictionary* (Oxford University Press, 2010).

85. Stevens, L. A., Coresh, J., Greene, T. & Levey, A. S. Assessing kidney function—measured and estimated glomerular filtration rate. *N. Engl. J. Med.* **354**, 2473–2483 (2006).

86. Delanaye, P. How Measuring Glomerular Filtration Rate? Comparison of Reference Methods. in *Basic Nephrology and Acute Kidney Injury* (2012).

87. Mensink, M. A., Frijlink, H. W., van der Voort Maarschalk, K. & Hinrichs, W. L. J. Inulin, a flexible oligosaccharide I: Review of its physicochemical characteristics. *Carbohydr. Polym.* **130**, 405–419 (2015).

88. Shannon, J. A. & Smith, H. W. The Excretion Of Inulin, Xylose And Urea By Normal And Phlorizinized Man. *J. Clin. Invest.* **14**, 393–401 (1935).

89. Pottel, H. Measuring and estimating glomerular filtration rate in children. *Pediatr. Nephrol.* **32**, 249–263 (2017).

90. Richards, A. N., Westfall, B. B. & Bott, P. A. Renal Excretion of Inulin, Creatinine and Xylose in Normal Dogs. *Exp. Biol. Med.* **32**, 73–75 (1934).

91. Hostetter, T. H. & Meyer, T. W. The development of clearance methods for measurement of glomerular filtration and tubular reabsorption. *Am. J. Physiol.-Ren. Physiol.* **287**, F868–F870 (2004).

92. Gutman, Y., Gottschalk, C. W. & Lassiter, W. E. Micropuncture Study of Inulin Absorption in the Rat Kidney. *Science* **147**, 753–754 (1965).

93. Marsh, D. & Frasier, C. Reliability of inulin for determining volume flow in rat renal cortical tubules. *Am. J. Physiol.-Leg. Content* **209**, 283–286 (1965).

94. Yusuf, M. M., Vajpayee, S., Picascia, T., Perciaccante, R. & Gretz, N. An overview of non-invasive methods for transcutaneous measurements of glomerular filtration. *J Exp Nephrol* **2**, 7–14 (2021).

95. Schock-Kusch, D. *et al.* Transcutaneous measurement of glomerular filtration rate using FITC-sinistrin in rats. *Nephrol. Dial. Transplant.* **24**, 2997–3001 (2009).

96. Schock-Kusch, D. *et al.* Transcutaneous assessment of renal function in conscious rats with a device for measuring FITC-sinistrin disappearance curves. *Kidney Int.* **79**, 1254–1258 (2011).

97. Schreiber, A. *et al.* Transcutaneous measurement of renal function in conscious mice. *Am. J. Physiol.-Ren. Physiol.* **303**, F783–F788 (2012).

98. Friedemann, J. *et al.* Improved kinetic model for the transcutaneous measurement of glomerular filtration rate in experimental animals. *Kidney Int.* **90**, 1377–1385 (2016).

99. Rajagopalan, R. *et al.* Hydrophilic Pyrazine Dyes as Exogenous Fluorescent Tracer Agents for Real-Time Point-of-Care Measurement of Glomerular Filtration Rate. *J. Med. Chem.* **54**, 5048–5058 (2011).

100. Poreddy, A. R. *et al.* Exogenous fluorescent tracer agents based on pegylated pyrazine dyes for real-time point-of-care measurement of glomerular filtration rate. *Bioorg. Med. Chem.* **20**, 2490–2497 (2012).

101. Huang, J. & Gretz, N. Light-Emitting Agents for Noninvasive Assessment of Kidney Function. *ChemistryOpen* **6**, 456–471 (2017).

102. Huang, J. *et al.* Zwitterionic near infrared fluorescent agents for noninvasive real-time transcutaneous assessment of kidney function. *Chem. Sci.* **8**, 2652–2660 (2017).

103. Huang, J. *et al.* Fluorescently Labeled Cyclodextrin Derivatives as Exogenous Markers for Real-Time Transcutaneous Measurement of Renal Function. *Bioconjug. Chem.* **27**, 2513–2526 (2016).

104. PubChem. Iotalamic acid. https://pubchem.ncbi.nlm.nih.gov/compound/3737.

105. Erol, K. & Yigitaslan, S. Chemistry, Physicochemical Properties and Pharmacokinetics of Iodinated Contrast Agents. in *Medical Imaging Contrast Agents: A Clinical Manual* (eds. Erturk, S. M., Ros, P. R., Ichikawa, T. & Saylisoy, S.) 5–15 (Springer International Publishing, 2021). doi:10.1007/978-3-030-79256-5_2.

106. Rehling, M., Nielsen, L. E. & Marqversen, J. Protein binding of 99Tcm-DTPA compared with other GFR tracers. *Nucl. Med. Commun.* **22**, 617–623 (2001).

107. Odlind, B., Hällgren, R., Sohtell, M. & Lindström, B. Is 125I iothalamate an ideal marker for glomerular filtration? *Kidney Int.* **27**, 9–16 (1985).

108. Brown, S. C. W. & O'Reilly, P. H. Iohexol Clearance for the Determination of Glomerular Filtration Rate in Clinical Practice: Evidence for a New Gold Standard. *J. Urol.* **146**, 675–679 (1991).

109. Frennby, B. & Sterner, G. Contrast media as markers of GFR. *Eur. Radiol.* **12**, 475–484 (2002).

110. Berg, U. B. *et al.* Comparison of Plasma Clearance of Iohexol and Urinary Clearance of Inulin for Measurement of GFR in Children. *Am. J. Kidney Dis.* **57**, 55–61 (2011).

111. Masereeuw, R., Moons, M. M., Smits, P. & Russel, F. G. M. Glomerular filtration and saturable absorption of iohexol in the rat isolated perfused kidney. *Br. J. Pharmacol.* **119**, 57–64 (1996).

112. Jiang, K. *et al.* A modified two-compartment model for measurement of renal function using dynamic contrast-enhanced computed tomography. *PLOS ONE* **14**, e0219605 (2019).

113. Daghini, E. *et al.* Comparison of Mathematic Models for Assessment of Glomerular Filtration Rate with Electron-Beam CT in Pigs. *Radiology* **242**, 417–424 (2007).

114. Tsushima, Y., Blomley, M. J. K., Kusano, S. & Endo, K. Use of contrast-enhanced computed tomography to measure clearance per unit renal volume: A novel measurement of renal function and fractional vascular volume. *Am. J. Kidney Dis.* **33**, 754–760 (1999).

115. Blomley, M. J. K. & Dawson, P. Review article: The quantification of renal function with enhanced computed tomography. *Br. J. Radiol.* **69**, 7 (1996).

116. Agha, N. & Persson, R. B. R. Comparative Labelling and Biokinetic Studies of 99mTc-EDTA(Sn) and 99mTc-DTPA(Sn). *Nukl. - Nucl.* **16**, 30–35 (1977).

117. Houlihan, C. *et al.* A comparison of the plasma disappearance of iohexol and 99m Tc-DTPA for the measurement of glomerular filtration rate (GFR) in diabetes. *Aust. N. Z. J. Med.* **29**, 693–700 (1999).

118. Brändström, E. *et al.* GFR measurement with iohexol and 51Cr-EDTA. A comparison of the two favoured GFR markers in Europe. *Nephrol. Dial. Transplant.* **13**, 1176–1182 (1998).

119. Rabito, C. A., Chen, Y., Schomacker, K. T. & Modell, M. D. Optical, real-time monitoring of the glomerular filtration rate. *Appl. Opt.* **44**, 5956–5965 (2005).

120. Mendichovszky, I. *et al.* How accurate is dynamic contrast-enhanced MRI in the assessment of renal glomerular filtration rate? A critical appraisal. *J. Magn. Reson. Imaging* **27**, 925–931 (2008).

121. Notohamiprodjo, M. *et al.* Comparison of Gd-DTPA and Gd-BOPTA for studying renal perfusion and filtration. *J. Magn. Reson. Imaging* **34**, 595–607 (2011).

122. Bokacheva, L., Rusinek, H., Zhang, J. L., Chen, Q. & Lee, V. S. Estimates of glomerular filtration rate from MR renography and tracer kinetic models. *J. Magn. Reson. Imaging* **29**, 371–382 (2009).

123. Wahsner, J., Gale, E. M., Rodríguez-Rodríguez, A. & Caravan, P. Chemistry of MRI Contrast Agents: Current Challenges and New Frontiers. *Chem. Rev.* **119**, 957–1057 (2019).

124. Glassock, R. J. & Winearls, C. Screening for CKD with eGFR: doubts and dangers. *Clin. J. Am. Soc. Nephrol.* **3**, 1563–1568 (2008).

125. van Acker, B. A., Koopman, M. G., Arisz, L., Koomen, G. C. M. & de Waart, D. R. Creatinine clearance during cimetidine administration for measurement of glomerular filtration rate. *The Lancet* **340**, 1326–1329 (1992).

126. Eisner, C. *et al.* Major contribution of tubular secretion to creatinine clearance in mice. *Kidney Int* **77**, 519–526 (2010).

127. Pickering, J. W. & Endre, Z. H. GFR shot by RIFLE: errors in staging acute kidney injury. *The Lancet* **373**, 1318–1319 (2009).

128. Dent, C. L. *et al.* Plasma neutrophil gelatinase-associated lipocalin predicts acute kidney injury, morbidity and mortality after pediatric cardiac surgery: a prospective uncontrolled cohort study. *Crit. Care* **11**, R127 (2007).

129. Herget-Rosenthal, S., Bökenkamp, A. & Hofmann, W. How to estimate GFR-serum creatinine, serum cystatin C or equations? *Clin. Biochem.* **40**, 153–161 (2007).

130. Fanos, V., Mussap, M., Plebani, M. & Cataldi, L. Cystatin C in paediatric nephrology. Present situation and prospects. *Minerva Pediatr.* **51**, 167–177 (1999).

131. Masereeuw, R. *et al.* The Kidney and Uremic Toxin Removal: Glomerulus or Tubule? *Semin. Nephrol.* **34**, 191–208 (2014).

132. Koepsell, H. Polyspecific organic cation transporters: their functions and interactions with drugs. *Trends Pharmacol. Sci.* **25**, 375–381 (2004).

133. Eloot, S. *et al.* Estimated Glomerular Filtration Rate Is a Poor Predictor of Concentration for a Broad Range of Uremic Toxins. *Clin. J. Am. Soc. Nephrol.* **6**, 1266–1273 (2011).

134. Lowenstein, J. & Grantham, J. J. The rebirth of interest in renal tubular function. *Am. J. Physiol.-Ren. Physiol.* **310**, F1351–F1355 (2016).

135. Notghi, A., Merrick, M. V., Ferrington, C. & Anderton, J. L. A comparison of simplified and standard methods for the measurement of glomerular filtration rate and renal tubular function. *Br. J. Radiol.* **59**, 35–39 (1986).

136. Dowling, T. C., Frye, R. F., Fraley, D. S. & Matzke, G. R. Characterization of tubular functional capacity in humans using para-aminohippurate and famotidine. *Kidney Int.* **59**, 295–303 (2001).

137. Suchy-Dicey, A. M. *et al.* Tubular Secretion in CKD. *J. Am. Soc. Nephrol.* **27**, 2148–2155 (2016).

138. Chen, Y. *et al.* Prediction of Kidney Drug Clearance: A Comparison of Tubular Secretory Clearance and Glomerular Filtration Rate. *J. Am. Soc. Nephrol.* **32**, 459–468 (2021).

139. Sirich, T. L., Aronov, P. A., Plummer, N. S., Hostetter, T. H. & Meyer, T. W. Numerous protein-bound solutes are cleared by the kidney with high efficiency. *Kidney Int.* **84**, 585–590 (2013).

140. Seegmiller, J. C. *et al.* Tubular Secretion Markers, Glomerular Filtration Rate, Effective Renal Plasma Flow, and Filtration Fraction in Healthy Adolescents. *Kidney Med.* **2**, 670–672 (2020).

141. Bradberry, S. & Vale, A. Dimercaptosuccinic acid (succimer; DMSA) in inorganic lead poisoning. *Clin. Toxicol.* **47**, 617–631 (2009).

142. Peters, A. M., Jones, D. H., Evans, K. & Gordon, I. Two routes for 99mTc-DMSA uptake into the renal cortical tubular cell. *Eur. J. Nucl. Med.* **14**, 555–561 (1988).

143. Weyer, K. *et al.* Renal Uptake of 99mTc-Dimercaptosuccinic Acid Is Dependent on Normal Proximal Tubule Receptor–Mediated Endocytosis. *J. Nucl. Med.* **54**, 159–165 (2013).

144. Kobayashi, M. *et al.* Transport mechanism and affinity of [99mTc]Tc-mercaptoacetyltriglycine ([99mTc]MAG3) on the apical membrane of renal proximal tubule cells. *Nucl. Med. Biol.* **84–85**, 33–37 (2020).

145. Cao, X., Xu, X., Grant, F. D. & Treves, S. T. Estimation of Split Renal Function With 99mTc-DMSA SPECT: Comparison Between 3D Volumetric Assessment and 2D Coronal Projection Imaging. *AJR Am. J. Roentgenol.* **207**, 1324–1328 (2016).

146. Stokland, E., Hellström, M., Jacobsson, B., Jodal, U. & Sixt, R. Evaluation of DMSA scintigraphy and urography in assessing both acute and permanent renal damage in children. *Acta Radiol.* **39**, 447–452 (1998).

147. Esteves, F. P. *et al.* 99mTc-MAG3 Renography: Normal Values for MAG3 Clearance and Curve Parameters, Excretory Parameters, and Residual Urine Volume. *Am. J. Roentgenol.* **187**, W610–W617 (2006).

148. Jouret, F. *et al.* Single photon emission-computed tomography (SPECT) for functional investigation of the proximal tubule in conscious mice. *Am. J. Physiol.-Ren. Physiol.* **298**, F454–F460 (2010).

149. Algin, O. A new contrast media for functional MR urography: Gd-MAG3. *Med. Hypotheses* **77**, 74–76 (2011).

150. NC3Rs. NC3Rs Blood sampling: Mouse. *NC3Rs Blood sampling: Mouse* https://www.nc3rs.org.uk/3rs-resources/blood-sampling/blood-sampling-mouse (2021).

151. Jacobsson, B., Lignelid, H. & Bergerheim, U. s. r. Transthyretin and cystatin C are catabolized in proximal tubular epithelial cells and the proteins are not useful as markers for renal cell carcinomas. *Histopathology* **26**, 559–564 (1995).

152. Zhang, W. R. & Parikh, C. R. Biomarkers of Acute and Chronic Kidney Disease. *Annu. Rev. Physiol.* **81**, 309–333 (2019).

153. Kalliokoski, O. *et al.* Mice Do Not Habituate to Metabolism Cage Housing–A Three Week Study of Male BALB/c Mice. *PLOS ONE* **8**, e58460 (2013).

154. Ellery, S. J., Cai, X., Walker, D. D., Dickinson, H. & Kett, M. M. Transcutaneous measurement of glomerular filtration rate in small rodents: Through the skin for the win?: Transcutaneous measure of GFR in rodents. *Nephrology* **20**, 117–123 (2015).

155. Harwood, R. *et al.* Murine models of renal ischemia reperfusion injury: An opportunity for refinement using noninvasive monitoring methods. *Physiol. Rep.* **10**, e15211 (2022).

156. Schock-Kusch, D. *et al.* Reliability of Transcutaneous Measurement of Renal Function in Various Strains of Conscious Mice. *PLoS ONE* **8**, e71519 (2013).

157. Scarfe, L. *et al.* Measures of kidney function by minimally invasive techniques correlate with histological glomerular damage in SCID mice with adriamycin-induced nephropathy. *Sci. Rep.* **5**, 13601 (2015).

158. Mazze, R., Cousins, M. & Barr, G. Renal effects and metabolism of isoflurane in man. *Anesthesiology* **40**, 536–542 (1974).

159. Lee, H. T. *et al.* Isoflurane protects against renal ischemia and reperfusion injury and modulates leukocyte infiltration in mice. *Am. J. Physiol.-Ren. Physiol.* **293**, F713–F722 (2007).

160. Zhang, L. *et al.* Pre-treatment with isoflurane ameliorates renal ischemic–reperfusion injury in mice. *Life Sci.* **88**, 1102–1107 (2011).

161. Fusellier, M. *et al.* Influence of three anesthetic protocols on glomerular filtration rate in dogs. *Am. J. Vet. Res.* **68**, 807–811 (2007).

162. Diez, A. *et al.* Correlation between CT-based measured renal volumes and nuclear-renography-based split renal function in living kidney donors. Clinical diagnostic utility and practice patterns. *Clin. Transplant.* **28**, 675–682 (2014).

163. Patankar, K., Low, R. S.-T., Blakeway, D. & Ferrari, P. Comparison of computer tomographic volumetry versus nuclear split renal function to determine residual renal function after living kidney donation. *Acta Radiol.* **55**, 753–760 (2014).

164. Wei, Q. & Dong, Z. Mouse model of ischemic acute kidney injury: technical notes and tricks. *Am. J. Physiol.-Ren. Physiol.* **303**, F1487–F1494 (2012).

165. Polichnowski, A. J. *et al.* Pathophysiology of unilateral ischemia-reperfusion injury: importance of renal counterbalance and implications for the AKI-CKD transition. *Am. J. Physiol.-Ren. Physiol.* **318**, F1086–F1099 (2020).

166. Lange, D. *et al.* Renal volume assessed by magnetic resonance imaging volumetry correlates with renal function in living kidney donors pre- and postdonation: a retrospective cohort study. *Transpl. Int.* **31**, 773–780 (2018).

167. Jo, W. R. *et al.* Correlations between renal function and the total kidney volume measured on imaging for autosomal dominant polycystic kidney disease: A systematic review and meta-analysis. *Eur. J. Radiol.* **95**, 56–65 (2017).

168. Cox, E. F. *et al.* Multiparametric Renal Magnetic Resonance Imaging: Validation, Interventions, and Alterations in Chronic Kidney Disease. *Front. Physiol.* **8**, (2017).

169. Hysi, E. *et al.* Photoacoustic imaging of kidney fibrosis for assessing pre-transplant organ quality. *JCI Insight* (2020) doi:10.1172/jci.insight.136995.

170. Schley, G. *et al.* Multiparametric magnetic resonance imaging of experimental chronic kidney disease: A quantitative correlation study with histology. *PLOS ONE* **13**, e0200259 (2018).

171. Inoue, T. *et al.* Comparison of multiparametric magnetic resonance imaging sequences with laboratory parameters for prognosticating renal function in chronic kidney disease. *Sci. Rep.* **11**, 22129 (2021).

172. Drudi, F. M. *et al.* Multiparametric ultrasound in the evaluation of kidney disease in elderly. *J. Ultrasound* **23**, 115–126 (2020).

173. Razansky, D. Optoacoustic Imaging. in *Small Animal Imaging* 458–465 (Springer, 2017).

174. Xu, M. & Wang, L. V. Photoacoustic imaging in biomedicine. *Rev Sci Instrum* 23 (2006).

175. Haisch, C. Quantitative analysis in medicine using photoacoustic tomography. *Anal. Bioanal. Chem.* **393**, 473 (2008).

176. Weber, J., Beard, P. C. & Bohndiek, S. E. Contrast agents for molecular photoacoustic imaging. *Nat. Methods* **13**, 639–650 (2016).

177. MSOT inVision | iThera Medical. https://ithera-medical.com/products/preclinical-research/msot-invision/ (2022).

178. James, S., Neuhaus, K., Murphy, M. & Leahy, M. Contrast agents for photoacoustic imaging: a review of stem cell tracking. *Stem Cell Res. Ther.* **12**, 511 (2021).

179. Tan, J. *et al.* Real-Time Monitoring Renal Impairment Due to Drug-Induced AKI and Diabetes-Caused CKD Using an NAG-Activatable NIR-II Nanoprobe. *Anal. Chem.* (2021) doi:10.1021/acs.analchem.1c03926.

180. Buehler, A., Herzog, E., Razansky, D. & Ntziachristos, V. Visualization of mouse kidney perfusion with multispectral optoacoustic tomography (MSOT) at video rate. in vol. 7899 789914 (International Society for Optics and Photonics, 2011).

181. Hirasawa, T. *et al.* Dependence of photoacoustic signal generation characteristics on fluorescence quantum yields of small organic molecule based contrast agents. in vol. 10064 1006434 (International Society for Optics and Photonics, 2017).

182. Gujrati, V., Mishra, A. & Ntziachristos, V. Molecular imaging probes for multi-spectral optoacoustic tomography. *Chem. Commun.* **53**, 4653–4672 (2017).

183. Jiang, X., Du, B., Tang, S., Hsieh, J.-T. & Zheng, J. Photoacoustic Imaging of Nanoparticle Transport in the Kidneys at High Temporal Resolution. *Angew. Chem. Int. Ed Engl.* **58**, 5994–6000 (2019).

184. Yoon, S. *et al.* Deep optical imaging within complex scattering media. *Nat. Rev. Phys.* **2**, 141–158 (2020).

185. Kuniyil Ajith Singh, M., Sato, N., Ichihashi, F. & Sankai, Y. Clinical Translation of Photoacoustic Imaging—Opportunities and Challenges from an Industry Perspective. in *LED-Based Photoacoustic Imaging : From Bench to Bedside* (ed. Kuniyil Ajith Singh, M.) 379–393 (Springer, 2020). doi:10.1007/978-981-15-3984-8_16.

186. Regensburger, A. P. *et al.* Detection of collagens by multispectral optoacoustic tomography as an imaging biomarker for Duchenne muscular dystrophy. *Nat. Med.* **25**, 1905–1915 (2019).

187. Ntziachristos, V., Yodh, A. G., Schnall, M. & Chance, B. Concurrent MRI and diffuse optical tomography of breast after indocyanine green enhancement. *Proc. Natl. Acad. Sci.* **97**, 2767–2772 (2000).

188. Knieling, F. *et al.* Multispectral Optoacoustic Tomography for Assessment of Crohn's Disease Activity. *N. Engl. J. Med.* **376**, 1292–1294 (2017).

189. Waldner, M. J. *et al.* Multispectral Optoacoustic Tomography in Crohn's Disease: Noninvasive Imaging of Disease Activity. *Gastroenterology* **151**, 238–240 (2016).

190. Aguirre, J. *et al.* Precision assessment of label-free psoriasis biomarkers with ultra-broadband optoacoustic mesoscopy. *Nat. Biomed. Eng.* **1**, 1–8 (2017).

191. Yew, Y. W. *et al.* Investigation of morphological, vascular and biochemical changes in the skin of an atopic dermatitis (AD) patient in response to dupilumab using raster scanning optoacoustic mesoscopy (RSOM) and handheld confocal Raman spectroscopy (CRS). *J. Dermatol. Sci.* **95**, 123–125 (2019).

192. MSOT Acuity Echo | iThera Medical. https://ithera-medical.com/products/clinical-research/msot-acuity-echo/ (2022).

193. Razansky, D., Vinegoni, C. & Ntziachristos, V. Imaging of mesoscopic-scale organisms using selective-plane optoacoustic tomography. *Phys. Med. Biol.* **54**, 2769–2777 (2009).

194. Brochu, F. M. *et al.* Towards quantitative evaluation of tissue absorption coefficients using light fluence correction in optoacoustic tomography. *IEEE Trans. Med. Imaging* **36**, 322–331 (2017).

195. Yao, L., Sun, Y. & Jiang, H. Quantitative photoacoustic tomography based on the radiative transfer equation. *Opt. Lett.* **34**, 1765–1767 (2009).

196. Hupple, C. W. *et al.* A light-fluence-independent method for the quantitative analysis of dynamic contrast-enhanced multispectral optoacoustic tomography (DCE MSOT). *Photoacoustics* **10**, 54–64 (2018).

197. Bauer, A. Q., Nothdurft, R. E., Culver, J. P., Erpelding, T. N. & Wang, L. V. Quantitative photoacoustic imaging: correcting for heterogeneous light fluence distributions using diffuse optical tomography. *J. Biomed. Opt.* **16**, 096016 (2011).

198. Hussain, A., Hondebrink, E., Staley, J. & Steenbergen, W. Photoacoustic and acousto-optic tomography for quantitative and functional imaging. *Optica* **5**, 1579–1589 (2018).

199. Lutzweiler, C. & Razansky, D. Optoacoustic Imaging and Tomography: Reconstruction Approaches and Outstanding Challenges in Image Performance and Quantification. *Sensors* **13**, 7345–7384 (2013).

200. Gothelf, A., Hojman, P. & Gehl, J. Change in Hemoglobin Levels due to Anesthesia in Mice: An Important Confounder in Studies on Hematopoietic Drugs. *Biol. Proced. Online* **11**, 325–330 (2009).

201. Kai, S., Tanaka, T., Matsuyama, T., Suzuki, K. & Hirota, K. The volatile anesthetic isoflurane differentially suppresses the induction of erythropoietin synthesis elicited by acute anemia and systemic hypoxemia in mice in an hypoxia-inducible factor-2-dependent manner. *Eur. J. Pharmacol.* **732**, 43–49 (2014).

202. Masamoto, K., Fukuda, M., Vazquez, A. & Kim, S.-G. Dose-dependent effect of isoflurane on neurovascular coupling in rat cerebral cortex. *Eur. J. Neurosci.* **30**, 242–250 (2009).

203. Razansky, D., Buehler, A. & Ntziachristos, V. Volumetric real-time multispectral optoacoustic tomography of biomarkers. *Nat. Protoc.* **6**, 1121–1129 (2011).

204. Joseph, J. *et al.* Evaluation of precision in optoacoustic tomography for preclinical imaging in living subjects. *J. Nucl. Med.* **58**, 807–814 (2017).

205. Dima, A., Burton, N. C. & Ntziachristos, V. Multispectral optoacoustic tomography at 64, 128, and 256 channels. *J. Biomed. Opt.* **19**, 036021 (2014).

206. Cheng, P. *et al.* Fluoro-Photoacoustic Polymeric Renal Reporter for Real-Time Dual Imaging of Acute Kidney Injury. *Adv. Mater.* 1908530 (2020) doi:10.1002/adma.201908530.

207. Yang, X. *et al.* DHHC21 deficiency attenuates renal dysfunction during septic injury. *Sci. Rep.* **11**, 11146 (2021).

208. Yoneya, S. *et al.* Binding properties of indocyanine green in human blood. *Invest. Ophthalmol. Vis. Sci.* **39**, 1286–1290 (1998).

209. Song, W. *et al.* Comprehensive studies of pharmacokinetics and biodistribution of indocyanine green and liposomal indocyanine green by multispectral optoacoustic tomography. *RSC Adv.* **5**, 3807–3813 (2015).

210. Taruttis, A., Morscher, S., Burton, N. C., Razansky, D. & Ntziachristos, V. Fast multispectral optoacoustic tomography (MSOT) for dynamic imaging of pharmacokinetics and biodistribution in multiple organs. *PloS One* **7**, e30491 (2012).

211. Marshall, M. V., Draney, D., Sevick-Muraca, E. M. & Olive, D. M. Single dose toxicity study of IRDye 800CW in Sprague-Dawley rats. in vol. 7576 757609 (International Society for Optics and Photonics, 2010).

212. Sharkey, J. *et al.* A Noninvasive Imaging Toolbox Indicates Limited Therapeutic Potential of Conditionally Activated Macrophages in a Mouse Model of Multiple Organ Dysfunction. *Stem Cells Int.* **2019**, 7386954 (2019).

213. iThera Medical. *MSOT User Guide (User Manual - Part 3, Version 3.8)*. (2017).

214. Cubeddu, R., Pifferi, A., Taroni, P., Torricelli, A. & Valentini, G. A solid tissue phantom for photon migration studies. *Phys. Med. Biol.* **42**, 1971–1979 (1997).

215. Harwood, R. Investigating the physiology of ischaemia reperfusion injury of the mouse kidney and the efficacy of regenerative medicine therapies after acute kidney injury. (University of Liverpool, 2021).

216. Upputuri, P. K. & Pramanik, M. Recent advances in photoacoustic contrast agents for in vivo imaging. *WIREs Nanomedicine Nanobiotechnology* **12**, e1618 (2020).

217. Fratoddi, I., Venditti, I., Cametti, C. & Russo, M. V. How toxic are gold nanoparticles? The state-of-the-art. *Nano Res.* **8**, 1771–1799 (2015).

218. Pan, D., Kim, B., Wang, L. V. & Lanza, G. M. A brief account of nanoparticle contrast agents for photoacoustic imaging. *WIREs Nanomedicine Nanobiotechnology* **5**, 517–543 (2013).

219. Sharkey, J. *et al.* A Noninvasive Imaging Toolbox Indicates Limited Therapeutic Potential of Conditionally Activated Macrophages in a Mouse Model of Multiple Organ Dysfunction. *Stem Cells Int.* **2019**, (2019).

220. Minhas, A. S. *et al.* Measuring Kidney Perfusion, pH, and Renal Clearance Consecutively Using MRI and Multispectral Optoacoustic Tomography. *Mol. Imaging Biol.* **22**, 494–503 (2020).

221. Gao, L., Kwan, Y.-W., Bulmer, A. C. & Lai, C. W. Noninvasive Real-Time Characterization of Renal Clearance Kinetics in Diabetic Mice after Receiving Danshensu Treatment. *Oxid. Med. Cell. Longev.* **2018**, (2018).

222. Merčep, E., Burton, N. C., Claussen, J. & Razansky, D. Whole-body live mouse imaging by hybrid reflection-mode ultrasound and optoacoustic tomography. *Opt. Lett.* **40**, 4643 (2015).

223. Morscher, S. *et al.* Real-time imaging of renal clearance using multispectral optoacoustic tomography. in vol. 8223 822330 (International Society for Optics and Photonics, 2012).

224. Marshall, M. V., Draney, D., Sevick-Muraca, E. M. & Olive, D. M. Single-Dose Intravenous Toxicity Study of IRDye 800CW in Sprague-Dawley Rats. *Mol. Imaging Biol.* **12**, 583–594 (2010).

225. Tanaka, E. *et al.* Real-time intraoperative assessment of the extrahepatic bile ducts in rats and pigs using invisible near-infrared fluorescent light. *Surgery* **144**, 39–48 (2008).

226. Reactive dye | STAR FLUOR 770 NHS ester. *Cyanagen* https://www.cyanagen.com/products/star-fluor-770-nhs-ester/.

227. Grabolle, M., Pauli, J., Brehm, R. & Resch-Genger, U. Structural control of dye–protein binding, aggregation and hydrophilicity in a series of asymmetric cyanines. *Dyes Pigments* **103**, 118–126 (2014).

228. Yang, S. *et al.* Photodegradation of cyanine and merocyanine dyes. *Dyes Pigments* **49**, 93–101 (2001).

229. Gorka, A. P. & Schnermann, M. J. Harnessing cyanine photooxidation: from slowing photobleaching to near-IR uncaging. *Curr. Opin. Chem. Biol.* **33**, 117–125 (2016).

230. Laufer, J., Zhang, E. & Beard, P. Evaluation of Absorbing Chromophores Used in Tissue Phantoms for Quantitative Photoacoustic Spectroscopy and Imaging. *IEEE J. Sel. Top. Quantum Electron.* **16**, 600–607 (2010).

231. Pichai, E. & Lakshmanan, M. Drug Elimination. in *Introduction to Basics of Pharmacology and Toxicology: Volume 1: General and Molecular Pharmacology: Principles of Drug Action* (eds. Raj, G. M. & Raveendran, R.) 117–129 (Springer, 2019). doi:10.1007/978-981-32-9779-1_8.

232. Fuenzalida Werner, J. P. *et al.* Challenging a Preconception: Optoacoustic Spectrum Differs from the Optical Absorption Spectrum of Proteins and Dyes for Molecular Imaging. *Anal. Chem.* **92**, 10717–10724 (2020).

233. Ohnishi, S. *et al.* Organic Alternatives to Quantum Dots for Intraoperative Near-Infrared Fluorescent Sentinel Lymph Node Mapping. *Mol. Imaging* **4**, 15353500200505128 (2005).

234. Beard, P. Biomedical photoacoustic imaging. *Interface Focus* **1**, 602–631 (2011).

235. De Wolf, A. M. & Hendrickx, J. F. A. Effects on Liver Function. in *Personalized Anaesthesia: Targeting Physiological Systems for Optimal Effect* (eds. Hendrickx, J. F. A. & Gambús, P. L.) 245–256 (Cambridge University Press, 2020). doi:10.1017/9781316443217.017.

236. Zhang, Y.-D. *et al.* Feasibility study of high-resolution DCE-MRI for glomerular filtration rate (GFR) measurement in a routine clinical modal. *Magn. Reson. Imaging* **33**, 978–983 (2015).

237. Yoruk, U., Saranathan, M., Loening, A. M., Hargreaves, B. A. & Vasanawala, S. S. High temporal resolution dynamic MRI and arterial input function for assessment of GFR in pediatric subjects. *Magn. Reson. Med.* **75**, 1301–1311 (2016).

238. Khalifa, F. *et al.* Models and methods for analyzing DCE-MRI: A review: Models and methods for analyzing DCE-MRI. *Med. Phys.* **41**, 124301 (2014).

239. Hackstein, N., Heckrodt, J. & Rau, W. S. Measurement of single-kidney glomerular filtration rate using a contrast-enhanced dynamic gradient-echo sequence and the Rutland-Patlak plot technique. *J. Magn. Reson. Imaging* **18**, 714–725 (2003).

240. Jeong, S. *et al.* Estimation of renal function using kidney dynamic contrast material-enhanced CT perfusion: accuracy and feasibility. *Abdom. Radiol.* **46**, 2045–2051 (2021).

241. Klopper, J. F., Hauser, W., Atkins, H. L., Eckelman, W. C. & Richards, P. Evaluation of 99mTc-DTPA for the measurement of glomerular filtration rate. *J. Nucl. Med.* **13**, 107–110 (1972).

242. Rodby, R. A., Ali, A., Rohde, R. D. & Lewis, E. J. Renal Scanning 99mTc Diethylene-Triamine Pentaacetic Acid Glomerular Filtration Rate (GFR) Determination Compared With Iothalamate Clearance GFR in Diabetics. *Am. J. Kidney Dis.* **20**, 569–573 (1992).

243. Hilson, A. J. W., Mistry, R. D. & Maisey, M. N. 99Tc(m)–DTPA for the measurement of glomerular filtration rate. *Br. J. Radiol.* **49**, 794–796 (1976).

244. Mulligan, J. S., Blue, P. W. & Hasbargen, J. A. Methods for measuring GFR with technetium-99m-DTPA: an analysis of several common methods. *J Nucl Med* **31**, 1211–9 (1990).

245. Calamante, F. Arterial input function in perfusion MRI: A comprehensive review. *Prog. Nucl. Magn. Reson. Spectrosc.* **74**, 1–32 (2013).

246. Kovar, D. A., Lewis, M. & Karczmar, G. S. A new method for imaging perfusion and contrast extraction fraction: Input functions derived from reference tissues. *J. Magn. Reson. Imaging* **8**, 1126–1134 (1998).

247. Ahmed, Z. & Levesque, I. R. Pharmacokinetic modeling of dynamic contrast-enhanced MRI using a reference region and input function tail. *Magn. Reson. Med.* **83**, 286–298 (2020).

248. Krepkin, K. *et al.* Dynamic Contrast-Enhanced MR Renography for Renal Function Evaluation in Ureteropelvic Junction Obstruction: Feasibility Study. *Am. J. Roentgenol.* **202**, 778–783 (2014).

249. Mariager, C. Ø. *et al.* Can Hyperpolarized 13C-Urea Be Used to Assess Glomerular Filtration Rate? A Retrospective Study. *Tomography* **3**, 146–152 (2017).

250. Baumann, D. & Rudin, M. Quantitative assessment of rat kidney function by measuring the clearance of the contrast agent Gd(DOTA) using dynamic MRI. *Magn. Reson. Imaging* **18**, 587–595 (2000).

251. Laurent, D., Poirier, K., Wasvary, J. & Rudin, M. Effect of essential hypertension on kidney function as measured in rat by dynamic MRI. *Magn. Reson. Med.* **47**, 127–134 (2002).

252. Peters, A. Graphical analysis of dynamic data: the Patlak-Rutland plot. (1994).

253. Patlak, C. S., Blasberg, R. G. & Fenstermacher, J. D. Graphical Evaluation of Blood-to-Brain Transfer Constants from Multiple-Time Uptake Data. *J. Cereb. Blood Flow Metab.* **3**, 1–7 (1983).

254. Rutland, M. D. A single injection technique for subtraction of blood background in 131I-hippuran renograms. *Br. J. Radiol.* (1979) doi:10.1259/0007-1285-52-614-134.

255. Zhang, J. L., Rusinek, H., Chandarana, H. & Lee, V. S. Functional MRI of the kidneys. *J. Magn. Reson. Imaging* **37**, 282–293 (2013).

256. Zöllner, F. G. *et al.* Kidney Segmentation in Renal Magnetic Resonance Imaging - Current Status and Prospects. *IEEE Access* **9**, 71577–71605 (2021).

257. Liu, B., Ii, V. H. G., Kruger, R. A. & Stantz, K. M. Assessment of photoacoustic computed tomography to classify tissue in a polycystic-kidney disease mouse model. in *Photons Plus Ultrasound: Imaging and Sensing 2006: The Seventh Conference on Biomedical Thermoacoustics, Optoacoustics, and Acousto-optics* vol. 6086 54–61 (SPIE, 2006).

258. Deán-Ben, X. L., Buehler, A., Razansky, D. & Ntziachristos, V. Estimation of optoacoustic contrast agent concentration with self-calibration blind logarithmic unmixing. *Phys. Med. Biol.* **59**, 4785–4797 (2014).

259. Liang, Z. *et al.* Automatic 3-D segmentation and volumetric light fluence correction for photoacoustic tomography based on optimal 3-D graph search. *Med. Image Anal.* 102275 (2021) doi:10.1016/j.media.2021.102275.

260. Rosenthal, A., Razansky, D. & Ntziachristos, V. Quantitative Optoacoustic Signal Extraction Using Sparse Signal Representation. *IEEE Trans. Med. Imaging* **28**, 1997–2006 (2009).

261. Sadick, M. *et al.* Two non-invasive GFR-estimation methods in rat models of polycystic kidney disease: 3.0 Tesla dynamic contrast-enhanced MRI and optical imaging. *Nephrol. Dial. Transplant.* **26**, 3101–3108 (2011).

262. Jiang, K., Tang, H., Mishra, P. K., Macura, S. I. & Lerman, L. O. Measurement of murine single-kidney glomerular filtration rate using dynamic contrast-enhanced MRI. *Magn. Reson. Med.* **79**, 2935–2943 (2018).

263. Annet, L. *et al.* Glomerular filtration rate: Assessment with dynamic contrast-enhanced MRI and a cortical-compartment model in the rabbit kidney. *J. Magn. Reson. Imaging* **20**, 843–849 (2004).

264. Zöllner, F. G. *et al.* Simultaneous Measurement of Kidney Function by Dynamic Contrast Enhanced MRI and FITC-Sinistrin Clearance in Rats at 3 Tesla: Initial Results. *PLOS ONE* **8**, e79992 (2013).

265. Sourbron, S. P., Michaely, H. J., Reiser, M. F. & Schoenberg, S. O. MRI-Measurement of Perfusion and Glomerular Filtration in the Human Kidney With a Separable Compartment Model. *Invest. Radiol.* **43**, 40–48 (2008).

266. Srivastava, T. *et al.* Fluid flow shear stress over podocytes is increased in the solitary kidney. *Nephrol. Dial. Transplant.* **29**, 65–72 (2014).

267. Shimada, S., Yang, C., Kurth, T. & Cowley, A. W. Divergent roles of angiotensin II upon the immediate and sustained increases of renal blood flow following unilateral nephrectomy. *Am. J. Physiol.-Ren. Physiol.* **322**, F473–F485 (2022).

268. Liu, T., Dai, C., Xu, J., Li, S. & Chen, J.-K. The expression level of class III phosphatidylinositol-3 kinase controls the degree of compensatory nephron hypertrophy. *Am. J. Physiol.-Ren. Physiol.* **318**, F628–F638 (2020).

269. Lima, N. K. S. *et al.* Renal ischemia-reperfusion leads to hypertension and changes in proximal tubule Na+ transport and renin-angiotensin-aldosterone system: Role of NADPH oxidase. *Life Sci.* **266**, 118879 (2021).

270. Cheng, S.-Y. *et al.* Losartan reduces ensuing chronic kidney disease and mortality after acute kidney injury. *Sci. Rep.* **6**, 34265 (2016).

271. Masuda, S. *et al.* Identification and Functional Characterization of a New Human Kidney–Specific H+/Organic Cation Antiporter, Kidney-Specific Multidrug and Toxin Extrusion 2. *J. Am. Soc. Nephrol.* **17**, 2127–2135 (2006).

272. Hesketh, E. E. *et al.* Renal Ischaemia Reperfusion Injury: A Mouse Model of Injury and Regeneration. *J. Vis. Exp.* 51816 (2014) doi:10.3791/51816.

273. Aksu, U., Demirci, C. & Ince, C. The Pathogenesis of Acute Kidney Injury and the Toxic Triangle of Oxygen, Reactive Oxygen Species and Nitric Oxide. *Controv. Acute Kidney Inj.* **174**, 119–128 (2011).

274. Zuk, A. & Bonventre, J. V. Acute Kidney Injury. *Annu. Rev. Med.* **67**, 293–307 (2016).

275. Bonventre, J. V. & Zuk, A. Ischemic acute renal failure: An inflammatory disease? *Kidney Int.* **66**, 480–485 (2004).

276. Piers, D. A., Kosterink, J. G. & Meijer, S. Renal handling of technetium-99m DMSA: evidence for glomerular filtration and peritubular uptake. *J. Nucl. Med. Off. Publ. Soc. Nucl. Med.* **30**, 1219–1223 (1989).

277. Lee, B.-F. *et al.* Evaluation of Tc-99m (V) DMSA binding to human plasma proteins. *Kaohsiung J. Med. Sci.* **24**, 1–9 (2008).

278. Eshima, D. *et al.* Animal evaluation of technetium-99m triamide mercaptide complexes as potential renal imaging agents. *J. Nucl. Med. Off. Publ. Soc. Nucl. Med.* **28**, 1180–1186 (1987).

279. PubChem. Mertiatide. https://pubchem.ncbi.nlm.nih.gov/compound/60778.

280. Taylor, A. *et al.* Measuring Technetium-99m-MAG3 Clearance with an Improved Camera-Based Method. 7.

281. Herrler, T. *et al.* 99mTc-MAG3 scintigraphy for the longitudinal follow-up of kidney function in a mouse model of renal ischemia-reperfusion injury. *EJNMMI Res.* **2**, 2 (2012).

282. Roberts, J. *et al.* Detection of early changes in renal function using 99mTc-MAG3 imaging in a murine model of ischemia-reperfusion injury. *Am. J. Physiol.-Ren. Physiol.* **293**, F1408–F1412 (2007).

283. Dostbil, Z. *et al.* Comparison of split renal function measured by 99mTc-DTPA, 99mTc-MAG3 and 99mTc-DMSA renal scintigraphies in paediatric age groups. *Clin. Rev. Opin.* **3**, 20–25 (2011).

284. Kusuhara, H., Yoshida, K. & Sugiyama, Y. In Vivo Characterization of Interactions on Transporters. in *Transporters in Drug Development: Discovery, Optimization, Clinical Study and Regulation* (eds. Sugiyama, Y. & Steffansen, B.) 67–97 (Springer, 2013). doi:10.1007/978-1-4614-8229-1_4.

285. Cunningham, R. F., Israili, Z. H. & Dayton, P. G. Clinical Pharmacokinetics of Probenecid. *Clin. Pharmacokinet.* **6**, 135–151 (1981).

286. Shitara, Y., Sato, H. & Sugiyama, Y. EVALUATION OF DRUG-DRUG INTERACTION IN THE HEPATOBILIARY AND RENAL TRANSPORT OF DRUGS. *Annu. Rev. Pharmacol. Toxicol.* **45**, 689–723 (2005).

287. Robbins, N., Koch, S. E., Tranter, M. & Rubinstein, J. The History and Future of Probenecid. *Cardiovasc. Toxicol.* **12**, 1–9 (2012).

288. Landersdorfer, C. B. *et al.* Competitive Inhibition of Renal Tubular Secretion of Gemifloxacin by Probenecid. *Antimicrob. Agents Chemother.* **53**, 3902–3907 (2009).

289. Landersdorfer, C. B. *et al.* Competitive inhibition of renal tubular secretion of ciprofloxacin and metabolite by probenecid. *Br. J. Clin. Pharmacol.* **69**, 167–178 (2010).

290. Granados, J. C., Bhatnagar, V. & Nigam, S. K. Blockade of Organic Anion Transport in Humans After Treatment With the Drug Probenecid Leads to Major Metabolic Alterations in Plasma and Urine. *Clin. Pharmacol. Ther.* **n/a**,.

291. Lai, R. E., Jay, C. E. & Sweet, D. H. Organic solute carrier 22 (SLC22) family: Potential for interactions with food, herbal/dietary supplements, endogenous compounds, and drugs. *J. Food Drug Anal.* **26**, S45–S60 (2018).

292. Probenecid. https://go.drugbank.com/drugs/DB01032.

293. Sheikh, M. I. & Stahl, M. Characteristics of accumulation of probenecid by rabbit kidney cortical slices. *Am. J. Physiol.-Ren. Physiol.* **232**, F513–F523 (1977).

294. Masereeuw, R. *et al.* Probenecid interferes with renal oxidative metabolism: A potential pitfall in its use as an inhibitor of drug transport. *Br. J. Pharmacol.* **131**, 57–62 (2000).

295. Inotsume, N., Nishimura, M., Nakano, M., Fujiyama, S. & Sato, T. The Inhibitory Effect of Probenecid on Renal Excretion of Famotidine in Young, Healthy Volunteers. *J. Clin. Pharmacol.* **30**, 50–56 (1990).

296. Gisclon, L. G., Boyd, R. A., Williams, R. L. & Giacomini, K. M. The effect of probenecid on the renal elimination of cimetidine. *Clin. Pharmacol. Ther.* **45**, 444–452 (1989).

297. Maeda, K. *et al.* Inhibitory effects of p-aminohippurate and probenecid on the renal clearance of adefovir and benzylpenicillin as probe drugs for organic anion transporter (OAT) 1 and OAT3 in humans. *Eur. J. Pharm. Sci.* **59**, 94–103 (2014).

298. Huang, J. *et al.* Renal-clearable Molecular Semiconductor for Second Near-Infrared Fluorescence Imaging of Kidney Dysfunction. *Angew. Chem. Int. Ed.* **58**, 15120–15127 (2019).

299. Xue, X. *et al.* Critical Role of Organic Anion Transporters 1 and 3 in Kidney Accumulation and Toxicity of Aristolochic Acid I. *Mol. Pharm.* **8**, 2183–2192 (2011).

300. Emeigh Hart, S. G., Wyand, D. S., Khairallah, E. A. & Cohen, S. D. Acetaminophen Nephrotoxicity in the CD-1 Mouse. II. Protection by Probenecid and AT-125 without Diminution of Renal Covalent Binding. *Toxicol. Appl. Pharmacol.* **136**, 161–169 (1996).

301. Darnerud, P. O., Brandt, I., Feil, V. J. & Bakke, J. E. Dichlorovinyl cysteine (DCVC) in the mouse kidney: tissue-binding and toxicity after glutathione depletion and probenecid treatment. *Arch. Toxicol.* **63**, 345–350 (1989).

302. Trumper, L., Monasterolo, L. A. & Elías, M. M. Probenecid Protects against In VivoAcetaminophen-Induced Nephrotoxicity in Male Wistar Rats. *J. Pharmacol. Exp. Ther.* **284**, 606–610 (1998).

303. Liao, X. *et al.* Leflunomide increased the renal exposure of acyclovir by inhibiting OAT1/3 and MRP2. *Acta Pharmacol. Sin.* **41**, 129–137 (2020).

304. Baudoux, T. E. R. *et al.* Probenecid prevents acute tubular necrosis in a mouse model of aristolochic acid nephropathy. *Kidney Int.* **82**, 1105–1113 (2012).

305. Turner, K. C. & Brouwer, K. L. R. In Vitro Mechanisms of Probenecid-Associated Alterations in Acetaminophen Glucuronide Hepatic Disposition. *Drug Metab. Dispos.* **25**, 1017–1021 (1997).

306. de Miranda, P. *et al.* Alteration of zidovudine pharmacokinetics by probenecid in patients with AIDS or AIDS-related complex. *Clin. Pharmacol. Ther.* **46**, 494–499 (1989).

307. Burckhardt, G., Bahn, A. & Wolff, N. A. Molecular Physiology of Renal p-Aminohippurate Secretion. *Physiology* **16**, 114–118 (2001).

308. Even-Sapir, E. *et al.* Kidney Allografts and Remaining Contralateral Donor Kidneys Before and After Transplantation: Assessment by Quantitative 99mTc-DMSA SPECT. 5.

309. Burckhardt, B. C. *et al.* The Renal Na+-Dependent Dicarboxylate Transporter, NaDC-3, Translocates Dimethyl- and Disulfhydryl-Compounds and Contributes to Renal Heavy Metal Detoxification. *J. Am. Soc. Nephrol.* **13**, 2628–2638 (2002).

310. Faucher, Q., Alarcan, H., Marquet, P. & Barin-Le Guellec, C. Effects of Ischemia-Reperfusion on Tubular Cell Membrane Transporters and Consequences in Kidney Transplantation. *J. Clin. Med.* **9**, 2610 (2020).

311. Matsuzaki, T. *et al.* Downregulation of organic anion transporters in rat kidney under ischemia/reperfusion-induced acute renal failure. *Kidney Int.* **71**, 539–547 (2007).

312. Schneider, R. *et al.* Downregulation of organic anion transporters OAT1 and OAT3 correlates with impaired secretion of para-aminohippurate after ischemic acute renal failure in rats. *Am. J. Physiol.-Ren. Physiol.* **292**, F1599–F1605 (2007).

313. Bischoff, A., Bucher, M., Gekle, M. & Sauvant, C. PAH clearance after renal ischemia and reperfusion is a function of impaired expression of basolateral Oat1 and Oat3. *Physiol. Rep.* **2**, e00243 (2014).

314. Zhang, R. *et al.* Upregulation of Rat Renal Cortical Organic Anion Transporter (OAT1 and OAT3) Expression in Response to Ischemia/Reperfusion Injury. *Am. J. Nephrol.* **28**, 772–783 (2008).

315. Kwon, T.-H., Frøkiær, J., Han, J. S., Knepper, M. A. & Nielsen, S. Decreased abundance of major Na+ transporters in kidneys of rats with ischemia-induced acute renal failure. *Am. J. Physiol.-Ren. Physiol.* **278**, F925–F939 (2000).

316. Huls, M., Heuvel, J. J. M. W. van den, Dijkman, H. B. P. M., Russel, F. G. M. & Masereeuw, R. ABC transporter expression profiling after ischemic reperfusion injury in mouse kidney. *Kidney Int.* **69**, 2186–2193 (2006).

317. Bonventre, J. V. & Weinberg, J. M. Recent Advances in the Pathophysiology of Ischemic Acute Renal Failure. *J. Am. Soc. Nephrol.* **14**, 2199–2210 (2003).

318. Khalid, U. *et al.* Kidney ischaemia reperfusion injury in the rat: the EGTI scoring system as a valid and reliable tool for histological assessment. *J. Histol. Histopathol.* **3**, 1 (2016).

319. Benigni, A., Perico, N. & Remuzzi, G. Pathophysiology of Disease Progression in Proteinuric and Nonproteinuric Kidney Disease. in *Comprehensive Clinical Nephrology* (Elsevier, 2019).

320. Ricardo, S. D., Goor, H. van & Eddy, A. A. Macrophage diversity in renal injury and repair. *J. Clin. Invest.* **118**, 3522–3530 (2008).

321. Tampe, D. & Zeisberg, M. Potential approaches to reverse or repair renal fibrosis. *Nat. Rev. Nephrol.* **10**, 226–237 (2014).

322. Zeisberg, M., Strutz, F. & Müller, G. A. Role of fibroblast activation in inducing interstitial fibrosis. *J. Nephrol.* **13 Suppl 3**, S111-120 (2000).

323. Bechtel, W. *et al.* Methylation determines fibroblast activation and fibrogenesis in the kidney. *Nat. Med.* **16**, 544–550 (2010).

324. Prigent, A. *et al.* Consensus report on quality control of quantitative measurements of renal function obtained from the renogram: International consensus committee from the scientific committee of radionuclides in nephrourology. *Semin. Nucl. Med.* **29**, 146–159 (1999).

325. Durand, E. & Prigent, A. Can dimercaptosuccinic acid renal scintigraphy be used to assess global renal function? *Eur. J. Nucl. Med. Mol. Imaging* **27**, 727–730 (2000).

326. Terlouw, S. A., Masereeuw, R. & Russel, F. G. M. Modulatory effects of hormones, drugs, and toxic events on renal organic anion transport. *Biochem. Pharmacol.* **65**, 1393–1405 (2003).

327. Fan, X. *et al.* Use of a reference tissue and blood vessel to measure the arterial input function in DCEMRI. *Magn. Reson. Med.* **64**, 1821–1826 (2010).

328. Yang, C., Karczmar, G. S., Medved, M. & Stadler, W. M. Estimating the arterial input function using two reference tissues in dynamic contrast-enhanced MRI studies: Fundamental concepts and simulations. *Magn. Reson. Med.* **52**, 1110–1117 (2004).

329. Yankeelov, T. E. *et al.* Quantitative pharmacokinetic analysis of DCE-MRI data without an arterial input function: a reference region model. *Magn. Reson. Imaging* **23**, 519–529 (2005).

330. Miner, J. H. Glomerular filtration: the charge debate charges ahead. *Kidney Int.* **74**, 259–261 (2008).

331. Comper, W. D. Resolved: Normal Glomeruli Filter Nephrotic Levels of Albumin. *J. Am. Soc. Nephrol.* **19**, 427–432 (2008).

332. Moeller, M. J. & Tenten, V. Renal albumin filtration: alternative models to the standard physical barriers. *Nat. Rev. Nephrol.* **9**, 266–277 (2013).

333. Harvey, S. J. *et al.* Disruption of Glomerular Basement Membrane Charge through Podocyte-Specific Mutation of Agrin Does Not Alter Glomerular Permselectivity. *Am. J. Pathol.* **171**, 139–152 (2007).

334. Haraldsson, B., Nyström, J. & Deen, W. M. Properties of the Glomerular Barrier and Mechanisms of Proteinuria. *Physiol. Rev.* **88**, 451–487 (2008).

335. Herrler, T. *et al.* The Intrinsic Renal Compartment Syndrome: New Perspectives in Kidney Transplantation. *Transplantation* **89**, 40–46 (2010).

336. Beauvais, M., Patel, M., Balon, H. & Dalal, I. Modification of Tc-99m MAG3 preparation minimizes biliary excretion. *J. Nucl. Med.* **51**, 1558–1558 (2010).

337. Dogan, A. S. & Kirchner, P. T. Hepatobiliary excretion of MAG3. Simulation of a urinary leak. *Clin. Nucl. Med.* **18**, 746–750 (1993).

338. Bannister, K. M., Penglis, S., Bellen, J. C., Baker, R. J. & Chatterton, B. E. Kit preparation of technetium-99m-mercaptoacetyltriglycine: analysis, biodistribution and comparison

with technetium-99m-DTPA in patients with impaired renal function. *J. Nucl. Med.* **31**, 1568–1573 (1990).